THE UNIVERSITY *of* EDINBURGH

Instrumentation development for magnetic and structural studies under extremes of pressure and temperature

Gaétan Giriat

A thesis submitted in fulfilment of the requirements for the degree of Doctor of Philosophy

School of Engineering

The University of Edinburgh

May 2012

Abstract

The study of the magnetic and structural properties of matter under extreme conditions is a fast developing field. With the emergence of new techniques and innovative instruments for measuring physical properties, the need for compatible pressure generating devices is constantly growing. The work described in this thesis is focused on development, construction and testing of several high pressure (HP) cells of novel design. One of the cells is intended for single crystal X-ray diffraction (SXD) studies at low temperature (LT) and the other three HP devices are designed for a Magnetic Property Measurement System (MPMS), two of which are suitable for *dc* susceptibility studies and the other one is aimed at high frequency *ac* susceptibility measurements.

HP crystallographic studies are routinely carried out in diamond anvil cells (DAC) at room temperature while ambient pressure SXD studies are often conducted at LT to reduce atomic vibrations and obtain more precise structural data as well as to study LT phases. Combining HP with LT gives access to a whole new area on the phase diagrams but due to the size of the existing DACs this is generally achieved by cooling down the cells inside a cryostat and it is mainly possible at synchrotrons where dedicated facilities exist. A miniature DAC which can be used with commercially available laboratory cry-flow cooling systems and achieves pressures in excess of 10 GPa has been developed. The design of the pressure cell is based on the turnbuckle principle and therefore it was called TX-DAC. Its dimensions have been minimised using Finite Element Analysis (FEA) and the final version of the cell weighs only 2.4 g. The cell is built around a pair of 600 μm culet Boehler-Almax anvils which have large conical openings for the

diffracted beam. The TX-DAC is made of beryllium copper (BeCu) alloy which has good thermal conductivity and allows quick thermal equilibration of the cell.

The MPMS from Quantum Design is the most popular instrument for studies of magnetic properties of materials. It is designed to measure *ac* and *dc* magnetic susceptibility of sample with detectable signals as low as 10^{-8} emu. The MPMS has a sample chamber bore of 9 mm in diameter and this puts a constraint on the dimensions of the pressure cells. However, several types of clamp piston-cylinder cells and DACs have been designed for the MPMS. The former are used for measurements at pressure up to 2 GPa and the later can be used for studies at higher pressure. Taking advantage of the turnbuckle principle, a DAC (TM-DAC) and a piston-cylinder cell (TM-PCC) for *dc* magnetic studies were built. They allow HP measurements to be performed at the full sensitivity of MPMS. Both pressure cells are made of BeCu and their small dimensions combined with symmetrical design is the key to an ideal background signal correction. The TM-DAC is 7 mm long and 7 mm in diameter, it weighs 1.5 g and with 800 μm culet anvils it can generate a sample pressure of 10 GPa. Inherently the sample volume is limited to approximately 10^{-3} mm^3 and the signal corresponding to this volume of some weakly magnetic material remains below the sensitivity of the MPMS. This constraint led us to the development of the TM-PCC – a piston-cylinder variant of the turnbuckle design. With a 4 mm^3 sample volume it allows the study of weakly magnetic samples in the range 0-1.9 GPa. The TM-PCC uses two zirconia pistons of 2.5 mm in diameter; it is 10 mm long, 7 mm in diameter and weights 2.7 g.

Conventional metallic pressure cells perform well in *dc* mode however in *ac* susceptibility measurements, the Eddy currents set in the cells' body lead to a screening effect which can significantly obscure the signal from the sample. This problem was solved by designing a composite piston-cylinder cell made with Zylon fibre and epoxy resin. The sample is located in the middle of the

cell in the 2.5 mm bore and the pressure is transmitted through zirconia pistons. Keeping the metallic parts away from the sample resolves any interference issue. The composite cell performs well in a pressure range of 0-1 GPa.

The performance of the pressure cells developed within this project is illustrated by studies of various systems at high pressure.

Declaration

This thesis, and the work presented in it is of my own composition, except where otherwise indicated, and was carried out at the School of Engineering of The University of Edinburgh.

Gaétan Giriat

May, 2012

Acknowledgement

I would like to thank everyone who helped me throughout the course of this PhD. First and foremost my supervisor Dr Konstantin Kamenev offering me funding from EPSRC and for being always inspirational, supportive, enthusiastic and patient, very patient.

This research would not have been possible without the technicians Robert Louden and Paul Atkins who turned complicated virtual designs into reality, and Andrew Downie, and Ronnie Proc who produced parts on demand and solved the many problems I harassed them with.

Essential to this research are all my collaborators from the School of Chemistry at the University of Edinburgh; Dr Stephen Moggach and Prof. Simon Parson for the help and advices related to the single crystal X-ray diffraction technique, Dr Alessandro Prescimone, Dr Euan Brechin, Prof. Paul Attfield for providing samples and recommendations for the magnetic measurement, Dr Anya Kusmartseva for all the useful discussions about various parts of my project.

I am also thankful to the foreign groups of Prof. Talal Mallah (Institut de Chimie Moleculaire et des Materiaux d'Orsay, Universite Paris Sud 11, Orsay, France) and Prof. Peter Comba (Institute of inorganic chemistry, Heidelberg university, Heidelberg, Germany) for proving some samples for high pressure measurements.

I have to thank all CSEC residents for creating such a pleasant and enjoyable atmosphere both from a working perspective and from a more recreational view. I am grateful to the whole Kamenev group, Suresh, Weiwei, Junwei,

Xao and in particular Artur, Somchai and Javier for sharing, exchanging, and arguing ideas all along these precious years.

Last but most importantly, I am immensely indebted to my parents and to Sandra.

Contents

Chapter 1

Introduction

1.1 Pressure, a powerful tool

The application of pressure to chemical substances can greatly modify their physical properties (optical, magnetic, and electrical) and it can also be used to alter some chemical reactions. High pressure has been successfully used to synthesise diamond since the 1950s [1, 2] and today it is present, on various pressure scales, in many areas of scientific research, including biology, chemistry, physics, geophysics, and astrophysics [3]. In materials science in particular the use of pressure and other external stimuli combined with various analytical techniques such as Raman spectroscopy, X-ray and neutron diffraction, electrical and magnetic properties measurements, enable the determination of accurate phase diagrams for a multitude of interesting materials. The application of high pressure to magnetic materials allows the tuning of magnetic exchange interactions through increased orbital overlap, and may be used to manipulate functional magnetic and electronic devices

directly, and provide insight into the design of materials with improved functionality under ambient conditions. This approach may also provide powerful insight into the mechanism of exchange interactions, and the behaviour of strongly-correlated electronic materials in general.

1.2 Instrumentation

Since the beginning of the 1900s the number of studies of physical properties of matter under high pressure has increased and P. W. Bridgman has been one of the main contributors to the expansion of the high pressure field. He developed the seal based on the unsupported area principle for a piston-cylinder device as well as the so-called Bridgman anvil device (gasketed opposed anvil design) and reported the compression studies at pressures up to 10 GPa in 1941 [4] and resistivity measurements up to the same pressure in 1952 [5]. Both these techniques gave rise to modern static high pressure research. The advance in high strength materials, machining techniques and sealing methods enabled the piston–cylinder type cells to reach pressure of about 5 GPa, the details of these apparatus are well reviewed by M.I. Eremets 1996 [3]. The gasketed opposed anvil design led logically to the creation of the Diamond Anvil Cell (DAC) which revolutionized the high-pressure instrumentation field in terms of maximum attainable pressure and in terms of the device size. Invented independently by Weir *et al.* 1959 [6] (Figure 1.1) and Jamieson *et al.* 1959 [7] the DAC remains the most powerful tool available to chemists and physicists for studying matter under pressure on a scale extending from ambient pressure to more than 300 GPa.

The DAC design has been extensively developed and adapted to a number of various investigation techniques and there is today a countless number of designs and applications for these devices which are well described in books and review articles [3, 9-16].

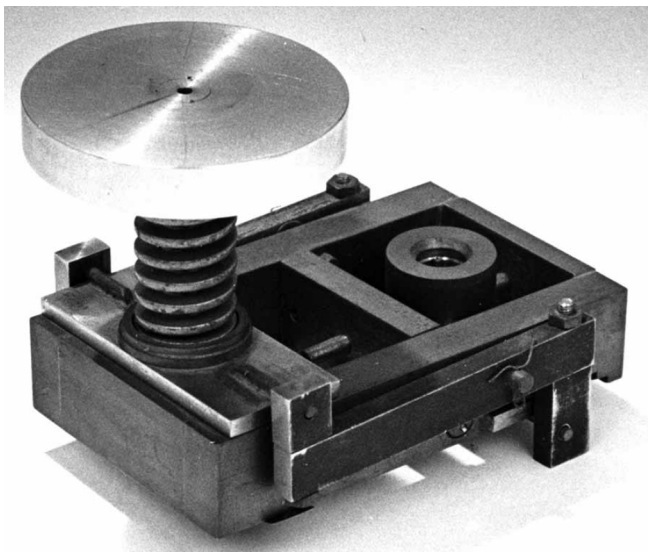

Figure 1.1 Diamond anvil cell made by Charles Weir in 1958 on display at NIST [8].

The work described here is focused on the design of pressure cells, of both - opposed anvil and piston-cylinder types, for magnetic measurements using the Quantum Design Magnetic Properties Measurement System (MPMS). The MPMS is a commercially available magnetometer based on a Superconducting Quantum Interference Device (SQUID), which is why it is also called a "SQUID" magnetometer. The instrument is designed to be used for measuring *ac* and *dc* magnetic susceptibility of materials. With the lowest detectable signal of 10^{-8} emu* it is the most sensitive technique available for this type of measurement.

In order to conceive an effective high pressure environment for a particular instrument, it is important to have a clear understanding of its operational principles and to take into consideration the various constraints characteristic to the instrument as well as the limitations intrinsic to the technique to be used. The detailed description of the MPMS and its operation is given in

* Electromagnetic magnetisation unit (emu) is a cgs unit used to quantify a magnetic moment. It is normally used to describe the bulk magnetisation of a sample. 1 emu (cgs) = 10^{-3} A.m^2 (SI).

Chapter 4, but its main limitations affecting the pressure cell design are outlined here. The sample chamber consists of a tube of 9 mm in diameter and the sample is inserted through a 250 mm long airlock chamber. During a standard susceptibility measurement the sample might be exposed to temperatures ranging from 1.8 K to 400 K. Therefore the pressure cells (including the mounting mechanism) for MPMS must fit into a cylinder of 9 mm in diameter by 250 mm long and they must be made of material exhibiting good mechanical properties over the full temperature range. Moreover, because SQUID measurements are used for studying the magnetic properties of samples and in order to keep the signal-to-noise ratio as high as possible, the pressure cell needs to be constructed from non-magnetic materials. Copper beryllium (BeCu) and nickel chromium aluminium (NiCrAl also known as "Russian alloy") alloys satisfy well the mechanical and magnetic requirements [17]. Because they are commercially available and machinable using standard workshop equipment these alloys are used in most of the existing pressure cells for magnetic measurements. A number of designs of both piston-cylinder [18-25] and opposed anvil [26-28] type cells compatible with the MPMS have been reported. The piston-cylinder type can reach a maximum pressure of 2 GPa while measurements under pressure as high as 20 GPa [29] have been reported for the opposed anvil type. These cells are bulky and have complicated designs which results in undesirable background magnetic signals and makes them difficult to use for studies of weakly magnetic samples. To overcome this limitation two pressure cells based on the turnbuckle principle which allows both type of cells to be made as small as reasonably possible and assembled from as few parts as possible have been developed. The fully symmetrical structure of these cells and their optimised dimensions allow detecting changes in the magnetic moment of the sample at the full sensitivity of the SQUID magnetometer (10^{-8} emu) and the apparatus to reach thermal equilibrium fast.

The MPMS is capable of probing *dc* susceptibility where the sample is exposed to a constant magnetic field and *ac* susceptibility whereby an alternating magnetic field is applied to the sample. All the pressure cells mentioned above perform well in *dc* susceptibility measurements but are not suitable for *ac* susceptibility measurements at high frequencies. This is due to the Eddy currents set up in the metallic body of the cell. Measurements show that for alternating frequencies higher than 10 Hz the screening effect of the currents set up in the cell can obscure the sample's signal significantly. An obvious way of solving this problem is to make a pressure cell from non-conductive/non-metallic material. The design of a composite piston-cylinder pressure cell intended for *ac* susceptibility measurements under pressure of up to 1 GPa and achieving pressure of up to 1 GPa is presented in this work. The full description of the composite cell and the results from mechanical testing and preliminary *ac* susceptibility measurements are given in Chapter 8.

A section of this work is devoted to the fabrication of a DAC for high pressure single crystal X-ray diffraction (SXD) at low temperature. X-ray diffraction (XRD) is a non-destructive analytical technique for structural study. While powder XRD leads to information on unit cell dimensions, SXD provides detailed information about the internal lattice of crystalline substances, including unit cell dimensions, bond-lengths, bond-angles, and details of atomic position. SXD is regarded as the best technique for crystal structure studies; it has been developed in the 1910s and high pressure experiments based on diamond anvil pressure cell have been reported by Piermarini and Weir from early 1960s [30, 31]. With the miniaturisation of DACs [32] it became possible to mount the pressure cell on a standard goniometer head and high pressure SXD quickly became a standard procedure. This technique is available in most X-ray laboratories which have single-crystal angle-dispersive diffractometers and at central facilities where dedicated beam lines are available.

SXD experiments under ambient conditions of pressure are often performed at low temperature using cry-flow systems. The single crystal is glued to the end of a glass fibre which is placed on a goniometer head. Once properly installed on the X-ray diffractometer the crystal is cooled to a set temperature by a flow of cold nitrogen or helium gas and the data collection begins. The description of the SXD setup composed of a Bruker APEX diffractometer and an Oxford Cryosystems Cryostream cooling system and its use is provided in Chapter 4.

The reasons for lowering the sample temperature are as follows: (i) routinely to reduce atomic vibrations and obtain more precise structural data, and (ii) to follow phase transition and study low temperature phases. The same considerations apply to and become even more important in high pressure experiments. Because of the smaller size of the sample and lower scattered intensity, more precise crystallographic data obtained at cryogenic temperatures are essential. More importantly combining high pressure with low temperature adds a new dimension to the phase diagram.

High pressure SXD is a well established technique. However in order to carry out this type of measurements at low temperature the DAC needs to be cooled down. Due to their large thermal mass standard SXD pressure cells such as the Merrill-Bassett DAC [32] or the membrane diamond anvil cell (MDACX) [33] designs require to be cooled inside a cryostat [34, 35] and the whole assembly has to be rotated in order to maximise the accessible reciprocal space. These apparatus are heavy and expensive and only available at central facilities (e.g. ESRF, Diamond Light Source and Spring 8) where some beam lines are optimised for cryogenic techniques.

A DAC for high pressure SXD at low temperature to be used on standard laboratory cryo-flow equipment has been engineered by taking advantage of both the turnbuckle principle DAC and the Boehler–Almax diamond anvil [36, 37] designs. Prior attempts to cool down small pressure cells in a flow of

cold nitrogen gas resulted in the formation of a snow ball around the cell body. This was due to the condensation and solidification of the atmospheric water vapour on the pressure cell surfaces. These tests revealed that the material from which the cell is made of and the dimensions of the cell are both important factors to be taken into account in order to avoid the icing effect. To ensure good thermal conductivity the cell has been made out of BeCu. With 80 wide opening angle, compact dimensions and the mass of less than 2.5 g the turnbuckle X-ray DAC (TX-DAC) has been successfully used in an in-house high pressure SXD experiments at temperature as low as 80 K using an Oxford Cryosystems Cryostream Plus cryo-cooler. Details of the test are presented in Chapter 7.

1.3 Thesis summary

This thesis describes the design, production, testing and use of new pressure cells for the study of magnetic and structural properties of materials. The pressure cells developed for magnetic study are specifically built for a Quantum Design MPMS and must satisfy a number of strict criteria. For crystallographic studies the goal was to engineer a DAC for high pressure low temperature SXD which can be used on standard laboratory angle dispersive SXD equipment without any modification to either the diffractometer or the cooling system.

An overview of the historical evolution of the pressure cells for studies of physical properties and the justification of the need for new devices is presented in Chapter 1. The theory of magnetism and X-ray diffraction is explained Chapter 2. Some basic principles of solid-state magnetism relevant to the materials used to test the cells and the theory of the influence of pressure on magnetism are established; the technique of SXD at high pressure and its importance in structural investigations are described; the

concept of finite elemental analysis is introduced. Chapter 3 is focused on the functioning principles of opposed anvil and piston-cylinder pressure cell and on a review of the relevant existing instruments. The design of the common XRD Merrill-Bassett DAC and its modifications as well as the design of the MDACX previously built for SXD studies at low temperature are explained. On the magnetic properties study side, the various strengths and limitations of the published DAC and piston-cylinder type pressure cells compatible with the Quantum Design MPMS are described. The techniques and the instruments used for carrying the studies of magnetic properties and structure determinations are detailed in Chapter 4 with a special emphasis on the pressure cell's design limitations and the restrictions imposed by each technique and instrument.

In Chapter 5, 6 and 7 the pressure cells that were successfully developed and tested are reviewed and the results obtained for each cell are examined. Chapter 5 describes the Turnbuckle Magnetic DAC (TM-DAC) and the results of measurements on four different samples (PBA - $Mn_3[Cr(CN)_6]_2$, UNi_2, $BiNiO_3$, $Cs_{0.5}NiCr(CN)_6$ nanoparticles) are discussed. Chapter 6 concentrates on the Turnbuckle Magnetic Piston-Cylinder Cell (TM-PCC). The Turnbuckle DAC for high pressure SXD (TX-DAC) at low temperature is explained in Chapter 7.

Chapter 8 is dedicated to the ongoing research on the production of a non-metallic piston-cylinder cell intended for *ac* susceptibility measurements in a Quantum Design MPMS. The design and the manufacturing process of this innovative pressure cell are given alongside some preliminary results.

The specific manufacturing techniques employed to produce the pressure devices presented are summarized in Chapter 9. Finally some general conclusions are given in Chapter 10.

Chapter 2

Theory

2.1 Magnetism

2.1.1 Introduction

Bulk magnetic properties can be measured in the laboratory by a number of techniques and used to reveal the nature of magnetic materials at a microscopic level – and often also the fundamental electrical and electronic properties. The aim of this chapter is to present the relationship between the magnetic character of isolated atoms, any exchange interactions, and co-operative magnetic behaviour, particularly that probed by bulk magnetic susceptibility measurements.

2.1.2 Isolated magnetic moments

Consider the relatively simple case of a magnet composed of isolated atoms with spin and orbital momentum quantum numbers S and L respectively, and let us assume that Russell Saunders coupling applies directly to total angular moment quantum number J. The moment μ_J associated with J is then given by:

$$\mu_J = g\beta\sqrt{J(J+1)} \tag{2.1}$$

g is the Landé factor, which in the case of Russell-Saunders coupling is given by:

$$g = \frac{3J(J+1)+S(S+1)-L(L+1)}{2J(J+1)} \tag{2.2}$$

β is the Bohr magneton, defined as

$$\beta = |e|h/4\pi mc \equiv 9.274\times10^{-24} JT^{-1} \tag{2.3}$$

where e is the charge of the electron, m is the mass of the electron and c is the speed of light. In the case of iron group salts the equation (2.1) is not valid anymore and the contribution of the crystal field has to be considered to determine μ_J. For magnetic ions of the first-row transition metals the 3d shell responsible for paramagnetism is not screened by significant distributions of charge. The partly filled 3d shell feels the effect of any anisotropic crystalline electric field produced by neighbouring ions. For such elements, the effects of the crystal field are stronger than those of spin–orbit coupling which result in a non-degenerate ground state, and the quenching of the orbital angular momentum.

2.1.3 Susceptibility of isolated magnetic moments

When a single magnetic ion is placed in a magnetic field, H, its ground state angular momentum J is split into $(2J+1)$ equally spaced levels denoted by m_J. This is known as Zeeman splitting and the energies E_{m_J} of these levels can be calculated using the following expression.

$$E_{m_J} = -m_J g \mu_B H \tag{2.4}$$

Each m_J level corresponds to a different orientation with regard to the external field and therefore a different projection of the magnetic moment:

$$\mu_{m_J} = m_J g \beta \tag{2.5}$$

The resultant magnetic polarisation, $\langle \mu_{m_J} \rangle$, may be found by calculating the Boltzmann average over all the m_J levels:

$$\langle \mu_{m_J} \rangle = \frac{\sum_{m_J=-J}^{J} \mu_{m_J} \exp(-E_{m_J}/kT)}{\sum_{m_J=-J}^{J} \exp(-E_{m_J}/kT)} \tag{2.6}$$

If the separation ΔE between adjacent energy levels is small in comparison with $k_B T$ the equation (2.6) simplifies to:

$$\langle \mu_{m_J} \rangle = \frac{g^2 \mu_B^2 B_0 J(J+1)}{3kT} \tag{2.7}$$

where B_0 is the magnetic flux in free space. The bulk magnetic polarisation induced in the sample by H is termed the magnetisation, M. In one mole there are N_A atoms, the total magnetic moment per mole is $M = N_A \langle \mu_{m_J} \rangle$ and the molar susceptibility χ is the ratio of the response M to H. Paramagnetic

susceptibities are temperature dependent and to a first approximation, relation (2.7) indicates that the susceptibility χ varies inversely with temperature, which is the Curie Law:

$$\chi = \frac{M}{H} = \frac{C}{T} \tag{2.8}$$

with the Curie constant, $$C = \frac{N_A g^2 \mu_B^2 J(J+1)}{3k} \tag{2.9}$$

The magnetic behaviour of a perfect paramagnet is well described by the Curie Law when the following assumptions are verified:

- The electronic state of the sample is not affected by temperature within the measured temperature range. Hence there is no energy level which population change significantly with temperature.
- There is no interaction between magnetic ions, no preference for a particular orientation of moments relative to one another.

2.1.4 Co-operative magnetism

Experimentally the observed susceptibility often deviates from the Curie Law, often because there are significant interactions between the magnetic centres, or single-ion anisotropies in the Hamiltonian. Where exchange interactions are significant, the magnetic behaviour may be described well at relatively high temperatures with a law of the form:

$$\chi = C/(T-\theta) \tag{2.10}$$

This is the Curie-Weiss law, where C takes the same value as in the Curie Law and the parameter θ, called the paramagnetic Curie temperature or Weiss temperature, is positive for a ferromagnet and negative for an

antiferromagnet. As a magnet with exchange interactions is cooled from a high temperature to a temperature at which $k_B T$ is just a few multiples of the exchange energy, the magnetic moments start to show some degree of short-range correlation; neighbouring moments are no longer randomly oriented, but show a mild preference for a mutual orientation that reflects the nature of the exchange. This cooperative effect reduces or increases the bulk susceptibility of the sample below the critical temperature for an antiferromagnet or ferromagnet respectively – hence the negative or positive value of θ. One simple method of quantifying this effect starts by assuming that there is a local field that favours the appropriate correlation between neighbouring moments which is proportional to the value of M for the sample. This *mean-field* approximation (MFA) then leads to the following relationship between θ and other fundamental properties of the system [38]:

$$\theta = \frac{2zJ(S+1)}{3k_B} \tag{2.11}$$

where z is the number of nearest neighbours of the magnetic ions. However, if such a system is cooled sufficiently, the moments may order spontaneously to an array whose energy minimises the exchange energy; the temperature at which this transition occurs is called the Curie (T_C) or Néel (T_N) temperature for ferro- and antiferromagnets respectively. The magnetic behaviour below these temperatures is best probed by techniques such as neutron scattering which reveal the magnetic structure and excitations. Just above the ordering temperatures mean-field approaches do not work well, and more specialised methods such as series expansions, which treat short-range correlations more carefully must be used. Mean-field methods also do not work particularly well for low-dimensional magnets even well above any ordering temperature [39]. Theory predicts that there is no long-range magnetic order in a 1D or 2D magnet, except the 2D Ising case, at finite temperature. The fact that ordering is seen in many model 1D and 2D systems reflects the fact that

there will always be some finite interaction between chains or planes of moments, and 3D long-range order will set in at a temperature proportional to both the size of this smaller-scale interaction and the extent of the magnetic correlations within chains or planes in the magnet. One consequence of this is that there can be very significant short-range correlations between moments in the more strongly coupled directions in the magnet well above T_N or T_C, and therefore large deviations from mean-field behaviour and the Curie-Weiss Law. However, the greater mathematical tractability of such systems means that there are often exact models – or, at least, very good approximations – to treat their susceptibility [40].

2.1.5 Exchange interaction

Magnetic exchange between ions is a consequence of the coulombic repulsion between electrons, the Pauli Exclusion Principle and Hund's rule of maximum multiplicity. If we restrict the discussion to insulating materials, there are two broad categories of exchange: when the magnetic centres are relatively close, direct orbital overlap may be significant and direct exchange takes place; more commonly such overlap is negligible and any exchange is via bridging diamagnetic atoms or ligands. This second mechanism is known as 'superexchange' [40].

The strength and sign of the exchange constant, J, is controlled by three principal factors: (a) the character of the magnetic ions (M) (*i.e.* the geometry and occupancy of the orbitals containing the unpaired electrons), (b) the geometry of the exchange pathway between M ions and (c) the character of the diamagnetic bridging ion (X). To illustrate the role of these factors, consider the case of two metal atoms, each bearing an unpaired spin on a d_{xy} orbital, where x is the direction between the metal centres. If the metal atoms are bound through σ bonds to p orbitals on bridging ions X such that the angle M-X-M is θ, the sign of J for exchange through this pathway will

depend on θ. For θ = 90°, there is an orthogonal link in the exchange bridge and the sign of the exchange depends on the nature of the exchange between spins in the p_a and the p_b orbitals; in this case, Hund's first rule predicts that exchange is ferromagnetic Figure 2.1. However, if there is an admixture of orbitals in the bridge – for example if θ differs significantly from 90°, then antiferromagnetic contributions will occur, driven by the Pauli Exclusion Principle.

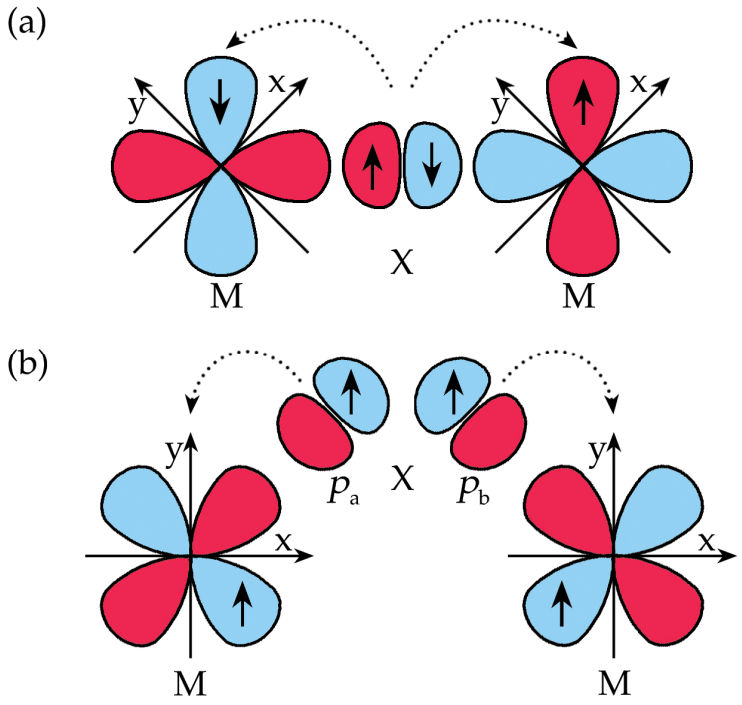

Figure 2.1 View of superexchange mechanisms between two metal atoms each with an unpaired electron on a d_{xy} orbital through the filled p orbital of a ligand (the blue zones are where the wave functions have negative values and the red zones denote wave functions with positive values): (a) Antiferromagnetic coupling in a linear 180 M-X-M system; the exchange is mediated by σ bonding with p orbitals on the bridging ligand X. (b) Ferromagnetic coupling in a 90 M-X-M arrangement. In this case the metal's d orbitals overlap with different p orbitals on the ligand. The p orbitals of the ligand (X) are separated (P_a and P_b) for clarity.

The antiferromagnetic terms are usually stronger than the ferromagnetic terms when they co-exist, and the circumstances under which the antiferromagnetic terms are zero - that is when there is some form of orthogonality in the link between appropriate orbitals on atoms M - are very rare, so ferromagnetic exchange is also rare.

For given M coupling through comparable bridges of the same geometry, the range of the superexchange interaction falls off rapidly with distance r, typically varying as r^{-9} to r^{-12} - while the magnetic dipole-dipole interaction has a relatively long range, decreasing as r^{-3} [41].

2.1.6 Pressure tuning of magnetic systems

The relationship between J and r has been studied experimentally for over 40 years, with the seminal work of Bloch establishing an empirical relationship between the crystal lattice and exchange interaction. Starting from observations of the variation of Curie parameter with interatomic separation in simple transition metal oxides (MO – M = Mn, Co…) and ferrite garnets ($5Fe_2O_3 \bullet 3M_2O_3$; M = Y, Gd, Tb, Dy, Er, Yb) [42-44], Bloch showed that the following expression held remarkably well: $|J| \sim r^{-n}$, with $n \cong 10$ [41]. Several others extended this work to a wider range of compounds [45], notably the layered and cubic perovskites, X_2MF_4 and XMF_3 respectively (X = K, Rb, Tl; M = Mn, Co, Ni), and found a similar empirical relationship, with a slightly higher value of exponent ($n \cong 12$). Since then, a modest number of other materials have been studied, but where co-operative magnetism is driven by what appears to be simple superexchange, nothing significantly different has been observed. At the outset, Bloch's relationship (also called the '10/3' rule on account of the exponent for the dependence of J on volume) was purely empirical. Attempts to test the theoretical principles that underpin it have largely shown that the calculated dependence of J on r is compatible with Bloch's observation [45-47]. The later work [47] was aimed primarily at predicting the way that J varies with temperature for a superexchange-coupled system on account of its thermal expansion, and pointed out that similar principles govern the response to P: that work started with a consideration of the exponential form of the exchange integrals, and showed that if parameters appropriate to transition metal fluorides were used, an exponent n of about 16 was found.

It is perhaps surprising that this field has not been studied to any great degree for almost 30 years - discounting the rather specialised cases of the response of high-temperature superconductors and their parent compounds to pressure (for which every conceivable parameter was studied to try to determine a mechanism for the effect), or the response of colossal magnetoresistors, where magnetostrictive effects - and hence P - can be very significant [48-51]. One reason for this may rest with the fact that magnetic measurements under pressure can be difficult to make and interpret. Difficulties in making good measurements sometimes yield contradictory results - for instance, there are still differences of opinion about the sign of $d\log T_N / dP$ in La_2CuO_4 [52, 53], and there are puzzling differences in the responses of materials with what ought to be very similar exchange pathways (for instance the difference in the response of K_2NiF_4 [54] and $KNiF_3$ [45]).

Interpretation is often complicated by changes introduced by pressure in other parameters that influence the collective properties; these include further-neighbour superexchange, dipole-dipole interactions and the single-ion anisotropy through changes to the ligand field. In some cases this can be turned to the experimentalist's advantage. Thus, in layered, metamagnetic systems such as FeX_2 (X = Cl, Br), the metamagnetic transition temperature is sensitive to the balance between competing exchange and ligand-field effects, and the transition itself is often accompanied by large changes in the susceptibility, so may give a clear signal that is relatively easy to detect. The use of the most incisive probes such as inelastic neutron scattering, allowing the determination of zone-centre energies and spin-wave dispersion, enabled experimentalists to track changes in several of the terms that give the magnetic excitations [55], complementing susceptibility [56, 57] and antiferromagnetic resonance data [58].

Susceptibility measurements require samples that are large compared to those needed for DAC work in an X-ray diffractometer; this problem is even worse for neutron scattering measurements [59]. Mossbauer studies have been performed at pressures up to the Mbar region [60] and μSR measurements can access greater than 10 kbar [61], but such measurements also require very specialised equipment.

Another area in which changes in magnetism may be very sensitive to pressure is that of magnetic systems in which the orbital contribution to the magnetic moment is significant and where it may also display a form of spatial correlation. A key example is K_2CuF_4 in which the Cu^{2+} ions are found in tetragonally distorted CuF_6 octahedra, arranged in an antidistortive array such that exchange pathway involves an orthogonal bridge and is ferromagnetic. Pressure suppresses this form of distortion, and with it the ferromagnetic component of exchange, resulting in a structural and magnetic transition at 9.5 GPa [62-64]. This type of phenomenon has important consequences for the response of a much wider range of orbitally ordered or disordered systems, including some magnetite CMR materials, to pressure [48-51].

2.2 X-ray diffraction

Single crystal X-ray diffraction is arguably the best technique to obtain structural information from most crystalline materials [65-67]. The nature of the diffraction depends on the crystal structure and on wavelength. When the wavelength of the radiation is comparable or smaller than the inter-atomic distance, which is the case for X-rays, diffracted beams may be diffracted through an angle $2\theta_{hkl}$ relative to the incident beam, where hkl are the Miller indices of a particular set of planes of atoms in the structure. The diffracted beams are found when the reflections from parallel planes of

atoms interfere constructively. When the path difference for rays of radiation reflected from adjacent atomic planes is equal to an integral number of wavelength constructive interference takes place. This observation is described by Bragg's law:

$$2d_{hkl}\sin\theta_{hkl} = n\lambda \tag{2.12}$$

where d_{hkl} is the distance between the planes, hkl, and λ is the wavelength of the incident radiation.

The nature of the allowed reflections allows the symmetry (space group) of the crystal to be determined. However, a full structural determination, including the location of all the atoms in the unit cell, also requires measurement and analysis of the intensity of the reflections. The intensity of scattered radiation is proportional to the structure factor, F_{hkl} squared; and F_{hkl} is dependent on both the position of each atom and its scattering factor; it is given by the equation

$$F_{hkl} = \sum_j f_j \exp[2\pi i(hx_j + ky_j + lz_j)] \tag{2.13}$$

where f_j is the scattering factor of the j^{th} atom and x_j, y_j, z_j are its co-ordinates. If the structure factors are known, it is possible to calculate the electron density distribution in the unit cell, and thus the atomic position.

2.3 Finite element analysis

Finite element analysis (FEA) is a numerical technique which is used for solving complex engineering problems. It is based on the finite element method (FEM) which is a mathematical method that was developed in early

1940s and was first used for solving an engineering problem - modelling airplane wings - by Boeing in the 1950s [68]. Solid parts and assemblies as well as the stress conditions they are exposed to can be represented by mathematical models which are governed by differential equations. Most of the time the intricate geometry and boundary conditions of structural problems render these equations too complex to be solved directly and the FEM uses integral formulations to offer an approximate solution to this set of equations. By breaking down a large complex problem into many smaller problems and connecting these through the boundary conditions using complicated mathematics, the FEM provides us with an approximate solution to the overall problem. With the general expansion of computational power the FEA has become the prevalent technique used for analysing physical phenomena in the field of structural, solid, and fluid mechanics as well as for the simulation of heat transfer and electromagnetic field problems.

The basic steps in FEA procedures are the followings:

- The pre-processing:

The solution domain is divided into a finite number of discrete elements. The volume under study is described by nodes and elements. This action is also referred to as the “meshing”. A set of equations providing an approximate solution for a generic element is developed. The elements are assembled to represent the entire problem thus constructing the global stiffness matrix. And finally the boundary conditions and the loading are defined.

- The Solving:

The equations are solved to obtain nodal results, such as displacement values or temperature values at different nodes.

- The post-processing:

It is the conversion of the nodal results into the physical quantities of interest such as stress, strain, heat flux, electrical or electromagnetic fluxes.

The simulations reported in this thesis have been conducted within the frame of linear static structural analysis aimed at assessing the stress generated in the various components of the cells when under load, hence optimising the design of pressure cells. The results are expressed in terms of von Mises stress distribution (see section 2.3.1). This is not the first time FEA is used in conjunction with the development of such high pressure devices. Since the 1980s [69] FEA has been used increasingly in the construction of DACs mostly to test the strength and improve the design of the anvils [70, 71] and that of the supporting plates [72-74].

Many commercial FEA packages are available to carry out engineering simulation and design optimisation. The calculations presented within this project have been made using ANSYS Workbench [75]. This software is an all-in-one solution to the design and the simulation of mechanical parts, it incorporates pre-processing (geometry creation, meshing), solver and post-processing modules in a unified graphical user interface. CAD models created in other software (Solid Edge in this case) can also be imported readily into ANSYS. Once the geometrical model is completed the course of action follows the standard FEA procedure. The mesh generation is an important step. In theory the finer the mesh the more accurate the model should be. However, increasing the number of nodes also increases considerably the computing resources and therefore the time needed to solve the model. In practice a simulation's solution should always be checked for convergence to prevent erroneous solutions. This means that after obtaining a first result based on the original mesh, the mesh is refined and a second

solution is generated. If the second solution gives a value within a set accuracy limit the process is completed. If the accuracy limit is exceeded then the process is repeated until the solutions converge within the limit. In the next step ANSYS solves the calculations for each node and returns the results corresponding to a defined physical quantity, e.g. stress or deformation, as colour map. Within the post-processing module it is possible to rotate and to slice a 3-D part in any direction in order to examine thoroughly the results.

In this work, the motivation for carrying out FEA is to determine the stress distribution inside the pressure cells' parts under load. Since the simulations presented took place in the elastic regime the only material's properties which needed to be specified in the pre-processing step were the Young's modulus and the Poisson's ratio.

2.3.1 Von Mises stress

The von Mises theory is a failure theory often employed to define the beginning of yield for ductile materials in which the multidirectional stress components present in a system are combined to define a failure criterion.

The von Mises stress σ_{eq} also known as the equivalent stress or the effective stress has become a widely accepted parameter allowing the determination of the yielding point of ductile materials. For 3-dimensional problems and in Cartesian coordinate system it is expressed by the following formula:

$$\sigma_{eq} = \frac{1}{\sqrt{2}}\sqrt{(\sigma_x - \sigma_y)^2 + (\sigma_y - \sigma_z)^2 + (\sigma_z - \sigma_x)^2 + 6(\tau_{xy}^2 + \tau_{yz}^2 + \tau_{zx}^2)} \qquad (1.14)$$

in terms of the stress components with shear stresses $\tau_{xy}, \tau_{yz}, \tau_{zx}$ and principal stresses $\sigma_x, \sigma_y, \sigma_z$. It is considered that a material yields when the value of the von Mises stress reaches the yield strength of the material.

Chapter 3

Literature review: the design and operational principles of opposed-anvil and piston-cylinder pressure cells.

3.1 Diamond Anvil Cell

Since its invention in 1959 the diamond anvil cell revolutionised the high pressure research. It is the method which allows the highest static pressures as high as 400 GPa to be applied to a sample in quasi-hydrostatic conditions. The basics of the DAC principle as well as a few examples of DACs developed for X-ray diffraction and for magnetic studies are described in this section. Further information on DACs construction and their use can be found in the literature cited in references [3, 9-16].

3.1.1 Practical consideration and nomenclature

The method relies on the following principle: a gasket with a hole containing a sample, a pressure calibrant and a pressure medium is clamped between a pair of diamond anvils (Figure 3.1). The sample chamber and therefore the sample size is inversely proportional to the maximum working pressure. To increase the pressure the two diamonds are pushed towards each other by a thrust generating mechanism (screw drive clamp, expandable membrane or external mechanism such as hydraulic ram), the gasket deforms and becomes thinner between the diamonds' culets thus reducing the sample volume. The gasket forms a perfect seal in contact with the culets and the sample can be either a gas a liquid or a solid.

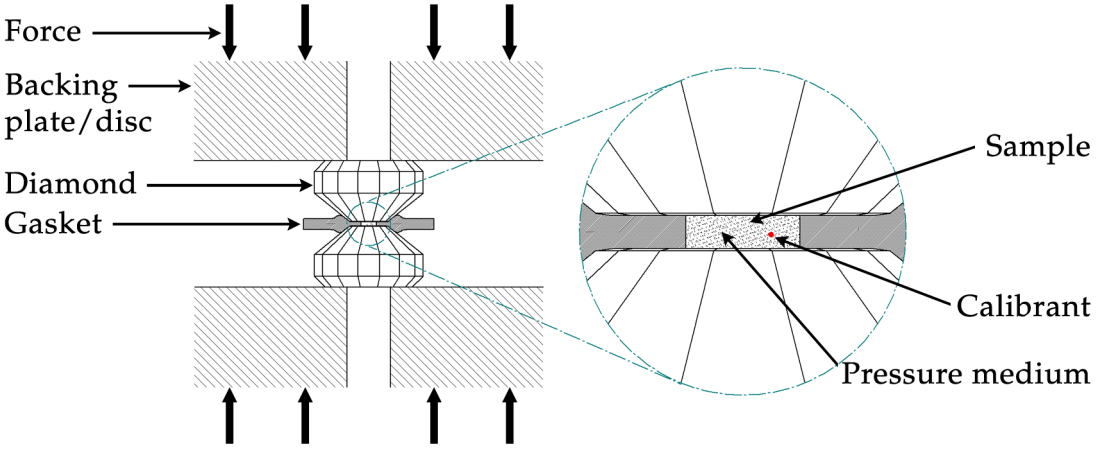

Figure 3.1 Opposed diamond anvil pressure cell principle.

Pressure transmitting medium

In order to maintain good hydrostatic conditions when studying a solid sample the sample chamber is filled with a pressure transmitting medium. It can be either a soft solid such as NaCl, AgCl or steatite, a liquid such as Daphne oil, Fluorinert or 4:1 methanol:ethanol or a gas such as nitrogen, argon or helium. The choice of the pressure medium depends on the

pressure regime and the temperature range at which the measurement will take place [76, 77]. The compatibility with the sample and with the technique of study as well as the ease of use are of course some important considerations too. Gases provide the best hydrostaticity and don't normally react with the samples, however they require a special loading procedure either cryogenically or within a pressurised vessel [78, 79] which are not always available for a particular design of the pressure cell. In terms of hydrostaticity, helium is by far the best pressure medium. While nitrogen and argon give some signs of uniaxial stress at about 10-13 GPa [80, 81] helium remains hydrostatic up to 30-50 GPa [80-82]. Liquid pressure media remain the best option for high pressure experiments and amongst them the mixture of 4:1 methanol:ethanol is the most commonly used medium for high pressure single crystal X-ray diffraction study. It provides good hydrostaticity at room temperature up to 10 GPa [83] but it can, in some cases, react with or dissolve the sample. When this is the case, pure hydrocarbon solution of petroleum ether, pentane, isopentane, Daphne 7373, Daphne 7474 or a mixture of hydrocarbon compounds can be employed. These are not suitable for neutron diffraction or proton-NMR studies and for this type of experiments some solution of fluorinated aliphatic compounds of various grade containing no hydrogen and branded Fluorinert (FC70, FC75, FC77, FC84, FC87) [84, 85] are available from 3M.

The room temperature solidification pressure of commonly used pressure media are presented in Table 3.1. Under the effect of increasing pressure or decreasing temperature or both, the fluids become solid resulting in pressure inhomogeneity and non-hydrostatic effects. This is true for all fluid pressure media when used at cryogenic temperature. On cooling down the liquid to solid transition of pure chemical is abrupt and comes with a sudden pressure drop which damages soft crystal samples. The use of chemicals mixture such as 1:1 Fluorinert FC-70 and FC-77, 4:1 methanol and ethanol, 1:1 *n*-pentane and isopentane or Daphne 7373 oil allows for a slower and smoother

transition. Daphne 7373, trademark of Idemitsu [86], is a mixture of olefins which presents the advantage of not having any discontinuous pressure drop when it solidifies. Moreover Daphne 7373 volume reduction on cooling from room temperature to liquid helium temperature is lower than that of other liquid pressure media [87-89]. It is also less volatile compared to ethanol and the pentane and allows for a slow sealing of the sample chamber. Recently Keizo Murrata reported on the development of Daphne 7474 which exhibits even higher solidification pressure than Daphne 7373 at room temperature.

Table 3.1 Room temperature solidification pressure P_s of commonly used pressure transmitting media. *For gases the quasi-hydrostatic pressure limits P_q do not necessarily coincide with P_s. For instance the P_q of argon, nitrogen and helium are respectively in the range 8-10 GPa, 10-13 GPa and 30-50 GPa [76, 80-82].

Medium	P_s (GPa)	Reference
Helium	11.5-12.1*	[80, 81, 90]
Nitrogen	2.4*	[80, 81]
Argon	1.5*	[80, 81]
Methanol ethanol 4:1	10.0-10.5	[76, 80]
n-pentane isopentane 1:1	7.0-7.3	[76, 77, 83]
Daphne 7474	3.7	[81, 89]
Daphne 7373	2.2-2.4	[76, 87, 88]
Fluorinert 84/87 1:1	2.3	[81, 85]
Fluorinert 70/77 1:1	0.8-1.2	[76, 85, 87]

Solid pressure transmitting media are used when the other types are not convenient. The use NaCl results in immediate non-hydrostatic effects on increasing pressure however above 5 GPa the hydrostaticity is comparable to that of solidified Fluorinert 70/77 or Daphne 7373 [76].

Pressure calibration

The ruby ($Al_2O_3:Cr^{3+}$) fluorescence technique is widely accepted as the gauge for DAC pressure determination. It has been introduced and developed by R. A. Forman, G. J. Piermarini, J. D. Barnett and S. Block, in 1972 [91, 92] and calibrated against the Decker's equation of state (EOS) for NaCl up to 19.5 GPa in 1975 [93] by the same group. Ruby has a strong luminescence doublet R_1 and R_2 associated with the chromium ion Cr^{3+} at 6942.5 Å and 6927.4 Å under ambient conditions. The pressure dependence of the R_1 line shift was determined to be nearly linear with the coefficient $\Delta\lambda / \Delta P = 0.364$ Åkbar^{-1}. In 1986, H. K. Mao, J. Xu, and P.M. Bell proposed a new calibration of the R_1 line shift against the EOS of copper under quasi-hydrostatic conditions up to 80 GPa [94] which was confirmed and extended to above 110 GPa in 1989 [95]. The calibration is described by (3.1)

$$P = \frac{1904}{B}\left[\left(1+\frac{\Delta\lambda}{694.24}\right)^{B} - 1\right] \tag{3.1}$$

where P is pressure in GPa, is the ruby R1 line wavelength shift in nm and B is equal to 5 for non-hydrostatic conditions and 7.665 for quasi-hydrostatic conditions.

Although this calibration has been revised many times in the recent years it remains correct for pressure smaller than 50 GPa with an error of ±0.03 GPa.

Temperature also affects the R_1 line wavelength however a low temperature study [96] showed that the pressure dependence of the R_1 shift, down to at least 10 K, is identical to the dependence observed at 300 K.

Anisotropic stress condition affects the R lines widths and position and to some extend they also depend on the chromium concentration (60-23500 ppm) and internal strains in the ruby. Usually ruby chips randomly cut from bulk crystal are used but greater accuracy and

reproducibility can be obtained using high-quality ruby sphere (1-50 μm in diameter) with homogenous luminescence characteristics and 3000 ppm chromium content [97]. Moreover such ruby spheres are convenient to handle, easy to identify visually and provide a strong signal. An extensive study on the effects of pressure on ruby which reviews the existing revisions of the ruby pressure scale has been published by Syassen [98] in 2008.

Another procedure for pressure determination at low temperature is based on the known pressure dependence of the superconducting transition temperature (T_c) of pure metals. This technique is especially well suited for magnetic studies since the transition can be followed accurately without the need for additional equipment. High purity lead (Pb), tin (Sn) and indium (In) undergo superconducting transitions at 7.20 K, 3.73 K and 3.40 K respectively under atmospheric pressure. Their pressure dependences have been calibrated up to 10 GPa in 1981 [99] and follow the expression given in Table 3.2. The linear pressure dependence of T_c for Pb has later been confirmed up to 15 GPa [100]. The high sensitivity of modern magnetometers allows the detection of the signal associated with the sharp T_c of a tiny amount of these metals which above T_c does not interfere with the signal of the sample under study.

Table 3.2 Pressure dependence of T_c for Pb, Sn and In up to 5 GPa [99].

Pb	$T_c(P) = T_c(0) - (0.365 \pm 0.003)P$
Sn	$T_c(P) = T_c(0) - (0.4823 \pm 0.002)P + (0.0207 \pm 0.0005)P^2$
In	$T_c(P) = T_c(0) - (0.3812 \pm 0.002)P + (0.0122 \pm 0.0004)P^2$

Alternative ways of pressure calibration encompass the study of lattice parameters of compounds with know EOS. NaCl can be used simultaneously as a pressure transmitting medium and as a 'manometer' based on Decker's EOS, and in the megabar pressure range the shift of the first-order Raman

band of the diamond anvil (1332 cm^{-1} at ambient pressure) can be used to estimate the pressure [14]. The later has recently been calibrated up to 410 GPa [101].

Gasket

Along with the anvil culet size and alignment, the gasket is an essential part of the DAC on which the maximum accessible pressure depends. The nature of the investigations as well as the working pressure range dictates the material and the dimensions of the gasket. As a general rule the gaskets which deform plastically on pressure increase must be made from high strength yet ductile materials and metals are an obvious choice. Conventional gaskets are made from simple metal sheets of initial thickness 150-300 μm and indented to the desired thickness by aligned anvils. Then the sample chamber is created by drilling a hole at the centre of the indentation, it is typically done by using spark erosion or laser cutting techniques which provide a high level of accuracy. A poorly centred hole leads to the hole enlarging in an asymmetric manner on pressure increase and results in failure when it reaches the culet edge. Figure 3.2 illustrates the preparation of a simple metallic gasket.

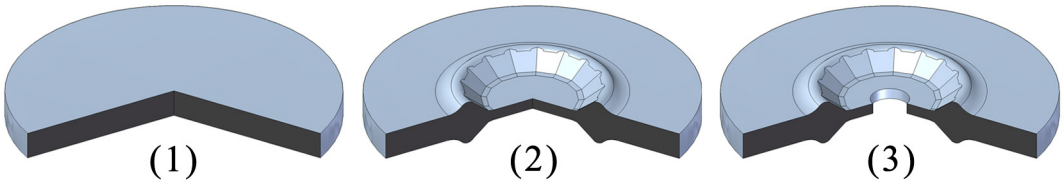

Figure 3.2 (1) Gasket 3 mm in diameter and 0.25 mm thick. (2) The gasket is indented to a thickness of 100 μm by a pair diamond anvil of 800 μm culet beveled to 900 μm. (3) A 350 μm diameter hole is drilled at the centre of the indentation.

The gasket acts as a sample containing volume and due to its plasticity it also has a large effect on the stress distribution in the diamond culet edges. As the gasket material is squeezed between the diamond culets it extrudes outwards and provides massive support to the anvils. Theoretical studies and FEA calculations [69, 70, 102-104] have shown that high-strength pre-thinned gaskets are vital for achieving high pressures without catastrophic failure. The frictional forces between the anvils and the gasket's inter-culets region allows the gasket to withstand the central hydrostatic pressure and the gasket material located outside of the culet region provides an essential support which increases significantly the working pressure of a gasket for a given thickness.

There is a trade-off between the sample chamber size and the maximum achievable pressure. The thinner is the gasket and the smaller is the central hole the higher is the accessible pressure. The mechanical properties of the material, the thickness of the indented gasket and the sample hole diameter must be chosen carefully for a particular pressure regime. As general rules and to ensure good stability of the DAC the sample holes should not exceed a third to half of the culet diameter and the thickness of the gasket should remain between 1/10 and 1/20 of the culet diameter.

Practically any metal is suitable for use as gaskets with stainless steels and tungsten being standard (tungsten becomes brittle at low temperature and should be avoided in this condition), BeCu is used for magnetic studies for pressures up to 10 GPa and a bimetallic BeCu/NiCrAl gasket can reach 30 GPa [105]. Inconel or rhenium are used for very high pressure regime. Some exotic non-metallic gaskets are based on mixture of epoxy resin and small particles of high compressive strength filler such as diamond powder, boron carbide, amorphous boron, cubic boron nitride and magnesium oxide and can achieve pressures of 40-65 GPa [106-108].

Other modifications to the conventional gaskets implementing insulation for laser heating [109, 110] or resistivity measurements [111], or sample volume increase [112-114] are regularly reported. In these cases a metallic gasket or at least a metallic ring providing support to the inter-culet material is always present with the addition of matrix and fillers similar to those cited above.

Anvils

Diamonds used in DAC generally have Drukker (Figure 3.3), brilliant, modified brilliant or Boehler-Almax design cuts [16, 36, 37]. The later, illustrated in Figure 3.9, is a significant improvement over the conventional anvil's shape. For similar anvil size, it allows for much larger aperture with a 4θ opening as large as 90 . With respect to its hardness, diamond as a single-crystalline material is the most suitable material to use as anvil in a high pressure cell. It is very strong in compression in certain directions, the culet and table are polished parallel to the (100) crystallographic diamond plane to take advantage of this strength, but it is also very weak in tension and in shear. To prevent diamond breakage, the support must be machined with great accuracy, the anvils must be properly aligned and often the culet is bevelled to avoid excessive stress concentration on the culet edges. Diamonds with a flat region of 20 μm in diameter surrounded by bevelled edges and a sample space of about 10 μm in diameter are used to reach the maximum pressure.

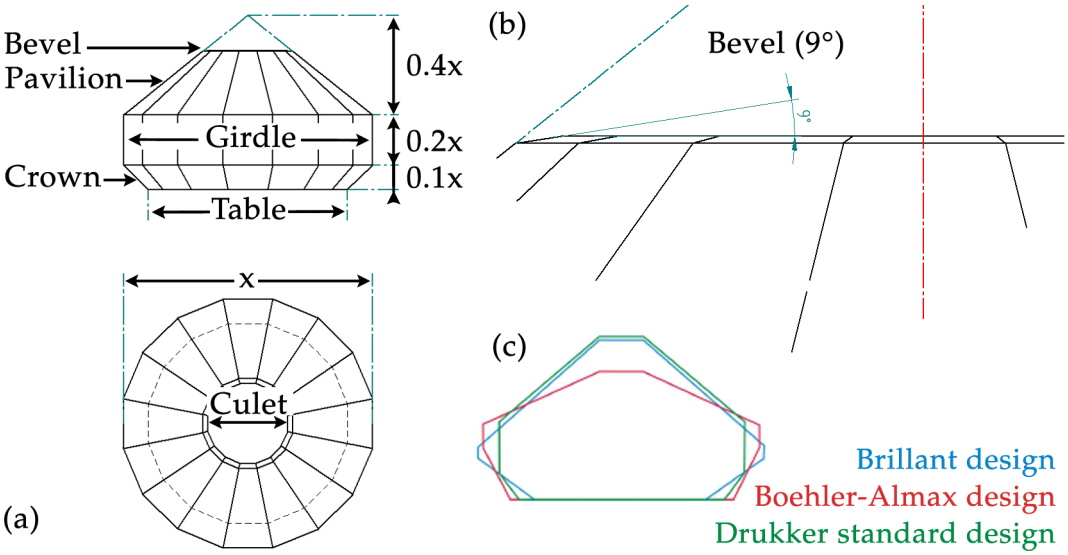

Figure 3.3 (a) Drawing of a 16-sided Drukker diamond anvil design. (b) Detail view of a standard 9 bevel on an 800 μm culet. (c) Overlaid cross-section contours of three designs of diamond anvils: Drukker standard (green), brilliant (blue) and Boehler–Almax (red) [16].

As a general rule the maximum pressure (GPa) for a simple flat culet of diameter d (mm) to be used in routine and safe manner is [115]:

$$P_{\max}(GPa) = 10/d(mm) \tag{3.2}$$

For instance an anvil with a culet of 0.8 mm can routinely be used to reach pressure of 12.5 GPa. This equation is valid for diamond of around 60 mg (0.3 carat) with table of 2 mm to 3 mm in diameter. Larger diamonds can be used however their cost which increases exponentially and the high probability that a flaw, which might lead to a failure, exist in the anvil act as limiting factors. In some cases the optical properties of the anvil might be of importance. The most frequently used diamonds in high pressure experiment are of type I. They are transparent to visible light and to short X-rays (above 10 keV) but their nitrogen impurities content results in some absorption in the UV and IR wavelength. For far-infrared and Raman studies type IIa diamonds which contain only traces of nitrogen are preferred.

Anvil's support

The backing plate also known as backing disk, backing seat or anvil seat (Figure 3.1) is, after the diamond and the gasket, the part of the DAC experiencing the highest level of stress. Therefore it has to be made of a strong material. Hardened BeCu, hardened steel, beryllium (Be) and tungsten carbide (WC) are all suitable candidates. The seat is designed to work almost exclusively in compression and the stress it withstands is easily calculated from the supported surface area of the anvil table and the maximum force applied to the anvil. It should not exceed the yield strength of the seat material. The anvil is generally placed on a plane surface of the plate, seats in a recess or, in the Boehler-Almax design, rests in a countersink matching accurately its shape (Figure 3.9) [36, 37]. With the exception of when the support is provided by a transparent material such as sapphire [116] or diamond [73, 117], a hole through the plate, larger than the culet size, gives optical access and allows anvil alignment.

The size and shape of the backing plate is linked to the alignment mechanism and the physical study technique that the pressure cell is designed for, however most of the time it consists of a disk a few millimetres thick with a conical hole in its centre for optical access.

Alignment of the anvils

A good anvil alignment is essential to reach any pressure without diamond or gasket failure. The alignment directions are depicted in Figure 3.4. The translation of the anvil in the XY plane ensures the culets concentricity and the angular movement or tilt alignment allows the tuning of the culets surface parallelism.

In order to reach the maximum pressure for a given culet size the diamond translational alignment must be achieved to an accuracy of a few μm and the parallelism of the culets should remain better than 0.2 degree. Greater misalignment causes the gasket to deform asymmetrically when increasing pressure and eventually leads to the failure of the setup and possible diamond breakage. Under moderate forces a larger degree of misalignment is acceptable, for instance with a force applied to the diamond of 5 kN a lateral misalignment of around 10 % remains acceptable; the gasket hole will move towards the edge of the culet but the diamond won't fail.

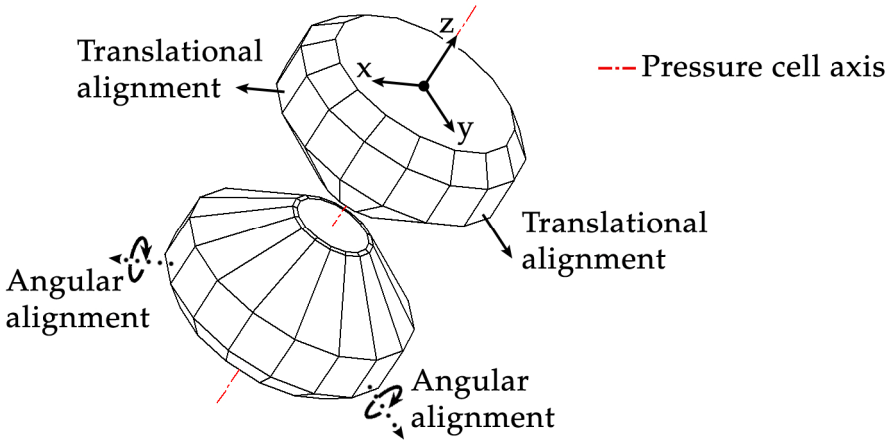

Figure 3.4 Schematic view of an aligned pair of diamond anvil. The culet and the table of the diamonds lie in the XY plane. The parallelism of the culets relies on the angular alignment.

Anvils are glued or clamped to their respective seats to form a solid assembly. It is the position of these assemblies which will be adjusted to obtain a good culet alignment. Seats can be of various shapes. A disk backing plate is adjusted laterally with three or more set screws lying in the XY plane to provide translational alignment. If both backing plates are disks the parallelism relies on the thrust mechanism as is the case in the Merrill-Basset pressure cell (Figure 3.5). To enable translational and angular alignment a disk backing plate should be paired up with a hemispherical seat. A hemispherical rocker is tilted in its socket to allow for the parallelism to be optimised. Another system used for complete alignment of the anvil is a pair

of semi-cylindrical rockers whose axes lie in the XY plane and are set perpendicular to each other account for alignment in all directions; they can be translated along and tilted about their respective axis using set screws.

It should be noted that with the accuracy of modern machining techniques various parts of the pressure cell can be produced with a tolerance of a μm and the parallelism of the culet and table of a diamond anvil is better than 0.085 degrees. As a result the parallelism alignment mechanism is not always necessary and some pressure cells operating in the Mbar range without such mechanism have been reported [118, 119], a modified version of the piston-cylinder Mao-Bell type cell [120, 121] is also commonly used in this pressure regime.

A more comprehensive review of the existing alignment mechanisms and their operation can be found in the following references [3, 12, 122].

3.1.2 Diamond Anvil Cell for X-ray diffraction

Single crystal X-ray diffraction is the technique providing the best insight into crystal structure determination and the ability to perform this type of measurements under high pressure gives information about induced structural phase transitions and offers the possibility to explore new regions of the phase diagrams.

The "Merrill-Bassett" DAC has been developed in 1974 for axial access single crystal X-ray diffraction studies. Its initial design shown in Figure 3.5 reveals the main strengths of this cell which are its small size, its simplicity and the possibility to access large segment of the sample's reciprocal space. Using the right materials and the optimised design Merrill and Bassett produced the first "miniature" DAC which can be mounted on a standard goniometer head and achieved a pressure of 2.5 GPa. The body of the cell consists of two triangular stainless steel plates. Each diamond is located in a little recess on a

Be disk itself located on one of the triangular plates. At the centre of the Be disk a 1 mm hole provides optical access to the sample. The thrust is generated by tightening the three symmetrically located screws which pull the triangular plates together. The Be disks used to support the diamonds also serve as X-ray windows and allow the measurement of 2θ angles up to 100 . There is no possibility of aligning the diamond in the XY plane and in order to keep the culets parallel the three screws have to be tightened uniformly in small increments.

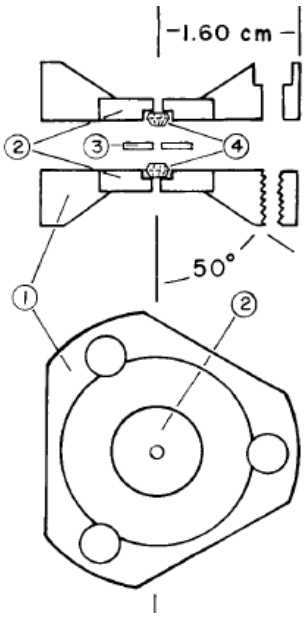

Figure 3.5 Diagram of miniature gasketed diamond anvil pressure cell. (1) stainless steel platens; (2) Be disks; (3) Inconel gasket; and (4) diamond anvils [32].

In 1977 Hazen and Finger proposed a modified design of the Merrill-Bassett DAC shown in Figure 3.6 in which the Be disks have been replaced by boron carbide disks without any hole or recess, the diamonds are attached to the centre of these disks with an epoxy-type cement. Both steel plates have been fitted with three threaded holes accommodating grub screws which allow a fine tuning of the boron carbide disk position relative to the centre of the triangle which in turn allows a perfect alignment of the diamonds in the XY plane. One of the plates, the "bottom half", is fitted with three guide pins and the other one, the "top half", features three matching holes so that the two

halves fit smoothly together and stay parallel. These alignment features bring more stability while applying pressure; however the culets parallelism is still relying on a uniform tightening of the three screws.

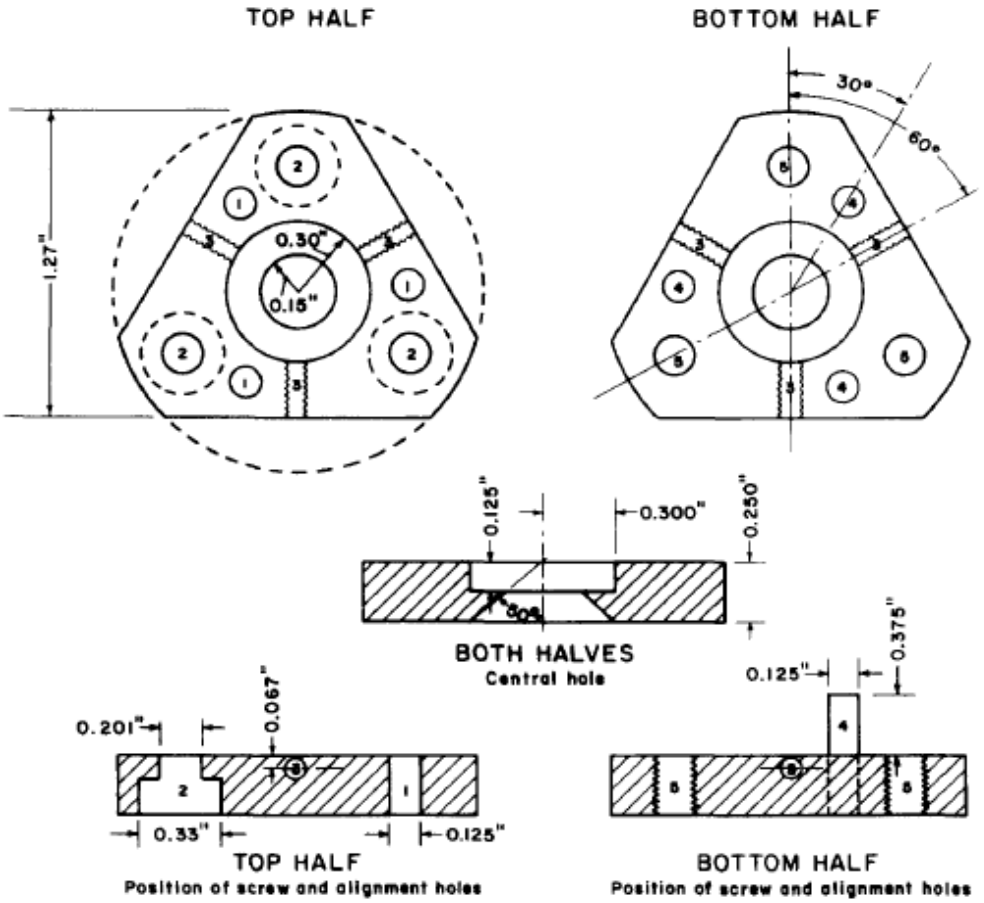

Figure 3.6 Triangular steel supports. Both halves have three-fold symmetry. (1) 0.318 cm hole for guide pin; (2) Well for Allen cap screws, i.d. = 0.51 cm, o.d. = 0.84 cm; (3) Tap for No. 3-48 screw; (4) Guide pin, 0.318 cm diameter; (5) Tap for No. 10-32 screw [123].

An exploded view of this cell adapted for high-temperature single-crystal studies is depicted in Figure 3.7. This version of the cell developed by Hazen and Finger [123] is suitable for the investigation of samples under pressure of 4 GPa and at temperature of 450 C. The heat is generated by a small resistance heater assembly fitted around the diamonds and in order to prevent an excess heat dissipation a pyrophyllite insulating ring is fitted around each boron carbide disk. When the cell is closed these rings come in contact with each other and form the walls of the "furnace". To provide

additional insulation a mica washer is placed between the boron carbide disk and its support steel plate. Despite the insulation, the whole cell assembly will heat up and to prevent a pressure drop due to the relaxation of the three "pulling" screws two Belleville spring washers are placed between each "pulling" screw head and the triangular plate.

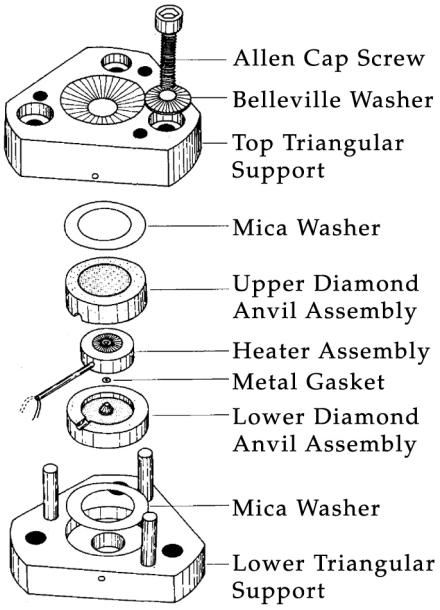

Figure 3.7 Exploded view of the PT cell assembly. Pyrophyllite components are stippled [123].

To prevent a premature failure of the gasket or the anvils and therefore to attain higher pressure a greater stability and a better alignment of the diamonds are required. In the design presented in Figure 3.8 Allan, Miletich and Angel [124] have modified the Merrill-Bassett cell to this effect. The triangular plates have been replaced by square plates featuring four guide pins and four pulling screws. The guide pins are larger and further away from the axis of the cell than in the previous designs. With a pitch of 0.5 mm the M5 pulling screws correspond to a metric fine pitch M5 thread which allows for a better control while applying pressure. To improve the stability one pair of screws is right-handed and the other is left-handed. A 15 conical hole through the centre of each Be backing disk provides optical access. The conical shape has several advantages over a straight hole, it offers a better

optical access thus maximising the ruby fluorescence signal. It can be sealed with a solid Be cone to provide a smooth and continuous X-ray absorption. Concerning the alignment of the anvils, one of the backing disks sits on a plate fitted with four grub screws ensuring the radial alignment of the backing disk whereas the second backing disk sits in a hemisphere which forms with its support plate a "ball-and-socket" arrangement [125] and provides the parallel alignment of the culets.

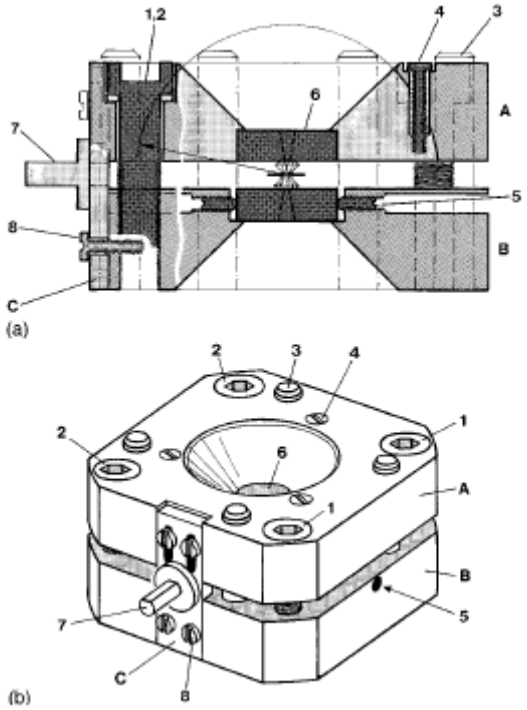

Figure 3.8 A multilayer cross-sectional view (a) and an axonometric view (b) of the diamond-anvil cell showing: (A) upper platen;(B) lower platen; (C) mounting bracket; (1) right-handed M5 bolts; (2) left-handed M5 bolts; (3) 5-mm-diameter guide pins; (4) M2 parallel alignment screws; (5) M2 radial alignment set screws; (6) Be backing disks; (7) mounting pin; (8) M2 mounting-bracket securing screws. The radius of the hemisphere is indicated by the arrow and the faint sector in (a) [124].

One of most remarkable advances in the development of DACs for XRD came recently from a new anvil shape. In 2004, Boehler and De Hantstters published the first Boehler-Almax diamond anvil design with conical support [36]. It provides several improvements over the conventional designs amongst which are superior alignment stability, a larger supported surface area and a wider aperture (up to 90) for identical anvil dimensions

around the culet. In the original anvil mount on a Be disk the X-rays are scattered through the Be allowing the full opening angle of the cell body to be utilised. However, the diffraction patterns obtained from this type of setup are contaminated with Be powder lines. With a Boehler-Almax design X-rays pass exclusively through the diamonds and this results in a much smoother absorption profile from the cell. These anvils can be used with metallic or WC backing seats, they have been integrated in many pressure cells and Moggach *et al.* reported on the incorporation of this design into the Merill-Bassett DAC [37] for high pressure SXD (Figure 3.9 and Figure 3.10).

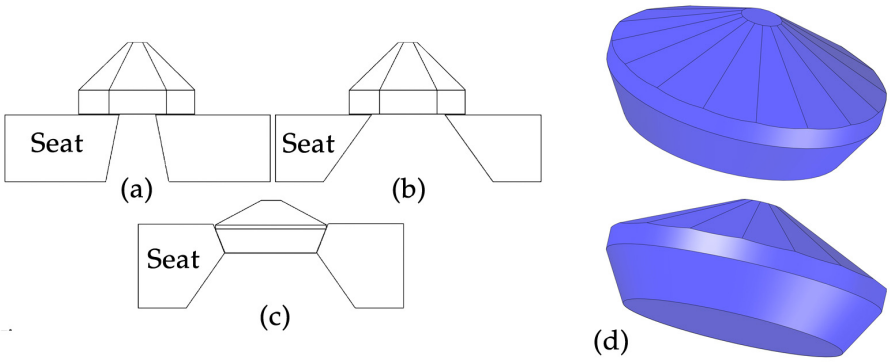

Figure 3.9 Backing seat and anvil design for (a) a beryllium backing seat with a modified brilliant-cut diamond anvil; (b) a WC or steel backing seat with a modified brilliant-cut diamond anvil; (c) a conical Boehler–Almax diamond anvil with a WC backing seat. Note the lack of support in (b) compared with (a) and (c) [37]. A 3D computer-aided view of Boehler–Almax diamond anvils (d) showing the faceted pavilion and smooth cylindrical girdle and conical crown.

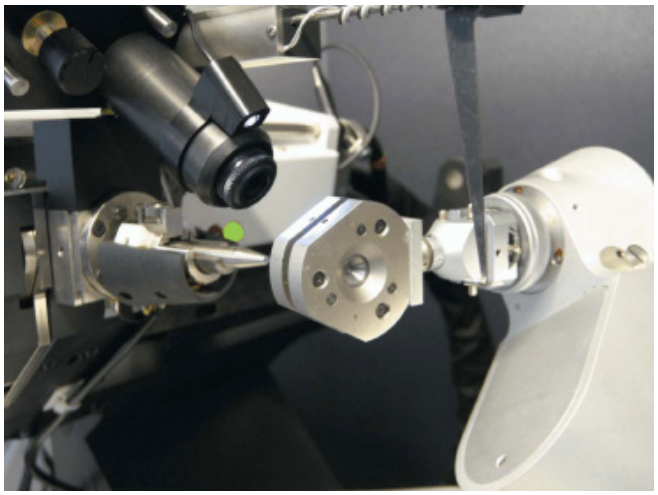

Figure 3.10 Merrill–Bassett DAC mounted on a Bruker Kappa APEX II diffractometer [37].

3.1.3 Diamond Anvil Cell for X-ray diffraction at low temperature

Regular DACs can be used at low temperature; however they are not optimised for this mode of operation. They are heavy and bulky and always require to be cooled down in cryostats which is an option only available at central facilities. Additionally when working with, for instance a Merrill-Bassett DAC, it is extremely time consuming to cycle the cell back and forth from low temperature to room temperature for each pressure change. The MDACX [33-35] designed by LeToullec offers the possibility of *in-situ* continuous pressure and temperature variation. The MDACX is illustrated in Figure 3.11. The components are essentially similar to those of other DACs: a high strength steel or non-magnetic steel body of piston-cylinder type, an alignment mechanism based on a combination of translational adjustment for one seat and parallelism tuning through hemispherical rocker for the other. In order to obtain a direction independent absorption of the X-ray beam over the 90 aperture the beryllium seats are hemispherical.

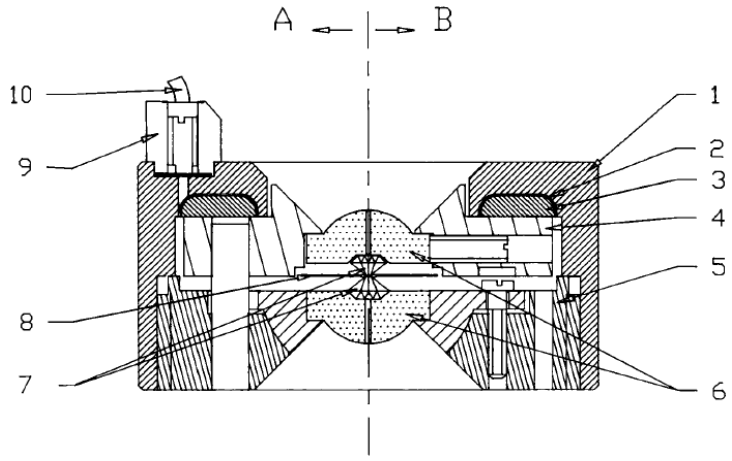

Figure 3.11 Half cuts of the Membrane Diamond Anvil Cell for X-ray, MDACX: (A) through the locating pins; (B) through the alignment screws. (1) retaining nut; (2) membrane; (3) push-piece to transmit the thrust to the piston; (4) piston; (5) lower platen; cell body; (6) beryllium seats; (7) diamond anvils; (8) gasket; (9) biconical connection with micro-valve; (10) capillary tubing. The diameter of the cell is 50 mm and its height is 25 mm [35].

The innovation is in the thrust mechanism which is based on the inflation of an annular metallic membrane. While the retaining nut (1) and the lower platen (5) are secured together the membrane located in between the retaining nut (1) and the sliding piston (4) supporting one anvil and its seat can be inflated to push the upper anvil against the lower. Due to the large surface area of the membrane a gas pressure of 100 bar produces a force of 4 kN which is sufficient to increase the sample pressure to the megabar range. The membrane is connected to a pressurisation unit (gas cylinder and pressure gage) through a metallic capillary (10). A set of micrometric valve give an accurate control over the gas pressure. There are several advantages in using a membrane to generate thrust:

- The force is being applied symmetrically which helps to maintain the diamonds' alignment when changing pressure.
- This force can be varied continuously and smoothly.
- The sample pressure can be remotely modified without moving the cell.
- A given pressure of the gas on the membrane always gives the same force on the diamonds. Therefore a membrane can be calibrated eliminating the need of secondary pressure calibrant.

A helium flow cryostat was designed specifically to host the MDACX. During the experiment the MDACX is located in a rotator activated from outside the cryostat by a stepper motor and the cryostat itself seats on the goniometer head. The pressure cell is rotated about its own axis which lies in the horizontal plane while the goniometer rotates the full assembly about a vertical ω axis. With this setup LeToullec reported a minimum temperature of 46 K and a maximum pressure of 20 GPa achieved. More recent versions of the MDACX make use of Boehler-Almax design anvils and WC seats and are adapted for Mbar pressures and with an improved cryostat they can be

cooled down to 3 K. The capillary system connecting the pressure cell to the pressurisation unit enable a change of sample pressure without taking the cell out of the cryostat at virtually any accessible temperatures and pressures as long as the gas in the capillary does not freeze into a solid.

3.1.4 Diamond Anvil Cell for magnetic measurement

DACs can be used for high pressure magnetic measurements in two distinct ways. Either the detecting coils are made a part of the DAC by being placed around the anvil, integrated into the gasket or incorporated into the diamond as it is the case in the examples presented in this section. Alternatively, the pressure cell is made to fit entirely into an independent magnetic measurement system as it is the case for the devices presented in section 3.1.5 which are specifically designed for an MPMS magnetometer.

A few examples of DACs with integrated magnetic measurement system are reported in the literature. The functioning principle remains similar in all designs. The sample is placed into a gasket hole as in a standard DAC and a set of excitation and a detection coils are placed in the vicinity of the sample. The sample response is measured by detecting the voltage induced in the sensing coil. Generally the sample position is fixed with respect to the detection coil and the measurement takes place in the *ac* mode [100, 126-131] but *dc* measurements can also be carried out with a vibrating detection coil located around the anvil pavilion [105, 132-134]. These methods permit to follow the pressure dependence of a given magnetic transition with a sensitivity similar to that of the MPMS (10^{-8}-10^{-10} emu) but unfortunately these systems can not be accurately calibrated and the sample magnetisation is always reported in arbitrary units. The main advantage of this approach is the absence of constraint on the DAC dimensions. Because it needs to fit into the relatively large bore of a cryostat the DAC's overall size is unimportant and a sturdy construction with accurate alignment mechanisms can be implemented.

Figure 3.12 is a schematic representation of the detection coil setup used by Bireckoven and Wittig to follow the evolution of the superconducting transition of Pb under pressure up to 50 GPa [100]. The excitation coil is outside of the DAC and it is not shown in this picture. The detection coil arrangement is embedded into epoxy resin (Stycast 1266). It is formed by an inner and an outer coil made from superconducting NbTi wire 0.05 mm in diameter and held in place with epoxy. The coil is placed in a radially compensated gradient coil configuration and the superconducting transitions are detected by a low frequency *ac* technique employing a SQUID system.

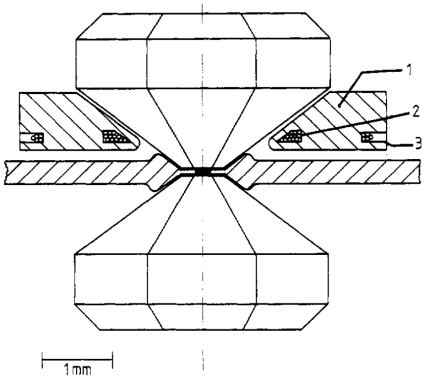

Figure 3.12 Schematic representation of the high-pressure cell and the pick-up coil. (1) coil former; (2) inner coil (12 turns); (3) outer coil (5 turns) [100].

Ishizuka presented an alternative design (Figure 3.13) in which the detection coil arrangement is also located around the anvil pavilion but it is not secured to the DAC and can be vibrated along the axis of the pressure cell. This method allows for *dc* susceptibility measurements with a sensitivity of 10^{-9}-10^{-10} emu to take place [132]. It has been tested on antiferromagnets, ferromagnets and at a pressure of 83 GPa on superconductors [133]. The detection coils shown in Figure 3.13 consist of one inner coil and one outer coil made from superconducting NbTi wire 0.05 mm in diameter, oppositely wound so as not to respond to a uniform magnetic field. The coils were fixed in a copper mount by Stycast No. 2850FT. The detection assembly is perpendicular to the cell axis and axially aligned with the sample (on the cell axis) and is located 0.65 mm away from the sample's centre along the cell

axis. It is connected to a set of three piezoelectric actuators which generate a stable vibration of the coils with an amplitude of 90 μm at 155 Hz.

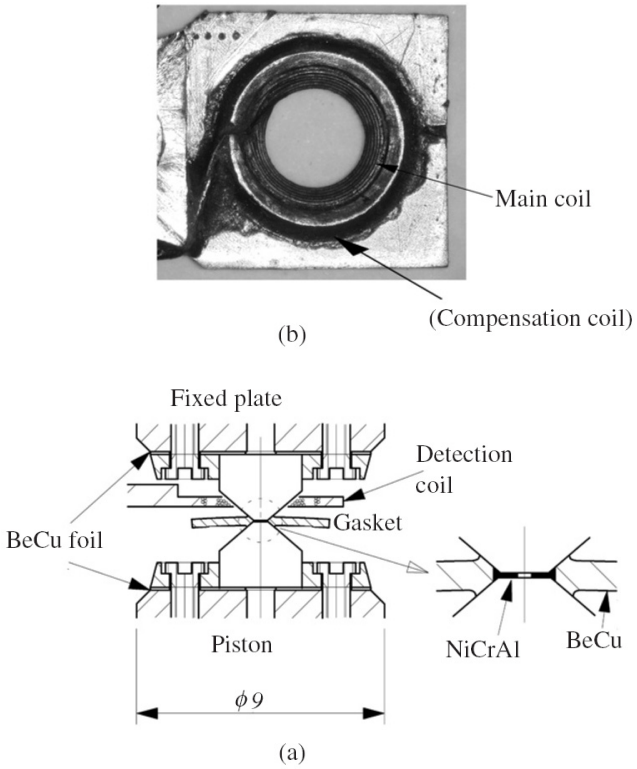

Figure 3.13 (a) Cross-sectional drawing of the area around the diamond anvils and (b) photograph of the detection coil. The inside of the main coil (20 turns) that has no bobbin was cone shaped. The compensation coil (10 turns), covered with Stycast No 2850FT, was located around the main coil, forming a concentric gradiometer [134].

More recently, high pressure *ac* magnetic susceptibility using designer diamond anvil have been reported [129-131]. Designer diamonds are anvils in which a thin-film metal circuit is encased. The microprobe is made by the sputter deposition of a 1 μm layer of tungsten onto a standard diamond anvil followed by the encapsulation of this circuit through epitaxial diamond deposition by microwave plasma chemical vapour deposition. This layer of synthetic diamond protects the microprobe against any damage and also provides electrical insulation. The integrated microprobes can be straight lines bringing electrical contact from the anvil's side to the sample space for

transport properties study [135, 136] or more complicated shapes such as the coil shown in Figure 3.4 (c) for magnetic measurements.

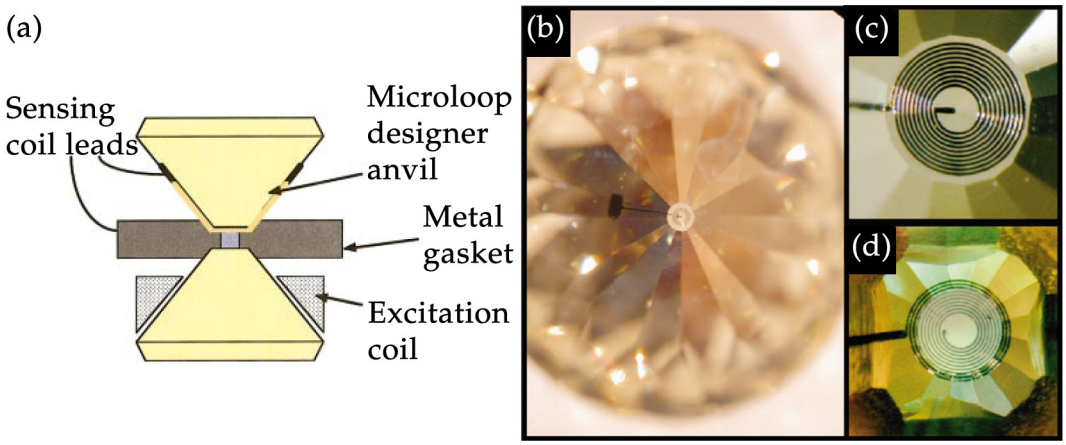

Figure 3.14 (a) Arrangement specific to designer diamond anvils used for *ac* susceptibility in which the sensing coil is located on the top diamond, and the 55-turn excitation coil is wrapped directly around the bottom diamond. The sensing coil protrudes through the culet and is grounded through the metal gasket [129]. (Right) A designer diamond anvil with a 10-turn magnetic sensing coil. The thin-film tungsten coil has an outer diameter of 280 μm, an inner diameter of 90 μm, and a linewidth of 5 μm. (b) A photograph of the entire diamond anvil, showing both the sensing coil and an electrical connection pad on the side of the anvil. (c) A magnified view of the culet showing the sensing coil in more detail. (d) The culet after being encased in a layer of diamond approximately 10 μm thick [130].

The schematic representation of the setup used for *ac* susceptibility is shown in Figure 3.14 (a). It consists of one designer anvil opposed to a standard anvil. An excitation coil is placed near the gasket on the standard anvil. In this system the sensing coil lies about 20 μm underneath the diamond's culet (or the sample) and electrical connections are provided through one lead on the side of the diamond and through the metallic gasket. This technique has been successfully used for magnetic studies at pressure going up to 28 GPa. The limit of this technology is to do with the fact that the implanted electrical circuit weakens the diamond and a slip fault can occur at high pressure.

3.1.5 Diamond Anvil Cell for the Quantum Design MPMS®

The MPMS from Quantum Design is the most widely used SQUID-based magnetometer. It is routinely used to measure the magnetisation of materials from 1.9 to 400 K in a magnetic field varying from 0 to 7 T with a sensitivity of 10^{-8} emu. Under ambient pressure conditions the sample is held in a gelatine capsule secured inside a plastic straw. For the measurement the straw is inserted into the sample volume of the MPMS of 9 mm in diameter through a 250 mm long airlock chamber. The detection system is such that the perfect sample shape would be a sphere of as small as possible diameter. A more detailed description of the MPMS operational principles is presented in Chapter 4.

Over the last decade several opposed-anvil pressure cells specifically developed for the MPMS have been reported. The constraints associated with the nature of the measurement and the space available in the MPMS define the size as well as the materials to use for the construction of these devices. They must have good mechanical properties compatible with low temperature conditions (2 K), low magnetic response and they must fit into a cylinder with a maximum diameter of ~8.8 mm. These prior conditions call for the use of non-magnetic high strength metals. The various alloys available for the construction of pressure cells suitable for low temperature work were reviewed by Walker in 2005 [17]. The four candidates which stand out for their low magnetic properties are the BeCu (BERYLCO 25 alloy), the "Russian alloy" (NiCrAl), the MP35N (CoNi alloy) and the titanium copper (Cu-3Ti). Their room temperature tensile yield strengths are respectively 1.2 GPa, 2.0 GPa, 1.84 GPa and 0.95 GPa and comparable with magnetic high strength steel. Although it is neither the strongest nor the less magnetic, BeCu 25 for its availability and machinability became the material of choice in the fabrication of DACs for MPMSs.

A first DAC, designed and published by Mito in 2001 [28] named the mDAC (miniature DAC) is made of hardened BeCu 25 and allows magnetic studies of samples exposed to pressures as high as 20 GPa [29]. The latest design of the mDAC is exemplified in Figure 3.15 [137]. The mDAC is 40 mm in length and has an outer diameter of 8.5 mm. One anvil is mounted on a backing plate (e), which can be adjusted in the XY plane by means of set screws (k). This assembly is part of the piston (f) which transmits the force in a linear motion along the cell axis from the closing nut (g) to the anvil. Using a long piston-cylinder arrangement to transmit the force ensures that the anvils' alignments are preserved as the pressure is increased [120, 121]. The second anvil is mounted on a hemispherical rocker (b) which seats in a socket on the grand nut (b) and gives the parallelism adjustment through three screws (h).

The sample is located in a hole in a hardened BeCu 25 gasket with initial thickness of 0.2 mm. The diamonds are glued to their respective seats using Stycast No. 2850FT. Holes through the grand nut (a), the seats (b and e), the piston (f) and the closing nut (g) provide optical access to the sample region. They are used for aligning the diamonds and for room temperature pressure calibration with the ruby fluorescence technique. Once the anvils are aligned, the sample is loaded in the gasket hole with a ruby and methanol:ethanol 4:1 as a pressure medium. The pressure is then increased by screwing the large closing nut (g). During this operation the piston rotation is prevented by the guiding screw (l). For the measurements, a 60 mm long dummy rod made from BeCu 25 (material of which the mDAC is made of) is attached on either ends of the mDAC. Room temperature pressure calibration compared to low temperature (~7 K) pressure calibration based on the pressure dependence of the superconducting transition of lead revealed that due to the thermal expansion of the various constituent of the mDAC a reproducible 10-14 % pressure increase occurs on cooling from 300 K to ~7 K.

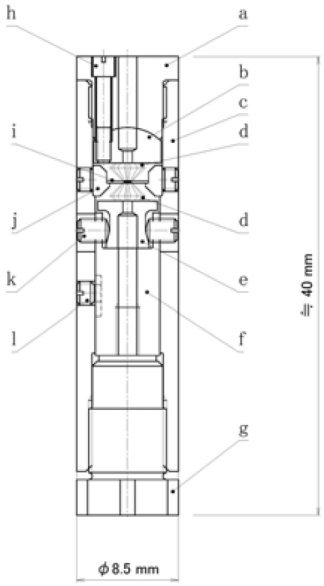

Figure 3.15 Overall cross-sectional view of the miniature diamond anvil cell for a SQUID magnetometer. (a) grand nut; (b) half-sphere seat for the upper diamond; (c) cylinder; (d) diamonds; (e) anvil plate for the lower diamond; (f) piston; (g) nut for applying pressure; (h) screw for tilt adjustments; (i) gasket; (j) supporter for the gasket; (k) screw for X-Y adjustments and (l) piston guide screw [137].

The mDAC is highly asymmetric and the complicated assembly of small parts located around the sample interferes with the sample's magnetic signal. Indeed the sensing coils of the SQUID are sensitive to any discontinuities in the magnetic signal and hence in the material/object being scan through them i.e. a long uniform rod or tube of material extending beyond the sensing coils while being scanned remains undetected. Despite the attempt to make the cell more symmetrical by adding the dummy rods, the complexity of the mDAC leads to an uneven material distribution around the sample which consequently affects the quality of signal generated by the detecting coils and reduces the sensitivity of the measurements by three orders of magnitude. Moreover no background removal procedure is possible. The mDAC is now commercially available from easylab under the name "Mcell Ultra" [138].

A second DAC design for a MPMS has been published by Alireza in 2007 [26]. This pressure cell is known as the "*L-A* cell". It is 64 mm long and 8.4 mm in diameter and it can by used to detect superconductive, ferromagnetic and antiferromagnetic phase transitions up to pressures above 10 GPa. The first version of this cell was made entirely of ultrapure BeCu and in order to minimize the magnetic background signal, the second version [139] was constructed from a specially made high-purity copper titanium (97% Cu and 3 % Ti, Cu-3Ti) alloy in which the diamagnetic susceptibility of copper and paramagnetic susceptibility of titanium cancel each other [140]. The magnetic susceptibility of Cu-3Ti is about two orders of magnitude smaller than that of BeCu 25 [25].

The sample is located near the centre of the cell body in a BeCu gasket hole (350 μm) as shown in Figure 3.16. On either side the anvils are supported by the pistons and the alignment is provided by the method described by Eremets and Timofeev [141]. As the lower piston is bolted into the body the pressure is increased by applying a force on the upper piston and locked by tightening the upper nut. A hole going through each part of the cell allows for pressure calibration with the ruby fluorescence technique. Comparison of room temperature pressure with low temperature pressure (Lead T_c) with Daphne 7373 oil as pressure medium indicated a pressure drop of 0.2–0.3 GPa on cooling from 300 K to ~7 K. In spite of not being fully symmetrical with respect to the sample, the high contrast between the magnetic susceptibility of the gasket itself or the gasket with the sample as a unit and their surrounding allows for a background removal process. The gasket alone placed in the cell generates a signal similar to that produced by a point dipole making possible a background measurement for the assembled cell without sample. Data are then collected with the sample loaded and the difference between the two data sets corresponds to the sample contribution only. In practise, the uneven distribution of material in the vicinity of the gasket deforms the raw signal (see Figure 4.2 for perfect

raw signal) from the sensing coils and it can not be integrated as such. The raw signal of each data point of the background measurement needs to be subtracted from the raw signal of the matching sample measurement data points. Then the magnetisation of the sample is obtained by the integration of this calculated raw signal. Following this technique, it is theoretically possible for the *L-A* cell to perform at the full sensitivity of the MPMS. However if the raw signal acquired during a measurement is too distorted it is difficult to ensure a good centring of the sample (or empty gasket) with respect to the scan length. And it might not be possible to compensate for the sample displacement associated with the thermal expansion of the long metallic sample holder rod. This uncertainty in the sample position might lead to the addition of small error on the calculated sample magnetisation.

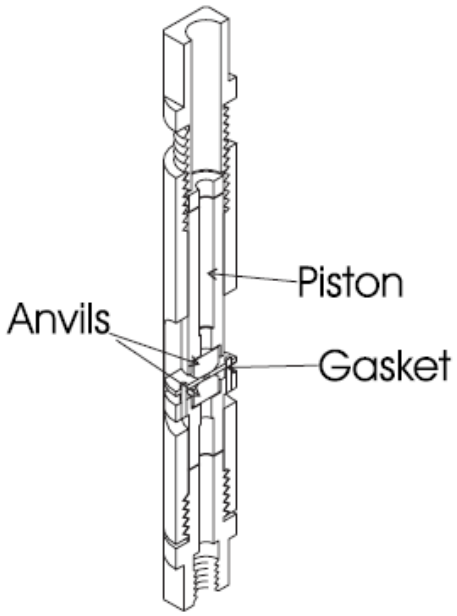

Figure 3.16 Schematic of the diamond anvil cell designed for the MPMS. The cell is 8.4 mm in diameter and 64 mm in length and is made up of two opposing diamond anvils supported by an ultralow magnetic susceptibility body composed of high purity copper (97%) and titanium (3%). The very low magnetic background signal of this diamond anvil cell allows to detect changes in the magnetic moment of the sample as low as 10^{7} emu [139].

An important limiting factor in the magnetic study of matter under high pressure is the restriction imposed by the sample size. The sample volume in the DACs mentioned above is limited to 10^{-2}-10^{-3} mm^3. If this volume of a

sample is not measurable in the conventional way then it is not possible to measure this sample in a DAC. Two opposed anvil pressure cells [27, 142] of simple design similar to that of the L-A cell and able to accommodate samples with a volume of the order of 1 mm^3 have been developed. A schematic view of these fully symmetrical cells made of BeCu is shown in Figure 3.17. The body of the cell is formed by a long tube threaded at either ends. The sample is located in a gasket (BeCu or NiCrAl) up to 1 mm thick at the centre of the cell with on either side a large anvil and a long force transmitting piston. The sliding fit of the anvils and the pistons in the cell body ensure the alignment of the culets. No other alignment mechanism is present. The pressure is increased by applying a force on the pistons and locked by tightening a nut at either ends of the body. The anvils are about 5 mm in diameter. They are made of zirconia (ZrO_2) [27] or of non-magnetic composite ceramic material (FCY20A Fuji Die) [142]. Due to their symmetrical design and the implementation of a large sample volume these cells are suitable for the study of weakly magnetic material. Unfortunately the sample volume increase comes at a cost over the accessible pressure range and for sample volume of around 1 mm^3 maximum working pressure is limited to ~4 GPa.

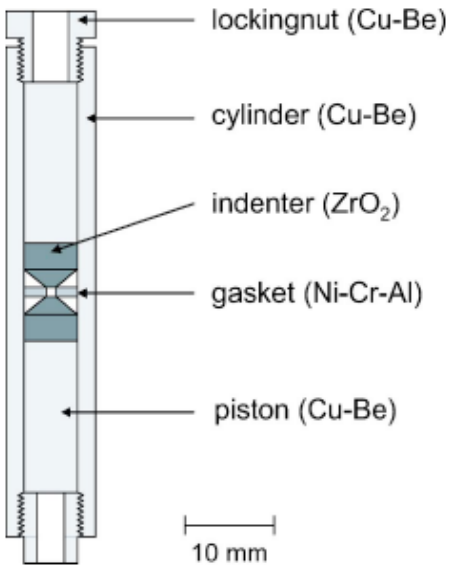

Figure 3.17 Cross-sectional view of the indenter cell for the commercial SQUID magnetometer [27].

3.2 Piston-cylinder cell

The piston-cylinder type cell is an obvious apparatus for hydrostatic high pressure environment. It has been used extensively and the theory of pressure cylinders is well covered in the literature (see for instance Eremets reference [3]). In this section the principal considerations relevant to the construction of a piston-cylinder pressure cell for magnetic studies are outlined. While some designs of piston-cylinder cell incorporate a built-in *ac* susceptometer [143-145] they remain very rarely used. Because they are free from size limitation they can take advantage of the full pressure range available to a piston-cylinder arrangement. However the vast majority of the pressure cells are adapted to fit in a commercial magnetometer. Some of these cells, developed for an MPMS, are reviewed in section 3.2.2 where their characteristics and their operational procedures are explained.

3.2.1 Practical consideration

Generating pressure in a piston-cylinder system is relatively simple. A sample is enclosed in a volume formed by a closed-end cylinder and a piston or by an open-end cylinder and two pistons. The application of an external force on the pistons (or piston) while the cylinder stands still initiate a displacement of the pistons and lead to a decrease of the sample volume and hence an increase in sample pressure. In order to successfully increase the sample pressure the following conditions should be fulfilled: the sample and the pressure medium must be properly confined to the sample volume; the cylinder deformation must remain in the elastic regime (plastic deformation is acceptable for single use); the piston must be strong enough to transfer the force at least equal to that corresponding to the sample pressure. These requirements highlight the three critical domains of a piston-cylinder cell which are the sealing of the sample, the cylinder's and the piston's

mechanical properties. Overall the upper pressure limit is directly related to the yield strength of the material used as pistons and cylinder.

Seal

Static and dynamic seals apply to different configurations. As indicated by its name a "static seal" operates exclusively in arrangements without moving parts. It involves the squeezing of a sealing material between two other parts made from a stronger material. It used for instance when one end of the cylinder is closed by a static plug and the pressure is increased by applying a force on a piston located at the opposite end of the cell [19]. In this case the seal has the shape of a specially designed copper washer.

By contrast, a "dynamic seal" allows for the displacement of the piston while providing an airtight barrier between the piston and the cylinder. Two types of dynamic seals are commonly employed. The mushroom-type seal based on Bridgman unsupported area principle is one of them. This technique ensures an airtight connection between the piston and the cylinder by filling up the existing clearance provided by the sliding fit. This sealing mechanism has been implemented in the pressure cell depicted in Figure 3.18. It consists of one or several rings of soft materials sandwiched between the two segments (supported part to which the force is applied and unsupported part on the sample side) of the piston.

As the pressure is increased the soft material extrudes outwards and is forced into the gap between the piston edge and the cylinder forming a perfect seal. A stack of washers made from materials of various strengths (for instance indium, tin and copper) deforms successively as the stress at which they are exposed increases, and results in a good seal over the whole pressure range. The use of an antiextrusion ring with a PTFE capsule is the second option for sealing a sample under hydrostatic pressure conditions.

The antiextrusion rings are made from ductile materials, typically annealed BeCu or pure copper; they are plastically deformable but hard enough to resist excessive flowing into the clearance gap between the piston and the bore. In this setup the sample and the pressure medium are contained in a PTFE capsule and one antiextrusion ring located on either side of the capsule prevents the PTFE from passing around the piston. Antiextrusion rings are washers with an isosceles right triangle cross section (Figure 6.1 and Figure 6.2). Once positioned within the pressure cell, the sides forming the right angle are in contact with a piston face and with the cylinder wall and the hypotenuse is in contact with the PTFE capsule. As the pressure is increased the ring is pushed against the piston and the cylinder walls and ensures a good seal. This arrangement is used in most of the piston-cylinder pressure cell designed for the MPMS. It is easy to implement and performed well up to the pressure limits set by the cylinder's and piston's strength.

Piston

A piston works in compression therefore the pressure limit is equal to the yield strength of the metal ~ 2 GPa or to the ceramic's compressive strength ~ 5 GPa depending on which class of material is used. Ceramics are strong in compression but they are also brittle and weak in tension. They are preferred to metals when the piston is short, of simple shape and adequately supported.

For non-magnetic pressure cells the choice of materials is somewhat limited. The available high strength alloys and their yield strength are: BeCu (1.2 GPa), NiCrAl (2.0 GPa) and MP35N (1.8 GPa). On the ceramic side the conventional materials are zirconia (2.0 GPa) [146] and non-magnetic WC such as Roctec 500 [147, 148]. Roctec 500 is a binderless WC and although no information about its mechanical properties is available it is known to

perform well above 2.0 GPa [148]. From a purely magnetic approach zirconia is the best material to use.

Cylinder

The cylinder is subjected to a more complex stress state than the piston. However the theory behind this problem, known as the thick wall cylinder case, is well documented. By approximation, it states that for a long cylinder the maximum internal pressure before plastic deformation of the bore surface is equal to about half the yield strength of the cylinder material. This is because the stress is not evenly distributed along the cylinder's wall thickness. Instead a very thin layer around the bore sustains the most of the load and the outer region of the cylinder is almost stress free. Supporting the cylinder or loading it by external pressure is a way of reaching higher internal pressure. In any case for a set material the maximum pressure that a cylinder can withstand is related to the ratio of the outer diameter to the inner diameter. It increases sharply at first and flatten out around a diameter ratio value of 3 to 4 [149].

Three different ways of achieving external loading exist:

- The addition of extra layers to the cylinder.

  Multi-layer cylinders are assembled so as to have an interference fit between the respective layers. This results in compressive residual stresses in the inner element and tensile residual stresses in the outer element. The cylinders assembly is accomplished by heating the outer elements which have a bore diameter slightly smaller than that of the respective inner element and shrinking it on to the cold inner cylinder or by having matched tapers on the inside and outside surface of the

outer and inner elements respectively and forcing the cylinders into each other by means of a press.

- The autofrettage technique.

  A thick-wall cylinder is subjected to an internal pressure exceeding its yield strength, plastic deformation initiates at the bore proceeding through the cylinder wall as the pressure is increased, until the plastic-elastic interface reaches the outer surface at which point, the cylinder material is in a complete overstrain state (plastically deformed). When the internal pressure is released the outer material, which has been deformed the least, attempts to return to its original diameter and the innermost material, tend to remain deformed. This results in a residual compressive stress at the bore and a residual tensile stress at the outer surface. Following this procedure the bore of the cylinder needs to be re-machined to the straight cylindrical shape.

- The winding reinforcement or wrapping.

  A high strength filament such as wire, tape, or fibre is wound under tension around a thick-walled cylinder thus producing the desired compressive residual stress in the cylinder.

From the multi-layer cylinder theory it appears that for a two-layer cylinder made from the same material the maximum accessible pressure is almost doubled compared to that of a single-walled cylinder with the same inner and outer diameters. Therefore it is almost equal to the yield strength of the material. Another special case in which the high-pressure limit is increased is the short cylinder geometry. In this configuration the volume under pressure is limited to a short section of the bore. The stressed cylinder's material around this volume has massive support from the surrounding material.

Consequently the long-cylinder approximation is not valid anymore and a high-pressure limit of up to twice the yield strength of the material can be achieved in the optimum conditions of such design.

Because the cylinder is exposed to a non-negligible amount of tensile stress it is generally made of metal although well supported ceramic might be used [150]. For the pressure cells considered hereafter the cylinder is made from one of the non-magnetic alloy previously described.

3.2.2 Piston-cylinder cells for the Quantum Design MPMS®

Since 1996, several piston-cylinder cell designs have been published [19-25, 151-153]. Due to the nature of the measurement, the size restriction of the available sample space within the MPMS and their purpose, all these pressure cells are made from high strength non-magnetic cryogenically compatible materials [17] and their bore and outer diameter ranges respectively from 2 mm to 3 mm and from 8.5 mm to 8.8 mm. The seals used are either the mushroom type or the antiextrusion ring and PTFE capsule combination, and although it is not always mentioned, the cylinder is normally strengthened by one of the external loading methods. The maximum operating pressures of these cells vary from 1 GPa to 2 GPa depending on the materials and the configurations involved.

3.2.2.1 Pressure transmitting medium

The pressure transmitting media used to obtain hydrostatic conditions are the Daphne oils and the Fluorinerts FC75 and FC77. Information about these fluids can be found in section 3.1.1 and Table 3.1.

3.2.2.2 Pressure calibration

The lack of optical access prevents the use of the ruby fluorescence technique. Instead the pressure is generally calibrated at low temperature by following the shift of the T_c of tin, indium or lead (see section 3.1.1 and Table 3.2). When the pressure is increased by means of an external tool (hydraulic press) and preserved by tightening a locking nut as it is the case in the pressure cells presented in Figure 3.19 and Figure 3.20 the room temperature sample's pressure can be calculated from the applied force. This method gives a good approximation of the sample pressure but since it is not a direct measurement, the frictional forces between the cylinder and the piston and the pressure drop induced by transferring the load from the pressurisation unit to the locking nut are not accounted for. Hence the inferior accuracy of this practice over other techniques. For long pressure cells, the room temperature pressure determination can also be accomplished by measuring the deformation of the pressure cell's body. The relations between the pressure and the deformation is characteristic of each individual cell design; Diederichs *et al.* used the elongation (*dL*) of the cylinder with the relation $dL/dP \simeq +42.2$ μm/GPa [151] and Kamenev *et al.* used the diameter increase (*dD*) of the cylinder in its centre with the relation $dD/dP = +16$ μm/GPa [24] to accurately establish the sample's pressure.

The above procedures provide the pressure value at room temperature and at low temperatures. By combining these methods it is possible to evaluate the absolute pressure change between the ambient and the low temperatures which results from the thermal expansion of the pressure transmitting medium and the various parts of the pressure cell. In most cases the pressure drop is considered to be linear along the temperature range. However, by measuring *in-situ* the resistivity of a Manganin coil embedded within the pressurized volume, Sanchez-Benitez *et al.* [19] showed that the pressure drop is not linear and that, in their particular cell, the error in pressure estimated from a linear drop could reach up to 15 % at a given temperature.

3.2.2.3 Piston-cylinder pressure cell designs for MPMS

The existing high pressure cells for MPMS can be divided into two groups:

- The long cells are symmetrical with respect to the sample to take advantage of the MPMS measurement principle and thus produce a low background level. They can be used for the study of weakly magnetic sample. They are difficult to produce and require special tools. The number of parts or the large volume of pressure media result in a large pressure drop on cooling.

- The short pressure cells are easier to fabricate and to use. Their small mass (~10 g) is an advantage for fast thermal equilibrium. But they are still too long to be assimilated to a normal sample and too short to extend over the sensing coil during a scan. As a result their background is consequent and only sample with large magnetic moments can be studied.

Three representative examples of the existing pressure cells available for MPMS are described below.

The design shown in Figure 3.18 is that of a long symmetric cell specially designed for the study of weak magnetic materials. The cell body consist of a two-cylinder assembly of total length equal to 13 cm. The outer diameter of the cell is 8.7 mm and in order to maximize the sample space the bore diameter is set to 3 mm. All parts of the cell are made of BeCu 25 alloy and the maximum pressure is 1 GPa.

The sample attached to a clover-shaped PTFE puck is positioned at the centre of the cylinder. The friction fit between the puck and the bore allows the puck to be positioned in the bore. On both cylinder's ends an oversized PTFE puck followed by a piston fitted with a mushroom seal with tin and copper

washers are positioned inside the bore. Each piston is backed up with a backing disk and a standard M6 screw. The cell is fully symmetric with respect to the sample and because the pressure is increased by applying a force on each piston it will remain symmetric at all pressures.

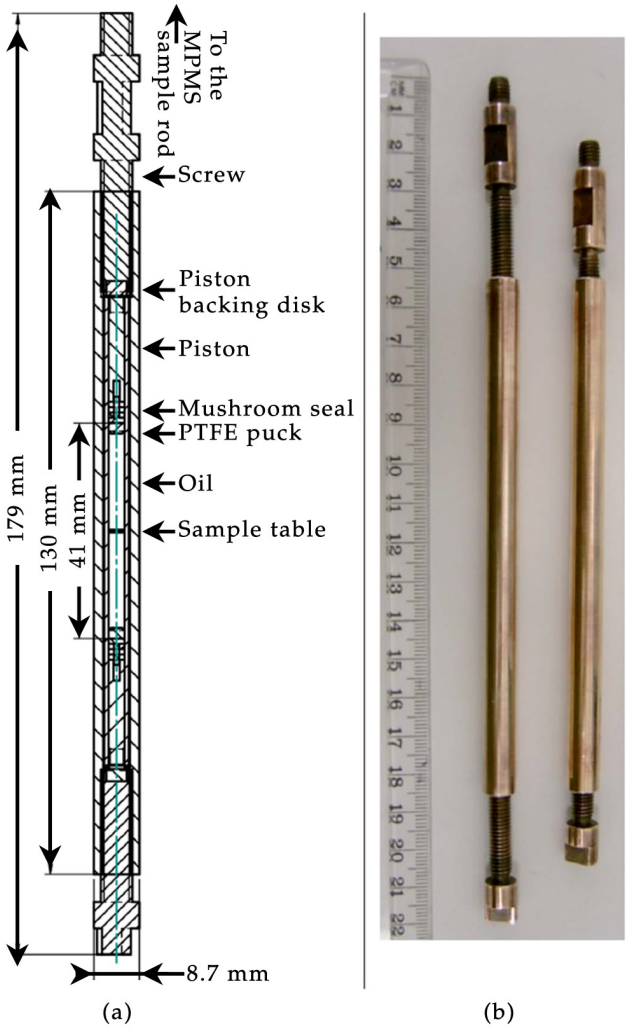

Figure 3.18 Long symmetric high-pressure cell for magnetic measurements: (a) drawing of the cell with the distance between the pistons shown for the top applied pressure; (b) photograph of the high-pressure cell at ambient pressure (left) and at top pressure (right) [24].

The way the pressure is increased is one of the features of this pressure cell. The force needed to generate the pressure is obtained by tightening the M6 screws instead of using an external press. Another distinctive feature is the pressure calibration which is calculated from the outer diameter increase (dD) measured at the centre of the cylinder ($dD/dP = +16$ μm/GPa).

This technique permits high pressure magnetisation studies to be carried out without the presence of manometers which in their superconductive state interfere with the sample signal. Below 7.2 K for Pb and 3.7 K for Sn their strong diamagnetic signal prevents a sample study from taking place. The pressure media used is the Daphne 7373 oil and a pressure drop of 0.24 GPa is observed when the cell is cooled from room temperature to ~7 K.

When both pistons are fully engaged the distance between them is 4.1 cm hence 2 cm of bore on either side of the sample contains oil only. In a standard 4 cm scan solely the sample passes through the MPMS sensing coils. This added to the perfect symmetry of this cell enable the SQUID response to remain symmetric and, therefore, integrable down to a signal of 10^{-7} emu.

A number of long pressure cells utilise the antiextrusion ring sealing mechanism instead of the mushroom type. This is the case of the devices presented by Kamishima *et al.* [25] and by Mito [20] in which the sample is confined to a 1 cm (at ambient pressure) long PTFE capsule sandwiched between two long zirconia pistons on each side. The design from Nakai *et al.* illustrated in Figure 3.19 uses antiextrusion rings as well but stands out by the dimension of the high pressure volume which with the pistons fully engaged has a length of 6 cm.

The cell body is a cylinder 15 cm long with outer and inner diameters of 8.5 mm and 2.5 mm, respectively. Several pistons made from non-magnetic WC, zirconia and NiCrAl and bodies made from MP35N and NiCrAl have been tested. The NiCrAl appeared to be the best compromise between mechanical and magnetic properties for both the piston and the body. A maximum pressure of 2.2 GPa at room temperature and 1.7 GPa at low temperature was achieved.

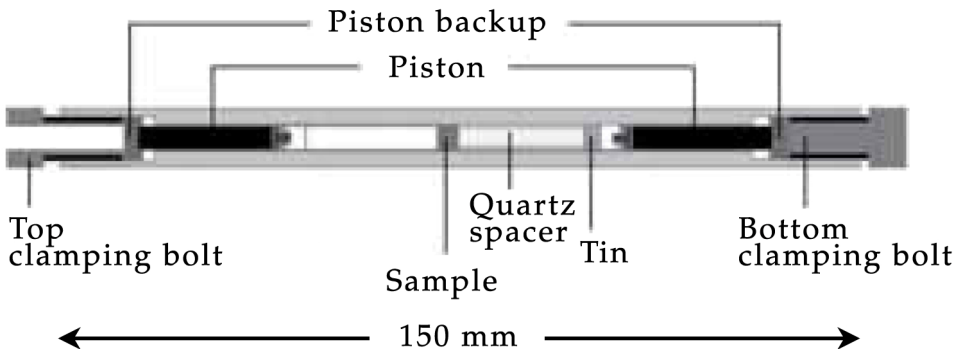

Figure 3.19 Cross section of the cell for the SQUID magnetometer [21]

The sample space is formed by a long PTFE tube closed by two PTFE caps and a BeCu antiextrusion ring placed on either side of the capsule ensure a good seal. A manometer (tin) is located in the bottom of the tube and a quartz spacer (sample holder) positioned between the tin and the sample maintains the later in the centre of the cell. Daphne oil is used as a pressure-transmitting medium.

The bottom clamp bolt and therefore the bottom piston is fully engaged before starting the pressurisation and the pressure is increased through the displacement of the top piston in the bore. An external tool applies the required force directly onto the top "piston backup" and the pressure is locked by tightening the "top clamping bolt".

The maximum pressure reported for this cell is limited by the strength of the pistons. And it is the highest pressure (room temperature) reached by a piston-cylinder device for an MPMS. On the other hand, the minimum magnetisation measurable within the cell is reported to be above 10^{-3} emu at 5 K. This value seems rather high for a long cell. It might be due to the fact that although the cell appears to be fully symmetric (omitting the quartz spacer and the tin) with respect to the sample when both pistons are fully engaged, it is not the case at ambient pressure when the top piston is much further away from the sample. As the pressure increases the top piston gets closer to the sample and the cell becomes symmetric. The unilateral presence

of the quartz spacer and the tin also has an impact on the overall magnetic signal and reduce the sensitivity of the technique.

Another approach to the MPMS piston-cylinder devices is the design of "micro cells". The aim being to produce a cell as small as possible so as to keep the magnetic background signal and the thermal mass to a minimum. The design by Umehara *et al.* is presented in Figure 3.20. The cylinder is 21 mm long and 8.8 mm and 2.7 mm and in outer diameter and inner diameter, respectively. The cylinder and the locking nuts are made of hardened BeCu alloy (C1720B-HT) while the pistons and backups are made of zirconia. The maximum pressure generated in this cell is reported as 2 GPa at 2 K.

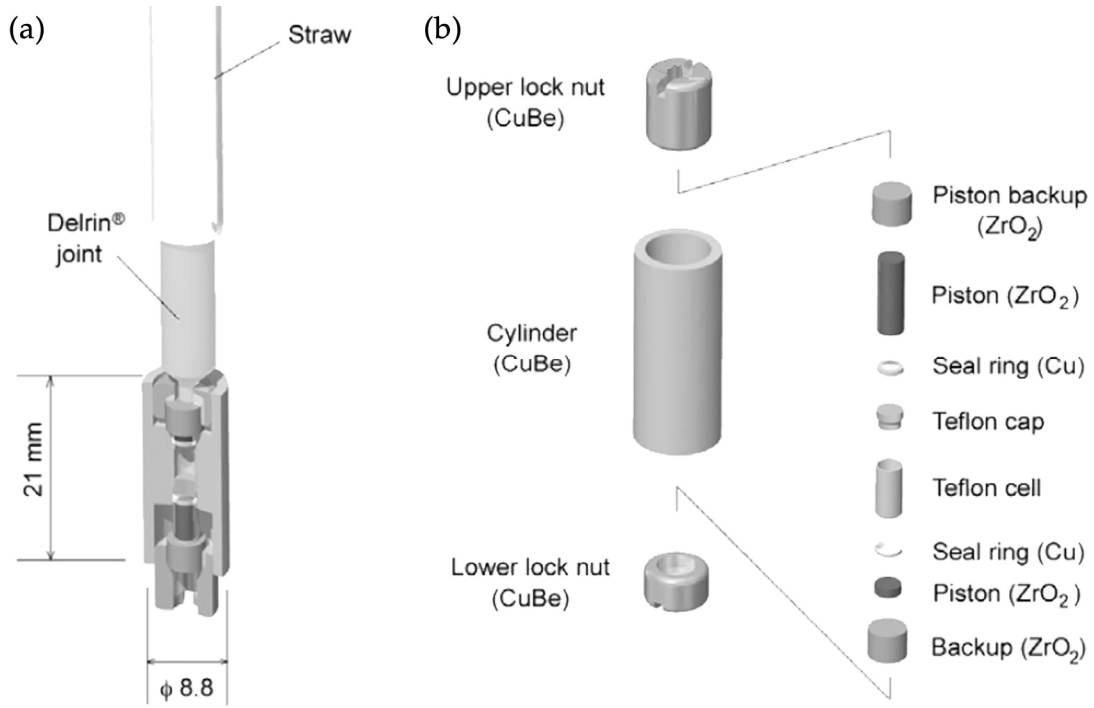

Figure 3.20 Design of a micro pressure cell for magnetisation measurements [18, 153]. (a) Micro cell (upside down) attached to a plastic straw setup for MPMS. (b) Exploded view of the pressure cell.

The high pressure space is sealed by the means of a PTFE capsule and antiextrusion copper rings. The sample, a piece of tin and the pressure transmitting media (mixture of Fluorinert or Daphne 7373) are loaded into

the 8 mm long PTFE capsule. On the lower side, a short piston supported by the "backup" and by the fully screwed in "lower lock nut" remains static. And at the upper end the long piston is used to increase the sample pressure. An external press is used to apply the required force onto the upper "backup" and the pressure is locked by tightening the "upper lock nut". The main advantages of this type of cell are the simplicity of fabrication and the ease of use as well as their small size. With a total weight of 9 g the micro cell reaches thermal equilibrium quickly and produces a low magnetic signal.

Unfortunately the cell is asymmetric with respect to the sample, too long to induce a good SQUID signal and at the same time too short to be magnetically homogeneous over the scan length, i.e. the body's and the nuts' extremities will generate a strong signal when passing through the sensing coil. As result this type of pressure cell is not suitable for studying weakly magnetic materials.

Chapter 4

Techniques and instrumentation

4.1 Magnetometry

4.1.1 SQUID magnetometer

4.1.1.1 Generalities

Magnetic measurements have been carried out using a SQUID magnetometer, the Quantum Design MPMS *XL7* system, which is the most sensitive commercial SQUID magnetometer available. It is based on a radio frequency (r.f.) SQUID [154, 155], which consists of a ring of superconducting material (generally niobium) interrupted by a thin insulating layer. This "weak link" is known as a Josephson junction, and its critical current density is affected by the presence of a small field so that the conduction state of the junction can be controlled by applying a magnetic field. The (r.f.) SQUID acts therefore as a very sensitive magnetic flux to voltage converter.

Because of its extreme sensitivity the SQUID sensor has to be shielded from fluctuation in the ambient magnetic field and from any large magnetic field produced by the superconducting magnet. The detection coil, made of a single piece of superconducting wire, is located in the region where the flux measurement is to be made, within the uniform and stable magnetic field. It is positioned at the centre of the superconducting magnet around the sample chamber so that the magnetic field from the sample couples inductively to the coil.

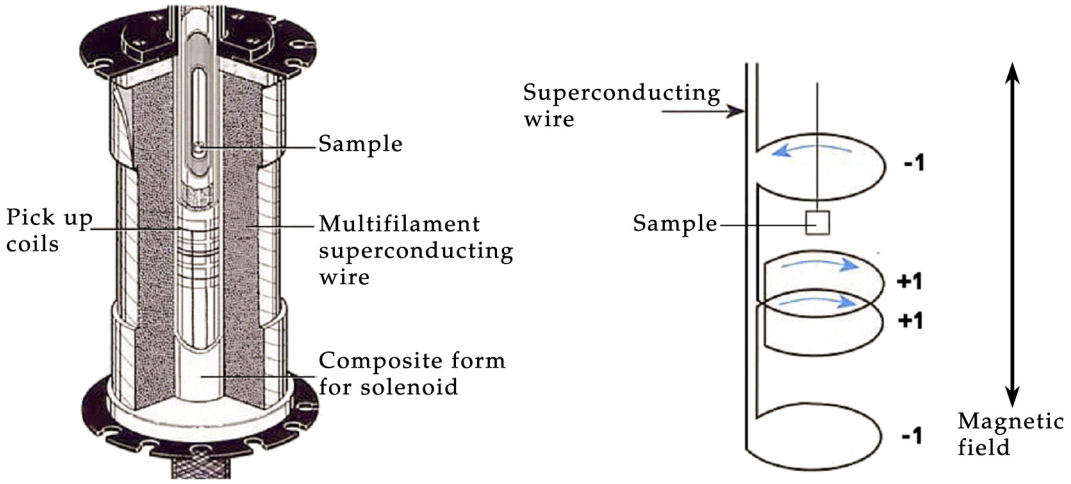

Figure 4.1 Location and configuration of the second-order gradiometer superconducting detection coil. The detection coils and the solenoid magnet sit in the liquid helium bath [156].

The detection coil consists of a set of three coils configured as a second-order gradiometer, shown in Figure 4.1. This arrangement reduces noise caused by fluctuations in the large magnetic field and minimises background drifts in the detection circuit caused by the relaxation of the magnetic field. The upper coil is a single one wound clockwise, the centre coil comprises two turns wound counter-clockwise, and the bottom coil is a single turn wound clockwise. This setup ensures that if the magnetic field is relaxing uniformly, the flux change in the centre coil will be exactly cancelled by the flux change in the top and bottom coils.

During a *dc* magnetic measurement the sample is magnetized by a known magnetic field and the magnetisation of the sample is measured. Measurements are performed by moving the sample relative to the set of pick-up coils, and the motion of the sample is determined by a computer controlled stepping motor, enabling the sample to be raised and lowered on a defined scan length (typically 4 cm or 6 cm for maximum sensitivity). The resulting flux change induces a current in the superconducting pick-up coil, which then produces a change in flux at the SQUID signal coil via the superconducting flux transformer. This gives rise to a change in the voltage output from the SQUID which is proportional to the magnetisation of the sample. The output voltage is measured as a function of the sample position (Figure 4.2) and the sample's magnetic moment is then extracted using a computer fitting routine.

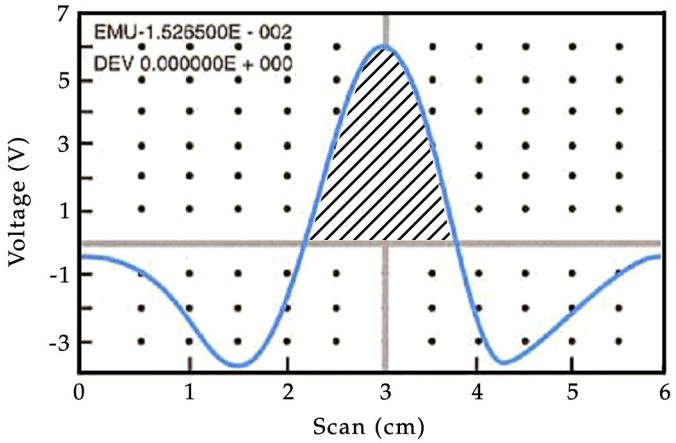

Figure 4.2 Signal voltage produced in the pickup coils due to the movement of a sample in a 6 cm scan. The value of the hatched area is proportional to the sample magnetisation [156].

Ideally the current induced in the detection coil is produced by the movement of a point source magnetic dipole in a non magnetic sample holder.If the sample is very long, extending beyond the detection coil during a scan, its motion will not be detected by the gradiometer since there would be no net change of the flux in the detection coil. This is the reason why a long uniform tube should be used as a sample holder.

The superconducting parts present in the SQUID magnetometer – superconducting magnet, detection circuit and the SQUID itself – are maintained in a superconducting state using liquid helium.

The most widely used SQUID magnetometer at present is the MPMS system from Quantum Design. This enables the magnetisation to be measured down to approximately 10^{-8} emu in temperatures ranging from 1.9 – 400 K. The maximum field depends on the particular model but is typically 1, 5 or 7 T.

4.1.1.2 Samples and Sample holder

For a standard powder measurement using the SQUID magnetometer, the sample is loaded in a gelatine capsule which is then secured within a plastic straw as sample holder (Figure 4.3). The gelatine capsule and the straw are very low in magnetic impurities, and specially screened for magnetic measurements. The plastic straw extends well beyond the coil during a scan therefore its motion will not produce any flux change in the detection coil. Depending on the size of the magnetic moment of the sample the mass needed can vary from less than a milligram to 10 mg or more for very weak magnets. It is also possible to measure the susceptibility of a single crystal in different orientation by fixing it directly in a straw using a small amount of vacuum grease or General Electric (GE) varnish.

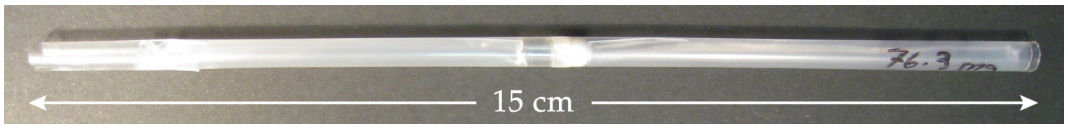

Figure 4.3 Conventional plastic straw sample holder. The sample (white powder) is enclosed in a gelatine capsule near the centre of the straw. A segment of plastic straw inserted on either side of the gelatine capsule prevents the opening or the displacement of the capsule during the measurement.

4.2 X-ray diffraction

4.2.1 X-ray diffraction systems

Laboratory SXD systems can be found at many university research departments. Reducing the atomic thermal vibrations is one of the ways of improving the quality of the diffraction data and it is common for the X-ray diffractometer to be accompanied by a cryo-flow cooling system. The operation of the diffractometer is controlled via a computer which is also used to record and analyse the data. The cooling system is either controlled by the same computer or via a dedicated temperature controller.

The essential elements of a diffractometer are an X-ray source, a goniometer and a detector. Figure 4.4 is a photograph of one of the system used in research described here. The various parts are identified and the rotation axes of the goniometer are indicated. X-rays are produced by an X-ray tube (1), they are collimated (2) and diffracted by the sample onto the detector (4). A beamstop (3) located between the sample and the detector protects the CCD from direct exposure to the incident X-ray beam. During a scan, the positioning of the sample and the detector is ensured by a three-circle goniometer (8); the detector can move around 2θ, and the sample can be rotated about ω and φ, but in this configuration χ is fixed at 54.76 . A four-circle goniometer would allow the rotation also around χ axis. The APEX II (4) is a charge-coupled device (CCD) area detector. Its active surface is 62 mm x 62 mm with a pixel size is 15μm x 15μm. The sum of the intensities of X-rays hitting each pixel is recorded as frames for subsequent analysis.

Before starting a measurement the sample must be properly centred on the goniometer. The single crystal is glued to the end of a short glass fibre and attached to the XYZ goniometer head (Figure 4.5) which allows small adjustments in three-dimensions. With the goniometer head secured onto the goniometer, the sample is visible via the previously aligned high

magnification camera (5), and its position is further adjusted by using the adjustment screws.

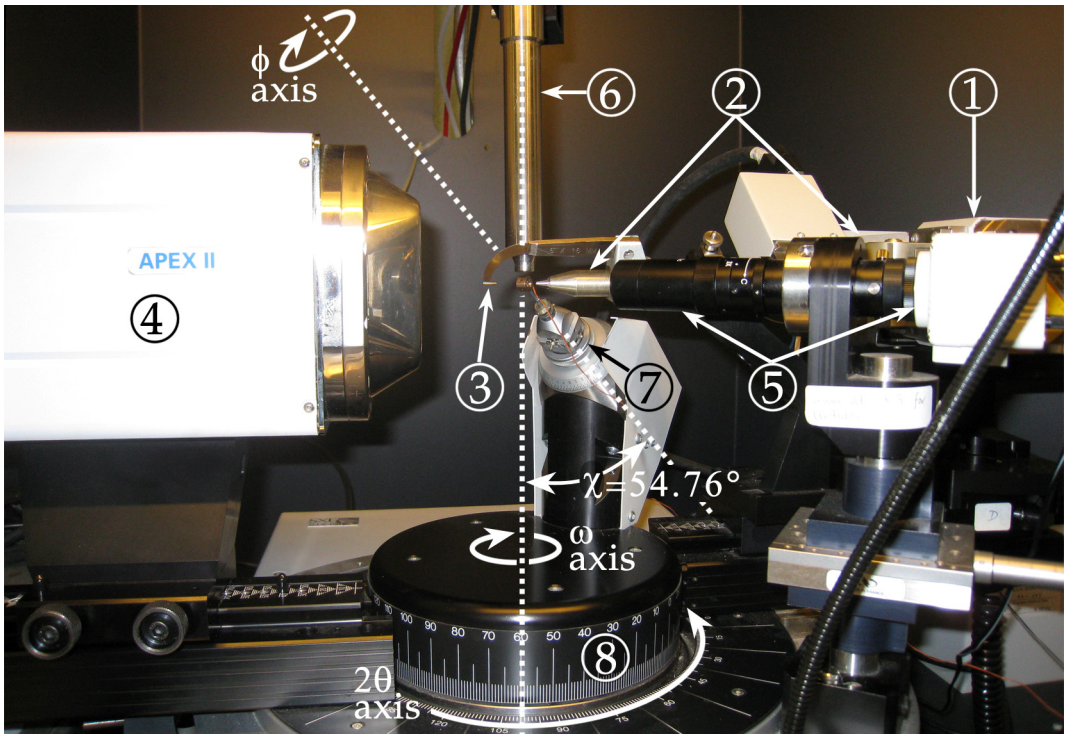

Figure 4.4 APEX II diffractometer from Bruker [157] with the TX-DAC at the sample position. (1) X-ray source; (2) collimator; (3) beamstop; (4) APEX II detector; (5) video camera and objective; (6) cryo-cooler's nozzle; (7) goniometer head; (8) goniometer.

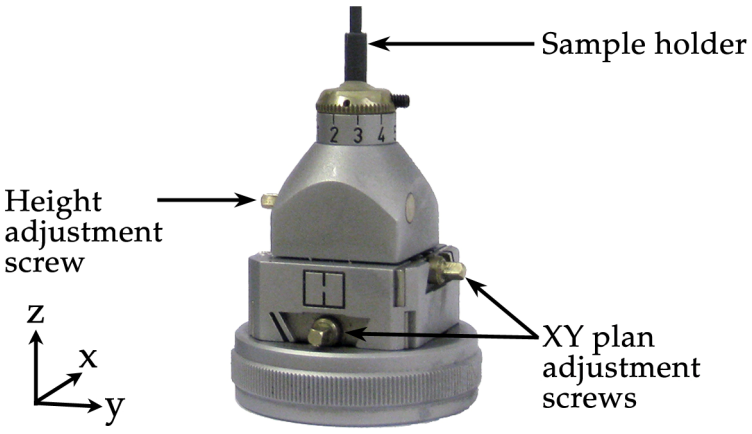

Figure 4.5 XYZ goniometer head from Bruker [157].

The cryo-cooler's nozzle (Figure 4.4 (6)) is that of a Cryostream Plus from Oxford Cryosystems Ltd [158]. This cooling system is used to maintain the

sample at a set low temperature by blowing temperature controlled nitrogen gas onto the sample located a few millimetres underneath the nozzle. The Cryostream Plus requires the supply of liquid nitrogen and operates in the temperature range between 80 and 400 K.

The second SXD system used in this project is a KAPPA APEX II from Bruker [157]. It is equipped with the same key components that can be found in the previously described system with the exception of the goniometer and the cooling system. The four-circle KAPPA goniometer allows positioning the sample at any set of angles which leads to the improved data collection. The cryo-cooler fitted on this diffractometer is the N-HeliX from Oxford Cryosystems [158]. As with other open flow cooling systems the temperature of the sample is controlled by the flow of the gas around it. The N-HeliX operates with nitrogen and helium gas depending on the temperature range. The gas passes through a heat exchanger where it is cooled to the appropriate temperature before being blown onto the single crystal. The accessible temperature range is 100-300 K with nitrogen gas and between 28-100 K with helium.

4.2.2 X-ray diffraction at high pressure

The earliest use of a high pressure device in combination with X-ray diffraction was reported by Cohn (1933) [159]. From 1962, the use of cells based on diamond Bridgman anvils arranged so that the X-rays enter and leave the sample through the anvils themselves is reported by Piermarini and Weir [31], and in 1965 Bassett and Takahashi [160], obtained a pressure of 10 GPa in their diamond anvil press. Today the most commonly used pressure cell for X-ray diffraction measurements is the DAC. While the design of the cell has improved, and the working pressure has increased, the principle is still the same. A metal gasket is used to contain the sample, a ruby chip and the hydrostatic pressure transmitting medium, generally methanol-ethanol mixture. The pressure is raised by applying a force on the

diamonds (screw mechanism), squeezing the sample placed between the tow tips. A ruby pressure scale has been developed to allow the exact pressure to be determined. The R1 fluorescence line of a ruby chip shifts with pressure ($\Delta\lambda / \Delta P = 0.365$ Åkbar^{-1}) [93, 125] but it also shift with temperature [161] making simultaneous measurements difficult.

DACs are routinely used for pressures up to at least 300 GPa and the highest pressures are achieved using bevelled diamond tips. There are however, some limitations with using DACs. Samples are restricted to a few micrograms because of the sample space size. Low energy X-rays are absorbed by the DAC and the background scattering from the diamonds can be very significant. The DAC is also bulky and so the volume of space over which scattered X-rays can be recorded is restricted. Blind regions are particularly crucial when carrying out single crystal X-ray measurements as they seriously deplete the completeness of the data. Be is often used to provide windows through which the X-rays pass. Be is weakly scattering due to the low number of electrons that it possesses but powder rings are still present in the collected data. These rings may overlap with diffraction peaks from the sample and this can result in difficulties when integrating the peaks. Be windows also limit the maximum pressure that can be reached to 20 GPa due to its softness. Different materials for these windows were tested with, the best material found so far to be single crystal diamond plates [162]. Powder rings were not generated from the window and pressures of over 50 GPa were achieved. With the introduction of the Boehler-Almax anvil design and its WC seat contamination free data set can be obtained with neither angle nor pressure limitation.

Miniature DACs developed for X-ray diffraction turned out to have some advantages - in particular they lend themselves to being combined with other extreme conditions such as very high magnetic fields or very low temperatures [163].

Chapter 5

Diamond anvil cell for SQUID magnetometer

5.1 Design

The operation of the TM-DAC is based on the turnbuckle principle. Conventionally such devices are used for creating tensile strain and for tightening cables (Figure 5.1). It consists of a central part and two parts threaded in opposite directions. In Figure 5.1 it is composed of a metal loop and an eyelet screwed into each end of the metal loop. When rotating the metal loop while constraining the hook and the eyelet to translational motion only, these are either pushed apart or pulled together.

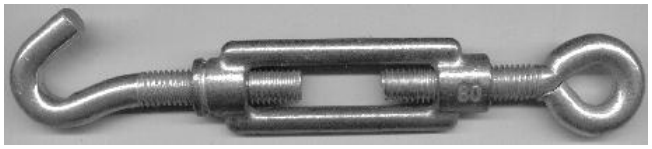

Figure 5.1 Turnbuckle device used to adjust the tension in cables.

In high pressure cells the turnbuckle is used for applying a compressive force by pushing the counterthreaded parts toward each other inside the body of the device. The main advantage of this approach is that the simplicity of the design allows the maximal miniaturisation of DACs. This idea was first applied to the design of a pressure cell by Tozer *et al.* [164-166].

The pressure cell built for magnetisation measurements is made of a fully hardened (Fully Heat Treated (FHT)) BeCu alloy (BERYLCO 25) supplied by NGK Berylco (UK) [167]. The design of the various parts are presented in Appendix A and the final assembled TM-DAC design (v3.2) is shown in Figure 5.2. It consists of a body and two end-nuts. The body is a cylinder 7 mm long and 7 mm in diameter with four flats made to fit a spanner around the body (6 mm flat to flat). It is internally threaded to a M5×0.5 on either side and in opposite direction to a depth of 3.25 mm. Four holes, 1 mm in diameter, have been machined in the sides for viewing the anvils and the gasket. The two end-nuts have three guiding blind holes drilled into them on one side and the diamond anvil sits in a 0.5 mm deep recess on the opposite side. A 1 mm hole going through the centre of the end-nut provides optical access to the sample.

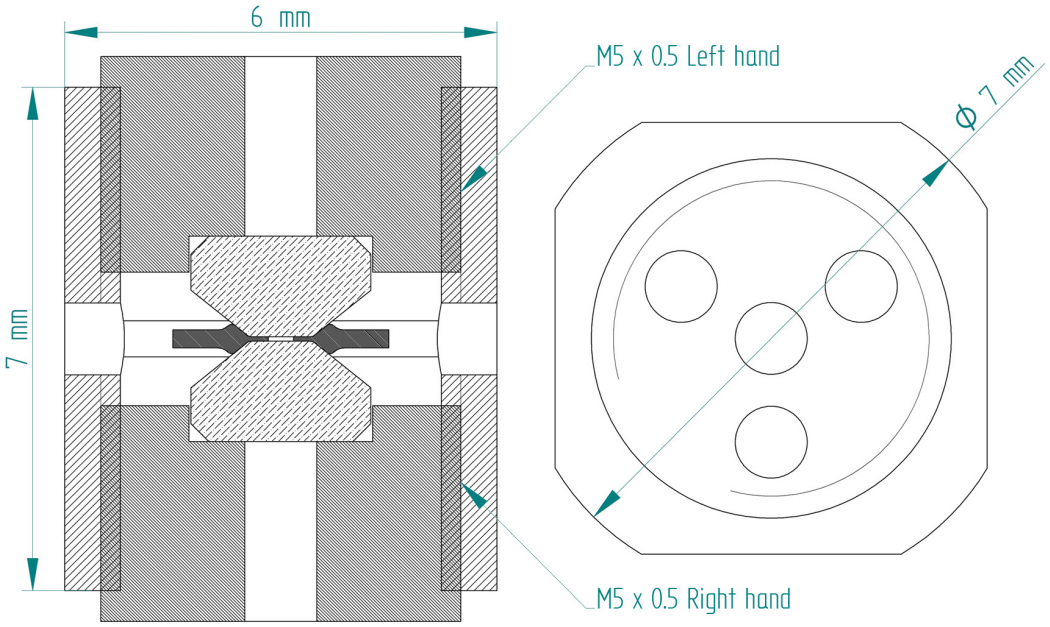

Figure 5.2 Drawings of the TM-DAC with key dimensions.

The end-nuts are identical apart from having the external M5×0.5 threads cut in opposite directions, i.e., left-hand for one end-nut and right-hand for the other one. In order to maximize the strength of the body and to minimize the amount of the cell material around the sample, the behaviour of the cell under load was modelled using finite element analysis [75]. The simulations results presented in section 5.2 show that the cell can hold loads in excess of 6 kN between the end-nuts.

The parts of the TM-DAC are shown in Figure 5.3. During the assembly of the pressure cell the diamonds are maintained in place in each end-nut by a small amount of vacuum grease in such a way that their culets are coaxial. There is no alignment mechanism and the anvil alignment is achieved through precision machining of the end-nuts and the body of the pressure cell. Details of the manufacturing process are given in Chapter 9.

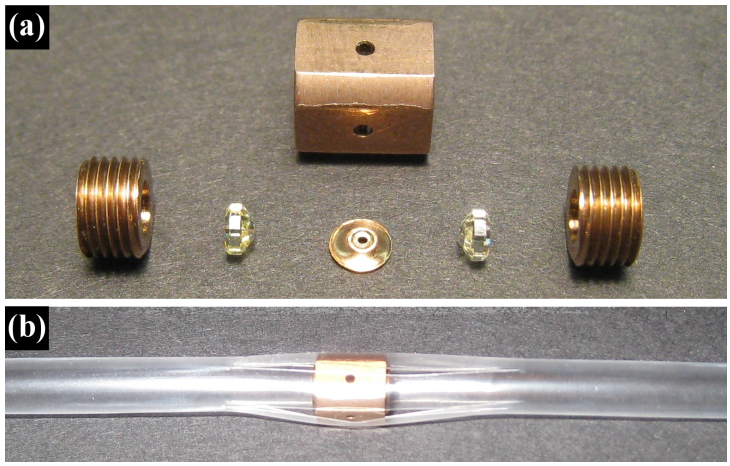

Figure 5.3 (a) Exploded view of the TM-DAC. From the centre to the outside, body, gasket (used), diamonds, end-nuts. (b) The assembled TM-DAC in the standard plastic straw holder of MPMS.

The gasket is a disk of 3 mm in diameter made from a 250 μm thick annealed (An) BERYLCO 25 foil. It is preindented from 250 μm to about 100 μm and a hole of 350 μm is drilled in its centre, making the initial sample volume equal to approximately 10^2 mm^3. During the tests and measurements discussed in this report, diamonds from ALMAX INDUSTRIES [168] with 800 μm culets of type standard design anvils 16 sided were used to achieve pressures in

excess of 10 GPa. Technical drawings of the diamonds are available in Appendix F. With smaller culets or larger diamond the ratio of culet surface area to table surface area would be increased and higher pressures could be reached.

The sample, a pressure marker (a ruby or a piece of Pb, Sn, or In is used to determine the pressure) and a pressure transmitting medium (liquid or compressed gas) are loaded in the gasket's hole. Depending on the requirements of the experiment the pressure inside the cell could be measured either by ruby fluorescence or by following the critical temperature T_c of a superconducting transition in a reference material with known T_c(P) such as Pb, Sn, or In [99]. Then the pressure cell is placed into a specially designed clamp shown in Figure 5.4 and entirely made of BeCu (FHT) to avoid magnetic impurities contamination.

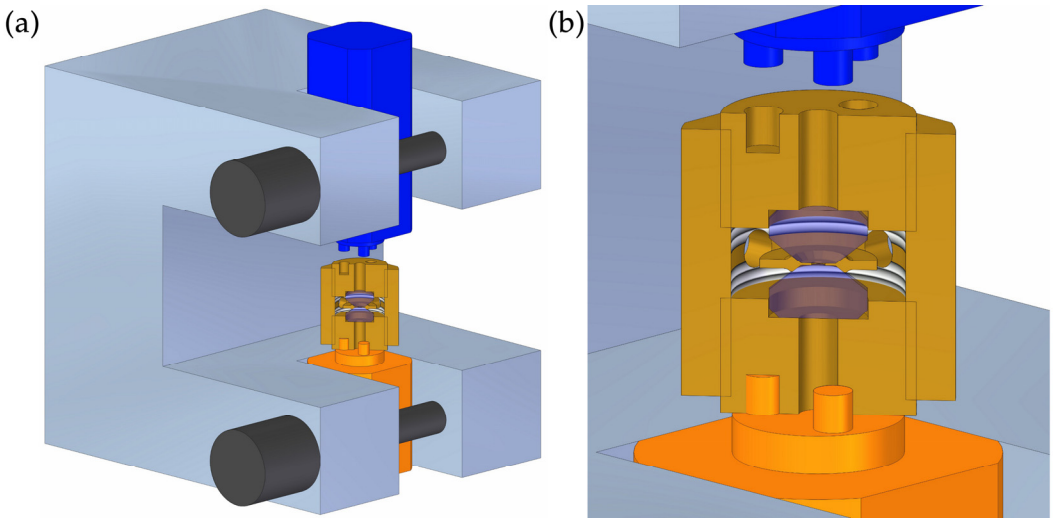

Figure 5.4 (a) Computer-aided design drawing of the clamp for applying load to the TM-DAC. (b) Detail view of the TM-DAC mounted on the clamp.

It is composed of one rigid body and two sliding pistons, each with three pins which engage into the three holes of the end-nuts. Pulling the pistons away from each other allows the pressure cell to be placed into the clamp and ensure that the pins engage fully into the end-nut's guide holes. While it is possible to generate some initial pressure by turning the body of the cell

held inside the clamp, at higher loads the friction on the thread between the body and the end-nuts becomes large.

In order to overcome this problem, the clamp is installed into a top bench hydraulic press and a load is applied to the pistons (Figure 5.5). The load, monitored by a sensitive load cell C2S from AEP *Transducers* [169], is increased in small steps.

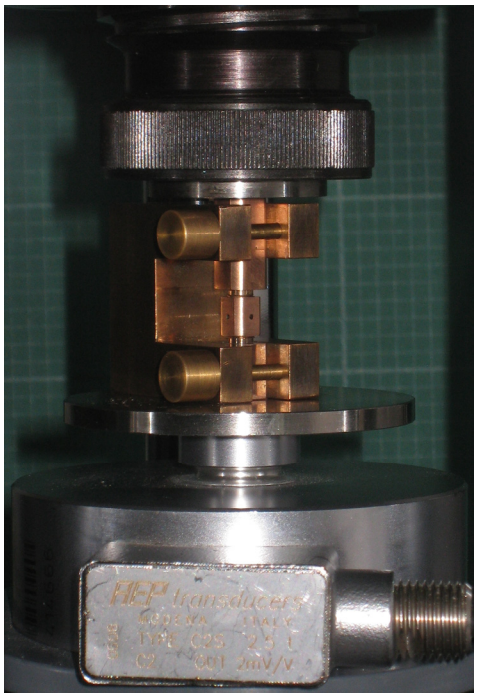

Figure 5.5 TM-DAC in the clamp sitting on the load cell while pressure is applied.

This process closes a small gap that appears between the threads of the end-nuts and the body of the cell due to the deformation along the pitch-line contact in the locked turnbuckle. This relaxes the threads which enables the operator using a spanner to lock the load by rotating the body of the cell with respect to the end-nuts. Once the desired pressure is achieved the pressure cell is placed in the holder for measurements in the magnetometer. A standard plastic straw recommended for use with the MPMS as shown in Figure 5.3 (b) was adapted for the measurements.

When using a compressed gas as pressure transmitting medium the cell containing the sample and the pressure marker, assembled but not totally closed, is placed into a gear box clamp (Figure 5.6) designed to fit in the pressure vessel of a NOVA SWISS [170] high pressure system. The gear box connect to the outside through a hex key fitting and once the vessel is filled with compressed gas the cell can be remotely closed sealing the compressed gas into the sample space. To further increased the pressure the gears are removed and the clamp including the pressure cell is installed into the top bench hydraulic press setup describe above and the same procedure is followed. Detailed drawing of the gear box parts are presented in Appendix C.1.

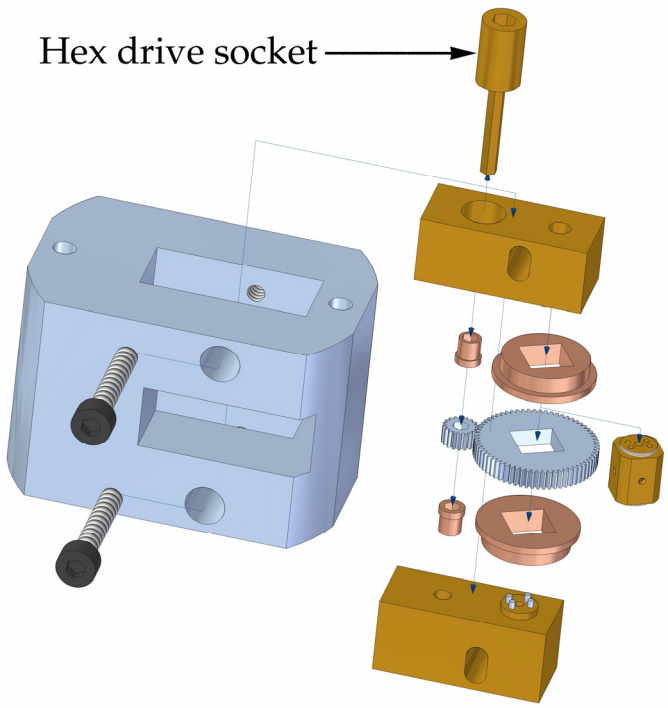

Figure 5.6 Gas loading gear box clamp designed by Weiwei Wang.

5.2 FEA analysis of the TM-DAC

The results of the static FEA calculation of the TM-DAC body and end-nut are presented in this section. The parts included in these simulations are all made of Berylco 25 and the following mechanical properties were assigned to the material: Young's modulus = 127 GPa; Poisson's ratio = 0.34.

5.2.1 End-nut FEA analysis

A full 3D analysis of the end-nut has been carried out and the result is presented as a section view of the part in Figure 5.8 (b). After an initial meshing of the part, an adaptive convergence process was setup so that smaller mesh would be generated until the obtained stress results converge. The anvil was not included in the simulation instead a downward force of 5026 N, corresponding to a pressure of 10 GPa applied on the surface area of the culet, is being applied on the contact surface area between the anvil and the end-nut. On Figure 5.8 (a), it represents a ring of 2 mm in diameter located on the recess surface around the central hole. A fixed vertical support is applied to the inferior surface of the thread. The end-nut is the part expected to be subject to the highest level of mechanical stress and indeed the stress mainly concentrates around the region supporting the anvil.

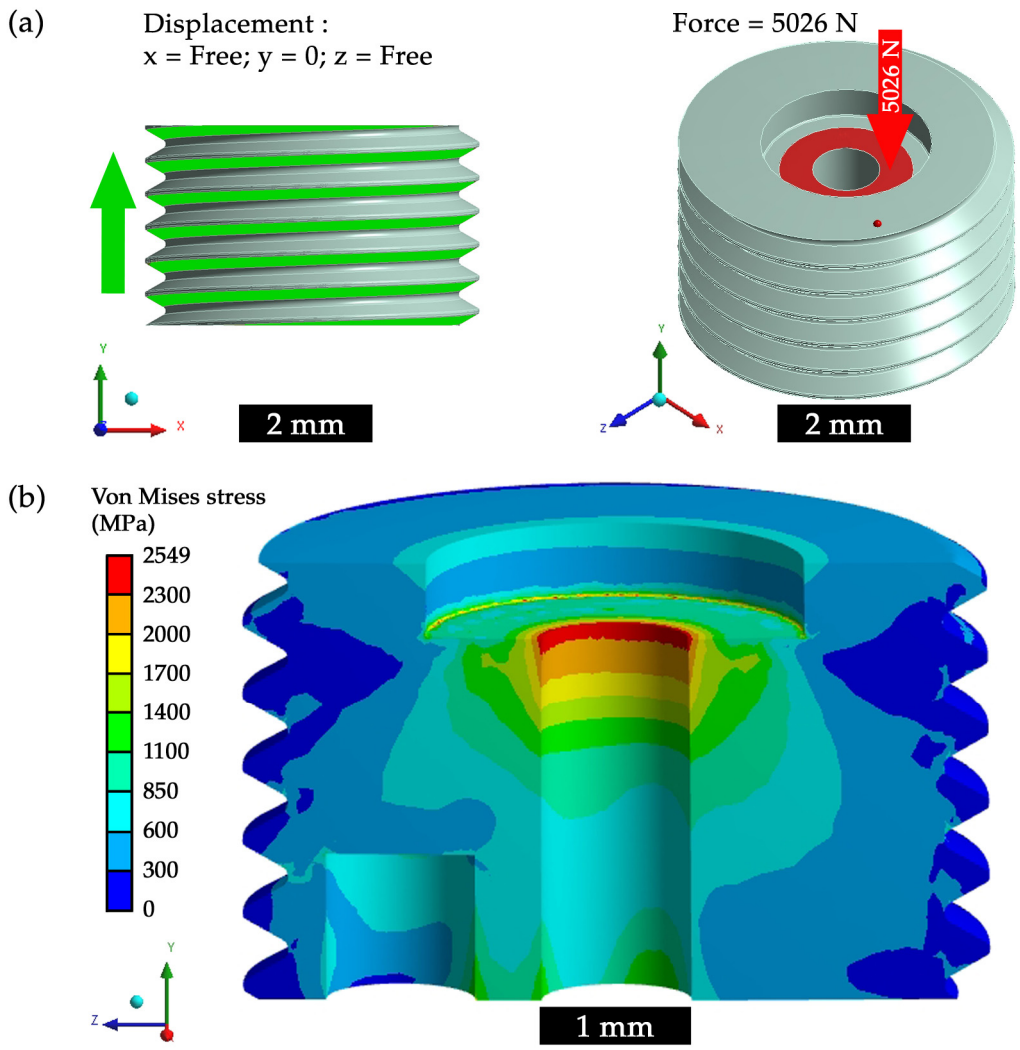

Figure 5.7 (a) Support and loading conditions for the FEA simulation of the TM-DAC end-nut. (b) Von Mises stress distribution in the TM-DAC end-nut when the pressure generated on the culet surface area is equal to 10 GPa.

The result shows that the level of stress remains lower than the yield strength of BeCu (1200 MPa) in most of the part with the exception of the region below the anvil base where it largely exceeds it. However two factors have to be taken into consideration:

- A force equivalent to 10 GPa of pressure was applied on the full surface area of the culet. The pressure distribution across the diamond culet depends on a number of factors, which include the gasket material, the pressure medium, the diameter of the sample hole in the gasket, etc. Therefore it is difficult to predict with precision what

pressure would be generated in the sample volume with what load, however, it is clear [3, 102] that the pressure would be at its maximum in the centre of the culet and close to zero at the edge of the culet. Therefore, in the simulation we presume the worst-case scenario in which the same pressure is generated uniformly on the whole surface of the diamond culet.

- If the stress is greater than the yield strength of the material plastic deformation will occur. The anvil will indent into the end-nut and it will result in work-hardening of the BeCu.

5.2.2 Body FEA analysis

Because the body is fully symmetrical along its length and due to its four-fold symmetry axis a 3D analysis of one eighth of the cell body is sufficient to obtain the stress distribution resulting from the force needed to hold the two end-nuts together.

The result is presented as a section view of the part in Figure 5.8. It is clear from the previous results that the stress concentration in the thread is not an issue and in this case the thread is not modelled. Instead a downward force of 1256.5 N, corresponding to a pressure of 10 GPa applied on the surface area of the culet, is applied on to the inside surface area of the body section (red area in Figure 5.8 (a)). The symmetry conditions which apply to this

section of the cell body are represented by the green surface on Figure 5.8 (a). For each face, no displacement is allowed in the direction normal to the plane of the face while displacements are free in other directions.

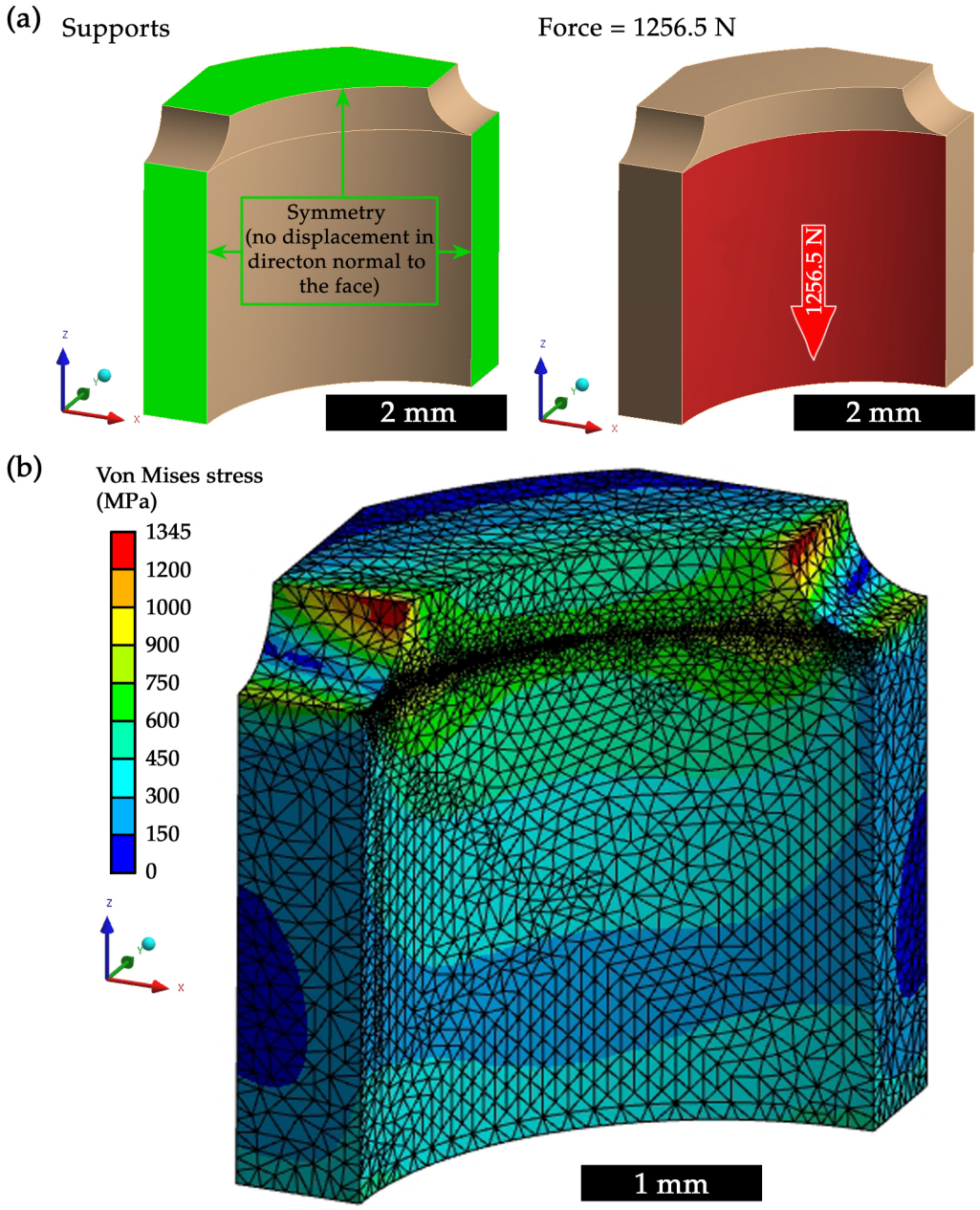

Figure 5.8 Von Mises stress distribution and mesh in the TM-DAC body when the pressure generated on the culet surface area is equal to 10 GPa.

The result shows that the maximum stress concentration arises around the four 1 mm viewing hole and it exceeds only very slightly the yield strength of BeCu (1200 MPa) on a localised region. Since the worst-case scenario is presumed and hence the applied force is in excess of the real target figure this result remains acceptable.

5.3 Testing

The first test is to look at the anvil alignment. Since it relies on the machining accuracy and cannot be adjusted it is essential that when the diamond culets are in contact the misalignment observed is less than 5 % of the culet diameter in the culet plane and that the wedge between the culets is kept to a minimum. Figure 5.9 shows a perfect alignment of the anvil in all directions.

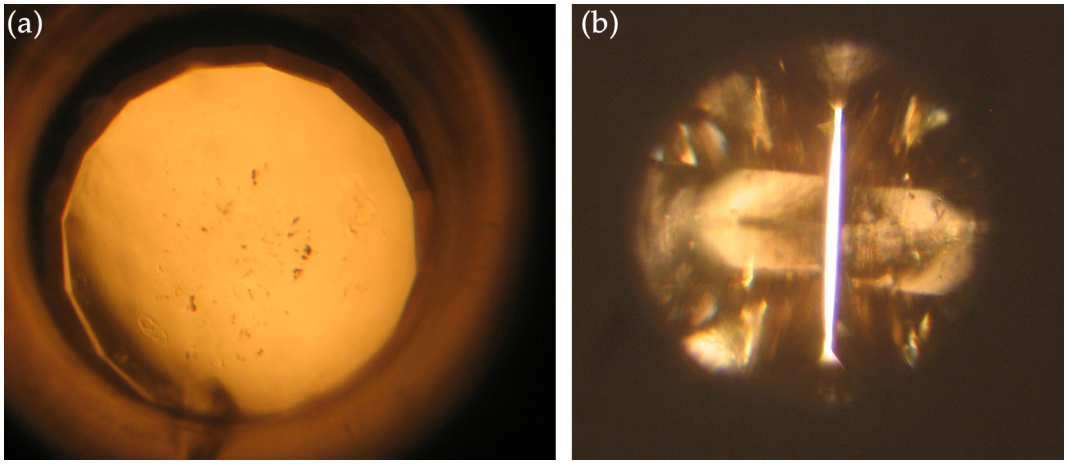

Figure 5.9 Diamonds alignment inside the TM-DAC. (a) looking through the anvil. The edge lines of each culet would be visible if they were not aligned, in the picture they are overlapping (It looks like the culets are off-centred with respect to the end-nut but this due to the alignment of the cell under the microscope). (b) looking through a side hole, no wedge is visible.

The next tests are to confirm that a pressure of more than 10 GPa can be applied to the sample and that due to its low magnetic signature the cell is suitable for the study of magnetic samples in a MPMS.

5.3.1 Pressure testing

Two pressure markers, a ruby sphere and a piece of lead (high purity 99.99+ %) are loaded into the gasket's hole (Figure 5.11) with some Daphne 7373 oil as pressure transmitting medium [88]. The pressure is then increased in six steps to reach a maximum of 10 GPa. For each step the pressure is measured at room temperature (~295 K) by the ruby fluorescence technique and at low temperature (~3-7 K) by following the critical temperature T_c of the superconducting transition of lead [99]. The results presented in Figure 5.10 show that the TM-DAC is capable of reaching 10 GPa and that there is no significant pressure drop when cooling the pressure cell from ~295 K to ~3 K.

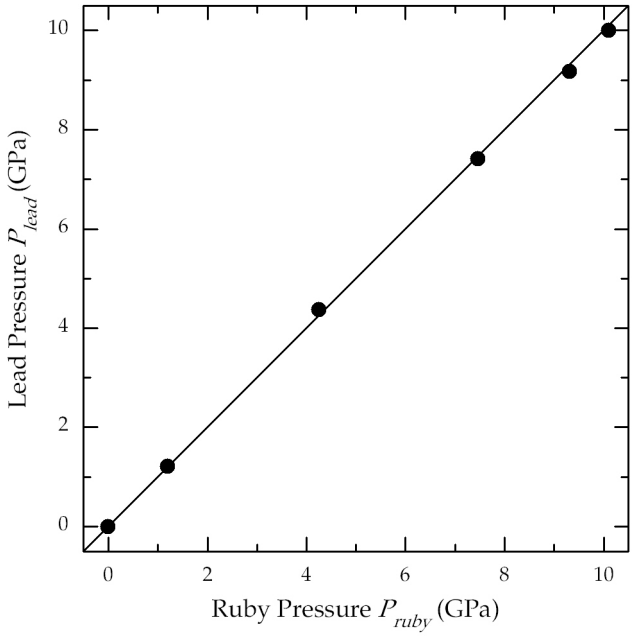

Figure 5.10 The pressure P_{lead} determined at the superconducting transition in lead at low temperature (T~3–7 K) vs the pressure P_{ruby} derived from the ruby fluorescence at ambient temperature (T~295 K). The solid line shows $P_{lead}=P_{ruby}$. The errors in determining the pressure are ±0.03 GPa for lead and ±0.02 GPa for ruby. The error bars are smaller than the symbols on the graph.

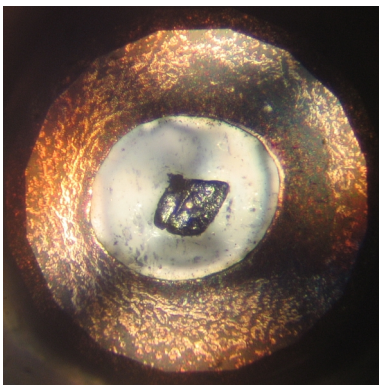

Figure 5.11 Lead and ruby sphere with Daphne 7373 oil at 4.3 GPa.

5.3.1.1 Gas loading

A ruby sphere is loaded into the pressure cell and using the gear box clamp the cell is loaded with compressed argon (Ar). The cell is closed under an Ar pressure of 0.2 GPa. By closing the cell and therefore applying some pressure on the gasket to make sure that the gas is properly sealed in the gasket's hole the pressure increased to 0.3 GPa (Figure 5.12).

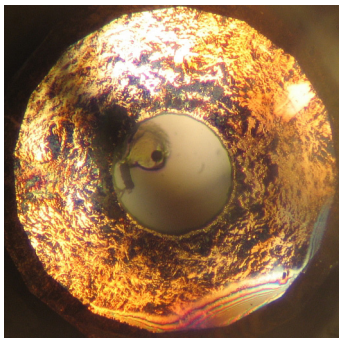

Figure 5.12 Ruby sphere held with some vacuum grease on a culet surface. Cell loaded with Ar as pressure transmitting medium and at 0.3 GPa.

The pressure is then increased to 0.6 GPa and the spectra obtained from the ruby fluorescence for these pressure points are shown in Figure 5.13. Unfortunately the gasket failed on the subsequent pressure increase but this result indicate that it is possible to load the TM-DAC with compressed gas and that with the right gasket the cell's maximum pressure could be reached.

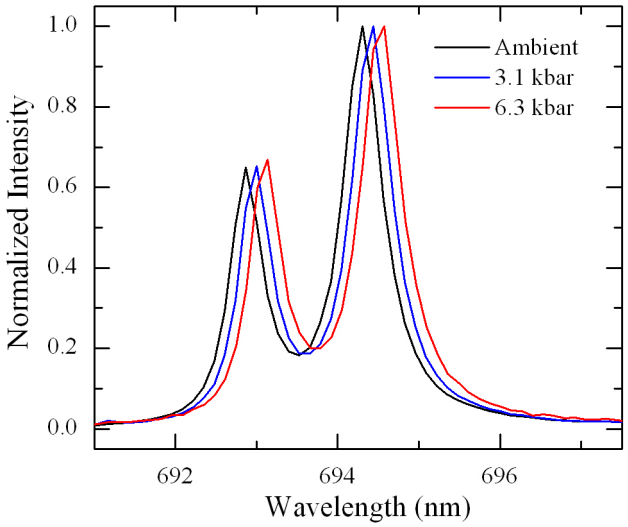

Figure 5.13 Ruby fluorescence spectra for the TM-DAC loaded with Ar as pressure transmitting medium.

5.3.2 Test of magnetic properties

To establish the magnetic properties of the cell the temperature dependence of the magnetisation of an empty TM-DAC from 2 K to 300 K and in various magnetic fields was measured, and the resulting susceptibility data sets are plotted in Figure 5.14. The curves are smooth and follow the known trend for BERYLCO 25 alloy.

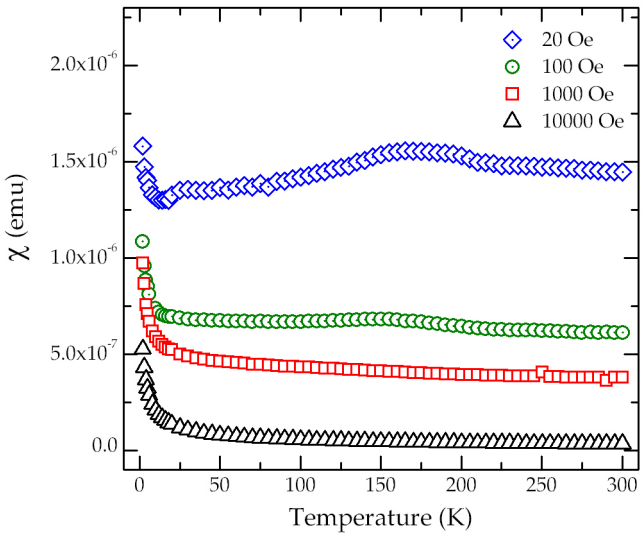

Figure 5.14 The temperature dependence of the magnetisation of an empty TM-DAC shown as $\chi = M/H$ for different magnetic fields.

Due to its small size (<10 mm long) and weight (~1.5 g) the pressure cell can be cooled down at a high rate and reaches thermal equilibrium quickly which helps to save time and cryogenic consumables during the measurements. But the most important asset of this pressure cell is related to its geometry. Indeed the ideal sample for a MPMS is a point (or spherical) sample this is generally not practically possible but Quantum Design recommendations to obtain the highest measurement sensitivity are to keep the sample symmetrical and with a total length less than 10 mm [171].

The TM-DAC is fully symmetrical along its length with respect to the sample and its length is inferior to 10 mm consequently the signal produced when scanning the cell through the MPMS gradiometer pick up coil (Figure 5.15) is very similar to the signal obtained from a perfect shape sample and its magnetisation can be measured accurately. It is important to be able to quantify the background contribution of the cell which can then be subtracted from a high pressure magnetisation data set to obtain the sample's magnetisation alone.

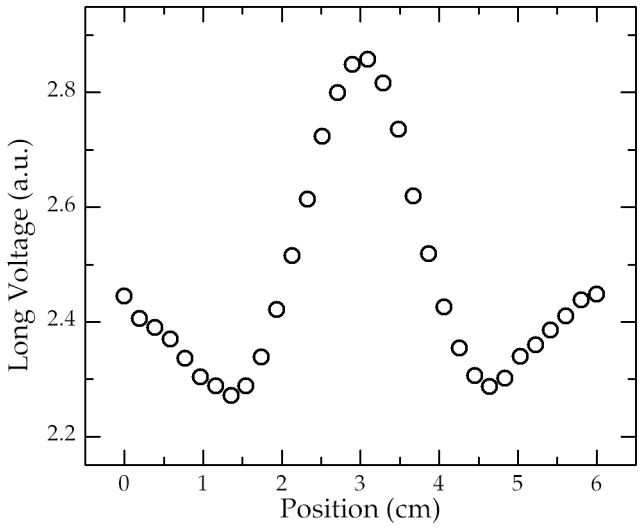

Figure 5.15 Raw MPMS data generated by a scan of the empty TM-DAC over a 6 cm distance in an applied field of 20 Oe at 300 K. The resulting integrated magnetisation as calculated by the MPMS software is 1.07×10^{-5} emu.

5.4 Results

5.4.1 PBA - $Mn_3[Cr(CN)_6]_2 \bullet xH_2O$

The magnetisation of a sample of $Mn_3[Cr(CN)_6]_2 \bullet xH_2O$ which belongs to the Prussian Blue Analogue (PBA) family has been studied. PBAs present a large variety of interesting electronic properties which can be tuned by means of magnetic field, light, temperature or pressure. Their magnetic behaviours, either ferromagnetic or antiferromagnetic with transition temperature ranging from 5 K to 376 K, have been extensively reviewed [172-175]. These molecular-based magnet materials have the general chemical formula $C_cA_a[B(CN)_6]_b \bullet xH_2O$, where A and B are typically transition metal ions and C is present as a univalent cation. When a = b, x = 0 and c = 0, a simple cubic array of $A(NC)_6$ and $B(CN)_6$ octahedra, linked through A-N≡C-B bonds from the structure. The introduction of C^+ allows some charge variation on A or B sites, while further variation in charge may occur when $a \neq b$, and vacancies in co-ordination polyhedra may be taken up to some extent with water, sometimes called 'zeolitic water'. This is the case with the material studied here. $Mn_3[Cr(CN)_6]_2$ is a ferrimagnetic material which consists of a cubic network of alternating $Mn(CN)_6$ and $Cr(NC)_6$ octahedra connected through the cyanide bridges [176]. The sample used here has been prepared during my Master's project; it has $x \sim 16$ and its preparation, structure, and magnetic properties up to 1 GPa pressure are reported elsewhere [177, 178].

$Mn_3[Cr(CN)_6]_2 \bullet xH_2O$ was loaded into the pressure cell with a ruby chip and a small piece of lead for independent pressure measurements at room temperature and at T ~ 7 K, respectively. Figure 5.16 shows photographs of the gasket hole taken through the microscope, which show the sample, ruby, and lead and also illustrate the performance of the gasket at high pressure.

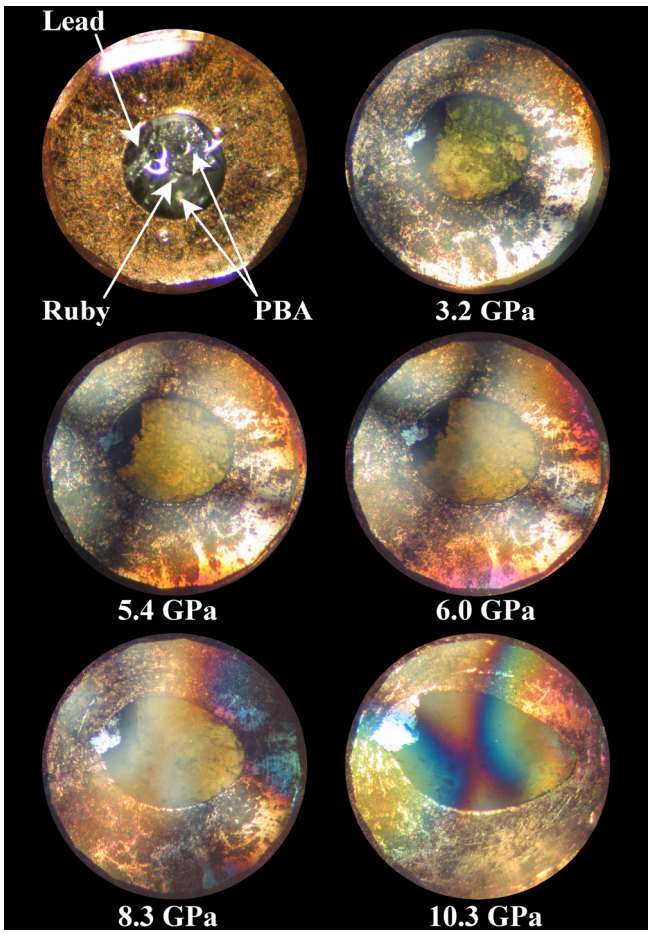

Figure 5.16 Photographs of the gasket hole taken at several pressure points during loading. The hole contains the sample of $Mn_3[Cr(CN)_6]_2 \cdot xH_2O$ PBA, a speck of Pb, and a ruby chip. The elongation of the sample hole illustrates the quality of the anvil alignment.

Pressure was applied in small steps after each of which the magnetisation was measured as a function of temperature (Figure 5.17). A small feature at T ~ 60 K is present in all the data sets and its magnitude and position are not affected by applied pressure. The temperature at which it is observed corresponds to the Curie temperature T_C of the PBA at ambient pressure, and therefore this feature is attributed to a minute amount of the sample left outside the pressurized volume of the cell during the loading procedure.

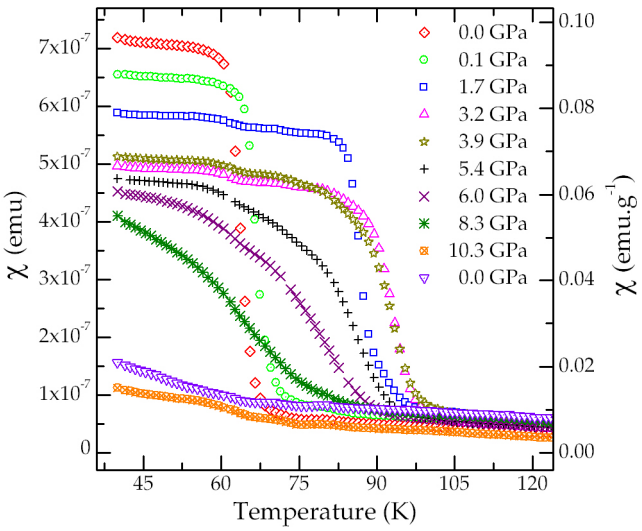

Figure 5.17 The temperature dependence of the magnetic susceptibility of $Mn_3[Cr(CN)_6]_2 \bullet xH_2O$ in a 100 Oe field at several pressures. The data have been collected on warming after cooling down in field and are corrected for the cell background. The final (inverted triangle) data are collected after the release of pressure. The left axis shows the susceptibility χ in emu while the right axis shows χ_m values normalized by the mass of the sample m = 7.5×10 $^{-3}$ mg, estimated from the comparison of the $\chi(T)$ measurements performed at ambient pressure on the sample in a plastic straw and in the TM-DAC.

The sample magnetisation M was measured in a field of 100 Oe and its susceptibility χ and mass susceptibility χ_m, where the sample mass was m = 7.5×10 $^{-3}$ mg are plotted in Figure 5.17. The mass of the sample present in the TM-DAC was calculated by comparing the value $\Delta\chi_m$ at P = 0.0 GPa obtained in the TM-DAC with the value $\Delta\chi_m$ obtained from a known mass of $Mn_3[Cr(CN)_6]_2 \bullet xH_2O$ measured in a gelatine capsule. The pressure variations of T_C, derived from the maximum of $d\chi/dT$, and $\Delta\chi_m = \chi_m(40K) - \chi_m(120K)$, taken as being proportional to the ferrimagnetic moment, are shown in Figure 5.18. The initial dT_C/dP =25 K/GPa is similar to the values reported in two previous studies at pressures below 1 GPa [178, 179].

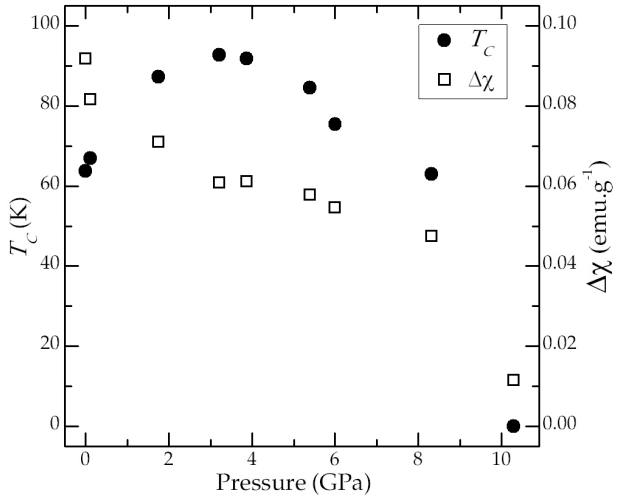

Figure 5.18 The pressure-temperature magnetic phase diagram of $Mn_3[Cr(CN)_6]_2 \bullet xH2O$. $\Delta\chi_m$ shows the difference between the values of mass susceptibility taken at 40 K, χ_m (40 K), and 120 K, χ_m (120 K) see Figure 5.17.

At higher pressures, a substantial but nonlinear increase in T_C from 63 K at ambient pressure to a maximum T_C = 93 K at 3.2 GPa pressure is discovered. This reflects an enhancement of the superexchange interactions between the transition metal cations as the bonds to cyanide are shortened with pressure. The ferromagnetic moment decreases as T_C is enhanced which may evidence increased tilting of the $Mn(CN)_6$ and $Cr(NC)_6$ octahedra. At pressures above 3.2 GPa the magnetic transition becomes much broader and T_C is suppressed to zero near 10 GPa, with a corresponding collapse of the ferromagnetic moment. This is consistent with a pressure-induced amorphization of the sample, as was observed in a similar PBA, $FeCo(CN)_6$ between 8 and 10 GPa [180]. The observation that the ferrimagnetism of $Mn_3[Cr(CN)_6]_2 \bullet xH_2O$ does not recover when the pressure in the pressure cell is released from 10 GPa, the last zero pressure point in Figure 5.17 supports this conclusion but a structural study up to 10 GPa will be needed for confirmation.

5.4.2 UNi_2

Actinide compounds display an interesting variety of low temperature electronic and magnetic properties ranging from Pauli paramagnetism to itinerant or localised magnetism, superconductivity and heavy-fermion behaviour. The 5-*f* orbital overlap defines the type of magnetism present in actinides. However, in intermetallic compounds, where actinides are coupled with 3*d* transition metals, the hybridization of the 5-*f* orbitals plays an important role in making the 5-*f* electrons either localised or itinerant. Among this family, three compounds with fascinating electronic properties have recently been reported. UGe_2, URhGe, and UCoGe display the coexistence of superconductivity with a ferromagnetically ordered state [181] with a Curie temperature significantly higher than the superconducting transition temperature. URhGe and UCoGe are superconductors at ambient pressure below 0.25 K and 0.8 K respectively [182, 183]. In UGe_2 the superconducting phase is pressure induced and exists in the pressure range 10 to 16 kbar with a maximum temperature of 0.75 K at 11.4 kbar [184, 185]. These materials are described as weak itinerant 5-*f* ferromagnets and feature a strong magnetic anisotropy.

In UNi_2 no superconductivity has been observed at ambient pressure but because it is very similar in terms of its magnetic properties [186] to other uranium-based materials mentioned above, it is expected that superconductivity can be induced by applied pressure. UNi_2 is a Laves phase crystallizing in the hexagonal $MgZn_2$-type structure. Reported Curie temperature varies from 21 K to 27 K depending on the nature of the sample, single crystal or polycrystalline, and on the physical property measured [187].

The sample has been provided by Prof. Andrew Huxley (School of Physics and Astronomy, The University of Edinburgh, Edinburgh, Scotland). The magnetisation of this compound has been measured using polycrystalline

sample in a gelatine capsule and followed on with a pressure study in the TM-DAC. A sample of UNi_2 was loaded in a 350 μm diameter hole in the gasket with Daphne 7474 as pressure transmitting medium and ruby spheres as pressure marker following the procedure described in 4.5.1. The data collected on warming up from 2 K to 300 K in a field of 1000 Oe are plotted in Figure 5.19 in the form of susceptibility as a function of temperature. The ambient pressure data reveal a clear ferromagnetic transition with T_C = 30.8 K and a very weak paramagnetic susceptibility above the T_C. The Curie temperature T_C was determined by differentiating the susceptibility as a function of temperature and fitting $d\chi/dT$ vs T with a Gaussian function in order to establish the position of the peak. This transition at 30.8 K is slightly higher than the one previously reported in literature. Since a small excess of nickel leads to the decrease of T_C [188], one possible explanation is that this sample is of better quality than the one previously studied.

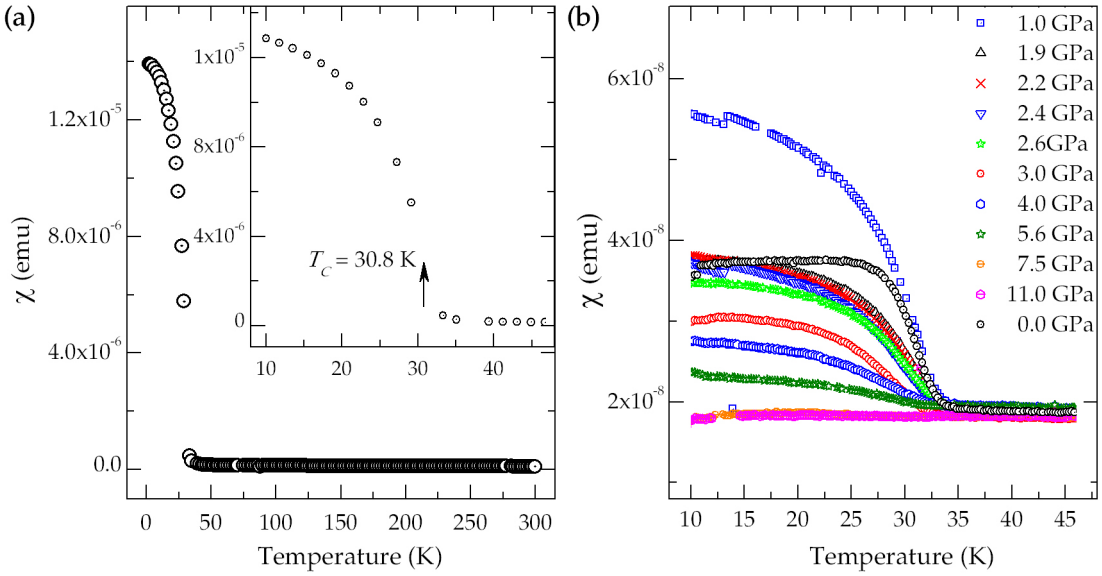

Figure 5.19 Temperature dependence of the magnetic susceptibility of UNi_2 in a 1000 Oe field. All the data were collected on warming from 10 K to 300 K. (a) UNi_2 measured in a gelatine capsule (sample mass 11.9 mg). (b) Low-temperature region of the measurements of a sample of UNi_2 in the TM-DAC at several pressures after background correction. The 0 GPa data were collected after downloading the pressure.

The high pressure data were corrected for the pressure cell background and the values for T_C were obtained by following the procedure mentioned above. The pressure study was started at 1 GPa and the pressure was increased in small steps for each new measurement up to the maximum pressure of 11 GPa. No superconductive phase was observed and the data presented below are focused on the pressure-induced changes in the Curie temperature. Then the pressure was released and an ambient pressure measurement (0 GPa) in the TM-DAC was carried out.

The pressure dependence of T_C and of the magnetic moment is illustrated in Figure 5.20. The latter is taken to be proportional to $\Delta\chi = \chi(15K) - \chi(100K)$. The ferromagnetic phase exists in the measurements under pressure up to 5.6 GPa and vanishes completely totally in the 7.5 GPa and 11 GPa data sets. The $dT_C / dP = -0.86\,\mathrm{K/GPa}$ is in good agreement with the value reported previously at pressures below 0.7 GPa [187]. The strong negative pressure dependence of $\Delta\chi$ is consistent with the 5-f itinerant nature of the sample magnetism.

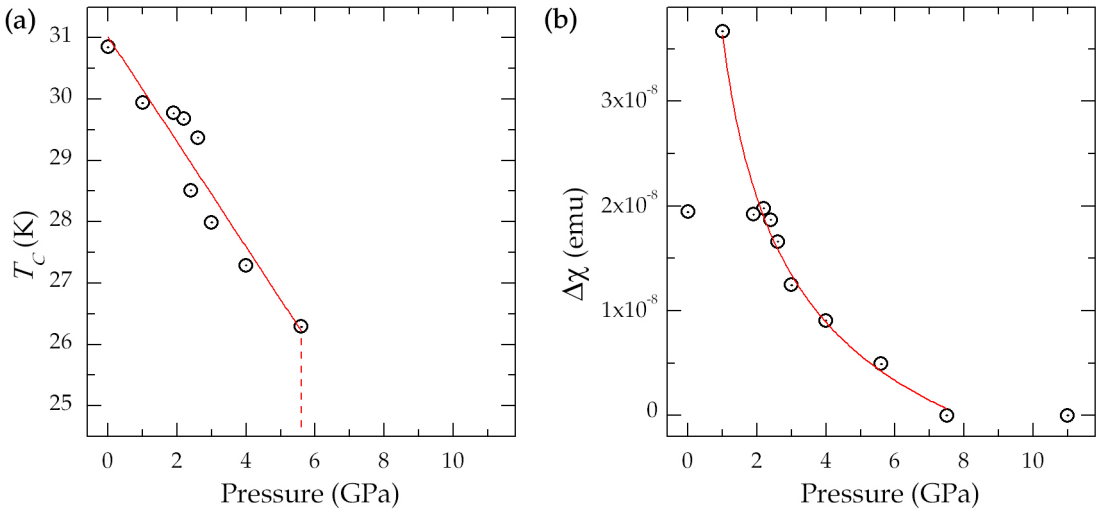

Figure 5.20 (a) The pressure-temperature magnetic phase diagram of UNi_2. The linear fit's slope indicates a T_C pressure dependence $dT_C / dP = -0.86\,\mathrm{K/GPa}$. (b) $\Delta\chi$ represents the amplitude between the susceptibility taken at 15 K and at 100 K. Please note that the zero pressure points are taken from the data collected after downloading pressure in the cell. The line in figure (b) is the guide to the eye.

It should be noted that the magnetisation value, for the data collected after pressure release (Figure 5.19 - 0 GPa) is lower than expected possibly because of a different orientation of the sample in the TM-DAC resulting from the opening of the pressure cell.

This study confirms the existing observation of the pressure effects on the magnetisation of UNi_2 and extends the phase diagram up to 11 GPa. No superconducting phase has been observed however the measurements carried out in the MPMS are limited to a base temperature of 2 K and UNi_2 might be superconducting below this temperature.

5.4.3 $BiNiO_3$

Perovskite-type transition metal oxides with 3*d* electrons exhibit a wide variety of fascinating electronic and magnetic phenomena such as ferromagnetism, spin-glass like behaviour, superconductivity and colossal magnetoresistance. The rare earth (*R*) nickelate perovskite $RNiO_3$ family has unusual properties for a metal oxide, in that (except for *R* = La) they show a metal-insulator phase transition.

$BiNiO_3$ is synthesised using a multi-anvil press at high pressure (6 GPa) and high temperature (1000°C) under oxidising atmosphere [189]. Under ambient conditions of pressure and temperature, $BiNiO_3$ is an insulator with a strongly distorted triclinic perovskite-type structure containing two inequivalent Bi and four Ni sites [190]. The insulating nature of the triclinic phase is due to the charge disproportionation of the A-site Bi ions and thus the divalent nature of the Ni ions. Its electronic state is described as $Bi^{3+}_{0.5}Bi^{5+}_{0.5}Ni^{2+}O_3$. A pressure-induced structural transition from the triclinic $P\bar{1}$ (insulating) to an orthorhombic *Pbnm* (metallic) phase which takes place around 3-4 GPa [191-194] at room temperature has been estimated to occur at 3.46 GPa by a theoretical first-principle study [195]. The metallisation of $BiNiO_3$ is attributed to the simultaneous melting of Bi charge

disproportionation and the charge transfer from Ni to Bi associated with a structural phase transition from triclinic to orthorhombic, thus leading to the $Bi^{3+}Ni^{3+}O_3$ electronic state.

The triclinic phase is magnetically ordered below 300 K with dominant antiferromagnetic (G-type) spin-spin interactions which is typical for ABO_3 perovskites with non-degenerate magnetic ions at B sites. $BiNiO_3$ is ferrimagnetic due to the inexact cancellation of opposing, inequivalent Ni ions moment.

The samples used in the measurements presented hereafter were provided by Prof. J. Paul Attfield (School of Chemistry, The University of Edinburgh, Edinburgh, Scotland). The magnetisation measurement of $BiNiO_3$ samples under ambient and high pressure conditions expressed as mass susceptibility are presented in Figure 5.21.

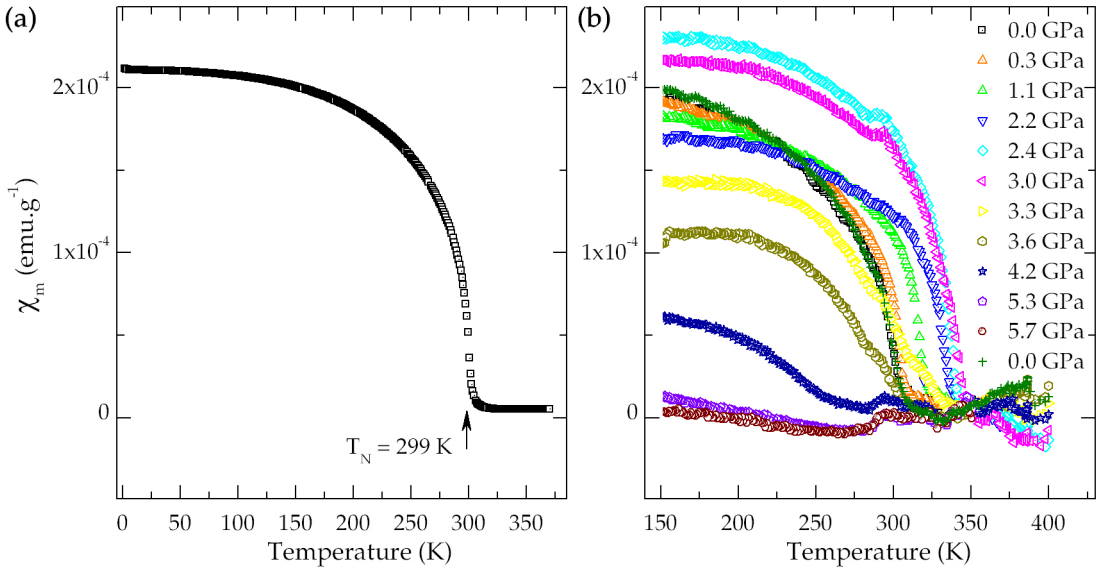

Figure 5.21 Temperature dependence of the magnetic mass susceptibility of $BiNiO_3$ in a 1000 Oe field. All the data were collected on cooling. (a) 6 mg of $BiNiO_3$ measured in a gelatine capsule from 300 K to 2 K. (b) Measurements of $BiNiO_3$ in the TM-DAC at several pressures after background correction. The data sets 0.0, 0.3, 1.1 and 2.2 GPa were obtained from the measurements of a 9.3×10^{-2} mg sample and the remaining high pressure data sets were collected from 7.7×10^{-3} mg of $BiNiO_3$.

All measurements have been carried out on cooling in a magnetic field of 1000 Oe and the data acquired using the TM-DAC have been corrected for the background of the pressure cell. The ambient pressure data (Figure 5.21 (a)) were collected on a 6 mg sample measured in a gelatine capsule. The antiferromagnetic transition temperature T_N = 299 K extracted from fitting the peak of the data's first order derivative curve with a Gaussian function is in good agreement with the literature value. The data sets of two series of pressure measurements in the TM-DAC are gathered in Figure 5.21 (b). In both cases the $BiNiO_3$ sample was loaded in a 350 μm gasket's hole with Daphne 7373 as pressure transmitting medium and ruby spheres as pressure marker.

The high-pressure measurement was performed in two steps requiring two separate sample loading into the cell. The first four data sets (0-2.2 GPa) obtained from 9.3×10^{-2} mg of $BiNiO_3$ form the first series and the second series consists of the remaining pressure data sets corresponding to the measurements of 7.7×10^{-3} mg of sample. In both cases, the masses of the samples under study were calculated by comparing the values $\Delta\chi_m$ at P = 0.0 GPa obtained in the TM-DAC with the value $\Delta\chi_m$ obtained from a known mass of $BiNiO_3$ measured in a gelatine capsule with $\Delta\chi = \chi(50K) - \chi(350K)$. A small feature located around 300 K appears on the second series data sets. This feature is not affected by pressure and corresponds to the ambient $BiNiO_3$ T_N thus it can be attributed to a small amount of material left outside the pressurised sample volume. The pressure dependence of T_N is plotted in Figure 5.22. A constant increase of T_N with pressure is observed up to 3.0 GPa at which point T_N drops sharply and the antiferromagnetic transition is not distinguishable beyond 4.2 GPa. The transition is fully reversible and the initial value of T_N as well as the magnitude of the susceptibility recover after pressure release. The rate of the critical temperature change with pressure $dT_N / dP = 15.2\,\mathrm{K/GPa}$ is generated from a good linear fit of the low pressure region up to 3 GPa.

The enhancement of T_N can be explained by enhanced antiferromagnetic super-exchange through the increase of 3*d*(Ni) and 2*p*(O) orbitals overlap and the shortening of the Ni-O bonds.

The sudden decrease of T_N above 3 GPa is associated with the starting point of the structural phase transition which reaches completeness at 4.2 GPa. The gradual reduction of T_N and of the saturated magnetisation indicate the coexistence of both phases in this pressure region. This hypothesis was previously reported [196] but this is the first time it has been validated experimentally.

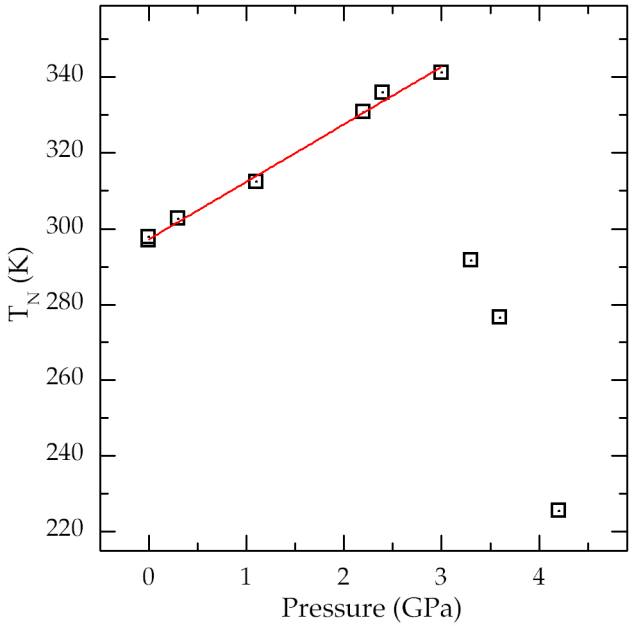

Figure 5.22 The pressure-temperature magnetic phase diagram of $BiNiO_3$. The linear fit's slope indicates a T_N pressure dependence $dT_N/dP = 15.2$ K/GPa. The sharp drop occurring between the 3 and 3.3 GPa is the consequence of the structural phase transition.

5.4.4 $CsNiCr(CN)_6$ nanoparticles

Nanomaterials differ from bulk materials because of two main factors: (i) the electronic state modification due to quantum confinement as a consequence of the reduced particle size, and (ii) the high surface/volume ratio corresponding to this particle size range. The second factor is important

because surface atoms can be considered different to inner ones as they exhibit lower coordination, non-saturated bonds and canted spins.

Nanoparticles based on Prussian Blue analogues (PBA) provide an insight into the electronic properties of 3D coordination networks at the nanoscale level where single-domain effect can lead to superparamagnetic behaviour. Synthesis and magnetic studies of PBAs nanoparticles incorporating different transition metals and of various sizes have recently been reported [197-200]. The magnetisation response to applied pressure of $CsNiCr(CN)_6$ nanoparticles in the range 0-7 GPa has been studied. The sample was provided by Prof. Talal Mallah (Institut de Chimie Moleculaire et des Materiaux d'Orsay, Universite Paris Sud 11, Orsay, France). Its preparation, ambient pressure magnetic properties as well as the particles size influence on the magnetisation are reported elsewhere [201, 202]. The particles are negatively charged with the formula $Cs_{0.5}NiCr(CN)_6^{0.5-}$ and are coated with a layer of dimethyldioctadecylammonium ($DODA^+$). The Bulk material $CsNiCr(CN)_6 \bullet 2H_2O$ is known to order ferromagnetically below T_C = 90 K [203]. This behaviour results from the combination of a short-range interaction between the orthogonal Cr^{3+} t_{2g} and the Ni^{2+} e_g orbitals and the onset of a 3D long range ferromagnetic order.

The magnetic response of a 0.6 mg sample of nanoparticles under ambient pressure and of a 4.4×10^{-3} mg of sample under various pressures in the range 0-6.7 GPa were studied. The mass of the sample studied was calculated by comparing the value $\Delta\chi_m$ at P = 0.0 GPa obtained in the TM-DAC with the value $\Delta\chi_m$ obtained from a known mass of $CsNiCr(CN)_6$ nanoparticles measured in a gelatine capsule ($\Delta\chi = \chi(T_{FCm}) - \chi(100K)$). The field cooled (FC) and zero field cooled (ZFC) magnetisation of the samples was measured in a magnetic field of 30 Oe and in the 2-300 K temperature range. The data obtained from the measurement in a gelatine capsule and the low

temperature region of the data collected using the TM-DAC and corrected for the pressure cell signal background are shown in Figure 5.23.

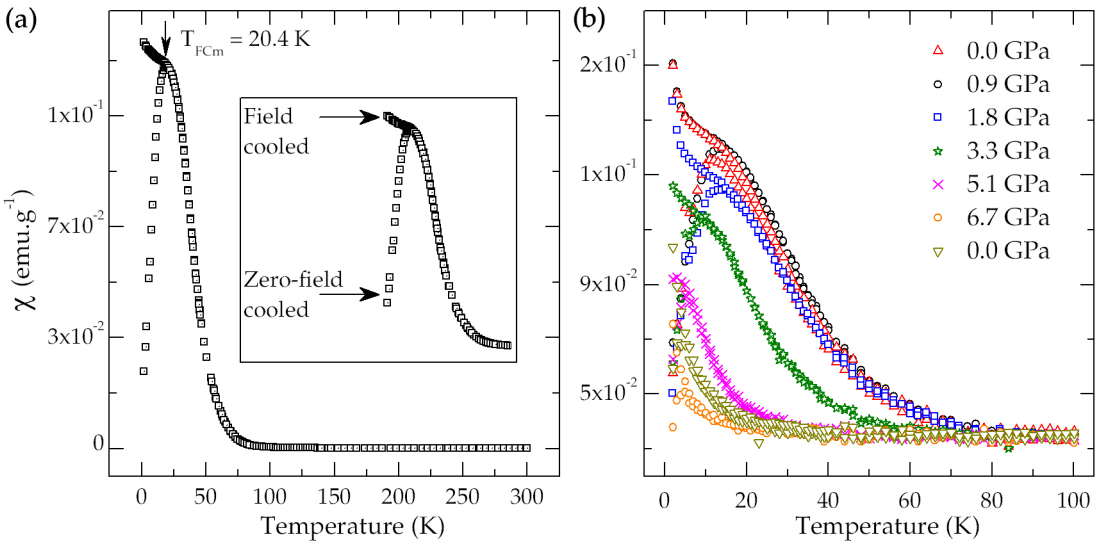

Figure 5.23 Field cooled and zero-field cooled (see insert) temperature dependence of the magnetic susceptibility of $CsNiCr(CN)_6$ in a 30 Oe field. The data were collected on warming up from 2 to 300 K. (a) 0.6 mg of $CsNiCr(CN)_6$ measured in a gelatine capsule. (b) Measurements of $CsNiCr(CN)_6$ in the TM-DAC at several pressures after background correction.

In all instances the FC and ZFC curves coincide from 300 K down to the FC magnetisation curve's maximum T_{FCm} (20.4 K at ambient pressure). The maxima of FC curves give a first indication of the blocking temperatures for single-domain particles or the Curie temperature in the multi-domain regime. On pressure increase, at first, T_{FCm} increases slightly to reach a maximum at a pressure of 1.8 GPa, before decreasing constantly with further pressure increase up to 6.7 GPa. The pressure dependence of T_{FCm} and $\Delta\chi$ are shown in Figure 5.24. $\Delta\chi$ is proportional to the magnetic moment of the sample and is calculated with the formula $\Delta\chi = \chi(T_{FCm}) - \chi(100K)$.

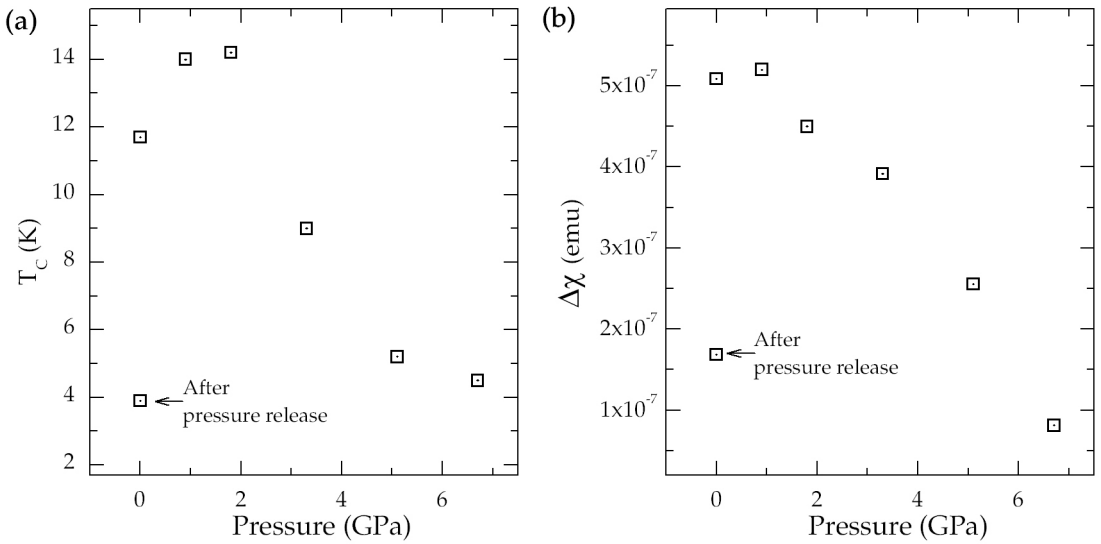

Figure 5.24 (a) The pressure-temperature magnetic phase diagram of $CsNiCr(CN)_6$. (b) The amplitude $\Delta\chi$ is the difference between the ZFC saturation susceptibility and the susceptibility at 100 K.

The small increase of T_{FCm} can be explained by a mechanical reduction of the inter-particles distances by compression of the organic DODA matrix. While as the pressure increase further (above 1.8 GPa) a second process of the isomerisation of the cyano-bridge (CN flipping) [204] leads to low spin Ni^{2+} and thus creates diamagnetic centers within the particles (or and on their surface) decreasing the magnetic moment and thus decreasing T_{FCm} because the magnetic moment of each particle decreases. This approach is supported by the pressure dependence of the magnetic moment at saturation which increases with pressure up to 1.8 GPa (Figure 5.25) and decreases continuously above this pressure. Similar results have been published for $Cs_3[Cr(CN)_6]_2$•nH2O nanoparticles in the 0-1 GPa pressure range [205].

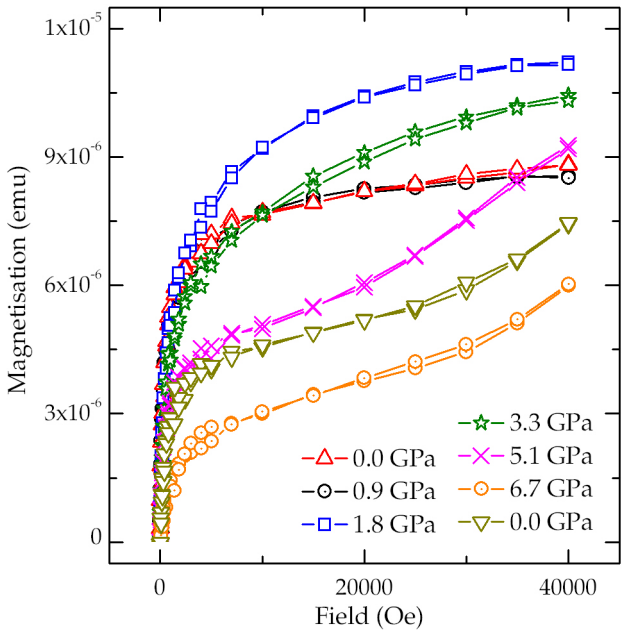

Figure 5.25 The field dependence of magnetisation of $CsNiCr(CN)_6$ nanoparticles under different pressures at 2 K.

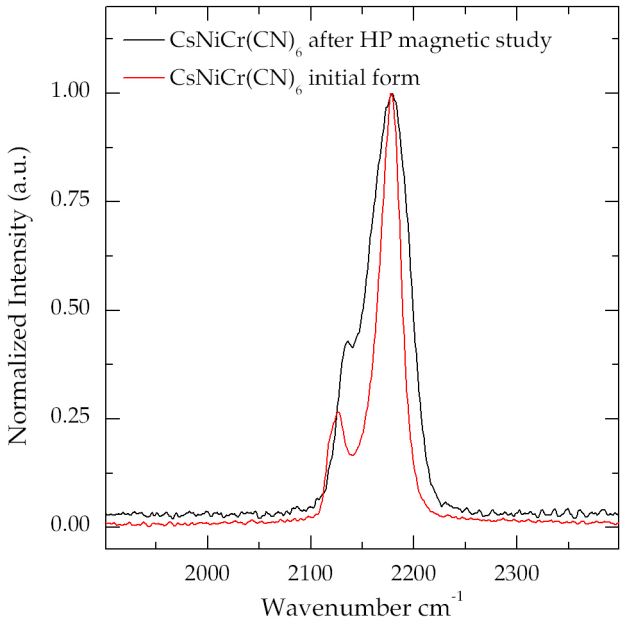

Figure 5.26 Raman spectra showing the pressure-induced linkage isomerisation of the cyanide ligand in the sample recovered after the high pressure magnetisation experiment. Intensities are normalized with respect to the high-frequency band.

The Raman spectra illustrated in Figure 5.26 were collected for the initial sample and for the sample recover from the TM-DAC after the high pressure measurements. The decrease of the 2170 cm^{-1} band and an increase of 2126 cm^{-1} peak are characteristic of a cyano-bridge linkage isomerisation followed by a spin change of the Ni^{2+} from high to low spin. The small change in the ratio of the peaks intensity agrees with the observation of last magnetisation data set (0.0 GPa) which indicates that at least part of the sample recovered its magnetic properties after being exposed to 6.7 GPa.

Chapter 6

Piston-cylinder cell for SQUID magnetometer

6.1 Design

The piston-cylinder cell presented in this section is based on the turnbuckle principle explained in section 5.1. The TM-PCC has been developed to study the magnetic properties of extremely weak magnetic sample in the pressure range of 0 kbar to 20 kbar. The sample volume is of 4 mm^3 and in the tests described in section 6.3, a pressure of 19 kbar was achieved at 300 K. The final TM-PCC design (v2.0) which is optimised for a 3:1 compression ratio, is presented in this section. The cell design is illustrated in Figure 6.1 and the various parts are detailed in Figure 6.2.

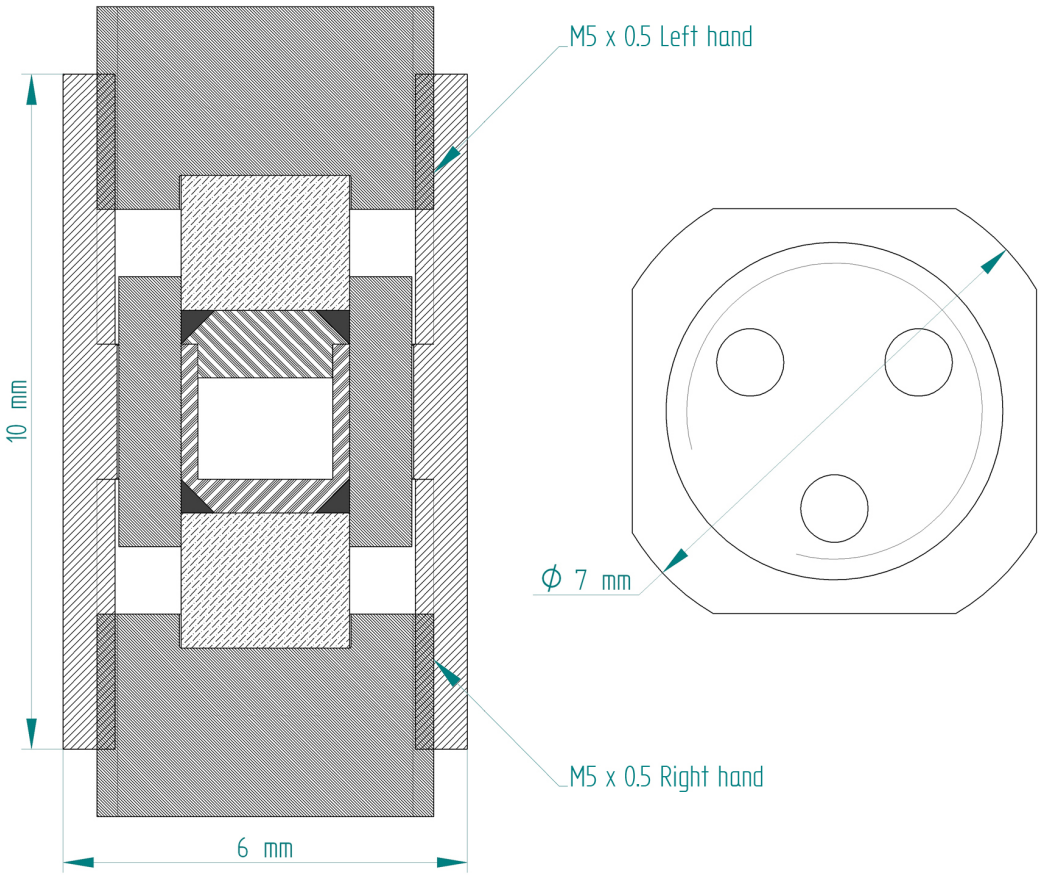

Figure 6.1 Drawings of the TM-PCC cell with key dimensions.

The TM-PC is mostly made of FHT BeCu (BERYLCO 25) supplied by NGK Berylco (UK) [167]. The pressure chamber is formed by the BeCu inner cylinder, 4 mm long with a bore of 2.5 mm and an outer diameter of 4.35 mm and two zirconia pistons 2 mm long and 2.5 mm in diameter supplied by DYNAMIC-CERAMIC LTD [146]. The sample container is a home-made PTFE capsule with an internal diameter of 2 mm and an internal depth of 1.25 mm. It is placed inside the pressure chamber and the sealing is ensured by two copper antiextrusion rings placed on either side of the PTFE capsule. The body of the cell is a BeCu cylinder 10 mm long and 7 mm in diameter with four flats made to fit a spanner around the body (6 mm flat-to-flat). It is drilled along its axis to form a bore of 4.4 mm and internally threaded to a M5×0.5 on either end and in opposite direction to a depth of 4 mm. The two end-nuts have three guiding blind holes drilled into them on one side and the zirconia piston sits in a 0.5 mm deep recess on the opposite side.

The end-nuts are identical apart from having the external M5×0.5 thread cut in opposite directions, i.e., left-hand for one end-nut and right-hand for the other. Detailed drawings of each part can be found in Appendix B.

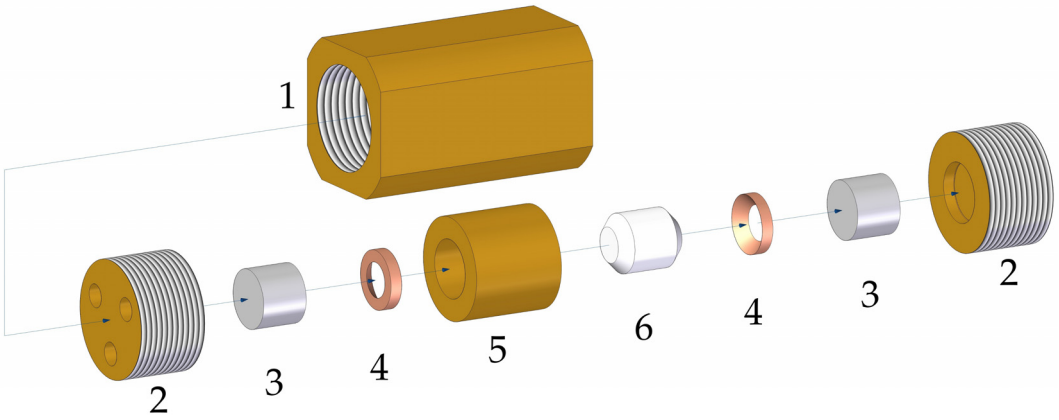

Figure 6.2 Exploded view of the TM-PCC: (1) body; (2) end-nut; (3) zirconia piston;(4) copper antiextrusion ring; (5) inner cylinder; (6) PTFE capsule. Please, note the inner cylinder (5) is inserted into the cell body (1) prior to assembling the other parts.

During the assembly of the cell, the sample is placed into the PTFE capsule with a pressure marker (Pb, Sn, or In [99]) and some pressure transmitting medium. The capsule is then closed and inserted in the inner cylinder and an antiextrusion ring is forced into the inner cylinder on either side of the capsule to form a small recess. The zirconia pistons are maintained in place in each end-nut by a small amount of vacuum grease. One end-nut is engaged into the body, then the inner cylinder is inserted into the body and the cell is closed by screwing the remaining end-nut into the open end of the body. Each end-nut is then screwed in by hand making sure they are engaged by the same depth when they come in contact with the antiextrusion rings, i.e. when some resistance is observed. This step ensures that the inner cylinder is properly centred in the middle of the body.

The pressure cell is then placed into a specially designed clamp shown in Figure 6.3 which is made exclusively of BeCu (FHT) to avoid magnetic

impurities contamination. It is composed of one rigid body and two sliding pistons, each with three pins which engage into the three holes of the end-nuts. Pulling the pistons away from each other allows the pressure cell to be placed into the clamp and ensure that the pins engage fully into the end-nut's guide holes.

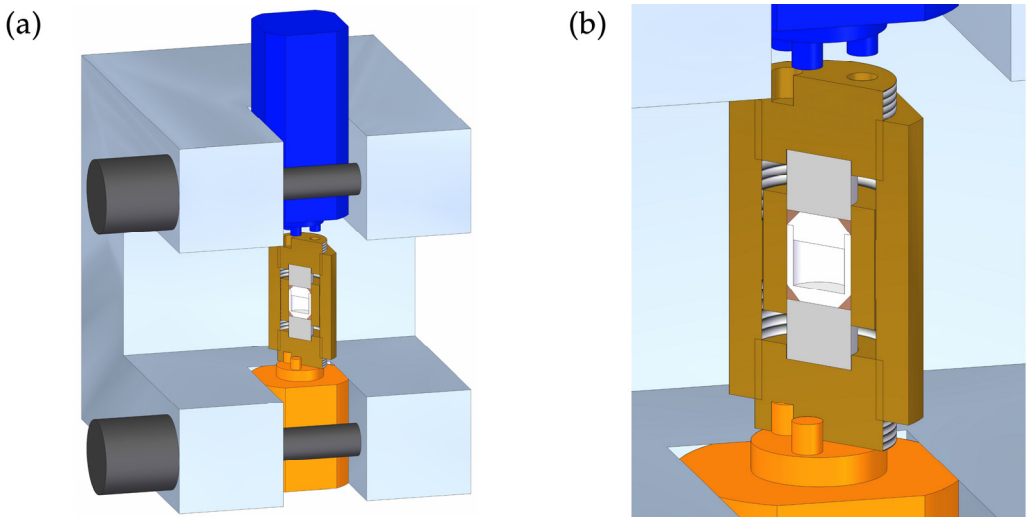

Figure 6.3 (a) Computer-aided design drawing of the clamp for applying load to the TM-PCC. (b) Detail view of the TM-PCC mounted on the clamp.

While it is possible to generate some initial pressure by turning the body of the cell held inside the clamp, at higher loads the friction on the thread between the body and the end-nuts becomes large. In order to overcome this problem, the clamp is installed into a top bench hydraulic press and a load is applied to the pistons. The load, monitored by a sensitive load cell C2S from AEP Transducers [87], is increased in small steps. The setup is similar to the one illustrated in Figure 5.5. This process closes a small gap that appears between the threads of the end-nuts and the body of the cell due to the deformation along the pitch-line contact in the locked turnbuckle. This relaxes the threads which enables the operator using a spanner to lock the load by rotating the body of the cell with respect to the end-nuts. Once the desired pressure is achieved the pressure cell is placed in the holder for measurements in the magnetometer. A standard plastic straw recommended

for use with the MPMS as shown in Figure 6.4 was adapted for the measurements.

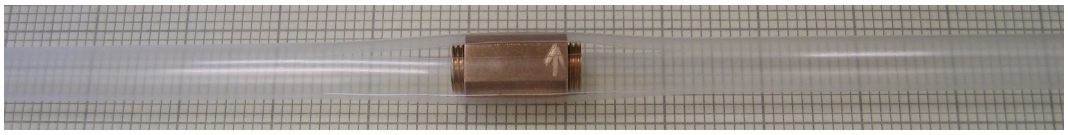

Figure 6.4 The assembled TM-PCC in the standard plastic straw holder of MPMS.

When the cell is assembled there is a clearance of 25 μm between the inner cylinder and the body of the cell so that there is no friction between the two parts when the body is rotated the body can be rotated. As the pressure is increased the inner cylinder buckles and the clearance decreases until the two parts come into contact. From the FEA simulation results shown in section 6.2 the contact between the two parts occurs at a pressure of about 14.3 kbar. The interaction between the inner cylinder and the body leads to both, a positive and a negative consequences. The positive effect is that for higher pressure the body will provide a support to the inner cylinder and prevent it from deforming further. The negative consequence is the appearance of some friction between these two parts when rotating the body which will in turn generate a shear stress on the zirconia pistons. The ceramic pistons are strong in compression, however, they do not cope well with shear stress. The design is optimised to preserve the zirconia pistons and in the various cell failures the copper antiextrusion ring flowed between the piston and the deformed inner cylinder. The pistons were always recovered undamaged.

6.2 FEA

In this section, results of the static FEA calculation of the TM-PCC inner cylinder, body, piston and end-nut are presented. The metallic parts included in this section are made of Berylco 25 and the following mechanical

properties were used: Young's modulus = 127 GPa; Poisson's ratio = 0.34. The zirconia piston's Young's modulus and Poisson's ratio are respectively 205 GPa and 0.3. In both simulations an adaptive meshing process was used and the results were check for convergence. The thread is identical to the one simulated in section 5.2 and known to withstand the load equivalent to a sample pressure of 2 GPa in the TM-PCC therefore it is not modelled on metallic parts.

6.2.1 Inner cylinder and body FEA analysis

In order to reduce the computational time the geometry of the body part is simplified. The simplification of the body part allows the simulation to be run in a 2D axisymmetric mode. To ensure meaningful results the worst case scenario settings were considered. The pressure is applied to a surface of the inner cylinder equivalent to the initial pressure chamber volume and the force needed to generate this pressure is applied to a surface of the body matching the engagement length of the end-nut in the body at its the initial position. In reality the volume of the pressure chamber decreases while the engagement of the end-nut in the body increases as the pressure rises but it is impossible to estimate precisely these variations and for the purpose of this simulation the dimensions of the surfaces to which the pressure and the force are applied are kept constant. The body is modelled by a hollow cylinder sized to fit the smallest dimensions of the actual design (6 mm flat to flat). Its outer diameter becomes 6 mm, its central inner diameter is 4.4 mm and the thread is replaced by a 5 mm diameter hole which corresponds to the thread's major diameter. The inner cylinder remains unmodified with 4.35 mm outer diameter, 2.5 mm inner diameter and 4 mm long. Because the cell is fully symmetrical along its length the axisymmetric model is simplified further and the analysis presented in Figure 6.5 is carried out on one half of the 2D model.

The results shown in Figure 6.5 and Figure 6.6 indicate that the inner cylinder will deform elastically for a pressure lower than 10 kbar. Above 10 kbar a plastic deformation of the inner cylinder which comes into contact with the body for a pressure of 14.3 kbar is observed. The plastic deformation of the inner cylinder after the tests was visible to the naked eye; the inner cylinder buckled in the middle and should be regarded as a consumable. At 20 kbar there is a very high stress concentration in the inner cylinder, however, the stress distribution in the body remains satisfactory and the maximum stress is lower than the yield strength of BeCu (FHT) for the part supporting the inner cylinder. The stress concentration arises in the body around the innermost point of the surface where the force is applied. It is slightly above the BeCu (FHT) yield strength but taking into account the body volume cutback of about 30% produced by its simplification this result remains very satisfactory.

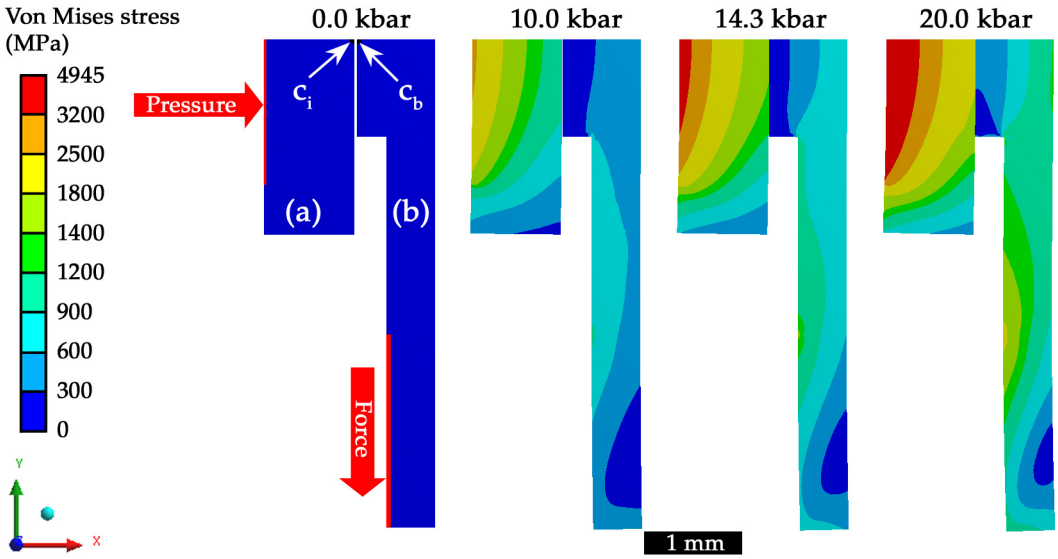

Figure 6.5 Von Mises stress distribution and deformation induced in the TM-PCC inner cylinder (a) and body (b) for various pressure generated on the sample. The points identified as c_i and c_b belongs to the surface of (a) and (b) respectively and enter in contact first at a pressure of 14.3 kbar. For clarity the results obtain for pressures of 14 kbar and 15 kbar are not presented in this figure.

Figure 6.6 shows that as the pressure is increased the inner cylinder and the body deform steadily along the x-axis but in opposite direction until the sample pressure reaches 14.3 kbar at which point they come into contact and the body starts to support the inner cylinder, the deformation of the body changes direction at this stage and the deformation of the inner cylinder slows down proportionally to the pressure increase rate. Simultaneously the contact pressure between the two parts increases and reaches a maximum of 1.2 kbar for a sample pressure of 20 kbar.

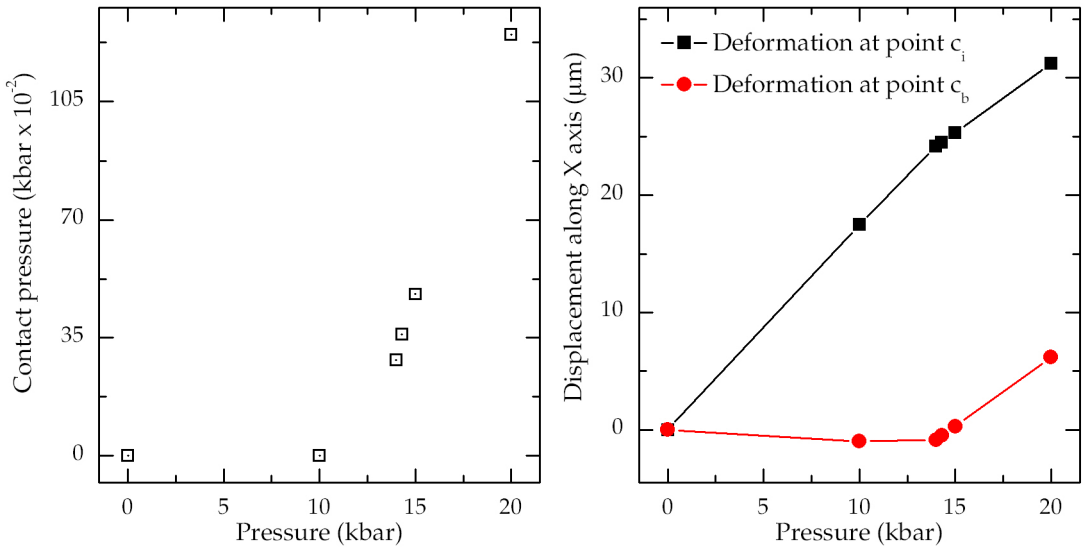

Figure 6.6 (a) Contact pressure on the interface between the inner cylinder and the body at points c_i and c_b. (b) Deformation along the x axis for the inner cylinder c_i and for the body c_b.

6.2.2 End-nut FEA analysis

For this simulation the end-nut part was simplified by removing the thread, and taking the thread minor diameter of 4.39 mm as the outer diameter of the part. The end-nut has 3-fold symmetry hence a 3D analysis of one third of the assembly of the zirconia piston located in the end-nut has been carried out.

In Figure 6.7 a pressure of 20 kbar is applied to the top surface of the zirconia piston, a support with free displacement along the X and Z directions and no displacement along the Y direction is assigned to the outer surface of the end-nut while the faces exposed from the cut-out are set as frictionless support (to imitate the symmetry condition).

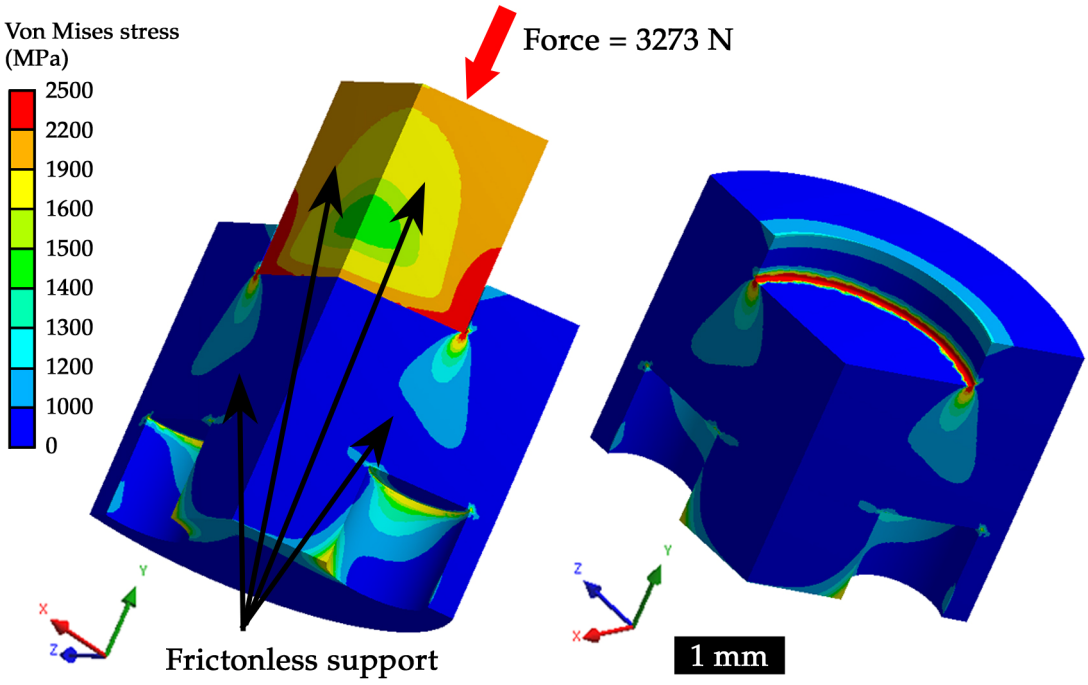

Figure 6.7 Von Mises stress distribution in the TM-PCC end-nut when the pressure generated on the sample is equal to 20 kbar. On the right the zirconia piston is hidden so as to view the stress distribution at the end-nut's surface.

The results show that a large part of the high stress is concentrated in the piston. It actually seems to exceed the zirconia yield strength around the circular edge of the piston which is in contact with the end-nut. Experimentally the piston is able to take the load and indent somewhat into the BeCu sit. On the BeCu end-nut the stress level is mostly under the yield strength value of BeCu (FHT) with the exception of two localised areas around the guiding pin holes where it exceeds it a little and around a ring surface matching the circular edge of the piston where the stress level becomes very large. However in this region the BeCu works purely in compression and although there is no available data relative to the strength

of BeCu in this particular condition it can be assumed that the part will deform to accommodate a better support of the piston without having any other consequences. The stress induced on the outer cylindrical surface of the end-nut, not visible in Figure 6.7, is uniform and very much lower than the yield strength of BeCu (FHT).

6.3 Testing

The TM-PCC has been tested for its ability to withstand the desired sample pressure and its characteristically low and smooth magnetic signature which makes it possible to study samples with an extremely low magnetic susceptibility.

6.3.1 Pressure testing

The pressure tests took place while running a standard measurement therefore the work was carried out in the exact same conditions as it would be when studying a sample. A powder sample with a small piece of pressure marker in its centre was gently compacted into the PTFE capsule. Then a few drops of Daphne oil 7373 acting as pressure-transmitting medium were added until the sample appeared to be wet. The PTFE capsule was closed and the cell was assembled as described in section 6.1. With the cell closed, the superconducting transition temperature of the pressure marker which gives the zero pressure (0.0 kbar) was measured. This is the reference value from which the subsequent sample pressures at low temperature will be calculated. After that the sample pressure was increased in small steps, using a load cell to estimate the pressure while increasing it and checking the low temperature sample pressure at each step, until the cell fails.

6.3.1.1 Superconducting transition in lead

The first test was carried out with a small piece of lead (high purity 99.99+ %) as pressure marker. The pressure steps are summarised in Table 6.1 and the measurements of the matching superconducting transition in lead, in the field of 10 Oe, are shown in Figure 6.8. The TM-PCC performed well until the run P5 and a sample pressure of 11.1 kbar at low temperature was observed. Unfortunately it failed while locking the pressure of the following run, P6. From the load applied on the end-nuts a pressure of 19.1 kbar could be estimated but it was not possible to confirm the low temperature sample pressure.

As predicted by the FEA calculation, the inner cylinder deformed plastically, buckled in its centre and an hydraulic press was used to extract it from the body. The failure was due to the excessive plastic deformation of the copper antiextrusion ring. The gap between the zirconia piston and the inner wall of the cylinder would increase with pressure and once it was large enough the copper antiextrusion ring (followed by the PTFE capsule and the sample) would flow in this gap.

Table 6.1 Summary of the pressures at 300 K ($P_{(Load)}$) estimated from the load applied using the hydraulic press, and the pressure at ~ 7 K ($P_{(Lead)}$) determined from the temperature shift of the superconducting transition of lead. $P_{(Drop)}$ represents the difference between ($P_{(Load)}$) and ($P_{(Lead)}$).

Run	Applied pressure $P_{(Load)}$ (kbar)	Low temperature pressure $P_{(Lead)}$ (kbar)	Pressure drop $P_{(Drop)}$ (kbar)
P0	0.0	0.0	0
P1	2.5	1.9	0.6
P2	4.5	3.7	0.8
P3	10.0	7.2	2.8
P4	13.0	9.6	3.4
P5	15.5	11.1	4.4
P6	19.1	N/A	N/A

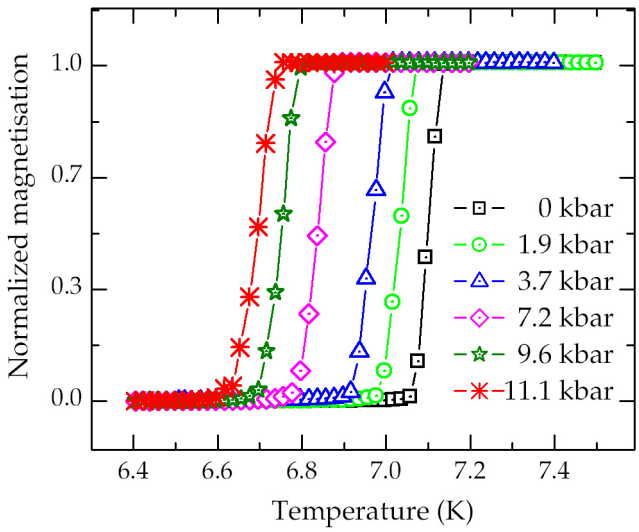

Figure 6.8 Superconducting transition of lead at various pressures measured in a field of 10 Oe.

The magnetisation measurements of the superconducting lead transition shown in Figure 6.8 exhibit, for each pressure, a clear and sharp transition which reflects good hydrostatic conditions within the sample space.

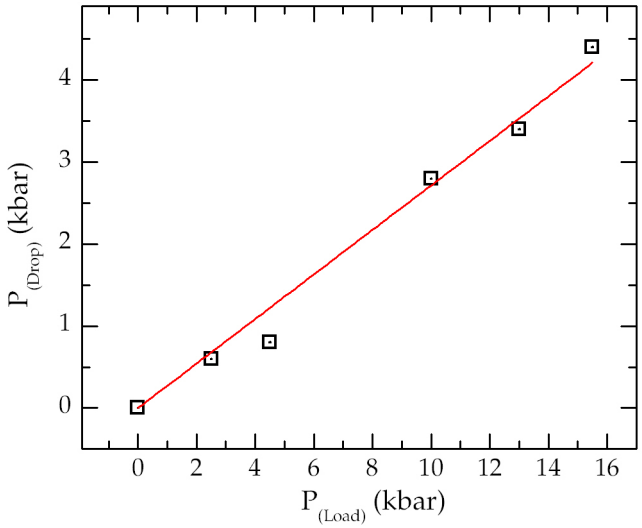

Figure 6.9 Pressure drop ($P_{(Drop)}$)from high temperature (T ~ 300 K) to low temperature (T ~ 6.6-7.2 K) plotted against the high temperature pressure ($P_{(Load)}$). The linear regression's intercept is fixed to zero and its slope is 0.27.

The pressure drop ($P_{(Drop)}$) between the high temperature pressure ($P_{(Load)}$) determined from the loading force applied to the end-nuts while locking the cell and the low temperature pressure ($P_{(Lead)}$) calculated from the

superconducting transition temperature of lead is plotted against $P_{(Load)}$ in Figure 6.9. It increases linearly with $P_{(Load)}$ and can be fitted with a linear regression of slope 0.27 with an intercept fixed to 0 kbar.

Unlike the case of the TM-DAC, the pressure locked in the TM-PCC at room temperature can't be measured – It can only be estimated from the load – which complicates the analysis of the data presented in Figure 6.9. However, the observed drop in pressure can be explained by considering contributions from several factors listed below in the order of likely importance:

- The friction between the pistons and the inner cylinder, which becomes progressively larger with increasing pressure as the Cu-rings extrude around the piston.

- The different rate of contraction of the various parts of the cell due to difference in thermal expansion coefficients. This includes the freezing of the relatively large volume of the pressure medium from liquid to solid state.

- The uncertainty in the clamping torque when the cell is locked before being taken out of the press. This is caused by the consistency with which the same locking torque is applied by the cell operator during the clamping procedure.

- The PTFE undergoes both temperature and pressure induced phase transition leading to volume decrease.

6.3.2 Tests in MPMS

In this test the temperature dependence of the magnetisation of an empty TM-PCC from 2 K to 300 K in a magnetic field of 1000 Oe was measured and the data are plotted in Figure 6.10. All parts of the cell were included into the assembly - the PTFE capsule, the copper antiextrusion rings, the inner

cylinder, the zirconia pistons, the end-nuts and the body. The magnetisation curve is smooth and follows the known trend for BERYLCO 25 and PTFE, the contribution from the copper ring and the pistons is negligible.

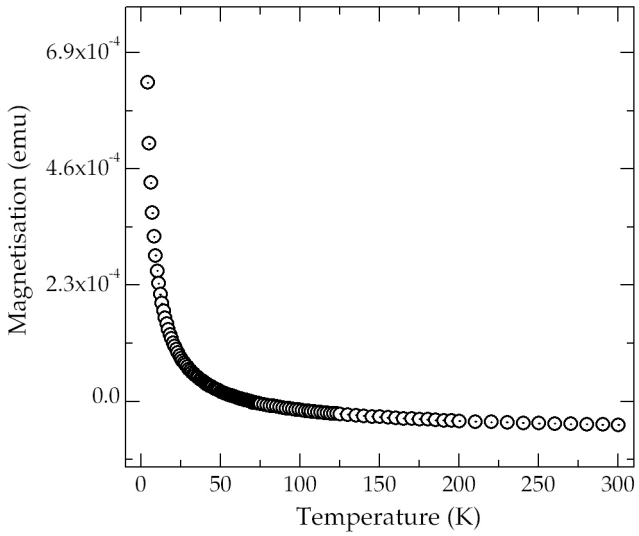

Figure 6.10 The temperature dependence of the magnetisation of an empty TM-PCC measured in a magnetic field of 1000 Oe.

Its small size (<12 mm long in the unloaded state) and weight (~2.7 g) makes the TM-PCC suitable for high rate cooled down and fast thermal equilibration. It also shares a number of other advantages with the TM-DAC. It is highly symmetric with respect to the sample inside. The samples measured in MPMS should ideally be a small sphere and although this is difficult to achieve the instrument manufacturer recommends to make the sample symmetrical and with a total length under 10 mm in order to obtain the highest measurement sensitivity [90]. The TM-PCC is fully symmetrical along its length with respect to the sample and its length is only marginally longer than the standard 10 mm long gelatine capsule. Therefore, the signal produced when scanning the cell through the MPMS gradiometer pick up coil (Figure 6.11) is very similar to the signal obtained from a perfectly shaped sample.

The signal can be fitted and integrated by the MPMS multiVu software to produce an accurate value of the magnetisation. Therefore the background

contribution of the cell can be quantified and then be subtracted from a high pressure magnetisation data set to obtain the sample's magnetisation alone.

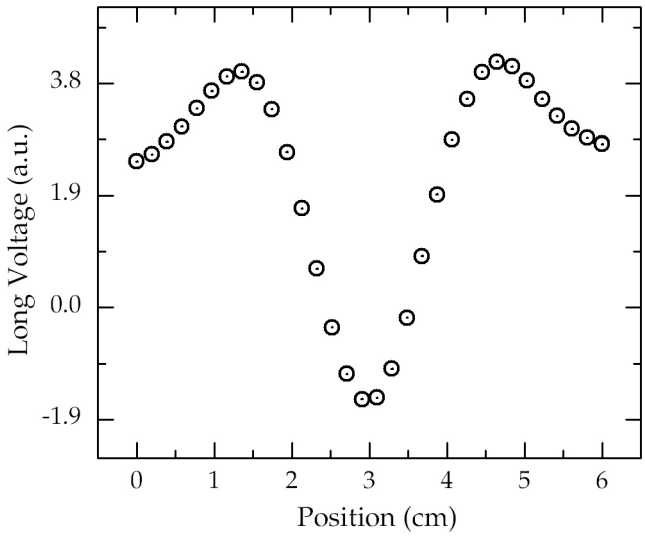

Figure 6.11 Raw MPMS data generated by a scan of the empty TM-PCC over a 6 cm distance in an applied field of 1000 Oe at 300 K. The resulting integrated magnetisation as calculated by the MPMS software is -4.62×10^{-5} emu.

6.4 Results

The TM-PCC has a large sample volume and is designed for weakly magnetic materials with susceptibility too low to be measured in a TM-DAC They should also be responsive to pressure so that its effect can be observed in the working range of the cell, i.e. up to 20 kbar.

6.4.1 $[\{Cu(N2Py3u)_2\}CN](BF_4)_3$

One of the sample which was studied in the TM-PCC was a dimer with the following formula $[\{Cu(N2Py3u)_2\}CN](BF_4)_3$ reefered to as SH-269. The two Cu centres are joined together by a cyano-bridge (one Cu attached to the C and the other to the N) and the remaining coordination sites are filled up by one N2Py3u ligand per copper centre. Where N2Py3u is an extremely large organic ligand with the following formula: Dimethyl 2,4-di-(2-pyridyl)-3-

(pyrid-2-ylmethyl)-7-methyl-3,7-diaza-bicyclo[3.3.1]nonan-9-one-1,5-dicarboxylate. And BF_4 act as counter anions. The study of this type of material provides an understanding of the relation between the molecular structure enforced by the ligands and the resulting specific molecular properties. This sample was provided by Prof. Peter Comba (Institute of inorganic chemistry, Heidelberg university, Heidelberg, Germany).

The TM-PCC was used to study magnetic susceptibility of SH-269 at high pressure and low temperature. The pressure of 11 kbar was applied but unfortunately the data did not reveal any pressure effect on the sample and it has been decided not to continue with further pressure increase. Despite this the data obtained for SH-269 are compared hereafter to exemplify the importance of the background removal process and to demonstrate the superiority of the TM-PCC over others existing PC cells.

The measurement of the sample SH-269 has been attempted in three different PC cells, the micro pressure cell of design identical to the one presented in Figure 3.20, the long symmetric high-pressure cell shown in Figure 3.18 which is known for its low magnetic signal and the TM-PCC. It is only in the TM-PCC that the magnetisation data from the measurements could be extracted. Figure 6.12 and Figure 6.13 show the data set obtained from the magnetisation measurement of 8.1 mg of SH-262 in the cell at ambient pressure and the data set resulting from the background subtraction respectively (the background data set is plotted in Figure 6.10). The data set are presented as the magnetisation per mg of sample as the function of temperature. The data set collected from the magnetisation measurement of 33.7 mg of SH-269 in a gelatine capsule is plotted in Figure 6.13 for comparison.

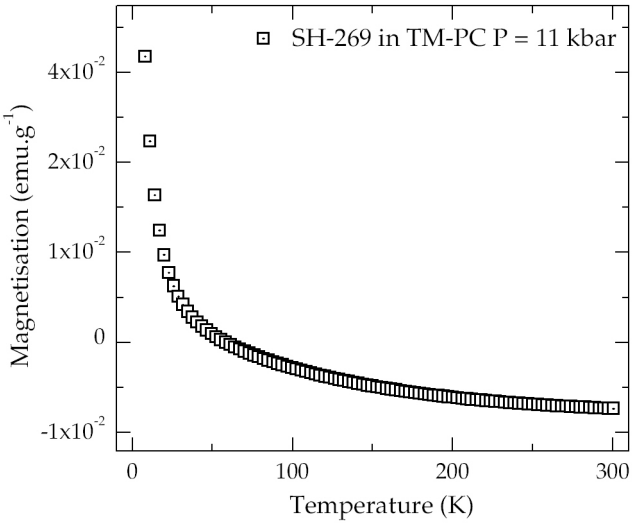

Figure 6.12 Temperature dependence of the magnetisation of 8.1 mg of SH-269 in a magnetic field of 1000 Oe in the TM-PCC at a pressure of 0 kbar. The data have not been corrected for the pressure cell magnetic background.

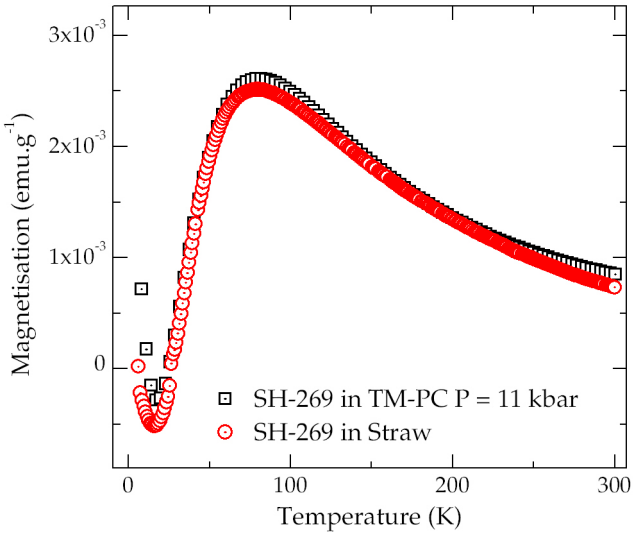

Figure 6.13 Temperature dependence of the magnetisation of SH-269 sample in the magnetic field of 1000 Oe and under standard pressure condition. (i) 8.1 mg of sample in the TM-PCC with the cell background removed (black square). (ii) 33.7 mg of sample in a gelatine capsule (red circle).

Although the data set resulting from the background subtraction is not a perfect match to the one obtained in a conventional measurement a good agreement can be observed and that the same features are present in both data sets in the whole temperature range. Working at the limits of sensitivity of the MPMS a better result could not be expected.

6.4.2 Fe(pyrazine){Pt(CN)$_4$}

As it has been mentioned above, the main advantage of the TM-PCC is a relatively large sample volume it can accommodate compared to that of a DAC. Another advantage is the ability for the pressure to be controlled and measured with precision at low-pressures applied to the sample. One of the samples studied using the TM-PCC is the spin-crossover coordination nanoparticles of the cyanide-bridged three-dimensional network Fe(pyrazine){Pt(CN)$_4$)}. The material belongs to the group of bistable spin-crossover systems are among the most challenging in molecular chemistry because these materials can serve as components in devices for switching, signal amplification, and information storage or as efficient contrast agents [206]. The sample of this material has been obtained through collaborative arrangement with the group of Prof. Talal Mallah (Institut de Chimie Moleculaire et des Materiaux d'Orsay, Universite Paris Sud 11, Orsay, France). The material is of particular interest to applications because at ambient pressure it has a transition from high-spin to low-spin on cooling with the transition temperature being dependent on the size of the nano-particles. As with all such system there's a question about the nature of the magnetic effects, i.e. to which extent they are defined by the interplay between the intra- and inter-particle interactions. Applying pressure modifies these interactions depending on the relative compressibilities of the nano-particles themselves and the material between them, and can shed light on the magnetic exchange in the material.

The results of the high-pressure studies are presented in Figure 6.14. Since the transition occurs near room temperature, the most accurate measurement of pressure can be done by use of a sensitive load-cell mounted under the TM-PCC in the hydraulic press during the application of pressure to the sample. It is clear from the data that the high- to low-spin transition in this material is suppressed by applying very small pressure. Indeed, by the time the pressure reaches about 1 kbar the transition has almost disappeared. This

indicates the extreme sensitivity of this material to stress and further studies of its crystallographic properties is currently underway in order to explain the anomalous behaviour.

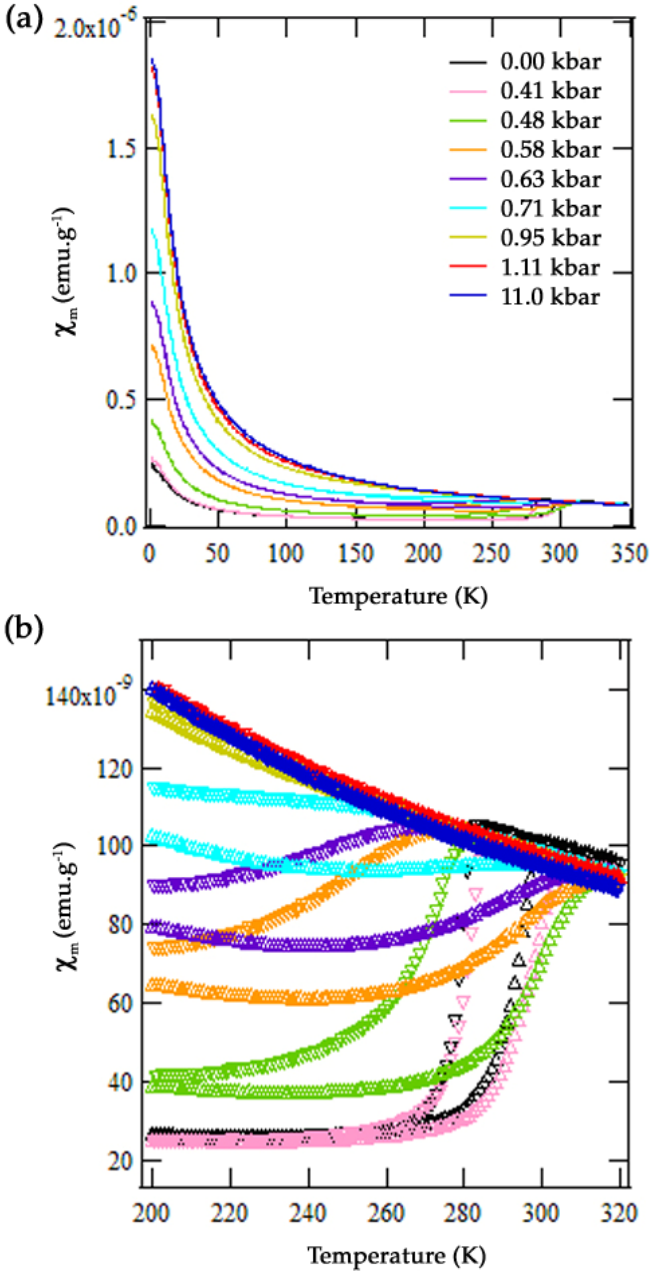

Figure 6.14 Pressure dependence of the magnetisation of the cyanide-bridged three-dimensional network Fe(pyrazine){Pt(CN)$_4$}: (a) between 2 and 340 K, and (b) in more detail between 200 and 320 K. The colours in (b) correspond to the colours in (a) and indicate the same pressure runs.

6.5 Conclusions

In conclusion of this section, the TM-PCC achieved a sample pressure of 19.1 kbar at room temperature which by extrapolation would result in a sample pressure of ~14 kbar at low temperature. The post-failure examination reveals that in every attempt it is the buckling of the inner cylinder under excessive stress which allows the copper ring to flow around the zirconia piston and leads to the collapse of the pressure chamber. Replacing the soft copper (yield strength ~ 0.075 GPa) antiextrusion rings by rings made of stronger yet ductile material such as annealed BeCu (yield strength ~ 0.200 GPa), as seen in existing PC cell designs [150, 207], could be the way of stabilizing the pressure chamber and reaching even higher pressure.

The magnetic properties of the TM-PCC resulting from a careful selection of materials and from its size and shape enable a magnetisation high pressure study to be carried out at the limits of sensitivity of the MPMS. In addition to performing well in terms of sample pressurisation and magnetic properties the TM-PCC is also economical to use. Indeed, the consumable parts are limited to the copper rings, the PTFE capsule and the inner cylinder. A very small amount of material is need for each part and their machining is simple.

Chapter 7

Diamond Anvil Cell for single crystal X-ray diffraction at high pressure and low temperature

There are a number of diamond anvil cells (DAC) developed for SXD such as for example the one developed by Merrill and Bassett [32] or by LeToullec [35]. Combining high pressure with low temperature gives access to a whole new area on the phase diagrams but due to the size of the existing DACs this is generally achieved by cooling down the pressure cell inside a cryostat and it is only possible at central facilities. A new design is proposed; due to its miniature dimensions can be used with commercially available laboratory cryo-flow cooling systems and achieves pressures in excess of 10 GPa.

7.1 Design

The TX-DAC is based on the turnbuckle principle explained in section 5.1. It is aimed at SXD study in the pressure range of 0-10 GPa and temperature range from room temperature to the base temperature of the available cryo-flow systems. The cell is build around a pair of 600 μm culet Boehler-Almax diamonds [36, 37] which provide a wide scattering angle of 80 for the scattered beam. The anvil's technical drawing is available in Appendix F. The final TX-DAC design (v3.0) is shown in Figure 7.1.

BeCu alloy BERYLCO 25 is a high strength material which is readily available and machines well. Its thermal conductivity of 104 $W.m^{-1}K^{-1}$ at 293 K is higher than the thermal conductivity of other common high-strength steels and this is why the TX-DAC is made entirely of BeCu (FHT) [83]. An exploded view of the TX-DAC, Figure 7.2, depicts all the parts of the cell.

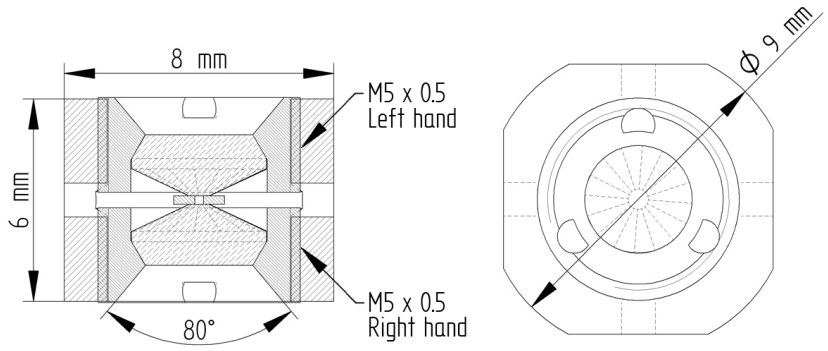

Figure 7.1 Drawings of the TX-DAC with key dimensions.

The pressure cell consists of a body and two end-nuts. The body is a cylinder 6 mm long and 9 mm in diameter with four flats made to fit a spanner around the body (8 mm flat to flat). It is internally threaded to an M6×0.5 on either side and in opposite direction to a depth of 2.75 mm. Four holes have been machined in the flat sides for viewing the anvils and the gasket. Three of them are 1 mm in diameter and another one threaded to a M1.6 is the anchor point for the PVC stand used to hold the cell on the goniometer head (Figure 7.4).

On one side, the end-nuts are designed to host the anvils with the maximum support; it corresponds to a straight hole 4.05 mm in diameter and 0.96 mm deep with a 60 V shape lateral support. On the opposite side they have three guiding blind holes drilled into them and an 80 conical opening cut to a depth of 1.1 mm, which is to provide the maximum scattering angle allowed by the anvils. Detailed technical drawings of each part can be found in Appendix D. The end-nuts are identical apart from having the external M6×0.5 thread cut in opposite directions, i.e., left-hand for one end-nut and right-hand for the other one. In order to maximize the strength of the body and to minimize the amount of the cell material around the sample, the behaviour of the cell under load was modelled using finite element analysis [84]. The simulations results presented in section 6.2 show that the cell can hold loads in excess of 6 kN between the end-nuts.

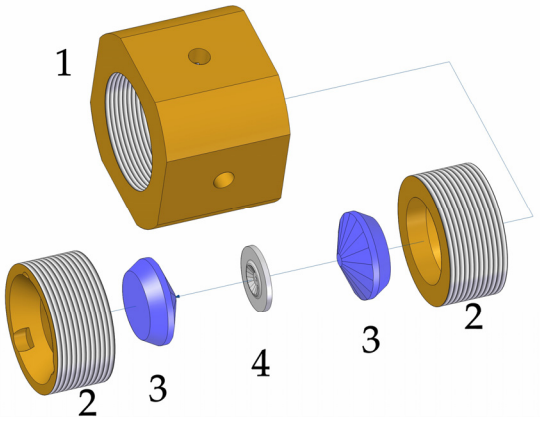

Figure 7.2 Exploded view of the TX-DAC. (1) body; (2) end-nut; (3) Boehler-Almax diamond anvils; (4) stainless steel gasket.

During the assembly of the pressure cell the diamonds are maintained in place in each end-nut by a small amount of Blu-Tack. There is no alignment mechanism and the anvil alignment is achieved through precision machining of the end-nuts and the body of the pressure cell. Details of the manufacturing process are given in Chapter 9.

The gasket needs to fit into a circle of 4 mm in diameter; disks of 3 mm in diameter and 250 μm thick made from either BeCu (An) or stainless steel foil were used. It is preindented from 250 μm to about 100 μm and a hole of 200 μm is drilled in its centre.

For the tests and measurements, diamonds from ALMAX INDUSTRIES [85] with 600 μm culets and a 4 mm diameter girdle of Boehler-Almax design anvils with 16 facets were used to achieve pressures in excess of 10 GPa. With smaller culets or larger diamond the ratio of culet surface area to supported surface area would be increased and higher pressures could be reached.

The sample, a tiny ruby sphere as pressure reference material and a pressure transmitting medium are loaded in the gasket's hole. Then the pressure cell is placed into a specially designed clamp shown in Figure 7.3. It is formed by two circular plates of Bohler 720 ECOBLANK, three high tensile M5 hexagon socket head screws and three silver steel dowels of 4 mm in diameter. The female plate features three threaded holes to accommodate the screws and three blind holes hosting the dowels while the male plate displays three counterbored holes in which the screws head will sit and three 4 mm holes allowing the male plate to slide on the dowels. At the centre of each plate a feature composed of three pins and a conical spacer (Figure 7.3) couples with the outer side of the end-nut (the three pins engage into the three blind holes) and allow the cell to be accurately positioned and secured between the two plates. A hole through the centre of each plate provides an optical access to the sample and allows for the constant monitoring of the sample pressure via the ruby fluorescence technique.

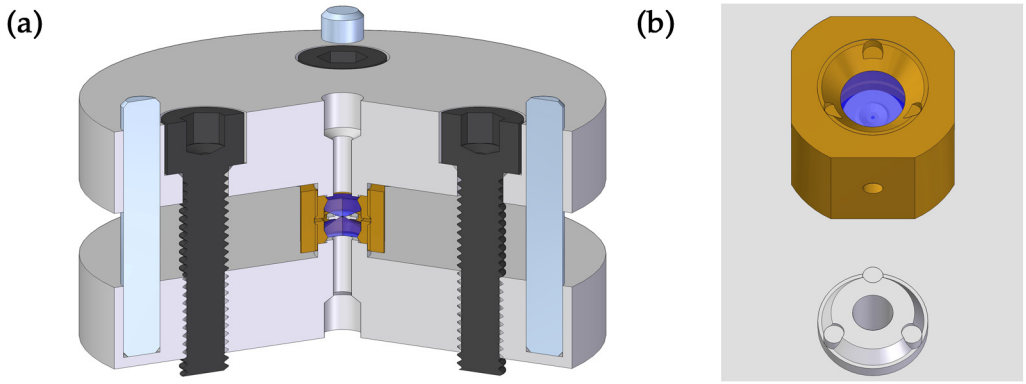

Figure 7.3 (a) Computer-aided design drawing of the clamp for applying load to the TX-DAC. A third of the assembly is cut-out for clarity. (b) Detail view of the feature, present at the centre of both the top and the bottom clamp, engaging in each end-nut when the cell is in the clamp.

When applying a load to the TX-DAC the three M5 screws pull the two plates together and the dowels ensure their alignment. The three screws are located 120 apart on a 30 mm circle coaxial with the plate, and the dowels are aligned with the screws on a 44 mm circle. The technical drawing of each part of the clamp is presented in Appendix E. This layout allows a spanner to fit around the TX-DAC, located in the centre of the clamp, with enough freedom (~70) to rotate the cell's body.

To increase the pressure inside the cell, once it is installed into the clamp, the M5 screws are tightened in small steps and with the same amount. This pulls the plates together and in turn generates a load on the end-nuts of the TX-DAC. This process closes a small gap that appears between the threads of the end-nuts and the body of the cell due to the deformation along the pitch-line contact in the locked turnbuckle. This relaxes the threads which enables the operator using a spanner to lock the load by rotating the body of the cell with respect to the end-nuts. Once the desired pressure is achieved the clamp is opened and the cell is placed on a cylindrical holder which is design to fit into a standard goniometer head as shown in Figure 7.4.

Figure 7.4 Merrill-Basset DAC (left) and TX-DAC (right) mounted on goniometer heads. The Merrill-Basset DAC sits on an aluminium table and the TX-DAC is held on a PVC stand.

The cylindrical holder screws into the threaded side hole of the TX-DAC body. It is made of PVC which has a low thermal conductivity of 0.19 $W.m^{-1}K^{-1}$ at 293 K and minimises the heat leak to the cell during the experiments.

7.2 FEA

In this pressure cell design the dimensions of the end-nuts are the most critical and to obtain the best a simulation has been run in 3D mode on the actual parts without any simplification. Because the cell is fully symmetrical (existence of a mirror in the plane normal to its length) only half the TX-DAC (Figure 7.5 (a)) was used for the simulation. This includes one anvil, one end-nut and one half of the body. The diamond to end-nut and end-nut to body contact regions are of particular interest. A static pressure of 10 GPa is applied to the 600 μm diameter anvil culet surface area while a fixed support is applied on the body's truncated surfaces (purple in Figure 7.5 (a)).

The results of static FEA calculation carried out in a 3D mode on the anvil, the end-nut and the body of the TX-DAC are presented below. The mechanical properties of the Berylco 25 parts are: Young's modulus = 127 GPa ; Poisson's ratio = 0.34. The Diamond s Young's modulus and Poisson's ratio are respectively 1050 GPa and 0.1. An adaptive meshing process was used and the results were check for convergence.

The contact between the two BeCu threads is defined as frictional with a friction coefficient of 0.147 [208]. Between the diamond anvil and the BeCu end-nut there are two distinct contact regions; one is between the diamond conical crown and the conical BeCu support and the second is between the diamond girdle and the cylindrical inner wall of the end-nut. A friction coefficient of 0.1 is applied to the former while the later which remains virtually stress free is set as frictionless.

The von Mises stress distribution results presented in Figure 7.5 (b) indicate that for a pressure of 10 GPa applied on the anvil's culet the stress concentration does not exceed the BeCu (FHT) yield strength either in the end-nut or in the body. A maximum of 1200 MPa is reached in the two high stress regions indicated in Figure 7.5 (b). In the end-nut the highest stress concentration occurs around the region in contact with the edge between the girdle and the conical part of the diamond.

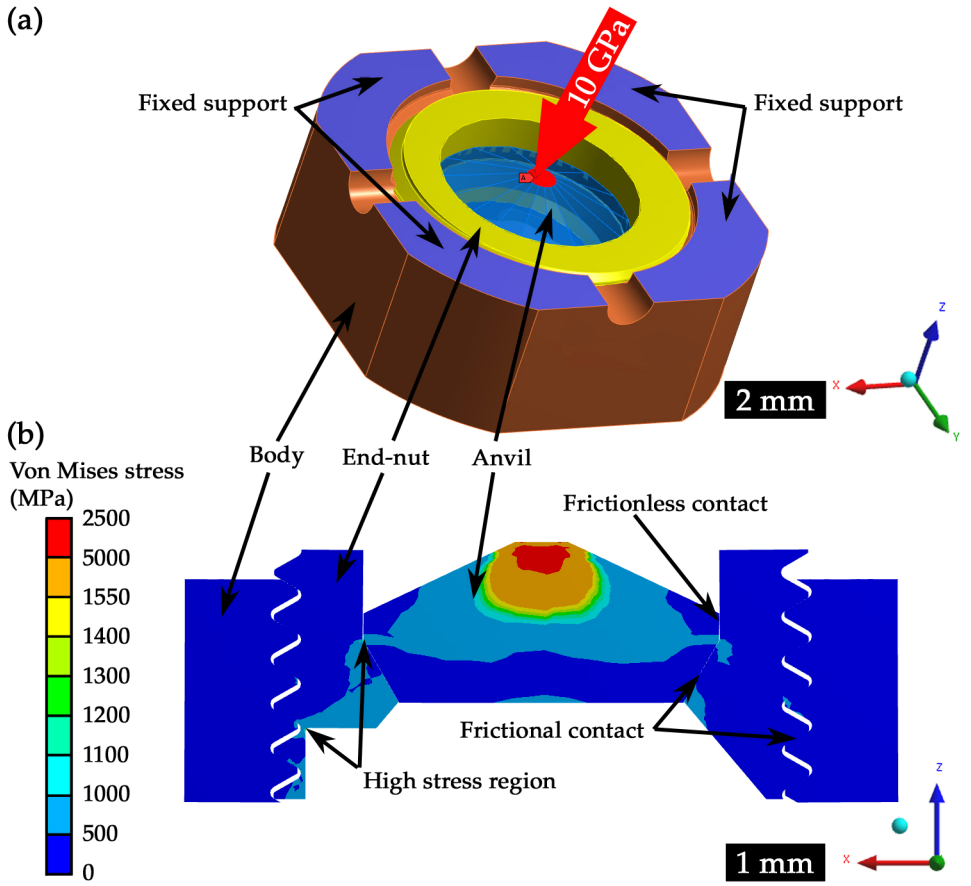

Figure 7.5 (a) 3D model of the half of the TX-DAC used for the FEA calculations; (b) a slice view of the von Mises stress distribution induced in the TX-DAC for an applied pressure of 10 GPa on the 600 µm diameter diamond culet.

7.3 Testing

In any DAC the diamonds alignment is critical to be able to achieve any pressure without catastrophic failure of the gasket and/or the diamonds. In the TX-DAC the anvils alignment relies exclusively on the machining accuracy and the first test on each new pressure cell is to verify that when the diamonds culets are in contact the misalignment observed is less than 5% of the culet diameter in the culet plane and that the wedge between the culets is kept to a minimum. Figure 7.6 shows a perfect alignment of the anvil in all directions.

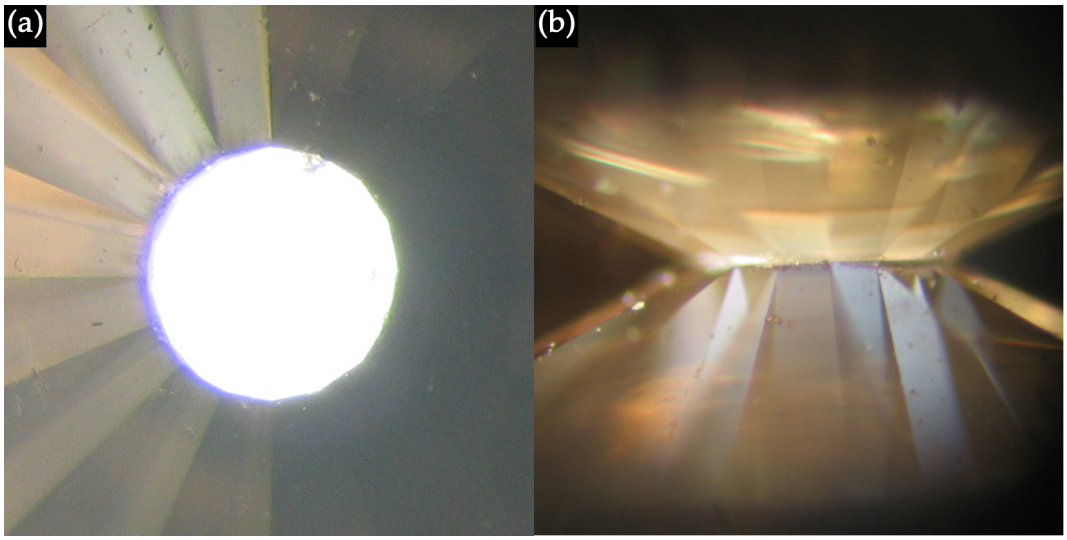

Figure 7.6 Diamonds alignment inside the TX-DAC. (a) looking along the axis of the anvil. The white slightly oval shape indicate a misalignment (left-right on the picture) however it is too small to be measured. (b) looking through a side hole, no wedge is visible.

The following tests are to confirm that a pressure in excess of 10 GPa can be applied to the sample and that it is possible to cool down the TX-DAC using a standard laboratory X-ray diffraction Cryostream cooling system.

7.3.1 Pressure testing

For this test a circular stainless steel gasket indented from 250 μm to 58 μm was used. A ruby sphere is loaded into the gasket's hole (200 μm) with a mixture methanol:ethanol 4:1 as pressure transmitting medium. Due to the volatility of this mixture, it has to be added once the cell is assembled. Leaving a small gap between one diamond and the gasket it is possible to inject the mixture with a syringe through a body's side hole and quickly close the gap by screwing the end-nuts.

The pressure is then increased in seven steps to reach the maximum of 10 GPa. For each step the pressure is measured at room temperature (~295 K) by the ruby fluorescence technique and the spectra obtained on a Raman spectrometer are presented in Figure 7.7. The sharpness of the peaks is constant throughout the test and it indicates good hydrostaticity.

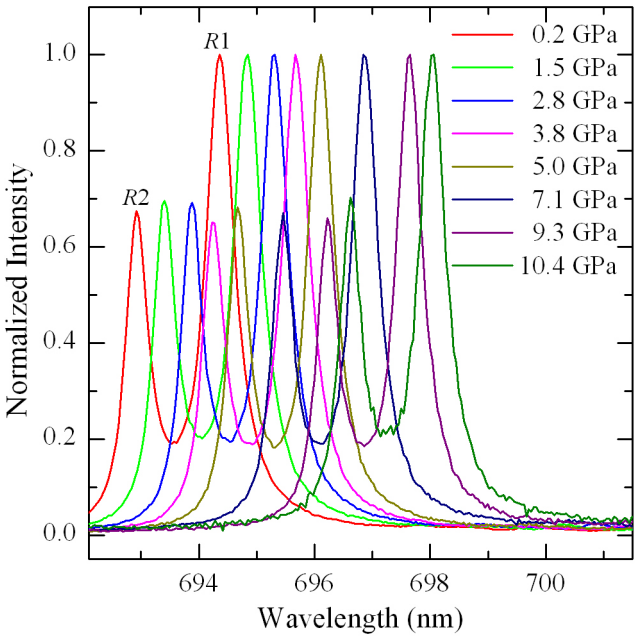

Figure 7.7 Ruby R1 fluorescence lines measured at 295 K for each pressure step.

Visual inspection of the gasket through the diamond allows following the evolution of the hole's shape at each pressure step. Figure 7.8 shows six photographs of the gasket. In the first one the cell is closed but no pressure is applied and in the last one the pressure is measured at 10.4 GPa. It is visible that the hole remains satisfactorily centred with respect to the culet up to the maximum pressure. Its shape changes progressively from a perfect circle to an ellipse. The deformation is minimal and reflects on the good parallelism of the culets' faces.

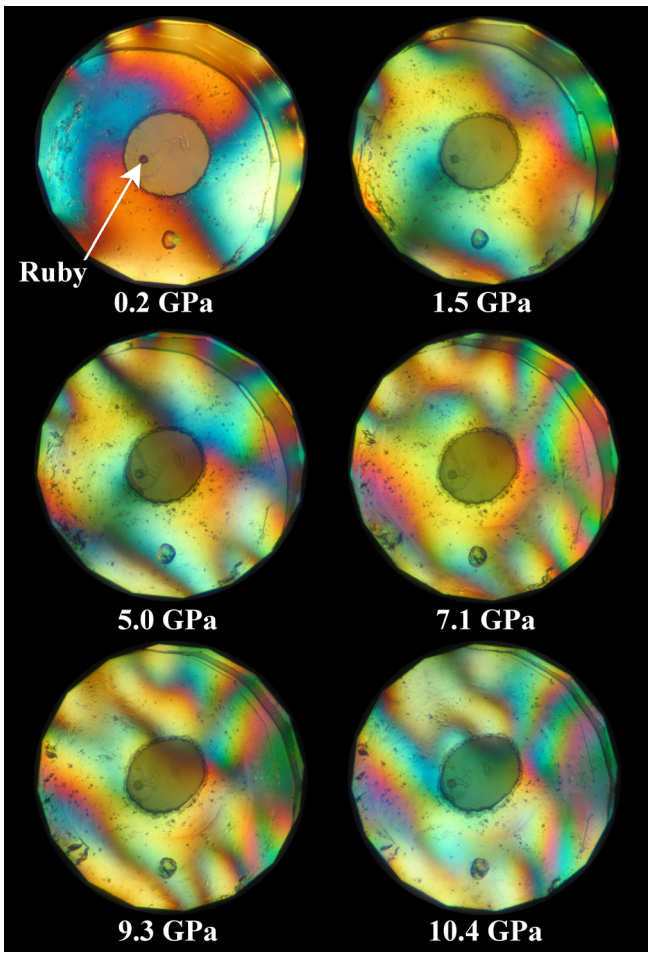

Figure 7.8 Photographs of the gasket hole taken at several pressure points during loading. The hole contains a ruby sphere and is filled with methanol:ethanol 4:1. The elongation of the sample hole illustrates the quality of the anvil alignment. The crescent present in the top left of each picture and decreasing in size as the pressure rises is due to a misalignment of the anvil and the original indentation.

After dismantling the cell the gasket was examined further. The gasket thickness after pressurisation is uniform and equal to 41 μm (58 μm originally). By looking at each side of the gasket it is possible to estimate the XY culet alignment at the final pressure (10 GPa). Figure 7.9 is constructed by taking a photograph of either side of the gasket, flipping one of them and adjusting its size and position until the gasket's hole of one picture matches the gasket's hole of the other picture. Then the culet position, visible on the gasket is marked with the colour circles. The red circle is paired with the indent visible on gasket side displayed while the blue circle symbolised the indent on the other side of the gasket.

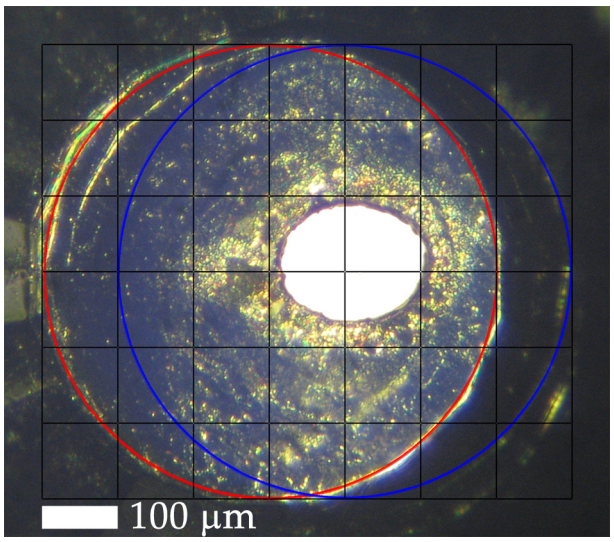

Figure 7.9 Photograph of the gasket after pressure testing. The red circle corresponds to the final (10 GPa) diamond culet position on the gasket's visible side. The blue circle represents the final (10 GPa) diamond culet position on the gasket's opposite side.

On the photograph, the hole appears to be off centre (~100 µm) from the culet edge (red circle) however looking at the opposite side culet's position, the blue line, the hole is perfectly central. The photographs of Figure 7.8 were taken on the gasket's side corresponding to the blue line. At 10 GPa the XY culets misalignment is of 100 µm or 16% of the culet diameter. It is acceptable at this pressure but it results in very high stress concentration in the anvils and at higher pressure it will lead to catastrophic failure of the diamonds.

7.3.2 Temperature testing

The TX-DAC has been tested in-situ using two different standard laboratory single crystal X-ray diffractometer cooling systems. Some tests were carried out on a Bruker APEX II diffractometer equipped with an Oxford Cryosystems Cryostream Plus [158] and the other tests took place on a KAPPA APEX II diffractometer from Bruker working with an Oxford Cryosystems N-HeliX [158]. Both setups are illustrated in Figure 7.10.

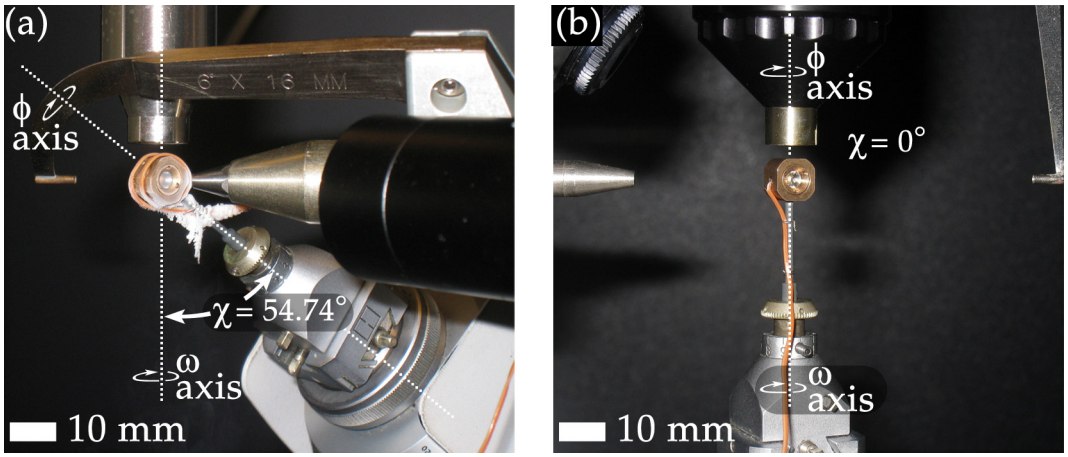

Figure 7.10 (a) TX-DAC with T type thermocouple at 122 K under an Oxford Cryosystems Cryostream Plus nozzle and (b) at 300 K under an Oxford Cryosystems N-HeliX nozzle. The ω axis is vertical and ϕ lie in a vertical plane. χ is the angle between ω and ϕ. When χ=0, ω and ϕ overlap as shown on (b).

The Cryostream Plus operation is based on a nitrogen gas stream surrounded by a stream of dry air which prevents atmospheric moisture from freezing on the crystal. The nitrogen gas is supplied from a liquid nitrogen dewar and the gas output temperature is regulated via gas heater and thermosensor located in the Cryostream head. From the technical specifications the base temperature of this system is 80 K but in reality 90 K is the minimum temperature at which a diffraction measurement can be run reliably.

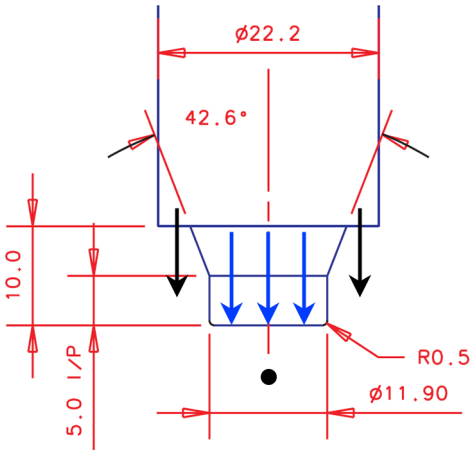

Figure 7.11 Oxford Cryosystems Cryostream Plus nozzle technical drawing. All dimensions are in mm. The sample position is indicated by the black dot. The nitrogen gas flow is represented by the blue arrows and the black arrows illustrate the dry air flow (obtained from Oxford Cryosystems [158]).

As shown in Figure 7.11 the nitrogen stream comes out of an 11.9 mm diameter nozzle and the dry air flows around this nozzle from a 22.2 mm diameter sleeve. At stable temperature the nitrogen gas flow rate is 5 L/min and the balanced dry air flow ensures a good barrier between the nitrogen cold stream and the air in the laboratory. In this case the TX-DAC with a diameter of 9 mm fits entirely into the nitrogen flow and during the cool down of the cell and after a prolonged time at low temperature a faint layer of ice was observed on the sides of the cell but the diamonds' surfaces and therefore the X-ray path remains free of ice contamination.

Using a handheld thermocouple thermometer HH66R from Omega Engineering Limited [209] with a type T thermocouple, the temperature of the TX-DAC was monitored during a cooling cycle. The Cryostream Plus temperature ($T_{Cryostream}$) was set to 200 K once a stable reading from the thermocouple ($T_{Thermocouple}$) was obtained $T_{Cryostream}$ was set to 100 K until a stable $T_{Thermocouple}$ was reached. The results obtained for this experiment are presented in Figure 7.12.

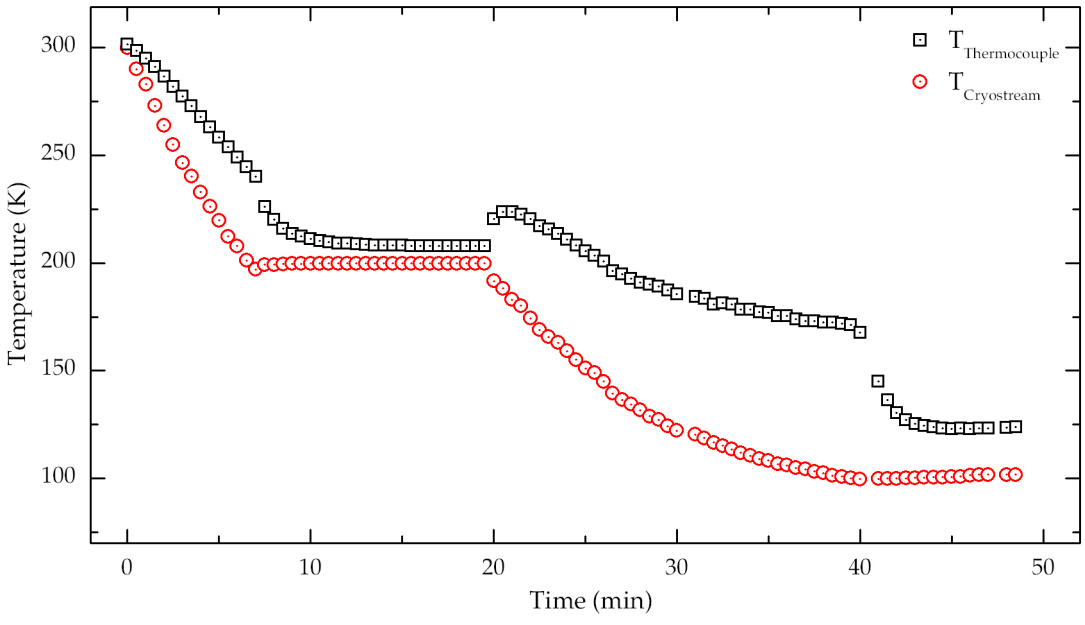

Figure 7.12 Cool down of the TX-DAC mounted on a Bruker APEX II diffractometer equipped with an Oxford Cryosystems Cryostream Plus.

During the cool-down stage the nitrogen flow increases to a maximum of 10 L/min, this creates more turbulence around the pressure cell and lessens the cooling efficiency. Once the set temperature is reached the flow go back to 5 L/min and the cooling rate of the cell increases. The manifestation of this phenomenon can be seen in Figure 7.12, at 7 min, once $T_{Cryostream}$ reached 200 K and at 40 min once $T_{Cryostream}$ stabilised at 100 K. It also explains the hump around 20 min when the set point has been changed from 200 K to 100 K, the flow increased suddenly and the TX-DAC temperature increased for a couple of minutes. Under the Cryostream Plus, the TX-DAC temperature stabilizes within less than 10 min after $T_{Cryostream}$ becomes stable at any set temperature, and a ΔT between $T_{Thermocouple}$ and $T_{Cryostream}$ equal to 8 K at $T_{Cryostream}$ = 200 K and ΔT = 22 K at $T_{Cryostream}$ = 100 K was observed.

On the APEX II diffractometer the sample can be rotated about the omega (ω) and phi (φ) axis while the chi (χ) axis is fixed at 54.76 (Figure 7.10). The data collection strategy used for high pressure measurements is based on the one developed by Dawson *et al.* [210] in which the sample rotates about ω to several discrete positions and about φ to two positions 180 apart. This means that the pressure cell orientation changes in the course of a measurement with respect to the fixed Cryostream nozzle which in turn might result in a variation of $T_{Thermocouple}$. In both positions about φ the cell axis lie in a plane perpendicular to the nozzle axis and because of the symmetry of the TX-DAC this move has no effect. Consequently to estimate the variation of $T_{Thermocouple}$ over a full measurement $T_{Thermocouple}$ was studied for each discrete position about ω required for high pressure diffraction studies.

Figure 7.13 illustrates the variation of the TX-DAC temperature as a function of the cell position about the ω axis. The pressure cell was moved to a new position every 5 seconds and a thermocouple temperature reading was recorded at each step. The average $T_{Thermocouple}$ is equal to 135 K and all the data fall between 133 K and 139 K with a standard deviation of 1.7 K. This

result shows a satisfactory cell temperature variation for a diffraction experiment.

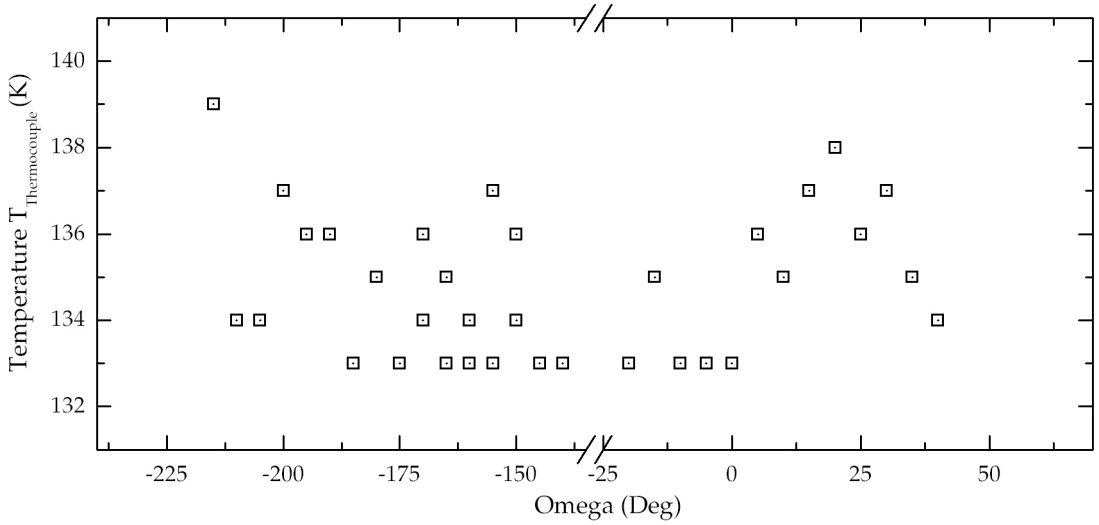

Figure 7.13 Temperature of the TX-DAC as a function of its orientation with respect to the Cryostream nozzle. The average thermocouple temperature reading is equal to 134.7 K with a standard deviation of 1.7 K.

The TX-DAC was also cooled down using an Oxford Cryosystems N-HeliX mounted on a KAPPA APEX II diffractometer. The N-Helix system is an open flow helium/nitrogen cooling apparatus capable of cooling samples to 30 K. The helium or nitrogen gas is supplied from cylinder; it is cooled by passing through heat exchangers of a two stage close cycle cooler, and passes out of the nozzle and over the sample. For economical reason nitrogen gas is used to cool down to 100 K and helium gas is used for temperature control between 100 K and 30 K. A second gas stream provides shielding for the cold stream and prevents ice building up on samples. In this setup both gas streams come out of the same nozzle (Figure 7.14), the total gas flow rate is ~ 8 L/min at stable temperature and increases during cool down.

The nozzle is a 10 mm diameter X-ray transparent Be tube which extends around the sample and provides an extra protection against atmospheric moisture. The TX-DAC is too large to fit inside the standard sample space, within the tube, and has to be placed a few millimetres below the nozzle,

allowing enough space for rotation. In these circumstances the pressure cell is not protected from atmospheric contamination and ice building up on it during the cool-down has to be expected.

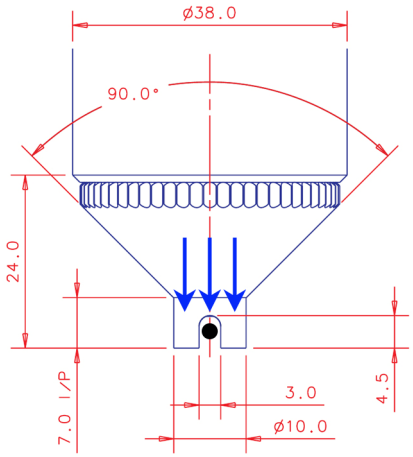

Figure 7.14 Oxford Cryosystems N-HeliX nozzle technical drawing. All dimensions are in mm. The black dot illustrates the standard sample position and the blue arrows indicate the direction of the helium gas flow (obtained from Oxford Cryosystems [158]).

The temperature of the TX-DAC ($T_{Thermocouple}$) was monitored using a thermocouple thermometer HH66R from Omega Engineering Limited [107] with a type T thermocouple while cooling down it down from 300 K. The N-HeliX temperature ($T_{N\text{-}HeliX}$) was set from 300 K to 50 K in 25 K steps and the last data point was taken at the N-HeliX base temperature, 30 K. At each step the data was recorded after $T_{Thermocouple}$ became stable. The data set as well as temperature difference, ΔT, between $T_{Thermocouple}$ and $T_{N\text{-}HeliX}$ are presented in Figure 7.15. ΔT increase as $T_{N\text{-}HeliX}$ decreases and reaches a maximum of 58 K for $T_{N\text{-}HeliX}$ = 30 K. The lowest temperature recorded on the TX-DAC cooled under the N-HeliX system is 88 K and as expected the appearance of frost was observed on the BeCu parts at 240 K and the growth of consequent amount of ice on the pressure cell, mostly on the cell side opposite to the N-HeliX nozzle, after some time at low temperature (Figure 7.17).

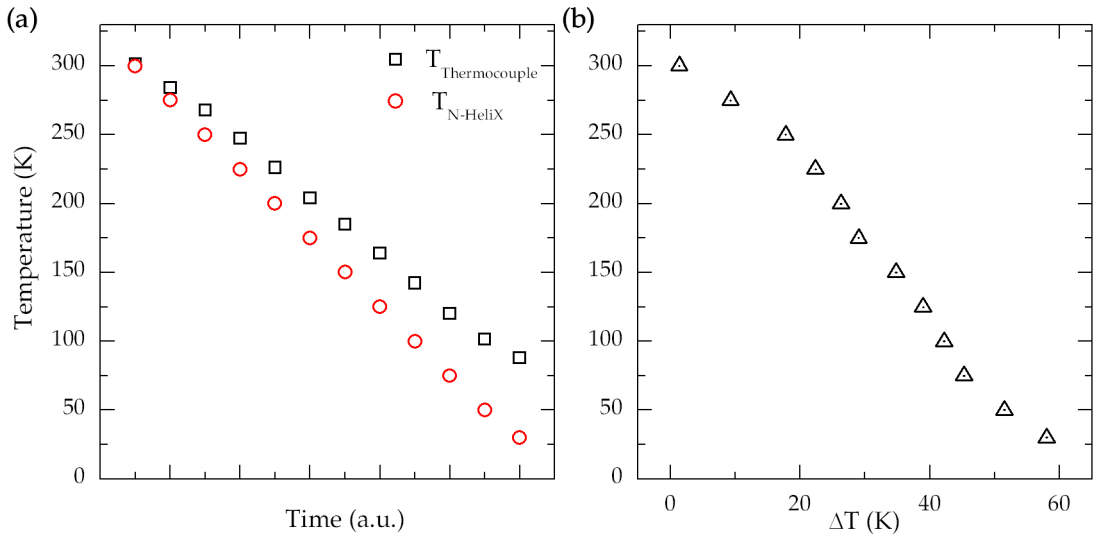

Figure 7.15 (a) Cool down of the TX-DAC mounted on a Bruker KAPPA APEX II diffractometer equipped with an Oxford Cryosystems N-HeliX. Data were recorded as a function of the N-HeliX Temperature at 25 K interval from 300 K to 50 K. The last data point is recorded at 30 K (base temperature of the N-HeliX). Each data point is recorded once $T_{Thermocouple}$ is stable. (b) Temperature difference between the temperature measured on the pressure cell and the temperature set of the N-HeliX system.

The KAPPA APEX II diffractometer from Bruker is a four-circle diffractometer on which the sample can be oriented about the ω, φ and χ axes (Figure 7.10). By following the data collection strategy developed by Dawson *et al.* [210] modified to introduce the degree of freedom about χ and due to the TX-DAC shape it is the rotation about χ which would lead to the most significant difference in the cell position with respect to the N-Helix Nozzle. In order to establish the TX-DAC orientation dependence of its temperature, the evolution of the pressure cell temperature was recorded while rotating the cell about χ in the range corresponding to a room temperature pressure measurement, from 0 to 80 at two different temperatures.

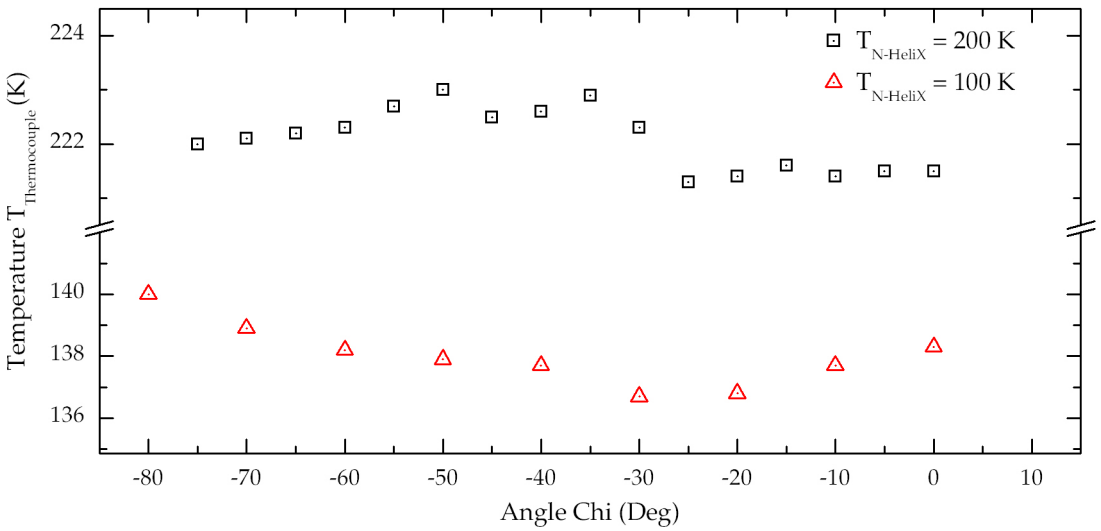

Figure 7.16 Temperature of the TX-DAC as a function of its orientation with respect to the Cryostream nozzle. The average thermocouple temperature readings are equal to 222.08 K and 138.02 K with a standard deviation of 0.55 K and 0.96 K respectively.

The results presented in Figure 7.16 show the $T_{Thermocouple}$ fluctuation as a function of the pressure cell orientation about χ. At an average temperature of 222 K the data lie between 221.3 K and 223 K with a standard deviation of 0.55 K and at an average temperature of 138 K the data lie between 136.7 K and 140 K with a standard deviation of 0.96 K. The temperature of the pressure cell was recorded at each orientation after $T_{Thermocouple}$ stabilisation. The TX-DAC temperature stability is of course not as good as the N-HeliX stability of 0.3 K announced by Bruker but it is still within acceptable limits for low temperature data collection.

Figure 7.17 TX-DAC under N-HeliX nozzle after a prolonged time at low temperature. (The BeCu stand visible in the picture is now obsolete)

Overall the TX-DAC is fully compatible with the Cryostream Plus system. It can easily be cooled down, its temperature stabilises quickly and remains stable in the various orientation of the pressure cell required for data collection furthermore there is no visible trace of ice contamination along the incident and scattered X-ray beam.

Under the N-HeliX system the situation is more delicate and some modification of the system would be required in order to carry out low temperature data collection. The temperature study showed that the TX-DAC could be cooled down successfully with good temperature stability. However, because the cell does not fit into the Be nozzle an accumulation of ice is observed on the metallic parts of the pressure cell which rapidly expands to cover the diamonds and gets in the way of the X-ray beam. To prevent this from happening a barrier between the TX-DAC and the laboratory atmosphere must be present. It can be a physical barrier, for instance a larger Be tube could be use or a thin wall tube made of non-crystalline material such as for example capton film, or alternatively an extra dry gas flow surrounding the pressure cell.

For routine low temperature high pressure data collection the sample temperature must be known accurately and it is important to understand the mechanisms by which the pressure cell temperature is affected.

Heat may be transmitted to the pressure cell by conduction, convection or radiation. By nature the radiation heat transfer is very small and in the temperature regime of interest it can be neglected. In the setup, it can be assumed that the pressure cell is wrapped in the cold gas stream which makes the convection heat transfer to the cell insignificant. Therefore the conduction is the predominant process through which heat can reach the TX-DAC and against which it is possible to act. The heat flow through the stand can be assessed using the equation (8.1) where q (W) is the heat flow rate, k ($W.m^{-1}K^{-1}$) is the conductivity of the material through which the heat

is flowing, A (m^2) is the area of transfer, x (m) is the length of material over which the heat transfer takes place and, in this case, ΔT (K) represents the difference in temperature between the TX-DAC and the goniometer head, and also between the TX-DAC and the surrounding laboratory atmosphere.

$$q = \frac{kA}{x}(\Delta T) \tag{8.1}$$

In the present setup x is irrelevant and equation (8.1) can be simplified to $q = kA(\Delta T)$. The stand has been made from PVC because of its low thermal conductivity, K_{PVC} = 0.19 $W.m^{-1}K^{-1}$ at 293 K and decreases continuously with temperature [211], and for its adequate mechanical properties. The cross-sectional area of the stand is 2.01 mm^2 therefore the heat flow to the TX-DAC through the PVC stand can be approximated to $q = 3.8\times10^{-7}(\Delta T)$ W at room temperature. For comparison, with a BeCu stand of the same size it would be $q = 2.1\times10^{-4}(\Delta T)$ W at room temperature.

For the temperature testing the TX-DAC was equipped with a T type thermocouple with its bead glued into a blind hole with some GE varnish. The T type is the probe to use with the hand held thermometer HH66R [209] for the low temperature range, it consists of a junction between a copper wire and a constantan wire. Each wire has a cross section area of 0.05 mm^2. The thermal conductivity of constantan is 22.7 $W.m^{-1}K^{-1}$ at 300 K and decreases slowly to a minimum of ~18.4 $W.m^{-1}K^{-1}$ at 125 K [212] before going back up to 19.1 $W.m^{-1}K^{-1}$ at 100 K and there are no available data for lower temperature whereas the copper thermal conductivity is 398 $W.m^{-1}K^{-1}$ at 300 K, 483 $W.m^{-1}K^{-1}$ at 100 K and continues to increase exponentially to reach a maximum of 1960 $W.m^{-1}K^{-1}$ at ~10 K [213]. With equation (8.1) the heat flow reaching the TX-DAC through the thermocouple wires can be approximately calculated. At 300 K the heat flow going through the wires, $q = 2.1\times10^{-5}(\Delta T)$ W, is two orders of magnitude greater than heat flow reaching the pressure cell through the PVC stand and due to the thermal

properties of copper it will increase as the temperature decreases. In this configuration the thermocouple probe itself is exposed to a large temperature gradient and because it also acts as a heat carrier the temperature reading from this probe must be used with care. The closer the temperature gradient is to the thermocouple tip the more the temperature reading will be affected. During the temperature measurement the thermocouple lead was wrapped around the cell body several times (Figure 7.10 (a)) in order to cool down a greater section of the thermocouple and to move the temperature gradient away from the thermocouple tip. However the temperature readings obtained might still be affected by the heat flow to the pressure cell and in fact the temperature difference between the TX-DAC and the cooling system set point could be smaller than the one presented in Figure 7.12 and Figure 7.15.

Several studies, numerical and experimental [214-218], have shown that the error intrinsic to invasive temperature measurement techniques result from the distortion in the thermal field around the probe and is proportional to the temperature gradient. For thermocouples, it is a combination of heat transfer along the thermocouple wires, heat conduction between the thermocouple wire and the system being measured; interfacial resistance between the thermocouple measuring bead and the system being measured.

The calibration of the TX-DAC temperature against the Cryostream temperature is a mandatory requirement before collecting reliable data sets. One solution to reduce the heat flow through to the TX-DAC would be to replace the thermocouple probe by a fibre optic temperature probe such as the low temperature version of the T1 from Neoptix [219] which would allow a heat flow to the TX-DAC $q = 3.9\times10^{-7}(\Delta T)$ W. But even this value is comparable to the heat flow along the PVC stand and therefore is not negligible.

A better solution would be to avoid using any contact temperature measurement method and to calibrate the temperature difference between the temperature sensor on the Cryostream and the actual temperature of the cell by using a material with known equation of state or with known phase transition occurring at low temperature. This procedure is ideal but it is very time consuming both in gathering the appropriate samples and in collecting and analyzing X-ray data sets.

Chapter 8

Composite piston-cylinder cell for SQUID magnetometer

The existing pressure cells designed for the MPMS perform well in *dc* susceptibility measurements but are not suitable for *ac* susceptibility measurements. This statement applies equally to pressure cells of both opposed anvil and piston-cylinder design, but in this chapter only the later will be considered. These cells are metallic and when they are exposed to a fast alternating magnetic field, Eddy currents set in the conductive body of the cell. For alternating frequencies higher than 10 Hz the screening effect of the currents set in the cell obscures significantly the sample's signal making high pressure *ac* susceptibility measurements difficult. The obvious solution to resolve this issue is to build a non-metallic and therefore non-conductive pressure cell. It is the recent advances in the field of high strength fibre reinforced composite material which makes possible the conception of such device [220].

Although, at equal mass, fibre composite materials are stronger than metals their exceptional tensile strength is directly related to the strength of the fibre while their compressive strength depends on the compressive strength of the matrix material [221]. This leads to materials with anisotropic strength along the fibre direction thus making it difficult to recreate the maximum strength of the fibre in a complex 3D shape. Furthermore a high filling factor (volume of the fibre/volume of the matrix) is an essential parameter in optimising the strength of the composite part and it is difficult to maintain in parts of complex shape working under non-unidirectional loading conditions.

The design of a conventional piston-cylinder cell for MPMS can be broken down into two distinct components: (i) the straight cylinder located around the sample which acts (with the pistons) as the pressure chamber and is subjected to hoop stress and tensile stress along its length, and (ii) the bolt and threaded end assembly located at either end of the cell which acts as a pressure locking mechanisms and is experiencing tensile and compressive stresses.

Of the two components described above the cylinder is a simple shape that can be made from fibre impregnated with epoxy resin [222] and therefore have high strength. The end-assemblies cannot be made of fibre because parts of them need to work at high compressive stress conditions. Indeed it is impossible to create a threaded shape of strength comparable with the tensile strength of the reinforcing fibre. Our approach to solve this issue was to create a 'hybrid' pressure cell in which the sample would be surrounded by non-metallic components and the end-assemblies would be a long distance away from the sample position, thus not interfering with the *ac* measurement. The body of the cell is to be made of a composite material and the pistons can be made of non-magnetic type of ceramic which performs well in compression. The end parts threads and their mating bolts are to be made of BERYLCO25 and would be identical to the parts used in the micro cell shown in Figure 3.20.

The *ac* technique implemented in the MPMS works in such a way that the sample is subjected to an alternating magnetic field and the measurement takes place in two steps. Firstly, the sample is aligned in the horizontal plane of the bottom loop of the superconducting detection coils. A nulling process aiming at removing any undesirable contribution takes place and a first signal is recorded. Then, the sample is moved vertically to be centred within the second-order gradiometer and a second response is recorded. The sample's signal is extracted by subtracting the signal obtained in the first measurement from the one obtained using the second coil. The full procedure is detailed in reference [223]. As opposed to the variable sample's motion accompanying *dc* measurements (typically within 4 cm and 6 cm range), in the *ac* mode the sample is only shifted along the axis of the magnetometer by 1.7 cm. Therefore, there is only a very short portion/section of the sample holder (pressure cell in this case) which is sensed by the set of the detection coils. Though the metallic end-assemblies still need to be far apart, the short translation of the cell makes it easier to implement the non-metallic cylinder in the hybrid cell design as shorter cylinders are easier to make and are more stable when loaded.

The manufacturing of the piston-cylinder composite pressure cell prototypes is explained hereafter with an emphasis on the development of a strong composite-to-metal interface. The experimental result obtained so far using the hybrid cell are also presented.

8.1 Concept and Design

The design of the fiber-composite piston-cylinder cell (FC-PCC) is based on the existing MPMS piston-cylinder micro cell (Figure 8.1) which can be used to generate a sample pressure of up to 20 kbar. Its design is similar to the one described in Figure 3.20. The body of the cell as well as the locking screws

are made of BeCu; the sample is contained in a PTFE capsule; the pistons are made of zirconia and copper antiextrusion rings are used to seal the pressure chamber. One of the bolts (Figure 8.1 - left end of the cell) is used to close one end of the cell while the second one (Figure 8.1 - right end of the cell), with a hole through its axis, is used to lock the zirconia pistons in place at each pressure increment. With the help of a hydraulic press a load is applied to the WC pusher which passes through the locking bolt and rests directly on the tip of a zirconia backup piston of 3.3 mm in diameter, which itself forces the 2.5 mm diameter piston into the cell's bore thus increasing the sample pressure. While the cell is under load in the press, the bolt is tightened to lock the pressure.

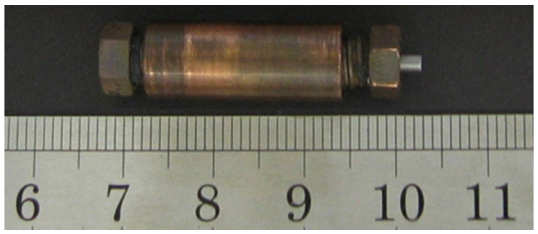

Figure 8.1 BeCu piston-cylinder micro cell for MPMS.

The locking bolts, the PTFE capsule, the zirconia pistons as well as the pressurisation routine were kept identical while the short metallic body was replaced by a long composite tube and the number of the 2.5 mm diameter zirconia pistons was increased (in the tests pistons either 2 or 4.5 mm long were used) to create the FC-PCC shown in Figure 8.2.

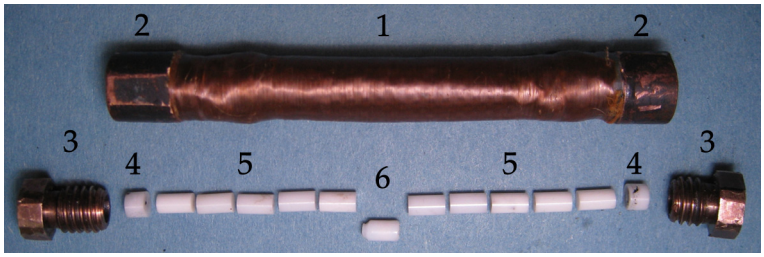

Figure 8.2 Photograph of the FC-PCC and its various parts: (1) body of the cell made of Zylon fibre and epoxy resin E-120HP; (2) BeCu end part; (3) BeCu locking screw; (4) zirconia piston backup (dia. = 3.3 mm, length = 2.0 mm); (5) zirconia piston (dia. = 2.5 mm, length = 4.5 mm); (6) PTFE capsule.

The cross-sectional view of the FC-PCC is shown in Figure 8.3. The cylinder is made of Zylon fibre and there were a number of technical challenges to be overcome in the design of the cylinder which are discussed below.

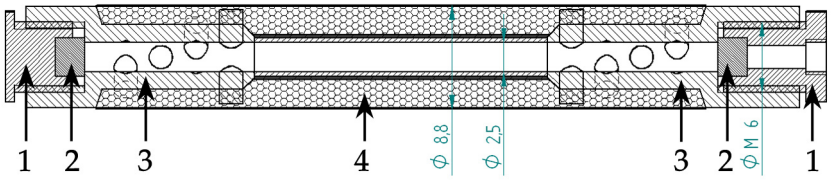

Figure 8.3 CAD drawing of the FC-PCC: (1) locking screws; (2) 3.3 mm diameter zirconia piston backup; (3) metallic end-part; (4) Zylon fibre and epoxy resin cylinder. The 2.5 mm diameter zirconia piston and the PTFE capsule are not shown for clarity.

8.2 Detailed design consideration of the FC-PCC

This section outlines the technical challenges that needed to be overcome in the design of the hybrid cell. These include the problems with connecting metallic parts with the fibre, termination of the ends of the fibre cylinder as well as winding a custom-shaped cylinder and reinforcing the bore of the cell with the core.

8.2.1 Magnetic and mechanical properties of materials used in the construction of the cell.

There are five materials used in the construction of the cell. The magnetic and mechanical properties of the BeCu alloy are well known and have been described in the previous chapters. The pistons of the FC-PCC are made of non-magnetic zirconia which is also non-metallic as there is no binder used in making the grade of the ZrO2 used in this cell. The sample is enclosed into a PTFE capsule which is also non-magnetic and non-metallic and its use has been described in the Chapter 6 on TM-PCC. The essential part of the design of the FC-PCC is a non-metallic cylinder surrounding the sample during the

ac measurement. Zylon, produced by Toyobo Co.,Ltd. [224], which is the strongest commercially available fibre with the tensile strength of 5.8 GPa and has previously been used in low temperature and high magnetic field environment [225] was chosen for making it. It consists of long chain molecules of poly(p-phenylene-2,6-benzobisoxazole). LOCTITE® Hysol® E-120HP™ which is a strong two component epoxy type resin was used as a matrix material. The core, which would form the bore of the cell and on which the fibre cylinder was wound was made of Tecamax, a high performance thermoplastic produced by Ensinger Inc. [226], with a compressive strength of 0.62 GPa.

In order to assess the suitability of these materials to making *ac* susceptibility measurements a test using a sample of dysprosium oxide has been conducted. Dy_2O_3 is used as a reference material for *ac* measurements because its susceptibility does not depend on the frequency of magnetic field at which the measurement is conducted [227]. In the test a sample of Dy_2O_3 was loaded into cylinders of the same dimensions (i.d. 2.5 mm, o.d. 8.5 mm) and its *ac* magnetic susceptibility has been measured as a function of temperature at several frequencies of the magnetic drive field. The results of the measurement are presented in Figure 8.4.

The results of the test clearly show the frequency-dependence of the data collected in the BeCu cylinder on χ''. The data collected on the sample inside the composite cylinder and inside the Tecamax cylinder show no frequency dependence of χ''.

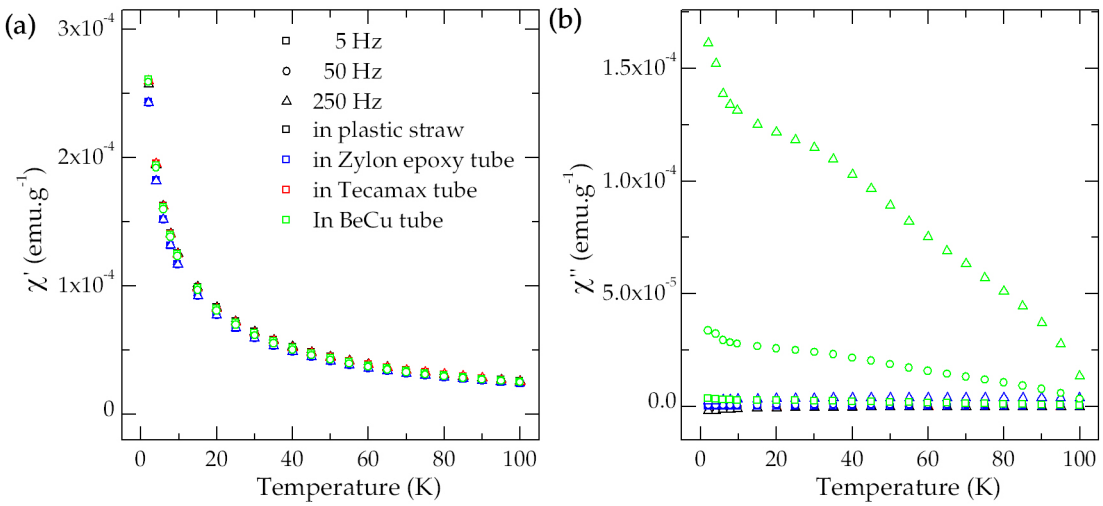

Figure 8.4 The magnitude χ′ (a) and the phase shift χ″ (b) response of Dy_2O_3 samples during *ac* susceptibility measurements in various sample holder. The conventional plastic straw, a Zylon epoxy tube, a Tecamax tube and a BeCu tube. The measurements took place in a stable field of 100 Oe and a drive field of 4 Oe with a 5, 50, and 250 Hz frequency and on the 2 K to 100 K temperature range.

8.2.2 Fibre and metal – making the connection

One of the biggest tasks in the design exercise was the challenge of mimicking the threaded connection between the cylinder and the locking screws in the conventional metallic piston-cylinder cell because as it was mentioned above a strong thread cannot be made out of a unidirectional fibre. Instead of making a thread in the composite cylinder, the fibre at the ends of the cylinder was terminated using metallic parts. These parts could have threads made in them so that they could be used with the locking screws. This in turn translated into the task of finding a suitable way of connecting metallic ends to the fibre taking into account the constraints imposed by the sample bore of the MPMS which is only 9 mm diameter.

The solution proposed for making a connection between the cylinder made of fibre and the parts made of metal is based on securing the loops of fibre around anchors made in the metallic part as illustrated in Figure 8.5.

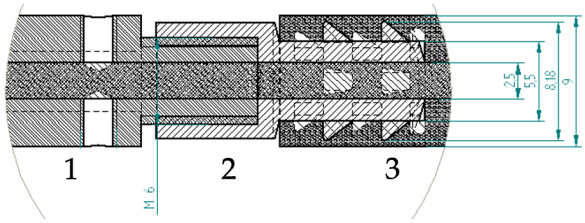

Figure 8.5 A CAD drawing of the anchoring system proposed for securing fibre on the metallic end-part: (1) split collets; (2) BeCu end-part; (3) Fibre and epoxy component.

A template on which the fibre would be wound has been made. The metallic end-parts made of BeCu were secure on a BeCu rode (2.5 mm diameter) using two split collets to form a solid assembly. The parts as well as the assembled template are shown in Figure 8.6.

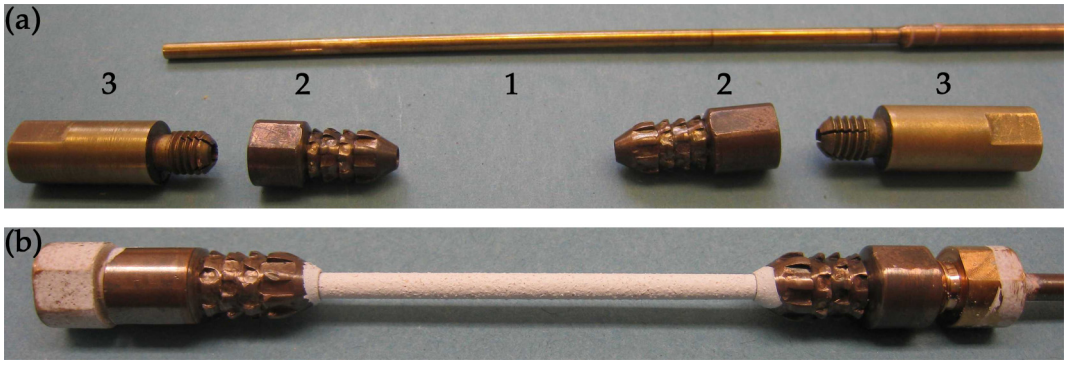

Figure 8.6 (a) Exploded view of the various parts composing the template: (1) BeCu rode; (2) BeCu end-parts; (3) split collets. (b) The template assembled (the central part appears white because it has been spread with a release agent).

The assembly was mounted on the spindle of the programmable coil-winding machine and one end of a single fibre strand was spot-glued to of the metal ends as shown in Figure 8.7. Once the glue set the fibre was tensioned and the cylinder was wound between the two end-parts with a controlled pitch of the fibre. A thin layer of epoxy has been applied to the strand as it was fed onto the winding fixture.

After the last layer of fibre was put on the cylinder, the assembly was left in the winding machine for the epoxy to set. After that the assembly was placed in an oven for curing the epoxy for 2 hours at 65°C. The final step in the

making of the cell was to pull out the 2.5 mm diameter BeCu rod. The cell was then assembled (a dummy sample was used) as shown in Figure 8.2 and ready for testing.

Figure 8.7 Programmable coil-winding machine used to wind the pre-tensioned strand onto the template. One end of the template is held in the chuck and the winding is ready to start.

A WC pusher was positioned through the locking screw (top end of the cell on Figure 8.8) and the cell was placed into a hydraulic press fitted with a sentive load cell. This setup allows an acurate monitoring of the load applied to the WC pucher. Figure 8.8 shows the FC-PCC clamped between the load cell (bottom) and the hydraulic press piston (top).

In the first round of mechanical testing a load equivalent to a sample pressure of 11 kbar has been applied and the pressure has been locked inside the cell using the locking screw. However, on releasing the load in the press

the cell failed. On examining the cell it appeared that the fibre secured on the anchors was cut under the large tensile stress which it was meant to sustain when locked. Figure 8.9 shows the damaged fibre next to the end-parts. It is clear that the fibre was cut against the sharp edges of the BeCu anchors.

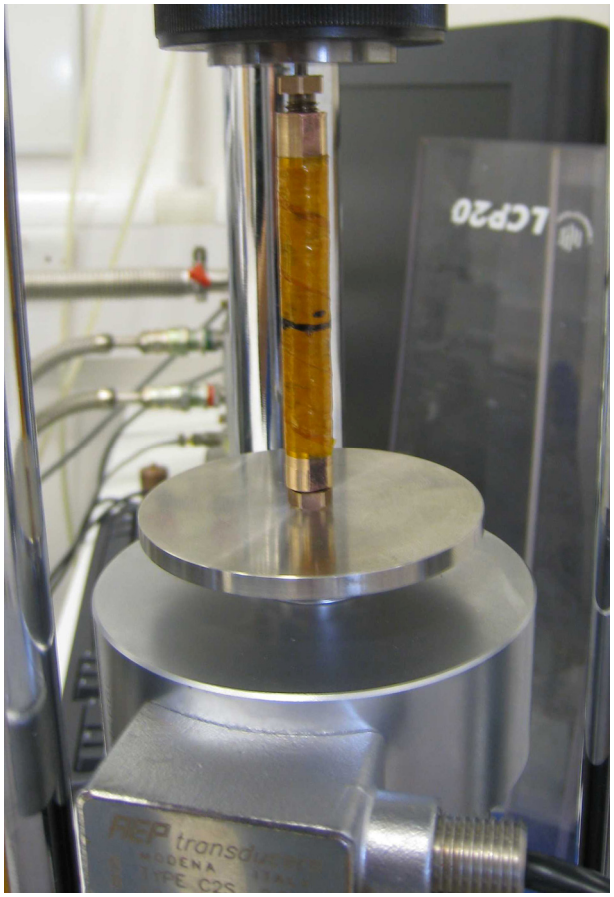

Figure 8.8 The FC-PCC positioned in the hydraulic press during the pressurisation process. The WC pusher is visible between the top locking screw and the press' piston. The lower end of the pressure cell rests directly on the load cell.

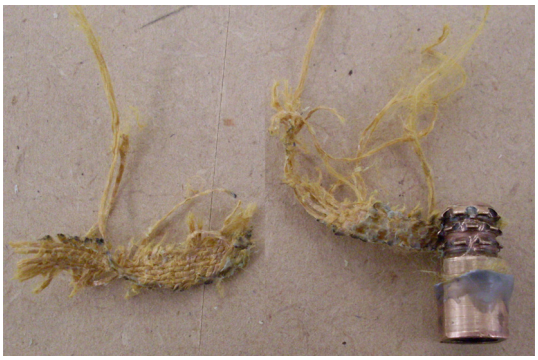

Figure 8.9 Under load the fibres get cut by the teeth shaped anchors present on the end-part.

The anchors were replaced with rounded studs to prevent sharp edges at the interface of fibre and the metal. The design of the end-part featuring height studs distributed around the part in a regular pattern is shown in Figure 8.10 and the FEA simulation results showing the stress distribution on a quarter of the part subjected to a load equivalent to a sample pressure of 20 kbar are presented in Figure 8.11

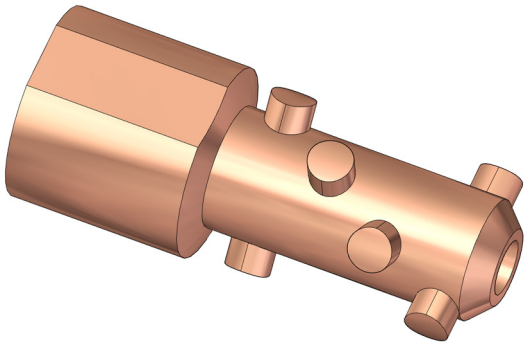

Figure 8.10 Computer-aided 3D model of the BeCu end-part featuring the stud anchors

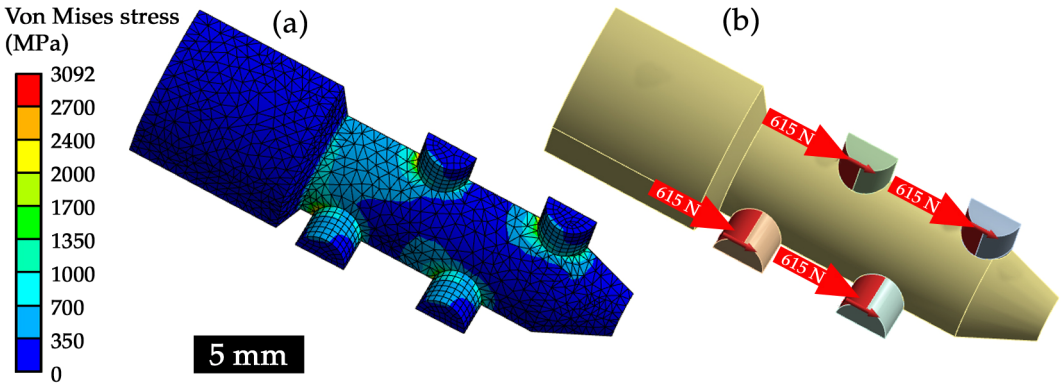

Figure 8.11 (a) The FEA of a quarter of the BeCu end part. The axial load equivalent to 20 kbar locked in the cell is applied to the red surface of the studs (red arrows in (b)).

The FEA simulation results show that the studs made of BeCu would be able to hold the sample pressure of 20 kbar (9840 N or 1230 N per stud). The stress distribution maps indicate that the yield strength of BeCu is only exceeded in very small areas localised at sharp corners. These results are due to stress singularities at the corners formed at the boundaries between the studs and the end parts. The corners have a zero radius of curvature and with this type

of boundary conditions the computed stress value tend to an infinite value. This is expected but does not reflect the reality and it can be overcome by including a small radius as it would be the case when machining the part. The majority of the part remains at an acceptable stress state. It is worth noting that if the load in the model is to be reduced to the equivalent of 10 kbar (the original aim for this pressure cell) the stresses would be halved accordingly and the maximum stress will not exceed the yield strength of BeCu.

8.2.3 Cylinder winding from single strand and fabric

Using the new optimised end-part various winding pitches and angles were tested. Large pitch of winding enhances the cylinder's ability to sustain high tensile load. However, it had a negative effect on the containment of the sample which under a large compressive load would tend to squeeze out by pushing the fibre apart. The best way of winding was to alternate the winding pitch. The first layers would be wound with a small pitch to provide a good support in the radial direction and then layers with a very long pitch (virtually going from one end part to the other in less than one turn) would reinforced the cell along its length.

Using Zylon fabric for winding the cylinder has also been experimented. The fabric consists of the fibre interwoven to provide the maximum strength in two directions at 90 degrees to each other in the plane of the fabric. Because of the high strength of Zylon fabric the only suitable way of cutting it is by laser cutting. Figure 8.12 (a) shows the layer of fabric being positioned on the table of the laser cutter. The table is located on the XY-stage and can be programmed to follow a particular path under the cutting head of the laser. The fabric cut with the laser is shown in Figure 8.12 (b).

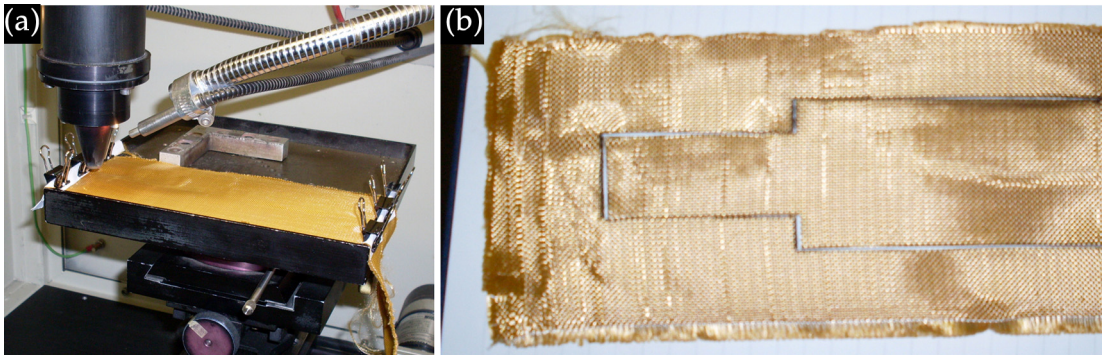

Figure 8.12 (a) Zylon fabric being cut using the laser cutter; (b) the shape of the cut in the fabric.

The fabric was cut in the progressively widening shape in order to reflect on the varying diameters of the winding fixture, i.e. there's more fibre to be wound around the bore of the cylinder. Once the outer diameter of the cylinder made around the central area matches the o.d. of the end-parts the fabric widens to cover those. After the pattern was cut, the two pieces of fabric were arranged on the core of the winding assembly and glued to the opposite sides of the core as shown in Figure 8.13.

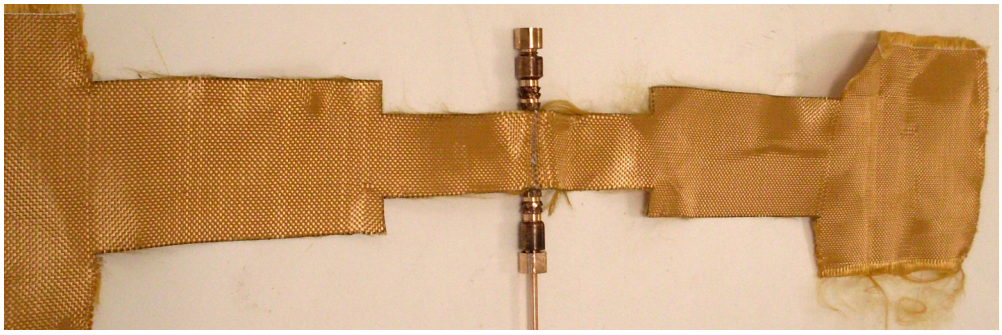

Figure 8.13 The two pieces of fabric are lined up on the winding fixture and glued at the lines of contact.

The winding fixture is then mounted on the winding machine and the tensioning load is applied to. The tensioning is needed to enhance the fibre-to-epoxy filling factor and also to pre-stress the cylinder against the bore. The tensioning strain on the single strand fibre was estimated from the pulling force applied and the cross-sectional area of the strand, and was found to be approximately 3 GPa (Figure 8.14 (a)). For the fabric which has an extended

surface of contact with the core the stress for the same load is smaller (Figure 8.14 (b)). However, this stress is sufficient to get rid of the excess epoxy and to pre-stress the cylinder.

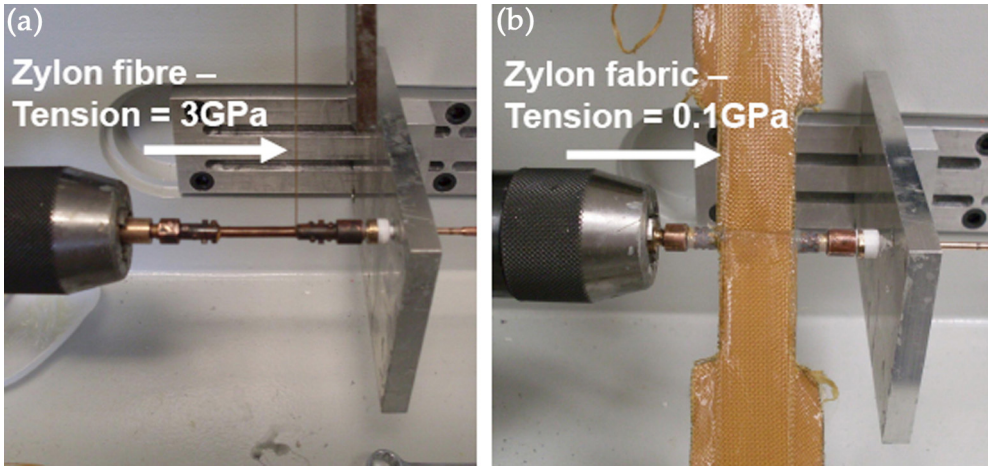

Figure 8.14 Winding of the Zylon fibre cylinder using a single strand (a) and fabric (b).

In order to make the bore smooth for zirconia pistons to slide in, a thin sleeve made of Tecamax was used as the cylinder core. The sleeve was put on the BeCu core rod of the winding fixture prior to winding.

8.3 Testing

The mechanical test of the cell was done in two stages. In the first approach the tensile strength of the cylinder was measured using an Instron tensile tester. In this test the tensile stress mimicking the stress produced by the reaction force acting on the pistons from the compressed sample was applied to the ends of the cylinder and its deformation was measured. The results for different types of cylinder are presented in Figure 8.15. The blue curve shows the load-elongation data for the cylinder made of fabric would on the end part which had a knurled surface feature rather than the anchored or studded profile. The red and the green curves show the same type of the

relationship but for the cylinder wound on the studded end-parts using fabric and single strand fibre, respectively.

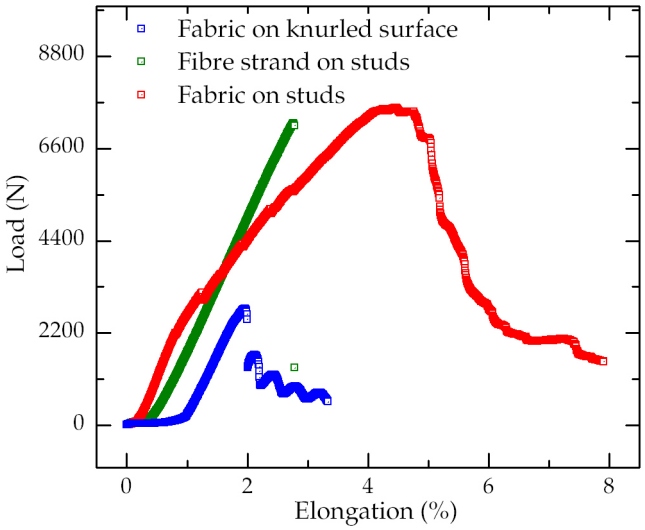

Figure 8.15 Tensile load in function of the elongation of the cell. Typical value obtained from three different type of cell.

The data presented in Figure 8.15 illustrates that using studs enhances the ability of the fibre-metal interface to maintain higher axial load that is otherwise possible without the studs. The maximum load achieved in these tests is around 7.3 kN which corresponds to approximately 15 kbar pressure clamped inside the pressure cell. The comparision between the green and red data sets shows that the cylinder made of fabric experiences a larger deformation for the same load compared to that of the cylinder made of a single strand fibre. It can be attributed to the lower degree of pre-tensioning control on the fabric during the winding process (Figure 8.14). Making the cylinder using a single strand fibre provides us with a better control over the winding process and results in a more robust part.

In the second test the FC-PCC pressure cells were assembled as for a standard measurment but with a dummy sample and a load was applied to them until they failed. The loading procedure is described in Section 8.2.2. The load of failure established in this test showed that the cells fail at the pressuer of about 11 kbar. This pressure is somewhat lower than the failure

pressure of 18 kbar found in the tensile stress test described above. An example of the failed part is shown in Figure 8.16. It is clear that when the failure manifests itself in the visible deformation of the cell at the sample position.

Figure 8.16 FC-PCC after destructive compression test. The cell body is bent at the sample position and its diameter expanded slightly.

By analysing the results of the destructive tests it becomes clear that the failure is caused not by the inability of the cell to withstand high tensile axial stress but rather by the weakness of the cell in the radial direction and its lack of ability to contain the plastically deformed sample. This problem can be resolved by either furhter optimisation of the winding pattern for the single strand fibre, or by using a better mateiral for the core sleeve, e.g. high density Al_2O_3 [150, 228].

Chapter 9

Manufacturing process

9.1 Turnbuckle pressure cells

The turnbuckle cells described in Chapter 5, Chapter 6 and Chapter 7 are all made of fully hardened BeCu and they have all been machined using the same techniques. BeCu is a hard material and it is subjected to age-hardening which makes it difficult to machine.

The first prototypes were made using conventional tools. The threads were cut out using the appropriate set of taps and dies, left-hand and right-hand M5×0.5 for and M6×0.5. Threads cut from taps and dies cannot be precisely matched to each other and this is a problem for obtaining the level of accuracy required in the diamond anvil turnbuckle cells. Another difficulty is that in the design of the cell's body the threads of opposite direction are ending up at the centre of the part, very close to one another and this is almost impossible to achieve with taps. For these reasons a more

sophisticated machining method based on a three axis CNC milling technique was chosen.

The various parts of the cells are produced on an XYZ Protrak SMX 3500 [229] except for the internal profile of the end-nuts of the TX-DAC which are machined on an XYZ Proturn ELX 1440 [229] with a style V 35 coated carbide boring bar from WhizCut® [230] , model C3NR V8. One of the advantages of working with the SMX 3500 is that most of the cuts can be machined without having to reposition the part. For instance, on the end-nuts of the TM-DAC, the thread, the recess and the central hole can all be machined at once and this gives a greater accuracy and ensures a perfect concentricity. The threads are cut out with a style single point micro partial profile 60 carbide thread mill tool from WhizCut® [230] model NS0404C10.0 illustrated in Figure 9.1. Standard carbide cutters of appropriate diameter are used for the other features.

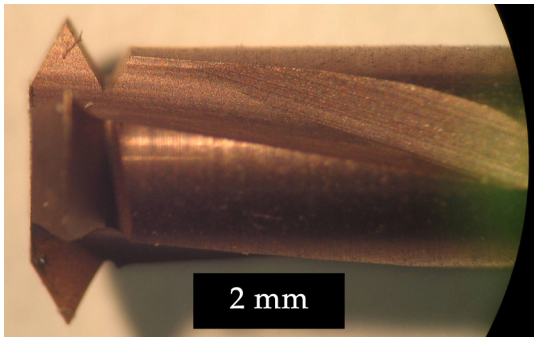

Figure 9.1 Photograph of the solid carbide single point micro partial profile 60 thread mill.

9.2 Composite piston cylinder pressure cell

The composite pressure cell described in more detail in Chapter 8 is composed of three distinct classes of materials. A plastic tube forming the inner bore is reinforced with a composite structure made of Zylon® fiber,

Zylon® fiber fabric and epoxy resin, and the extremities of the cell are metallic.

The plastic tube and the metallic parts, which can be assimilated to specially designed BeCu nuts and bolts, are machined using conventional cutting tools and the M6×1 thread is cut out using taps and dies.

Chapter 10

Conclusions and future directions

The original direction of the research to be done within this project was the design and development of new pressure cells for magnetic property measurements. This has been achieved through the use of turnbuckle design in creating the opposed-anvil TM-DAC and piston-cylinder TM-PCC. Both cells share certain advantages for magnetic property measurements in a SQUID magnetometer. They are fully symmetric with respect to the sample, which generates an integrable SQUID response. They are compact with overall dimensions similar to the standard MPMS sample and sample holder, which aids the magnetic measurement and the rapid temperature equilibration of the pressure cell and the sample. The TM-DAC has been shown to reach pressures of 10 GPa with 800 μm culets while the maximum pressure in TM-PCC approaches 2 GPa with substantially larger sample. Both cells have been used with a number of various materials and demonstrated their usefulness in high-pressure studies of magnetic materials.

The turnbuckle design has also been adapted for low-temperature high-pressure crystallography and use with free-flow cryogenic equipment. The minimalistic design has been used to make the TX-DAC fit under the stream of cold gas in order to reach low sample temperatures without having the ice formed on the surface of the pressure cell. In all turnbuckle designs use of computer-aided design tools such as finite element analysis has been the key proving to be an indispensable tool for optimisation and miniaturisation through the analysis of stresses and deformations in parts and assemblies.

Taking into account the widespread availability of MPMS magnetometers and cryo-flow systems for XRD, these pressure cells have a good commercial potential. Further improvement of the performance can be achieved by making further small adjustments to the design of the existing equipment. For example, a better cooling power for the TX-DAC in a Helix system can be achieved through enlarging the beryllium nozzle of the cryo-cooler in order to enclose the whole pressure cell within it. The talks are on-going with the manufacturer of the equipment (Oxford Instruments).

In terms of the future developments for magnetic property measurements the new pressure cells pave the way for a number of enhanced designs. One of them is the pressure cell that could be used with the iHelium3 insert into the MPMS. This insert is commercially available and can be used to cool samples below 1.85 K which is the limit of the MPMS in its standard configuration down to 0.5 K. However, the diameter of the available space inside the insert is 6 mm, and so any pressure cell that is to be used with it needs to be smaller than that. Of all the existing designs of the pressure cells the turnbuckle one is the only one that has the chance of satisfying the dimensional restrictions through further FEA analysis. Another improvement will be required in terms of the material used in the construction of such pressure cell as most alloys have a strong magnetic background at sub-Kelvin temperatures, and the CuTi(3%) alloy is probably the best candidate material.

Another interesting future development is the design of a fully non-metallic pressure cell for magnetic *ac* susceptibility measurements. This technology is currently not available as all the pressure cells made for magnetic measurements have metallic components around the sample. These components screen the sample from the *ac* field by generating eddy currents. There are two possible directions in which this work can progress. One is to use novel fibre-enforced polymers with the TM-DAC design to make all parts of the cell apart from the anvils. In such materials the fibre distribution is random. This has an advantage of making the material isotropic in terms of its strength and easy to machine, but it does not allow to use the strength of the fibre to its full potential. The other approach is to continue along the lines of the research described in Chapter 8 and to develop methods for making composite parts with directional properties matching the strength of the part to the required distribution and direction of stresses in the individual parts. This would allow to make much stronger parts capable of working to higher loads in high-pressure devices. One of the key challenges to be resolved is the termination of the fibre in such parts. However, once this challenge is resolved this technology could also be used in a number of other applications including the development of pressure cells for use with high pulsed magnetic fields and to a much wider use in high-strength industrial applications of composites.

Appendix A
TM-DAC v3.2 technical drawings

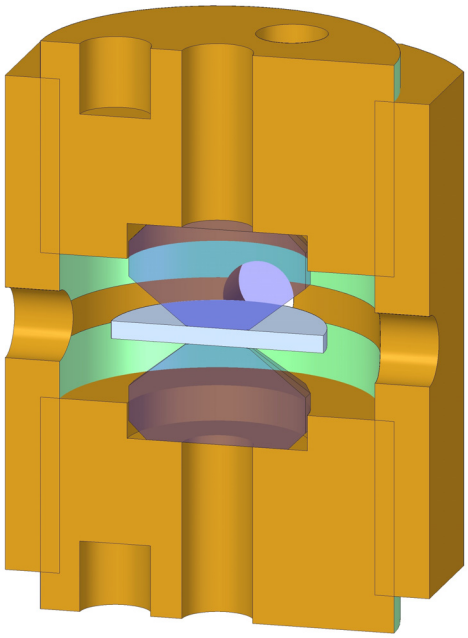

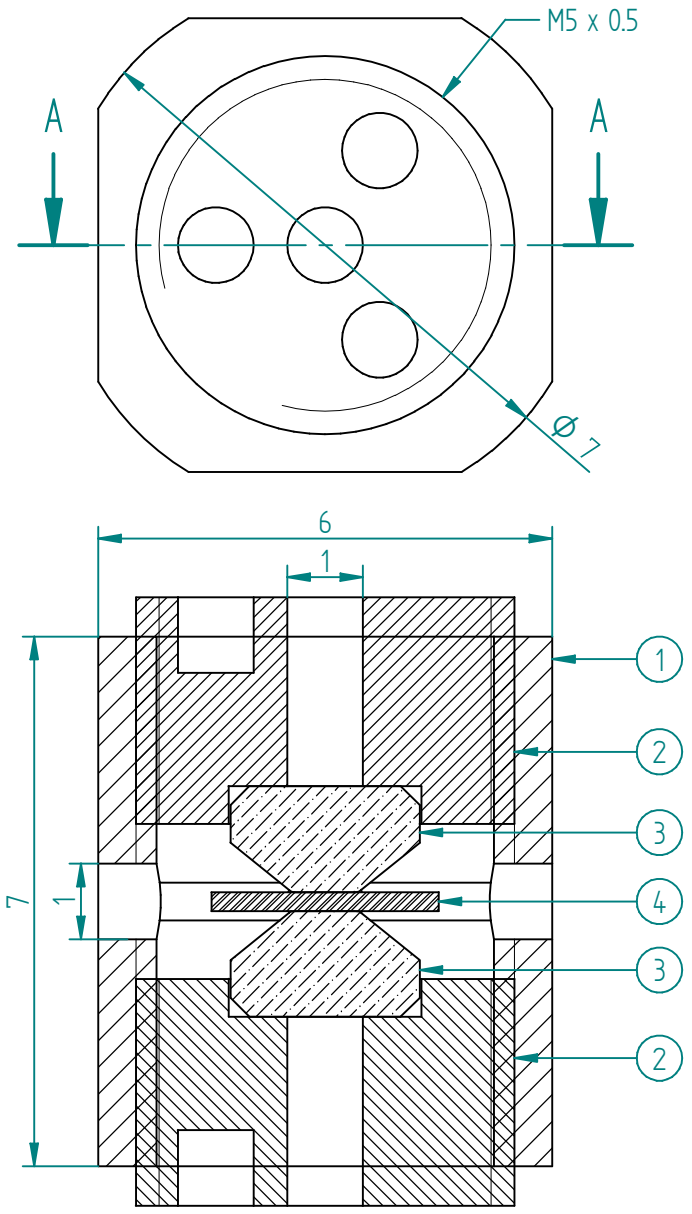

SECTION A–A

Item No.	DWG No.	Title	Material	Quantity
1	TM-D3.1a	Body	BeCu (FHT)	1
2	TM-D3.2a	End-nuts	BeCu (FHT)	2
3	SDD-800	Standard design diamond 800 μm culet	Diamond	2
4	TM-D1.0c	Gasket disk	BeCu (An.)	1

School of Engineering *The University of Edinburgh*		NAME	DATE
	DRAWN	G. Giriat	09/15/11
TITLE: TM-DAC v3.2 Assembly	DWG NO TM-D3.2	SCALE: 10:1	SIZE: A4
	MATERIAL:		

UNLESS OTHERWISE SPECIFIED
DIMENSIONS ARE IN MILLIMETERS
ANGLES ±0.1°
LINEAR DIMENSIONS ±0.01 mm

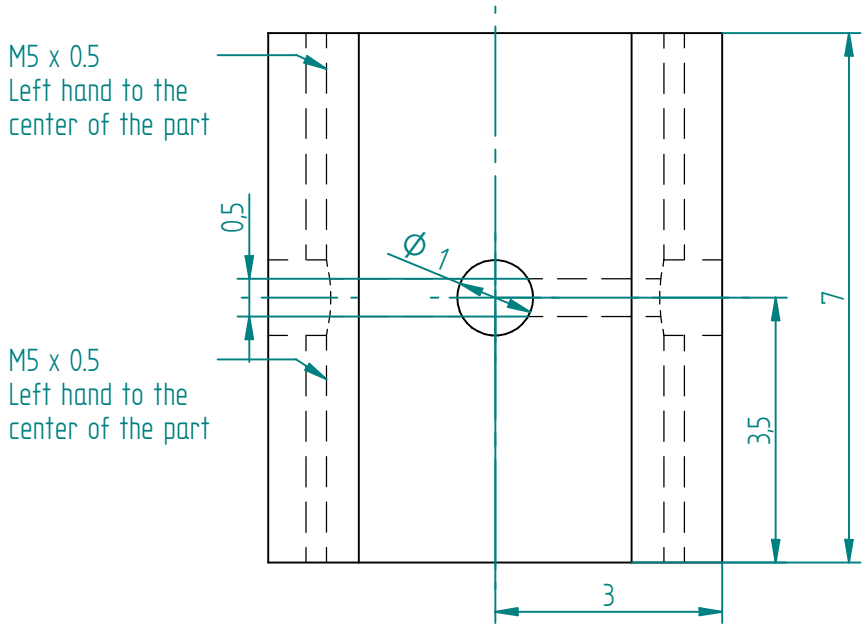

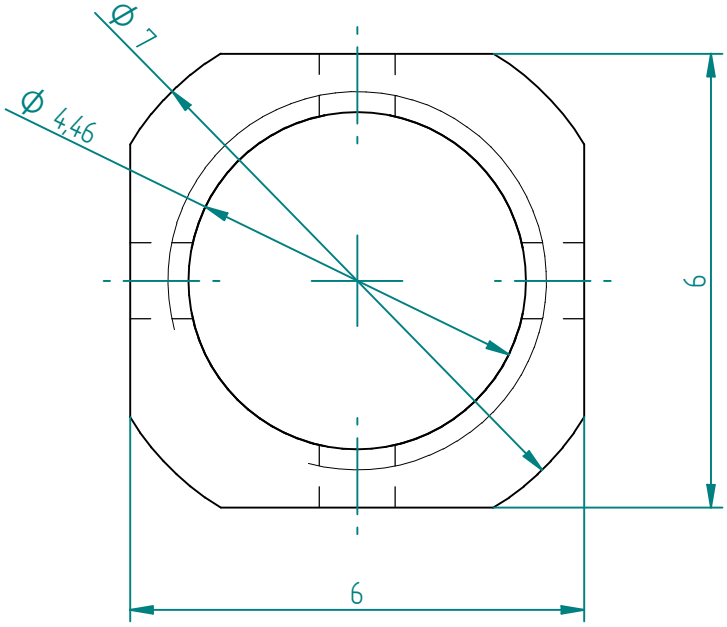

School of Engineering *The University of Edinburgh*		NAME	DATE
	DRAWN	G. Giriat	09/15/11
TITLE: Body	DWG NO TM-D3.1a	SCALE: 10:1	SIZE: A4
	MATERIAL: BeCu (FHT)		

UNLESS OTHERWISE SPECIFIED
DIMENSIONS ARE IN MILLIMETERS
ANGLES ±0.1°
LINEAR DIMENSIONS ±0.01 mm

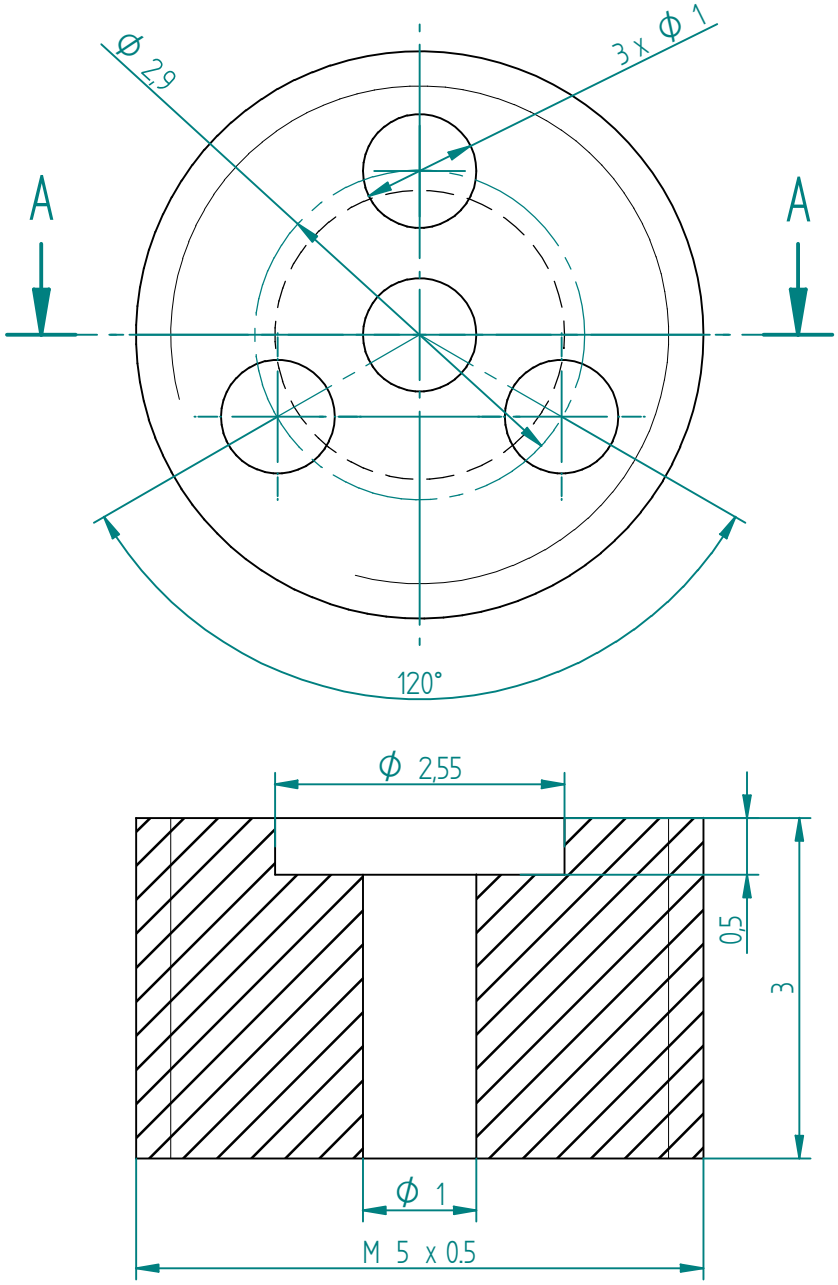

SECTION A-A

1 x M5x0.5 left hand thread
1 x M5x0.5 right hand thread

School of Engineering *The University of Edinburgh*		NAME	DATE	UNLESS OTHERWISE SPECIFIED DIMENSIONS ARE IN MILLIMETERS ANGLES ±0.1° LINEAR DIMENSIONS ±0.01 mm
	DRAWN	G. Giriat	09/15/11	
TITLE: End-nuts	DWG NO TM-D3.2a	SCALE: 15:1	SIZE: A4	
	MATERIAL: BeCu (FHT)			

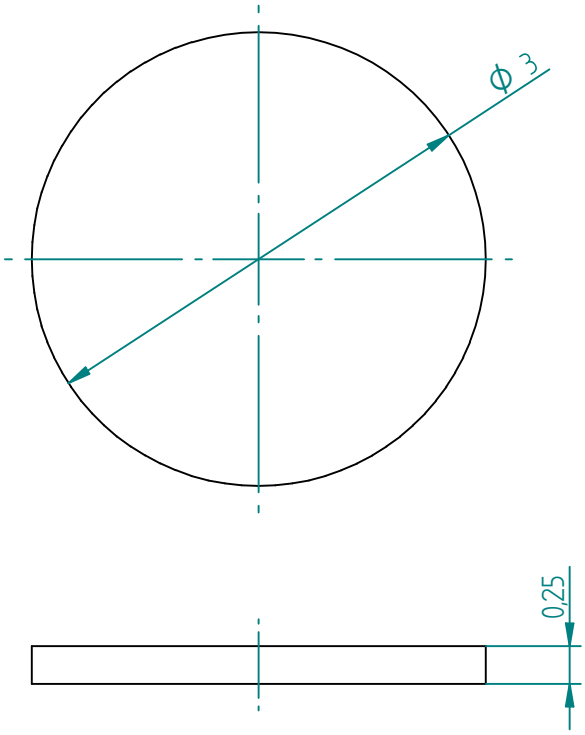

School of Engineering *The University of Edinburgh*		NAME	DATE	UNLESS OTHERWISE SPECIFIED DIMENSIONS ARE IN MILLIMETERS ANGLES ±0.1° LINEAR DIMENSIONS ±0.01 mm
	DRAWN	G. Giriat	09/10/11	
TITLE Gasket disk	DWG NO TM-D1.0c	SCALE: 20:1	SIZE: A4	
	MATERIAL: BeCu (An.)			

Appendix B
TM-PCC v2.0 technical drawings

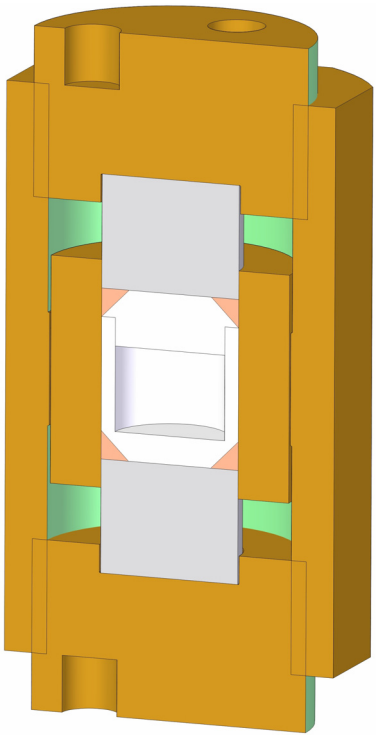

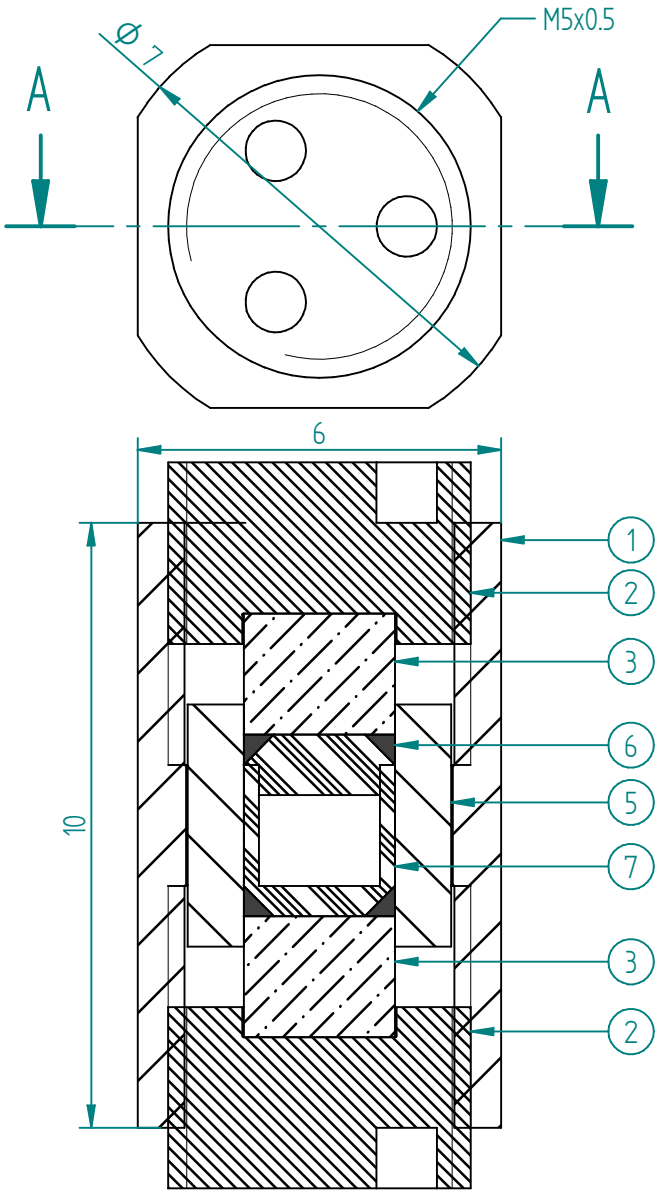

SECTION A-A

Item No.	DWG No.	Title	Material	Quantity
1	TM-PC2.0a	Body	BeCu (FHT)	1
2	TM-PC2.0b	End-nuts	BeCu (FHT)	2
3	PM-PC1.0b	Zirconia piston	Zirconia	2
4	TM-PC1.0c	Copper antiextrusion ring	Copper	2
5	TM-PC2.0c	Inner cylinder	BeCu (FHT)	1
6	PM-PC2.0d	PTFE capsule	PTFE	1

School of Engineering *The University of Edinburgh*		NAME	DATE
	DRAWN	G. Giriat	09/23/11
TITLE: TM-PC v2.0 Assembly	DWG NO TM-PC2.0	SCALE: 8:1	SIZE: A4
	MATERIAL:		

UNLESS OTHERWISE SPECIFIED
DIMENSIONS ARE IN MILLIMETERS
ANGLES ±0.1°
LINEAR DISTANCES ±0.01 mm

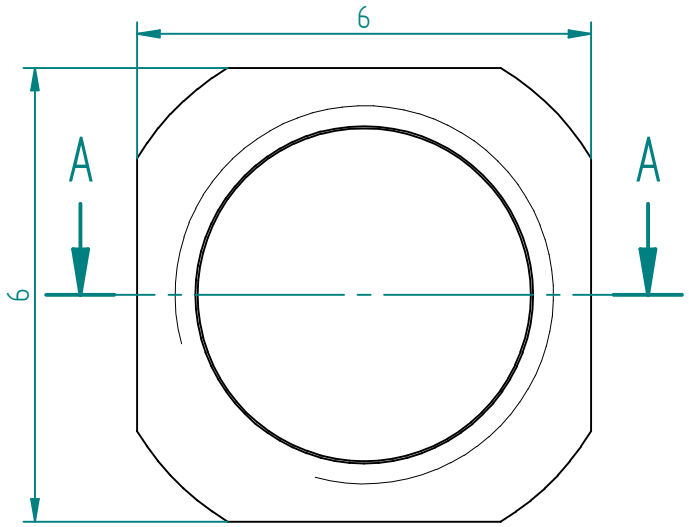

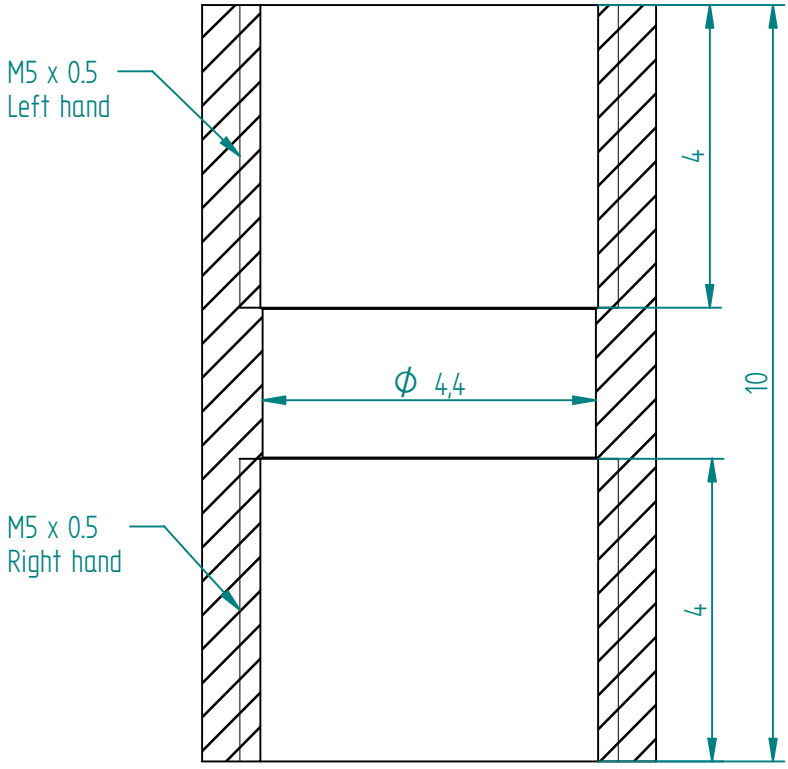

SECTION A–A

School of Engineering *The University of Edinburgh*		NAME	DATE
	DRAWN	G. Giriat	09/24/11
TITLE: Body	DWG NO TM-PC2.0a	SCALE: 10:1	SIZE: A4
	MATERIAL: BeCu (FHT)		

UNLESS OTHERWISE SPECIFIED
DIMENSIONS ARE IN MILLIMETERS
ANGLES ±0.1°
LINEAR DISTANCES ±0.01 mm

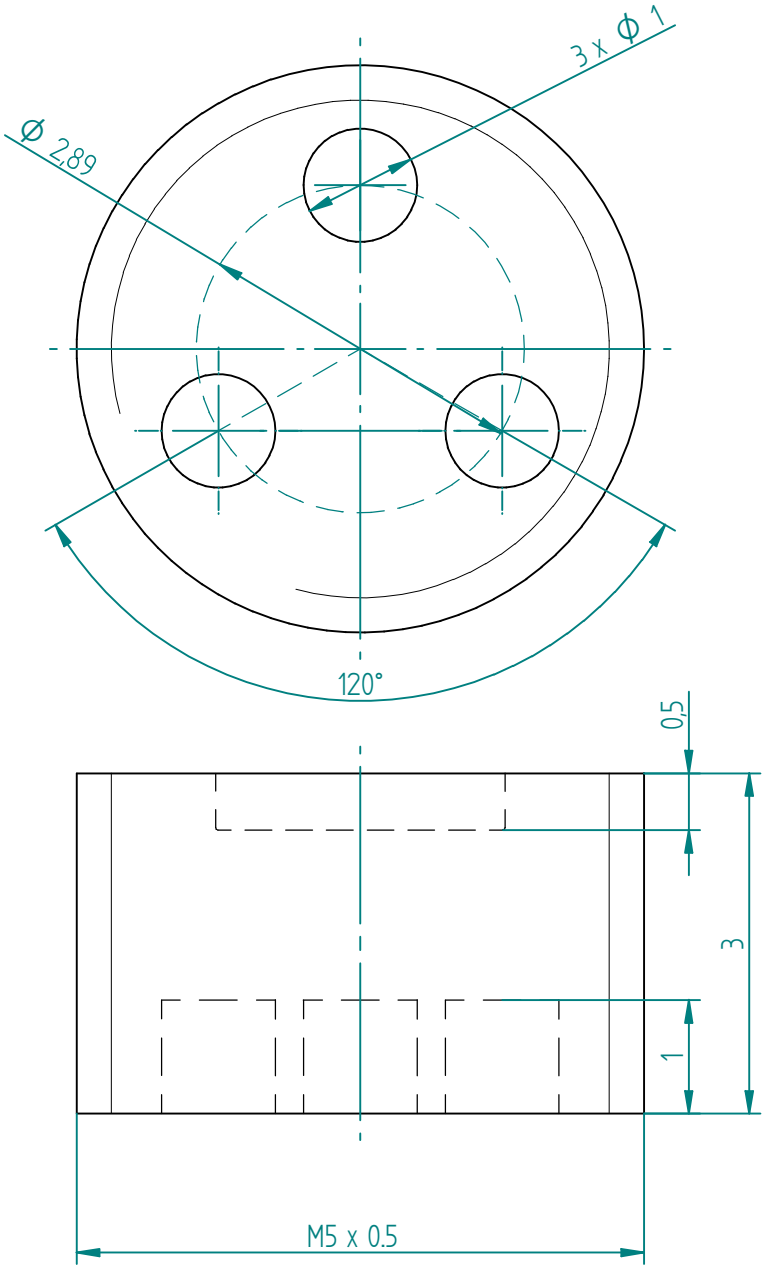

School of Engineering *The University of Edinburgh*		NAME	DATE	UNLESS OTHERWISE SPECIFIED DIMENSIONS ARE IN MILLIMETERS ANGLES ±0.1° LINEAR DISTANCES ±0.01 mm
	DRAWN	G. Giriat	09/24/11	
TITLE End-nuts	DWG NO TM-PC2.0b	SCALE: 15:1	SIZE: A4	
	MATERIAL: BeCu (FHT)			

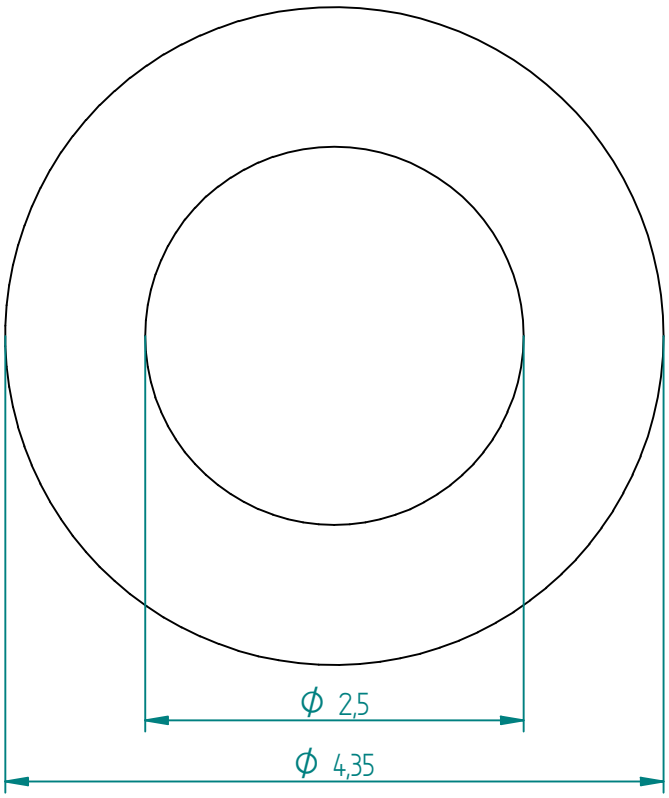

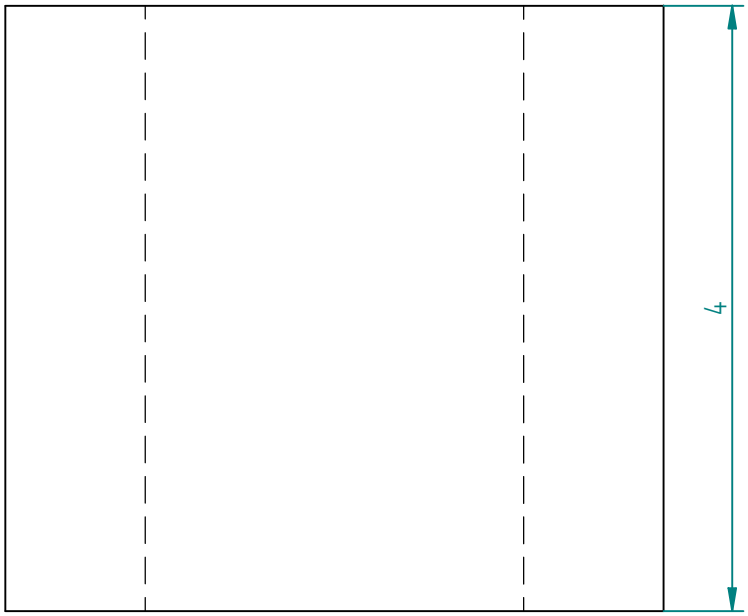

School of Engineering *The University of Edinburgh*		NAME	DATE	UNLESS OTHERWISE SPECIFIED DIMENSIONS ARE IN MILLIMETERS ANGLES ±0.1° LINEAR DISTANCES ±0.01 mm
	DRAWN	G. Giriat	09/24/11	
TITLE: Inner cylinder	DWG NO TM-PC2.0c	SCALE: 20:1	SIZE: A4	
	MATERIAL: BeCu (FHT)			

Section view of the PTFE capsule assembly

Note : Capsule cap and body are machined as drawn below.
The chamfer is done manually afterwards

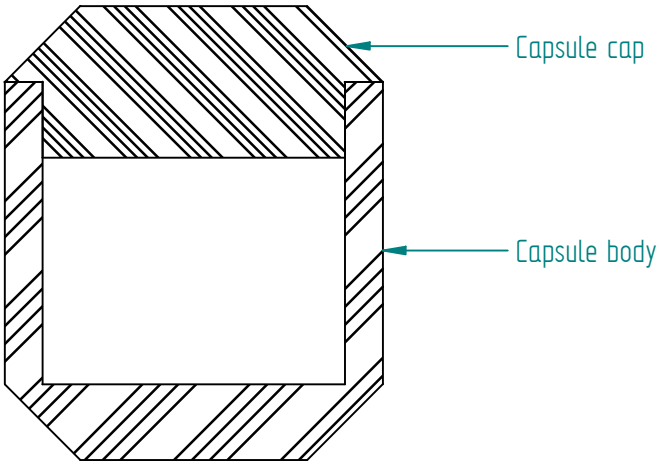

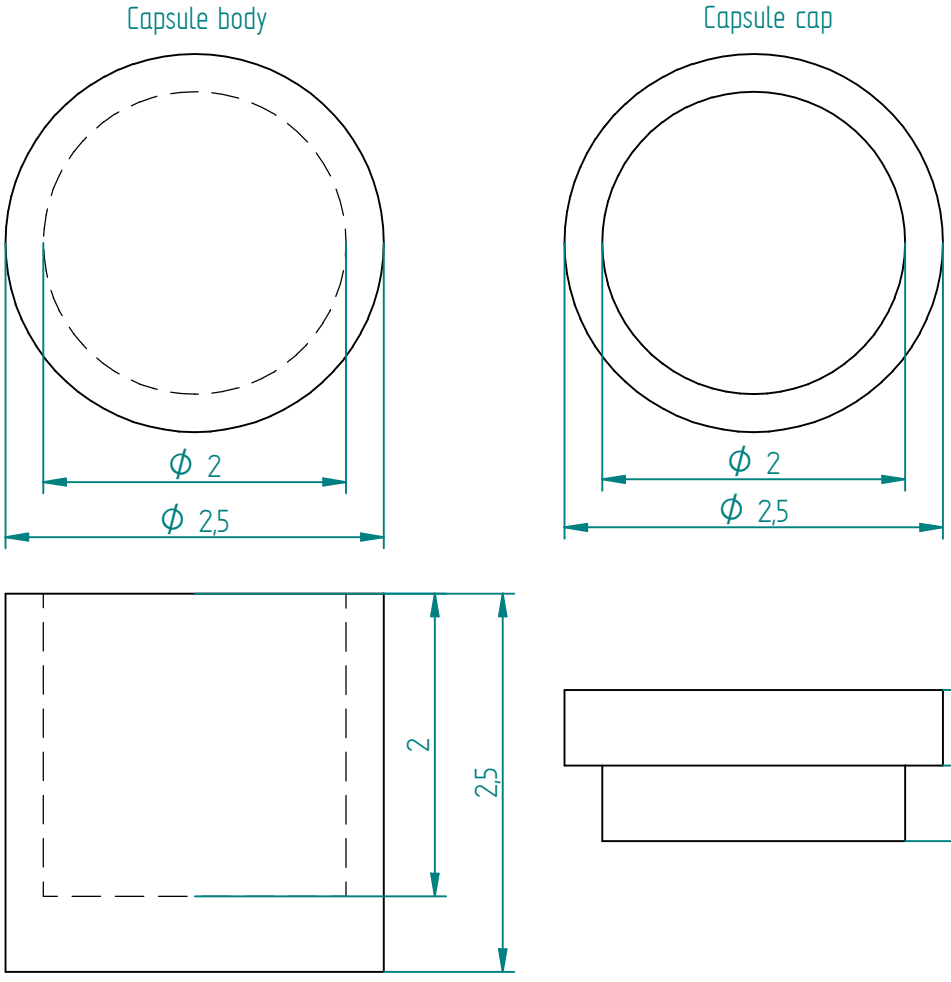

School of Engineering *The University of Edinburgh*		NAME	DATE	UNLESS OTHERWISE SPECIFIED DIMENSIONS ARE IN MILLIMETERS ANGLES ±0.1° LINEAR DISTANCES ±0.01 mm
	DRAWN	G. Giriat	09/24/11	
TITLE PTFE capsule	DWG NO TM-PC2.0d	SCALE: 20:1	SIZE: A4	
	MATERIAL: PTFE			

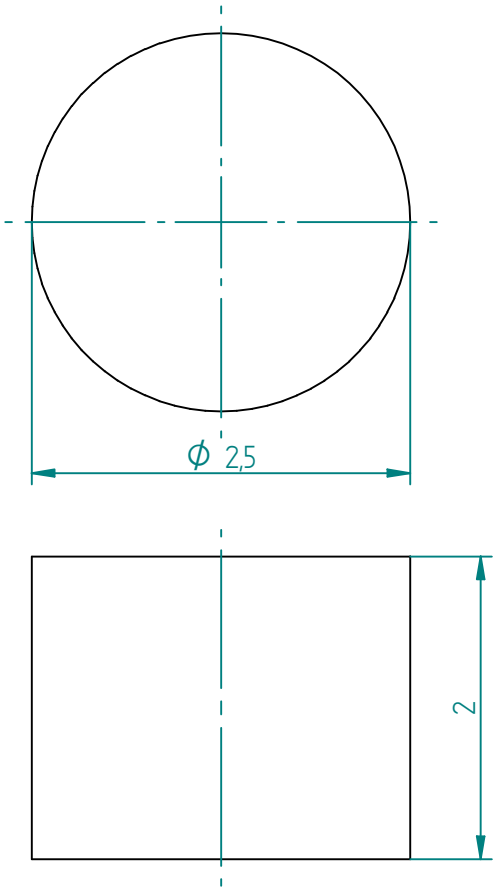

School of Engineering *The University of Edinburgh*		NAME	DATE	UNLESS OTHERWISE SPECIFIED DIMENSIONS ARE IN MILLIMETERS ANGLES ±0.1° LINEAR DISTANCES ±0.01 mm
	DRAWN	G. Giriat	09/23/11	
TITLE: Zirconia piston	DWG NO TM-PC1.0b	SCALE: 20:1	SIZE: A4	
	MATERIAL: Zirconia			

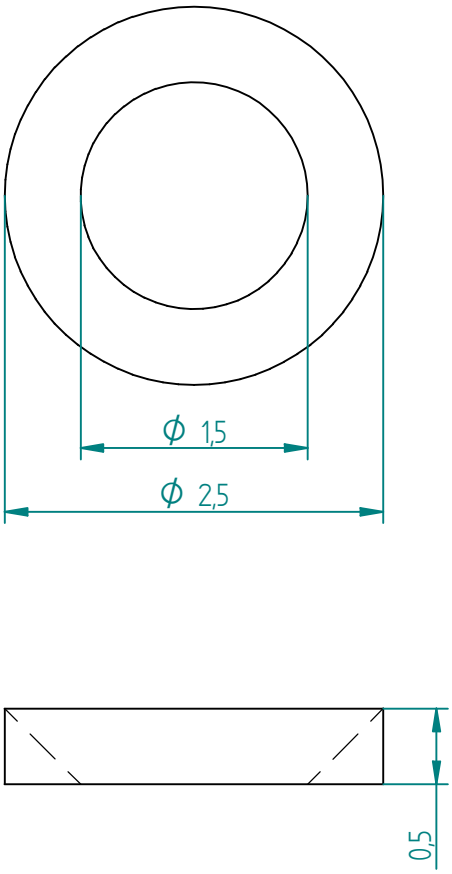

School of Engineering *The University of Edinburgh*		NAME	DATE	UNLESS OTHERWISE SPECIFIED DIMENSIONS ARE IN MILLIMETERS ANGLES ±0.1° LINEAR DISTANCES ±0.01 mm
	DRAWN	G. Giriat	09/23/11	
TITLE: Copper antiextrusion ring	DWG NO TM-PC1.0c	SCALE: 20:1	SIZE: A4	
	MATERIAL: Copper			

Appendix C
TM-DAC and TM-PC clamp devices

technical drawings

Appendix C.1 Gas loading TM-Clamp v1.0

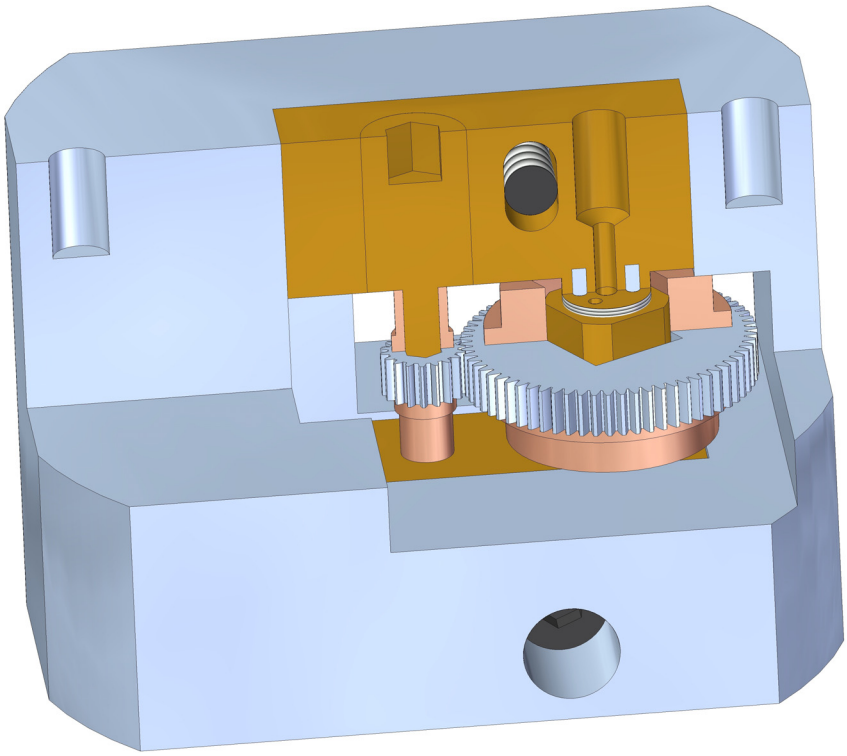

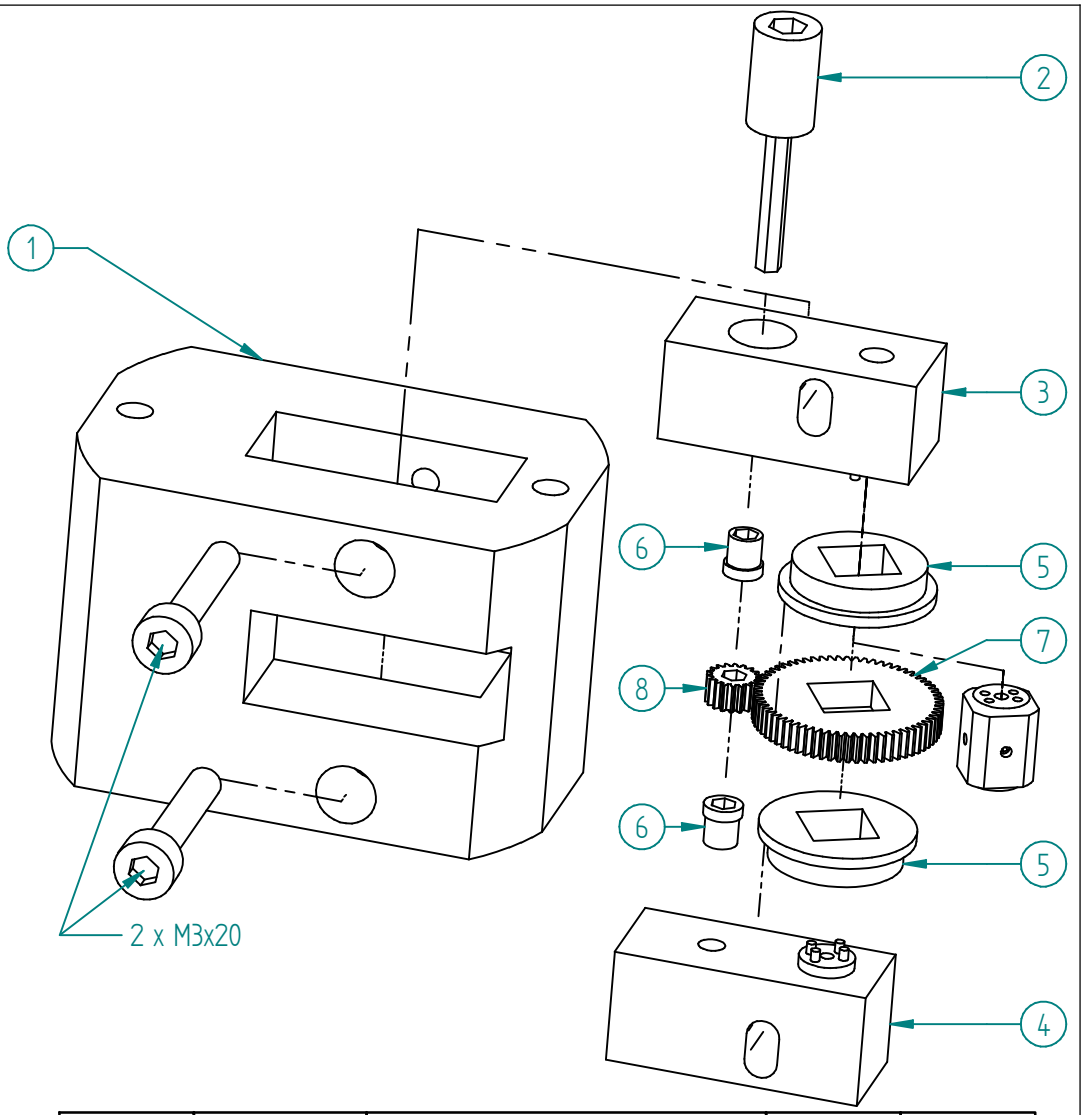

Item No.	DWG No.	Title	Material	Quantity
1	GLTMCl1.0a	Body	Steel	1
2	GLTMCl1.0b	Hexagonal driving shaft	BeCu (FHT)	1
3	GLTMCl1.0c	Short clamp	BeCu (FHT)	1
4	GLTMCl1.0d	Long clamp	BeCu (FHT)	1
5	GLTMCl1.0e	Large spacer	BeCu	2
6	GLTMCl1.0f	Small spacer	BeCu	2
7	GLTMCl1.0g	Gear 64T	S. Steel	1
8	GLTMCl1.0h	Pinion 20T	S. Steel	1

School of Engineering *The University of Edinburgh*		NAME	DATE	UNLESS OTHERWISE SPECIFIED DIMENSIONS ARE IN MILLIMETERS ANGLES ±0.1° LINEAR DISTANCES ±0.01 mm
	DRAWN	G. Giriat	09/22/11	
TITLE: Gas loading TM clamp	DWG NO GLTMCl1.0	SCALE: 1.5:1	SIZE: A4	
	MATERIAL:			

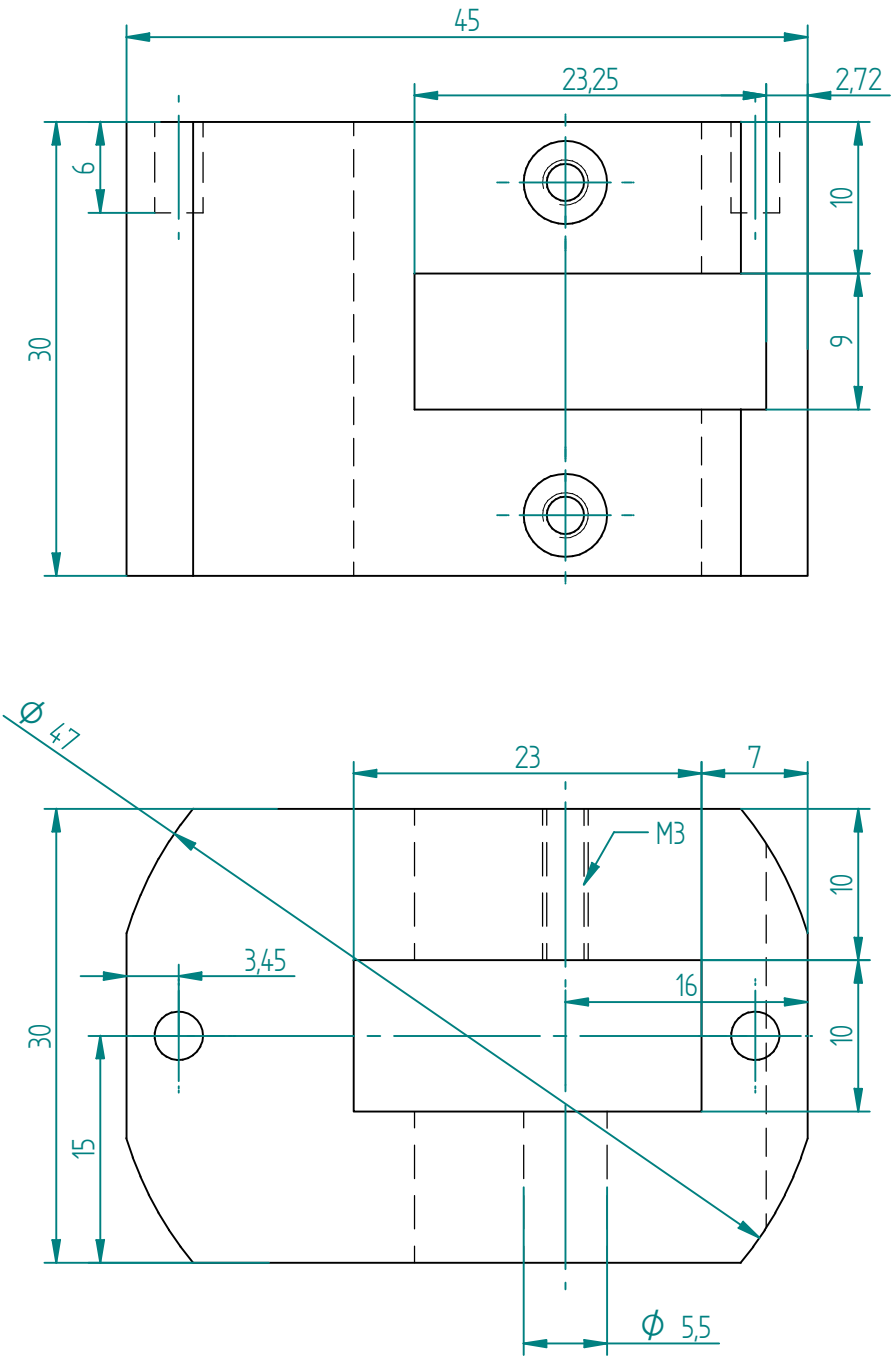

School of Engineering *The University of Edinburgh*		NAME	DATE	UNLESS OTHERWISE SPECIFIED DIMENSIONS ARE IN MILLIMETERS ANGLES ±0.1° LINEAR DISTANCES ±0.01 mm
	DRAWN	G. Giriat	09/22/11	
TITLE: Body	DWG NO GLTMCl1.0a	SCALE: 2:1	SIZE: A4	
	MATERIAL: Steel			

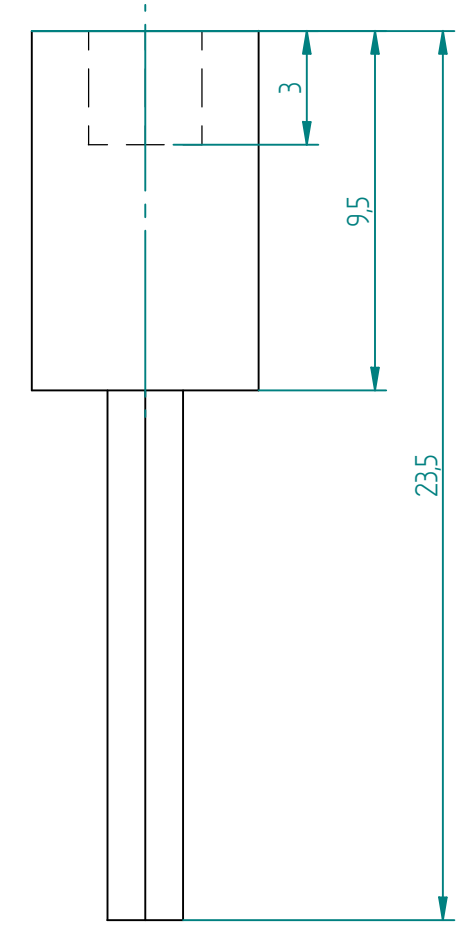

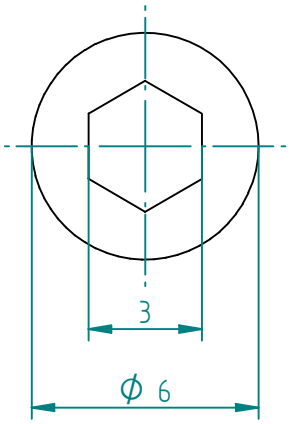

School of Engineering ***The University of Edinburgh***		NAME	DATE	UNLESS OTHERWISE SPECIFIED DIMENSIONS ARE IN MILLIMETERS ANGLES ±0.1° LINEAR DISTANCES ±0.01 mm
	DRAWN	G. Giriat	09/22/11	
TITLE Hexagonal driving shaft	DWG NO GLTMCl1.0b	SCALE: 5:1	SIZE: A4	
	MATERIAL: BeCu (FHT)			

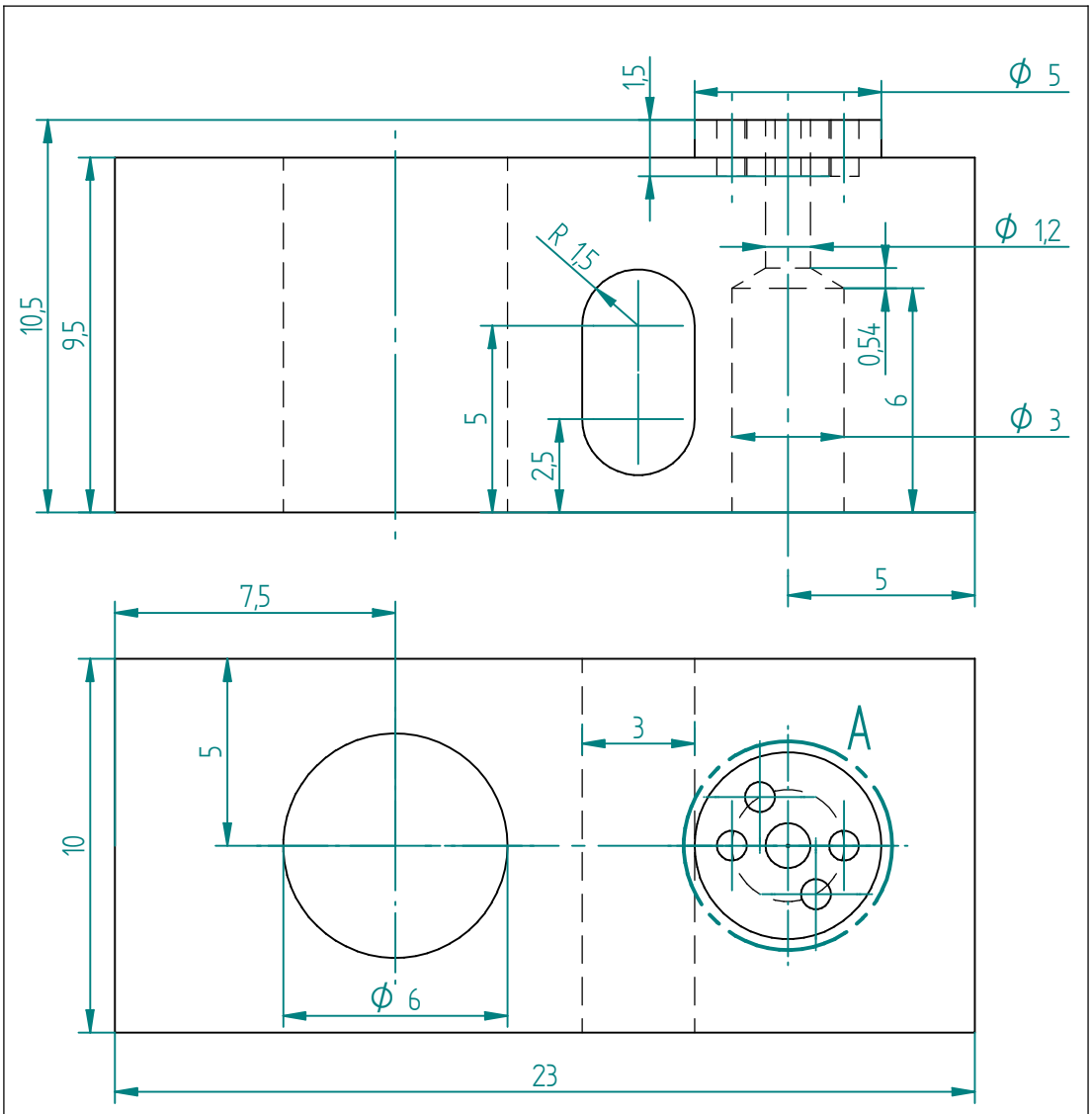

DETAIL A
10:1

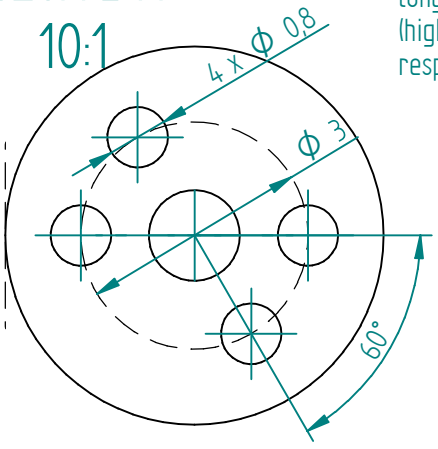

4 rods of 0.8 mm diameter and 3 mm long made by cutting a 0.8 mm drill bit (high speed steel) are pressed into there respectives holes to form the clamp.

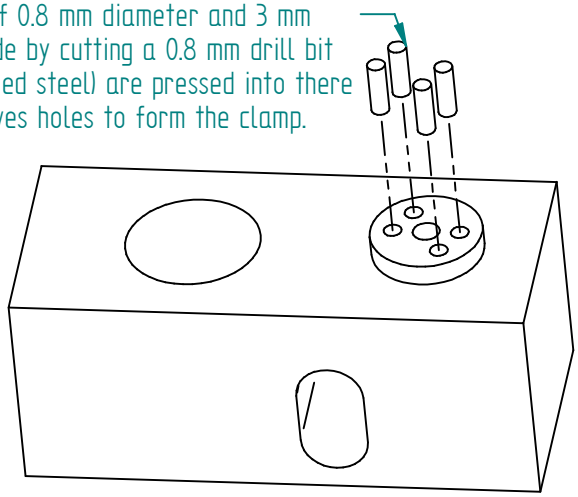

School of Engineering *The University of Edinburgh*		NAME	DATE	UNLESS OTHERWISE SPECIFIED DIMENSIONS ARE IN MILLIMETERS ANGLES ±0.1° LINEAR DISTANCES ±0.01 mm
	DRAWN	G. Giriat	09/22/11	
TITLE Short clamp	DWG NO GLTMCl1.0c	SCALE: 5:1	SIZE: A4	
	MATERIAL: BeCu (FHT)			

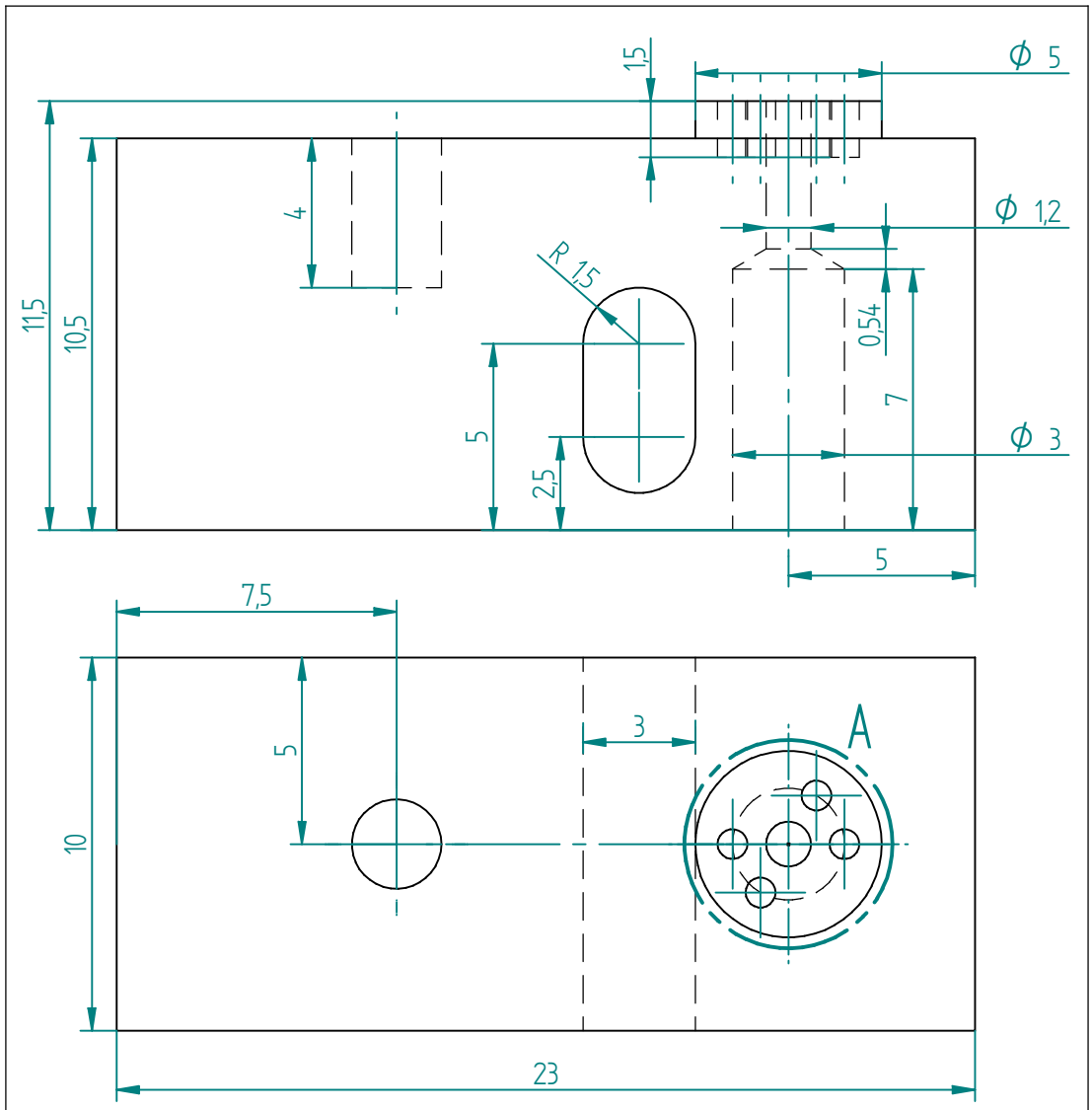

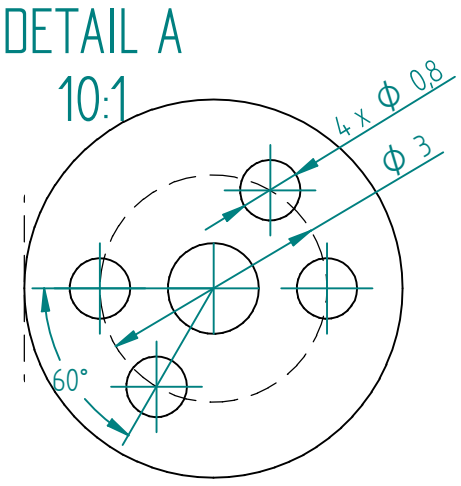

4 rods of 0.8 mm diameter and 3 mm long made by cutting a 0.8 mm drill bit (high speed steel) are pressed into there respectives holes to form the clamp.

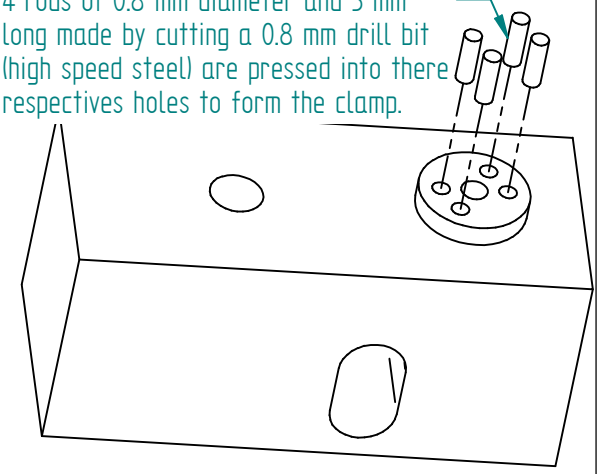

School of Engineering *The University of Edinburgh*		NAME	DATE	UNLESS OTHERWISE SPECIFIED DIMENSIONS ARE IN MILLIMETERS ANGLES ±0.1° LINEAR DISTANCES ±0.01 mm
	DRAWN	G. Giriat	09/22/11	
TITLE Long clamp	DWG NO GLTMCl1.0d	SCALE: 5:1	SIZE: A4	
	MATERIAL: BeCu (FHT)			

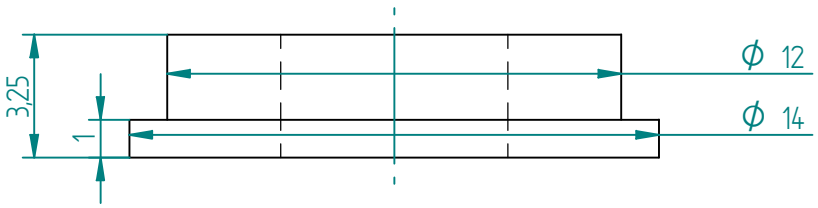

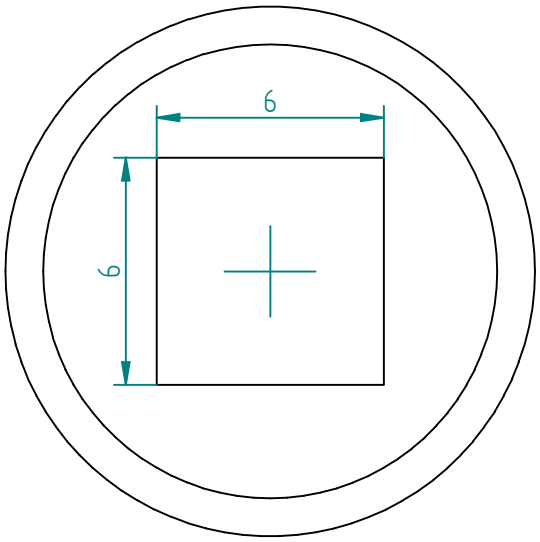

School of Engineering *The University of Edinburgh*		NAME	DATE	UNLESS OTHERWISE SPECIFIED DIMENSIONS ARE IN MILLIMETERS ANGLES ±0.1° LINEAR DISTANCES ±0.01 mm
	DRAWN	G. Giriat	09/22/11	
TITLE: Large spacer	DWG NO GLTMCl1.0e	SCALE: 5:1	SIZE: A4	
	MATERIAL: BeCu			

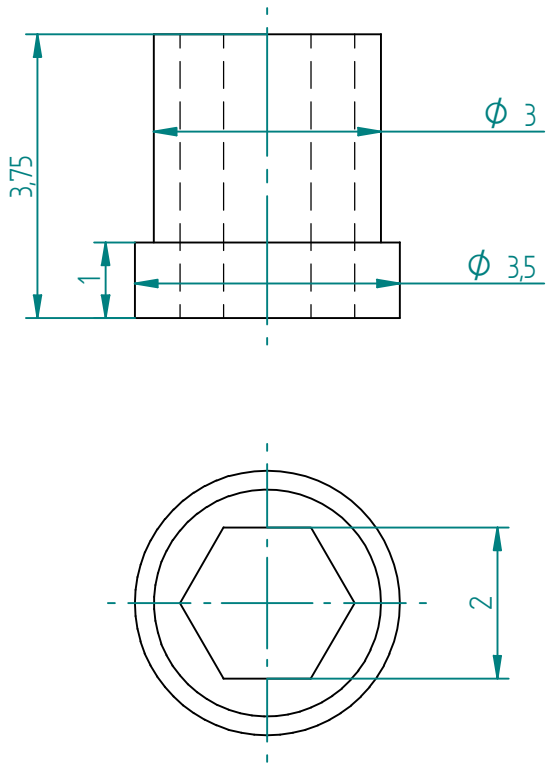

School of Engineering *The University of Edinburgh*		NAME	DATE	UNLESS OTHERWISE SPECIFIED DIMENSIONS ARE IN MILLIMETERS ANGLES ±0.1° LINEAR DISTANCES ±0.01 mm
	DRAWN	G. Giriat	09/22/11	
TITLE: Small spacer	DWG NO GLTMCl1.0f	SCALE: 10:1	SIZE: A4	
	MATERIAL: BeCu			

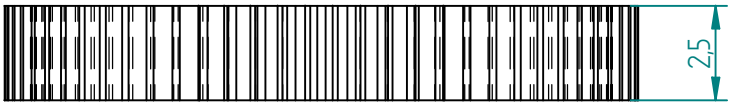

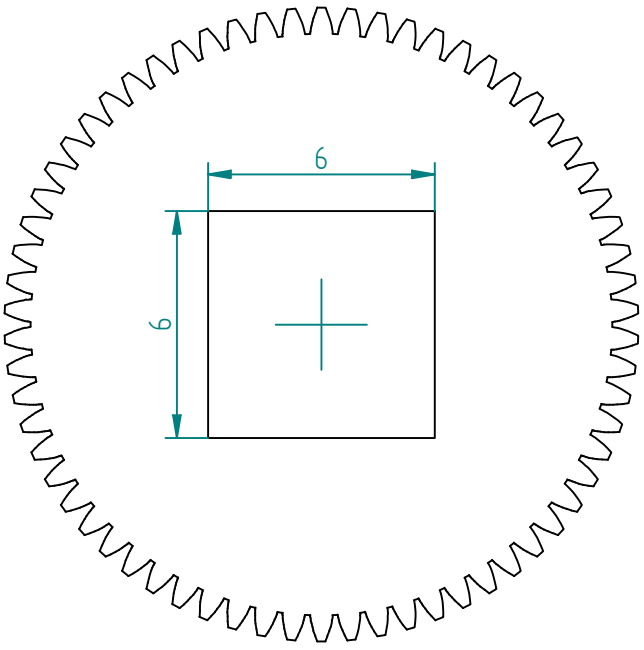

Gear from HPC Gears.
The square cut out is to be machined.

School of Engineering *The University of Edinburgh*		NAME	DATE	UNLESS OTHERWISE SPECIFIED DIMENSIONS ARE IN MILLIMETERS ANGLES ±0.1° LINEAR DISTANCES ±0.01 mm
	DRAWN	G. Giriat	09/22/11	
TITLE Gear 64T	DWG NO GLTMCl1.0g	SCALE: 5:1	SIZE: A4	
	MATERIAL: Stainless Steel 303S21			

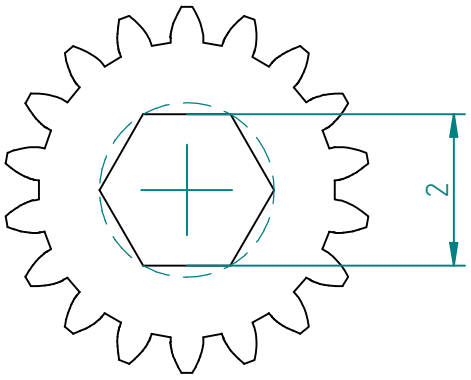

Pinion from HPC Gears.
The hexagonal cut out is to be machined.

School of Engineering *The University of Edinburgh*		NAME	DATE	UNLESS OTHERWISE SPECIFIED DIMENSIONS ARE IN MILLIMETERS ANGLES ±0.1° LINEAR DISTANCES ±0.01 mm
	DRAWN	G. Giriat	09/22/11	
TITLE Pinion 20T	DWG NO GLTMCl1.0h	SCALE: 10:1	SIZE: A4	
	MATERIAL: Stainless Steel 303S21			

Appendix C.2 TM-Clamp v2.0

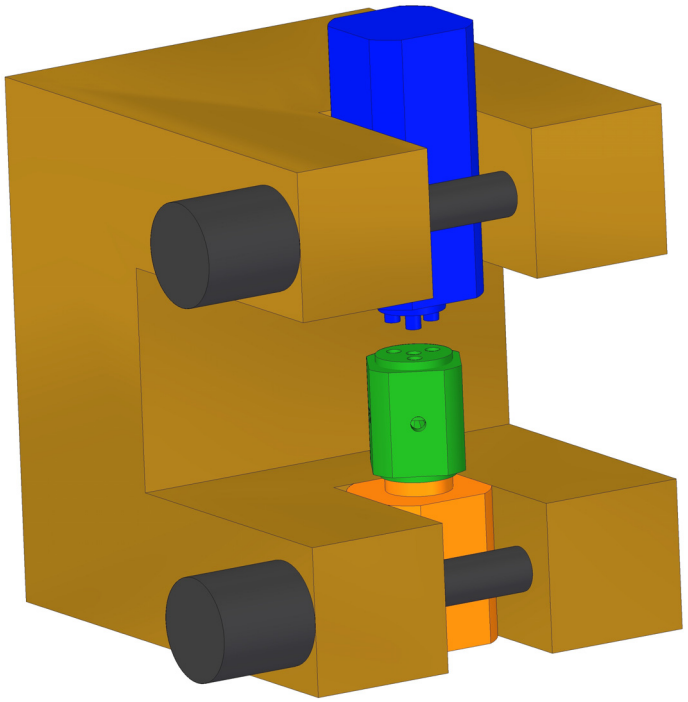

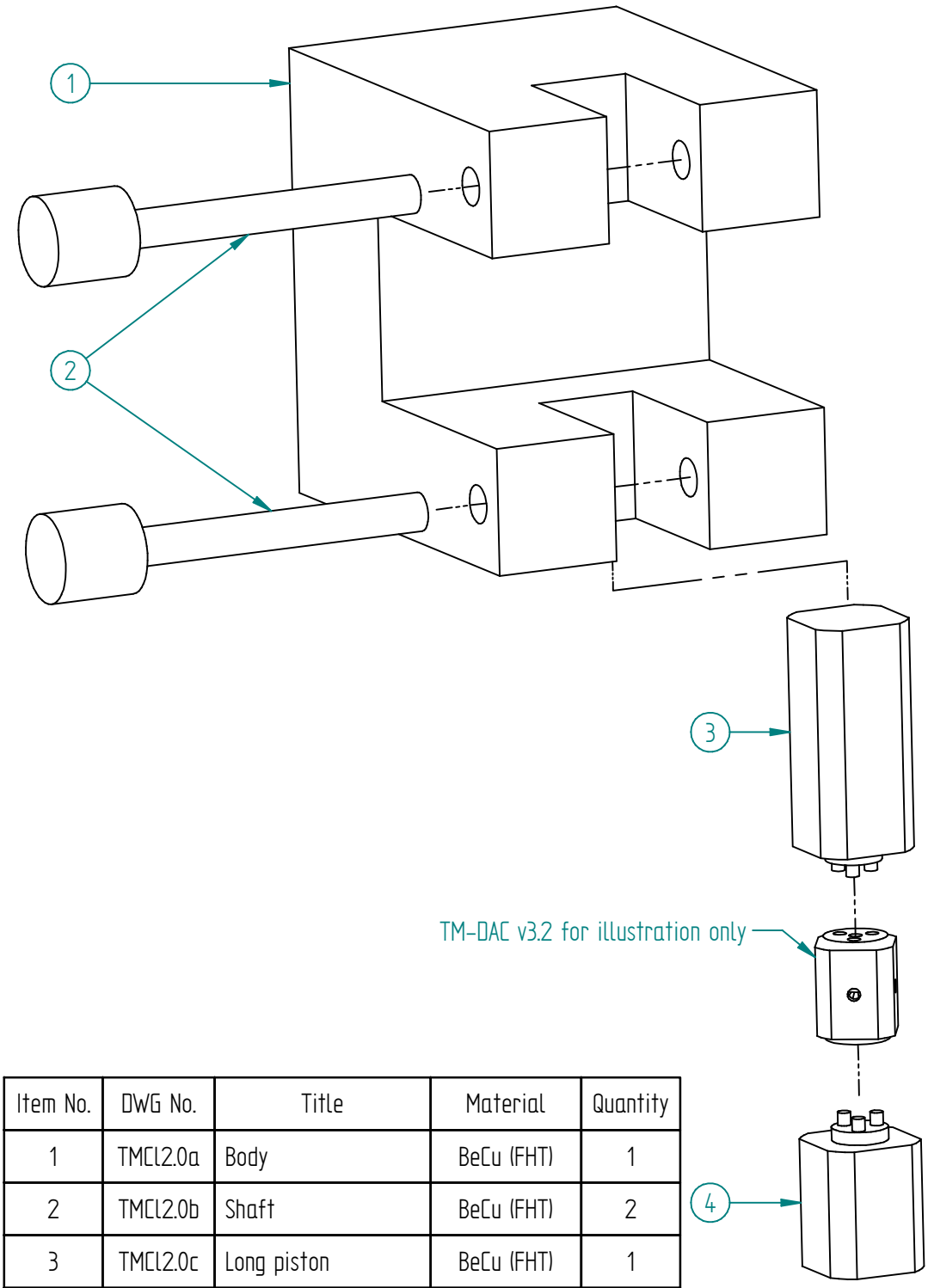

Item No.	DWG No.	Title	Material	Quantity
1	TMCl2.0a	Body	BeCu (FHT)	1
2	TMCl2.0b	Shaft	BeCu (FHT)	2
3	TMCl2.0c	Long piston	BeCu (FHT)	1
4	TMCl2.0d	Short piston	BeCu (FHT)	1

School of Engineering *The University of Edinburgh*		NAME	DATE
	DRAWN	G. Giriat	09/21/11
TITLE: TM clamp Assembly	DWG NO TMCl2.0	SCALE: 2:1	SIZE: A4
	MATERIAL:		

UNLESS OTHERWISE SPECIFIED
DIMENSIONS ARE IN MILLIMETERS
ANGLES ±0.1°
LINEAR DISTANCES ±0.01 mm

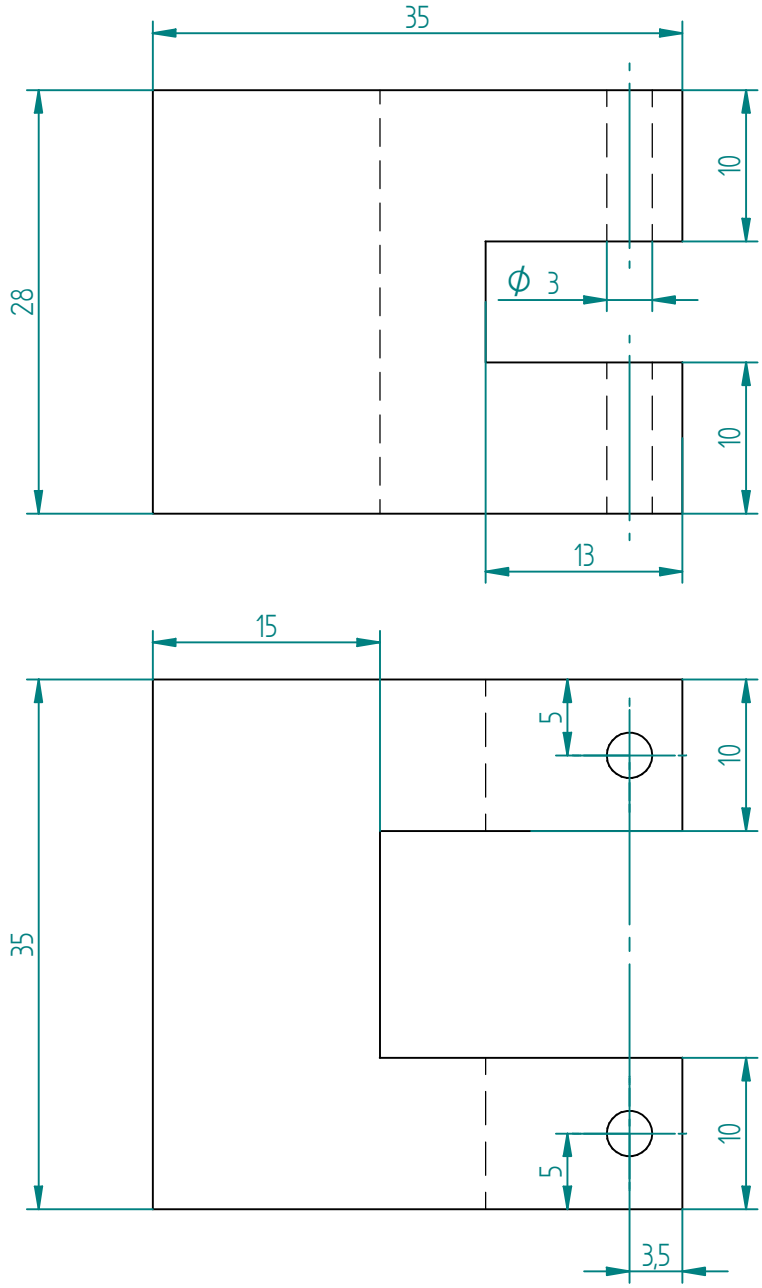

School of Engineering *The University of Edinburgh*		NAME	DATE	UNLESS OTHERWISE SPECIFIED DIMENSIONS ARE IN MILLIMETERS ANGLES ±0.1° LINEAR DISTANCES ±0.01 mm
TITLE Body	DRAWN	G. Giriat	09/20/11	
	DWG NO TMCL2.0a	SCALE: 2:1	SIZE: A4	
	MATERIAL: BeCu (FHT)			

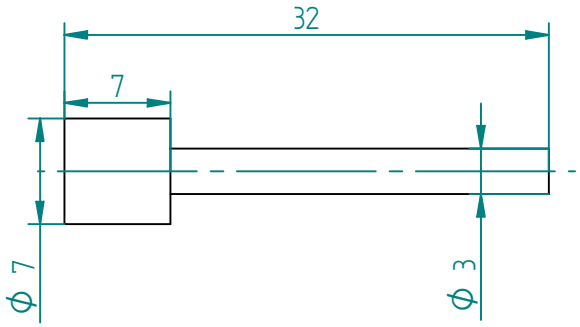

School of Engineering *The University of Edinburgh*		NAME	DATE	UNLESS OTHERWISE SPECIFIED DIMENSIONS ARE IN MILLIMETERS ANGLES ±0.1° DISTANCES ±0.01 mm
	DRAWN	G. Giriat	09/20/11	
TITLE Shaft	DWG NO TMCl2.0b	SCALE: 2:1	SIZE: A4	
	MATERIAL: BeCu (FHT)			

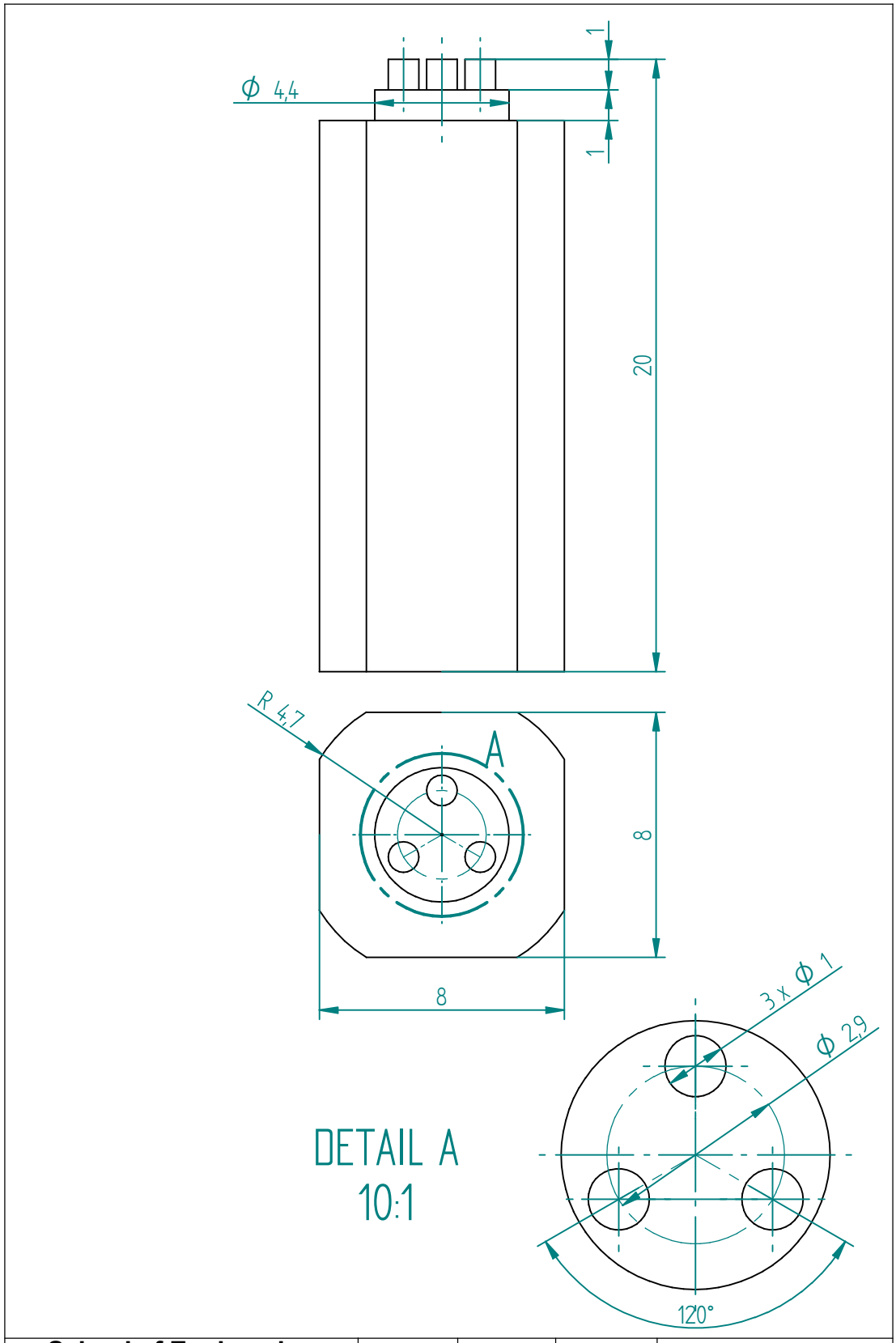

School of Engineering *The University of Edinburgh*		NAME	DATE	UNLESS OTHERWISE SPECIFIED DIMENSIONS ARE IN MILLIMETERS ANGLES ±0.1° LINEAR DISTANCES ±0.01 mm
	DRAWN	G. Giriat	09/20/11	
TITLE Long piston	DWG NO TMCl2.0c	SCALE: 5:1	SIZE: A4	
	MATERIAL: BeCu (FHT)			

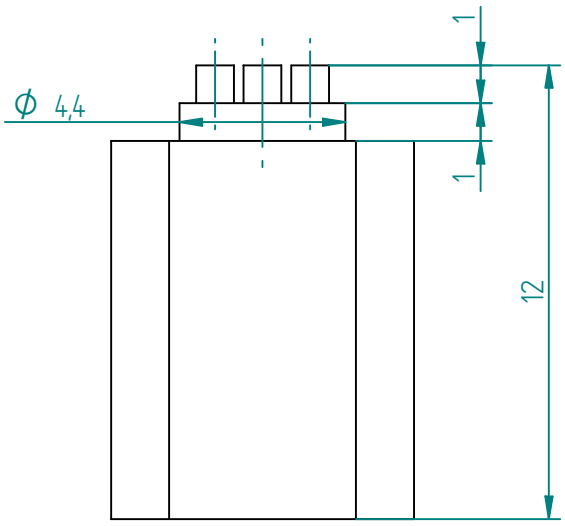

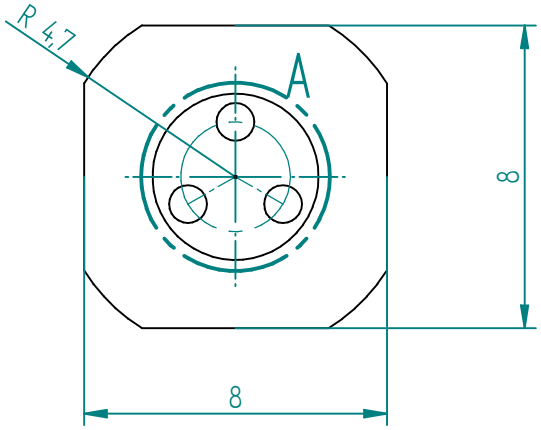

DETAIL A
10:1

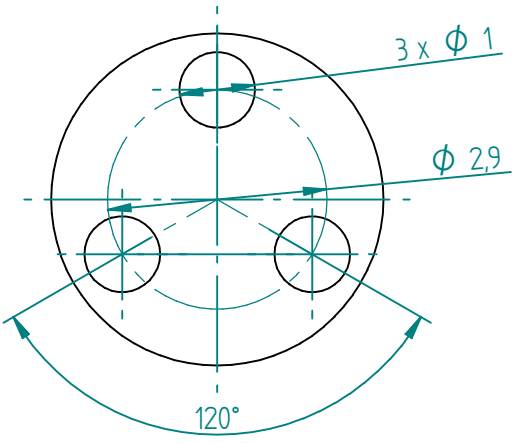

School of Engineering *The University of Edinburgh*		NAME	DATE	UNLESS OTHERWISE SPECIFIED DIMENSIONS ARE IN MILLIMETERS ANGLES ±0.1° LINEAR DISTANCES ±0.01 mm
	DRAWN	G. Giriat	09/20/11	
TITLE Short piston	DWG NO TMCL2.0d	SCALE: 5:1	SIZE: A4	
	MATERIAL: BeCu (FHT)			

Appendix D
TX-DAC v3.0 technical drawings

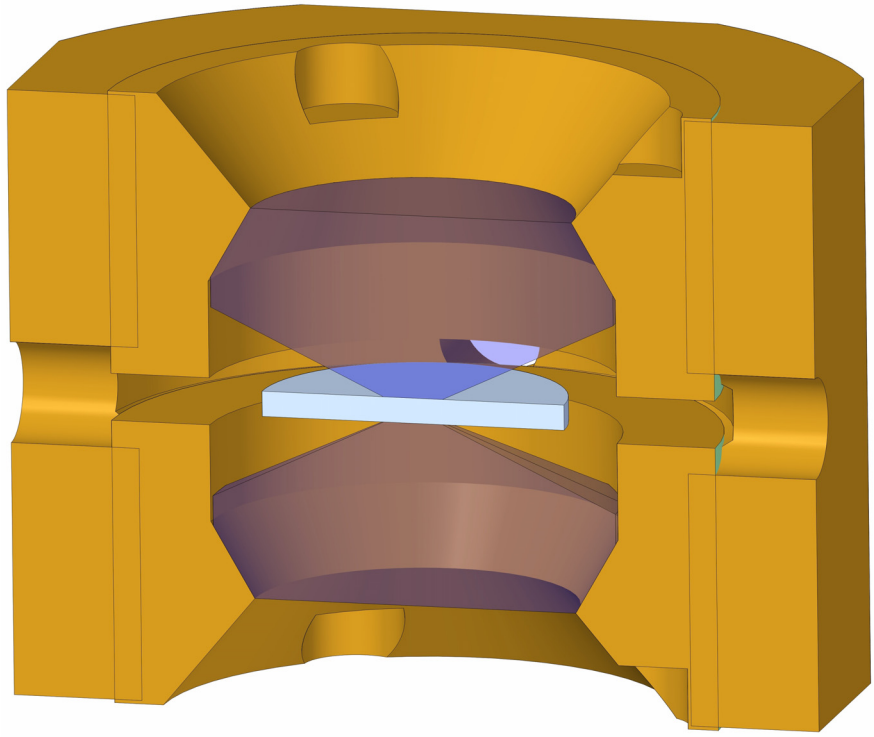

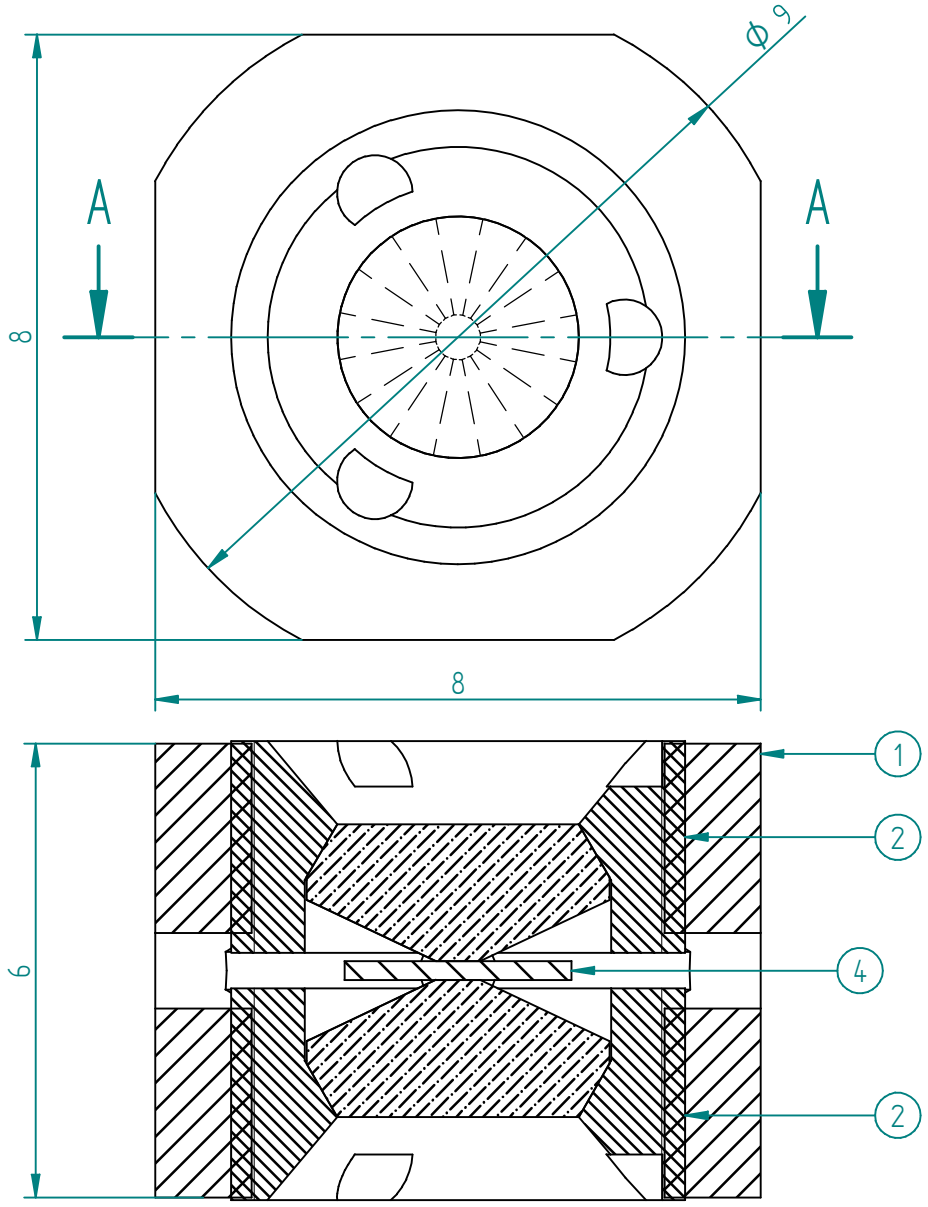

SECTION A–A

Item No.	DWG No.	Title	Material	Quantity
1	TX-D3.0a	Body	BeCu (FHT)	1
2	TX-D3.0b	End-nuts	BeCu (FHT)	2
3	BAD-600c	Boehler Almax design diamond 600 μm culet	Diamond	2
4	TX-D1.0c	Gasket disk	S. Steel	1

School of Engineering *The University of Edinburgh*		NAME	DATE
	DRAWN	G. Giriat	09/24/11
TITLE: TX-DAC v3.0 Assembly	DWG NO TX-D3.0	SCALE: 10:1	SIZE: A4
	MATERIAL:		

UNLESS OTHERWISE SPECIFIED
DIMENSIONS ARE IN MILLIMETERS
ANGLES ±0.1°
LINEAR DISTANCES ±0.01 mm

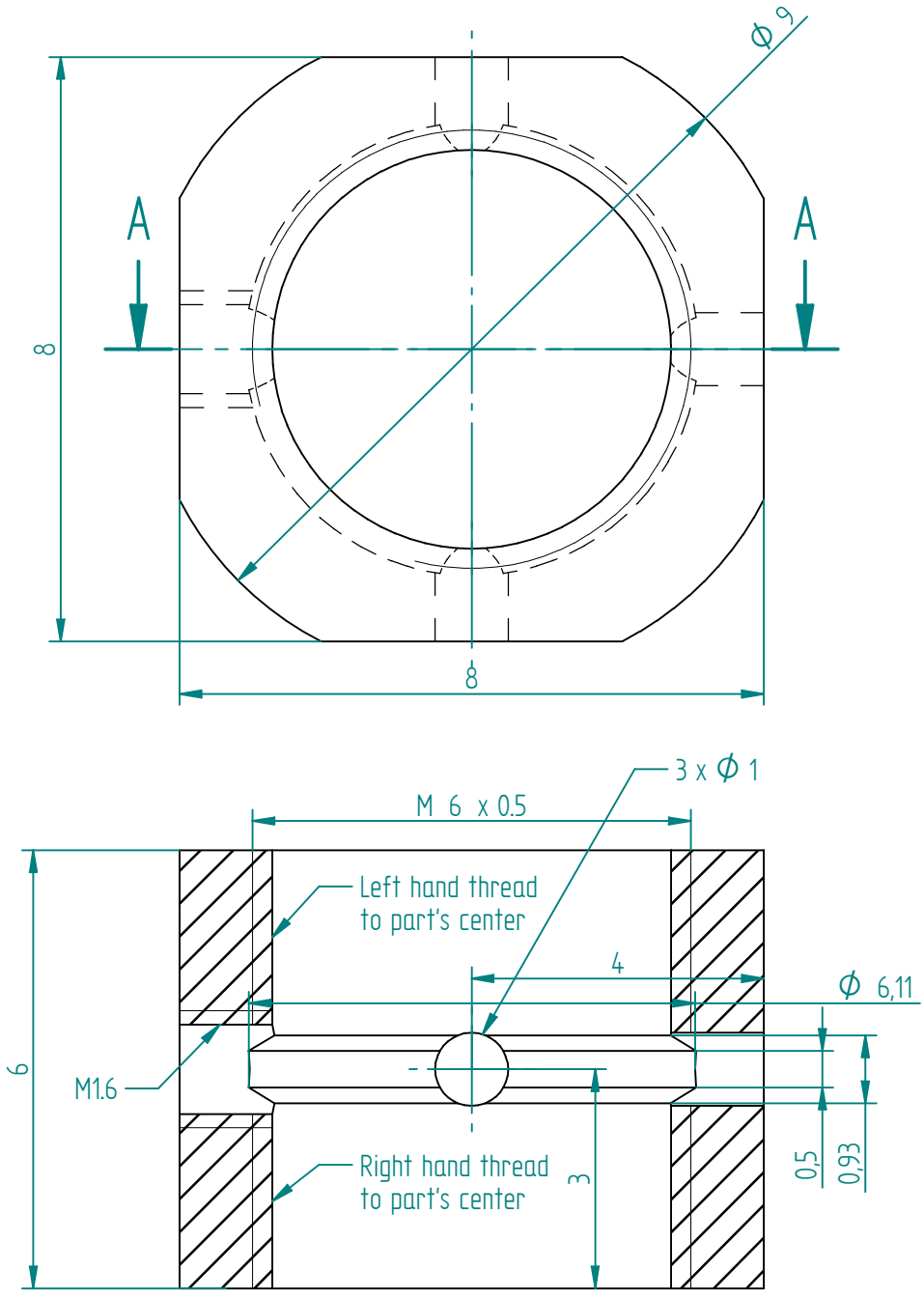

SECTION A–A

School of Engineering *The University of Edinburgh*		NAME	DATE	UNLESS OTHERWISE SPECIFIED DIMENSIONS ARE IN MILLIMETERS ANGLES ±0.1° LINEAR DISTANCES ±0.01 mm
	DRAWN	G. Giriat	09/24/11	
TITLE Body	DWG NO TX-D3.0a	SCALE: 10:1	SIZE: A4	
	MATERIAL: BeCu (FHT)			

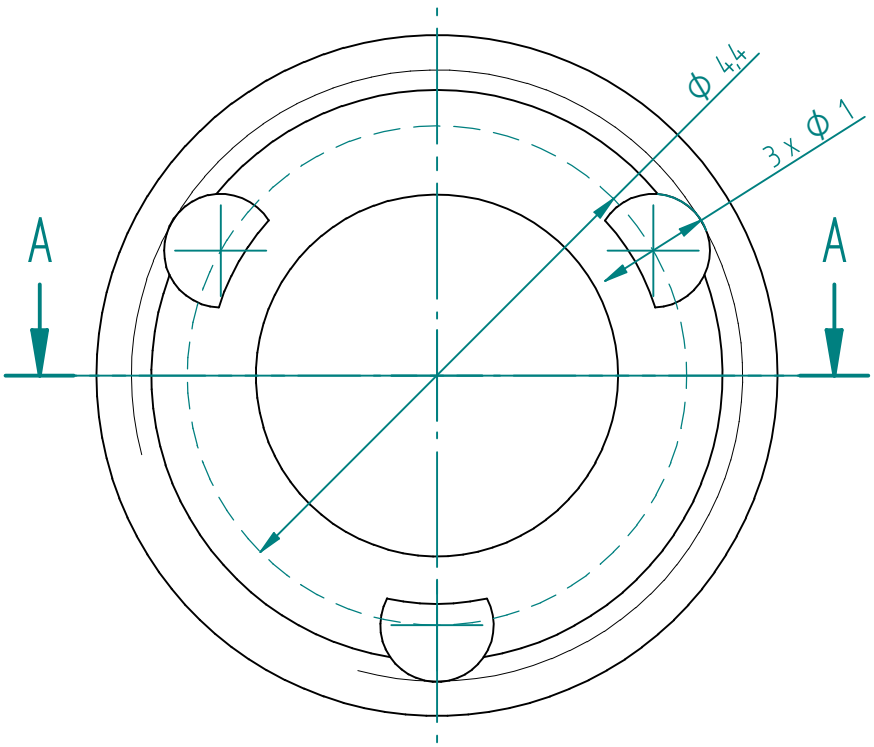

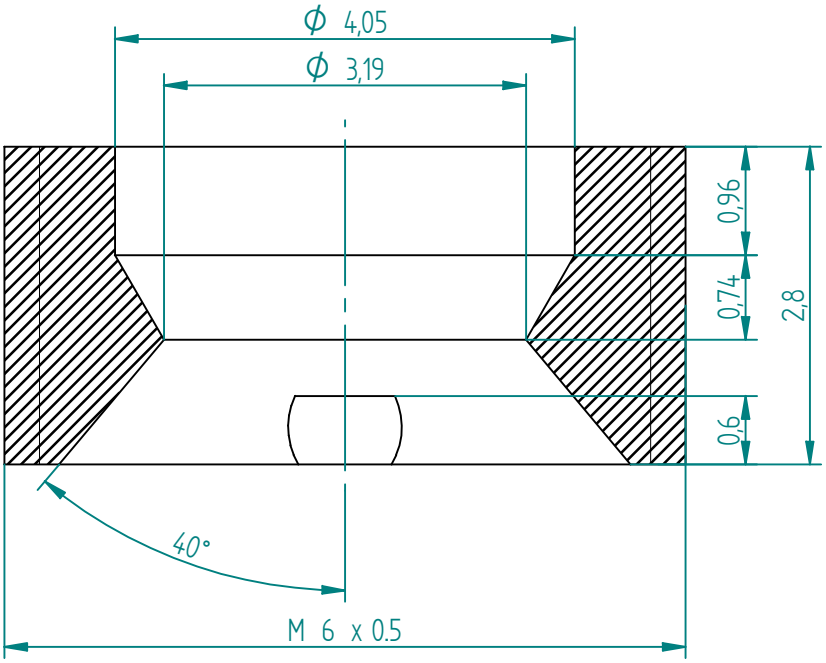

SECTION A-A

1 x M5x0.5 left hand thread
1 x M5x0.5 right hand thread

School of Engineering *The University of Edinburgh*		NAME	DATE	UNLESS OTHERWISE SPECIFIED DIMENSIONS ARE IN MILLIMETERS ANGLES ±0.1° LINEAR DISTANCES ±0.01 mm
	DRAWN	G. Giriat	09/24/11	
TITLE End-nuts	DWG NO TX-D3.0b	SCALE: 15:1	SIZE: A4	
	MATERIAL: BeCu (FHT)			

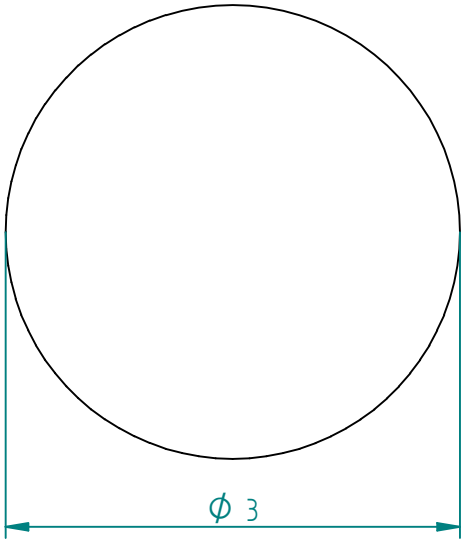

School of Engineering *The University of Edinburgh*		NAME	DATE	UNLESS OTHERWISE SPECIFIED DIMENSIONS ARE IN MILLIMETERS ANGLES ±0.1° LINEAR DISTANCES ±0.01 mm
	DRAWN	G. Giriat	09/24/11	
TITLE: Gasket disk	DWG NO TX-D1.0c	SCALE: 20:1	SIZE: A4	
	MATERIAL: Stainless steel			

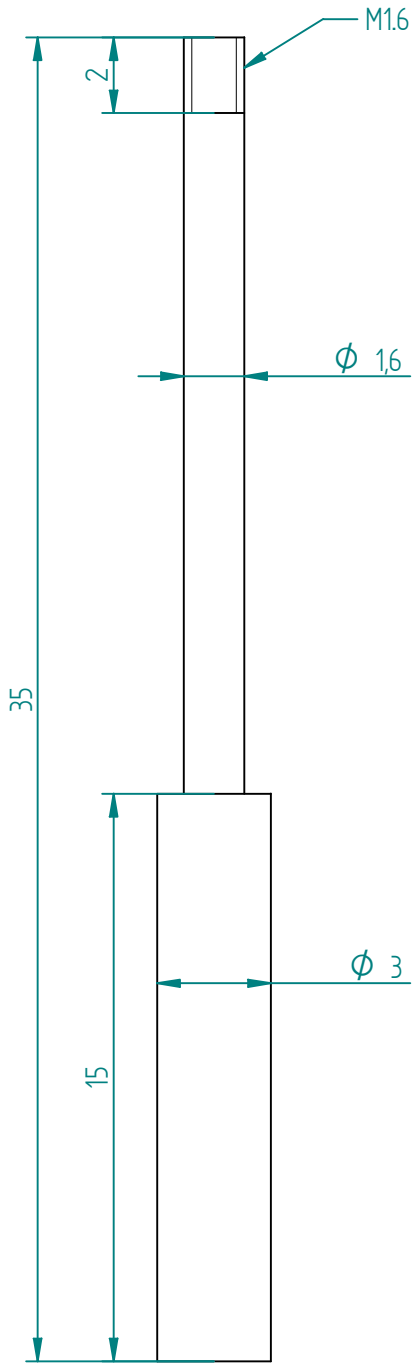

School of Engineering *The University of Edinburgh*		NAME	DATE	UNLESS OTHERWISE SPECIFIED DIMENSIONS ARE IN MILLIMETERS ANGLES ±0.1° LINEAR DISTANCES ±0.01 mm
	DRAWN	G. Giriat	09/24/11	
TITLE: PVC Stand	DWG NO TX-D1.0d	SCALE: 5:1	SIZE: A4	
	MATERIAL: PVC			

Appendix E
TX-DAC clamp v2.0 technical drawings

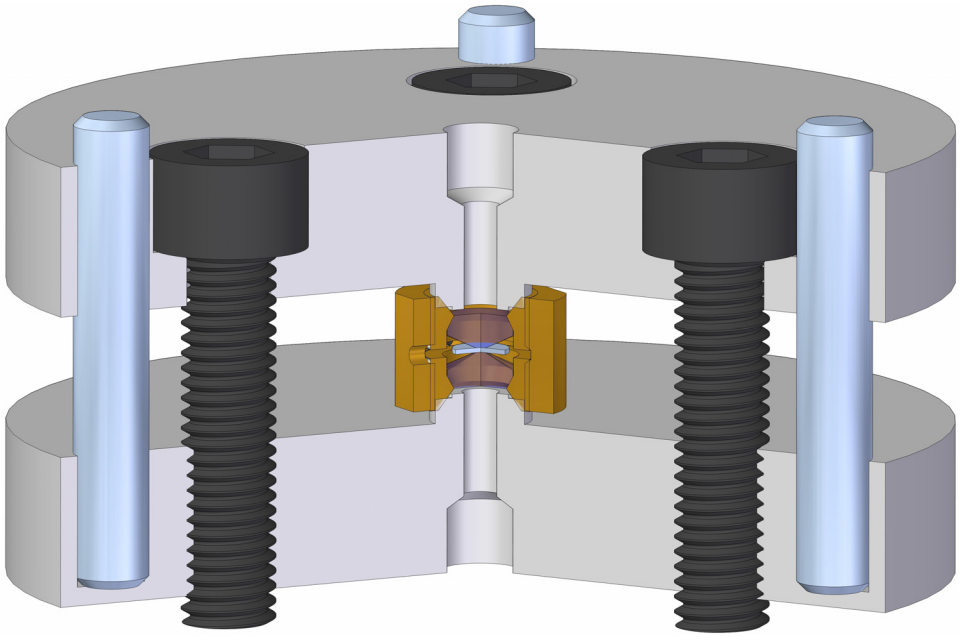

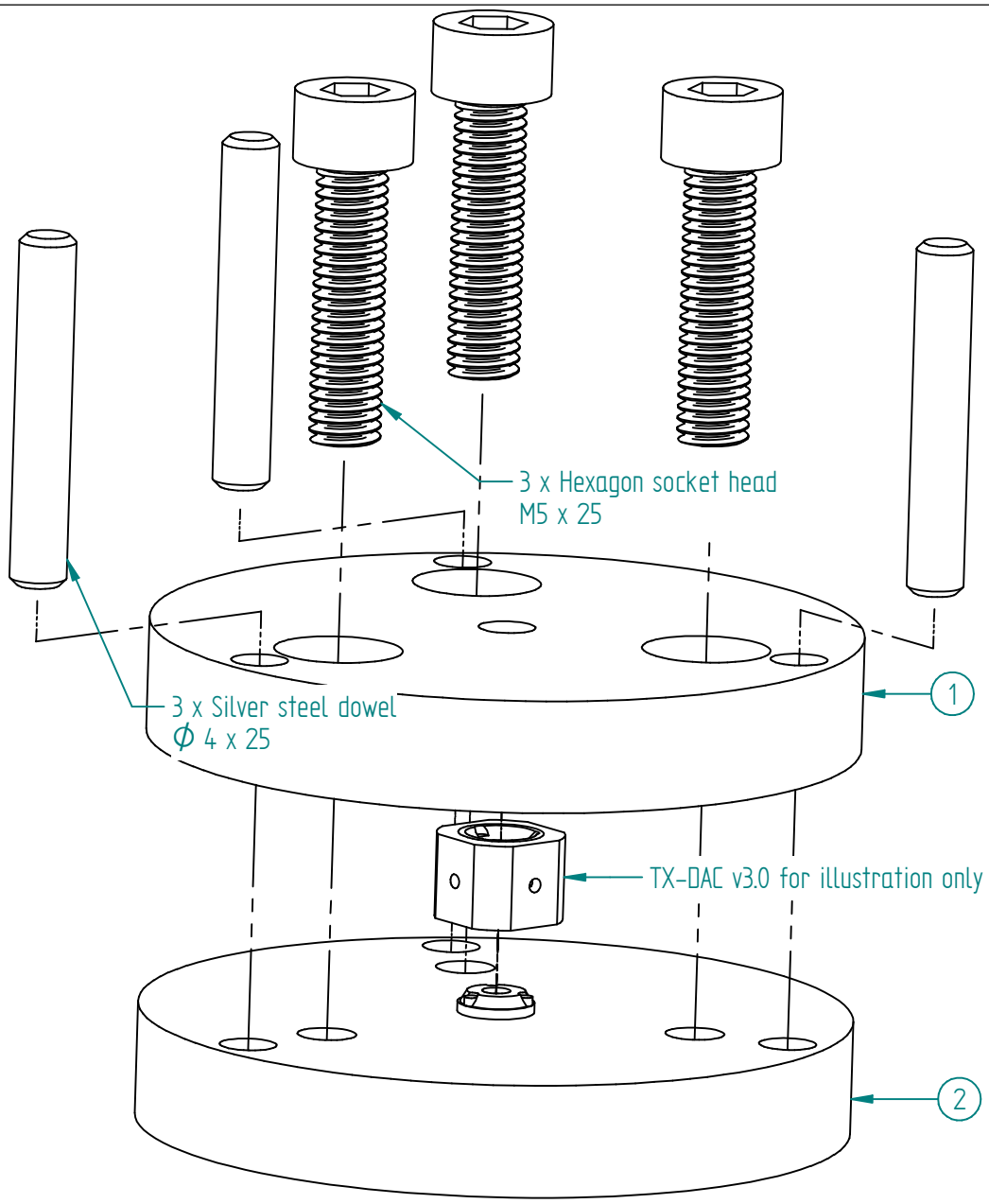

Item No.	DWG	Title	Material	Quantity
1	TXCl2.0a	Plate male	N/A	1
2	TXCl2.0b	Plate female	N/A	1

School of Engineering *The University of Edinburgh*		NAME	DATE	UNLESS OTHERWISE SPECIFIED DIMENSIONS ARE IN MILLIMETERS ANGLES ±0.1° LINEAR DISTANCES ±0.01 mm
	DRAWN	G. Giriat	09/25/11	
TITLE: TX clamp v2.0 Assembly	DWG NO TXCl2.0	SCALE: 2:1	SIZE: A4	
	MATERIAL:			

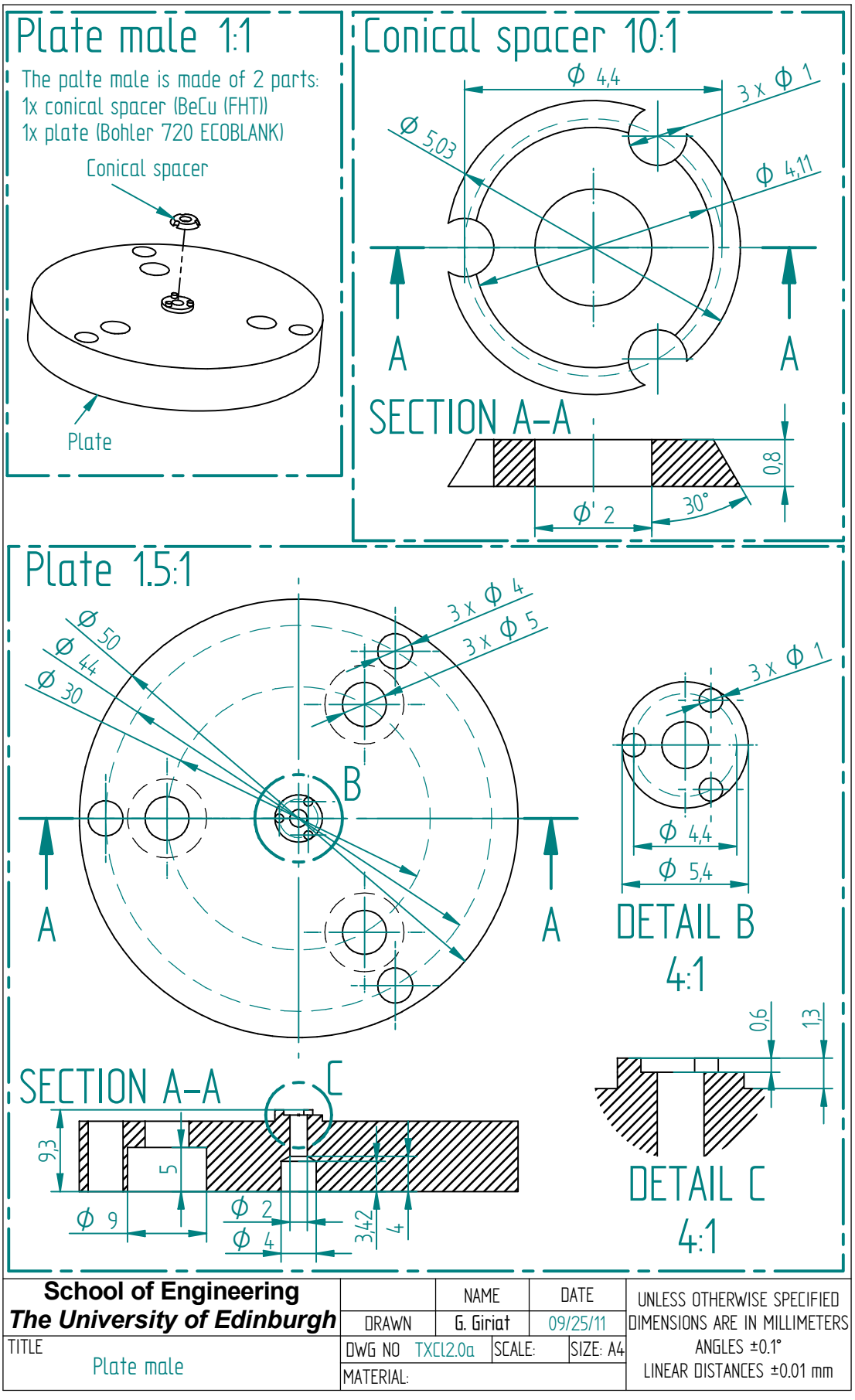

School of Engineering *The University of Edinburgh*		NAME	DATE	UNLESS OTHERWISE SPECIFIED DIMENSIONS ARE IN MILLIMETERS ANGLES ±0.1° LINEAR DISTANCES ±0.01 mm
	DRAWN	G. Giriat	09/25/11	
TITLE Plate male	DWG NO TXCL2.0a	SCALE:	SIZE: A4	
	MATERIAL:			

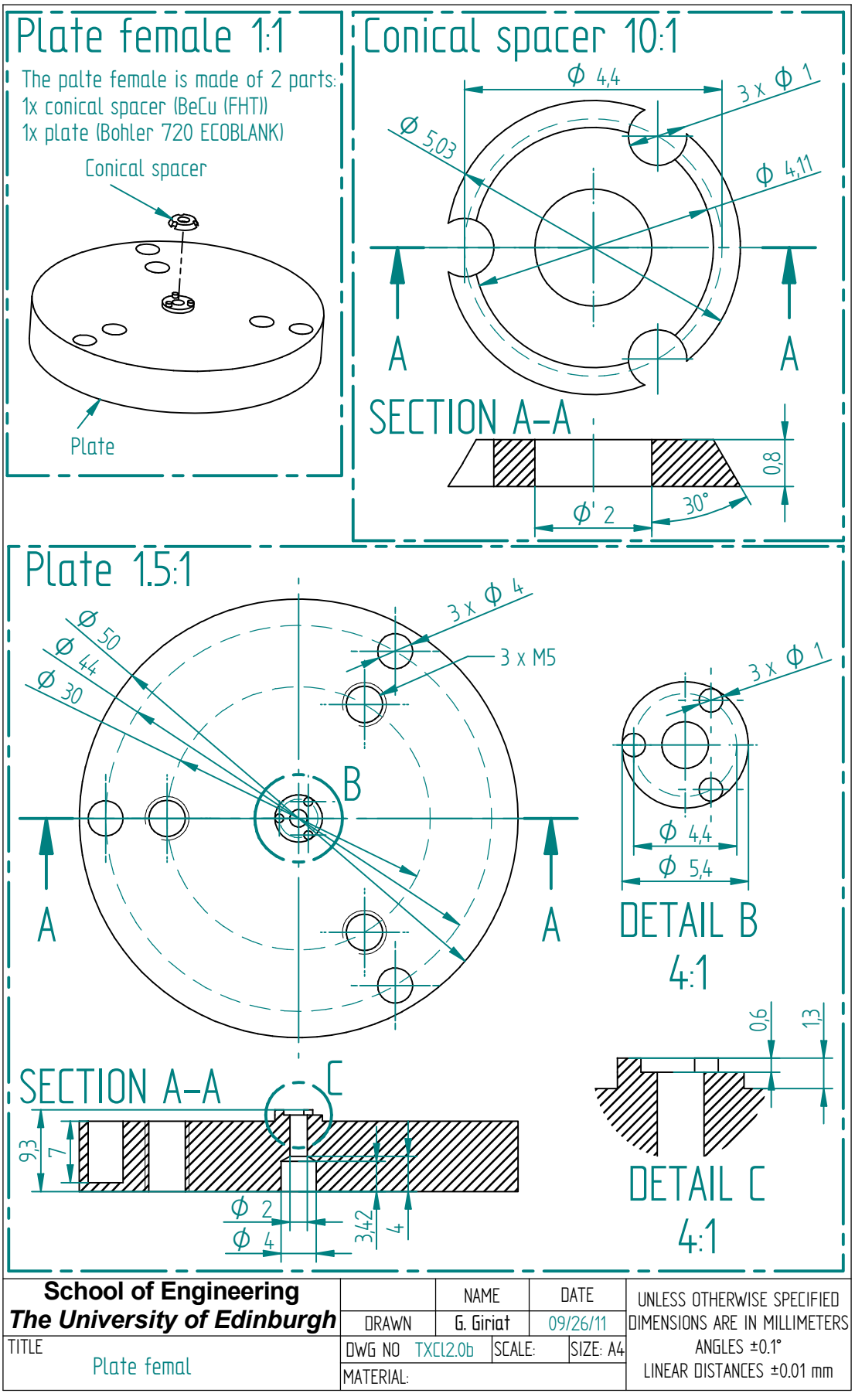
Plate female 1:1
The palte female is made of 2 parts:
1x conical spacer (BeCu (FHT))
1x plate (Bohler 720 ECOBLANK)
Conical spacer
Plate
Conical spacer 10:1
Ø 4,4
3 x Ø 1
Ø 5,03
Ø 4,11
A
A
SECTION A-A
0,8
Ø 2
30°
Plate 1.5:1
3 x Ø 4
3 x M5
Ø 50
Ø 44
Ø 30
B
A
A
3 x Ø 1
Ø 4,4
Ø 5,4
DETAIL B
4:1
SECTION A-A
C
9,3
7
Ø 2
Ø 4
3,42
4
0,6
1,3
DETAIL C
4:1
School of Engineering
The University of Edinburgh
DRAWN
NAME
G. Giriat
DATE
09/26/11
TITLE
Plate femal
DWG NO TXCL2.0b
SCALE:
SIZE: A4
MATERIAL:
UNLESS OTHERWISE SPECIFIED
DIMENSIONS ARE IN MILLIMETERS
ANGLES ±0.1°
LINEAR DISTANCES ±0.01 mm

Appendix F
Anvils technical drawings

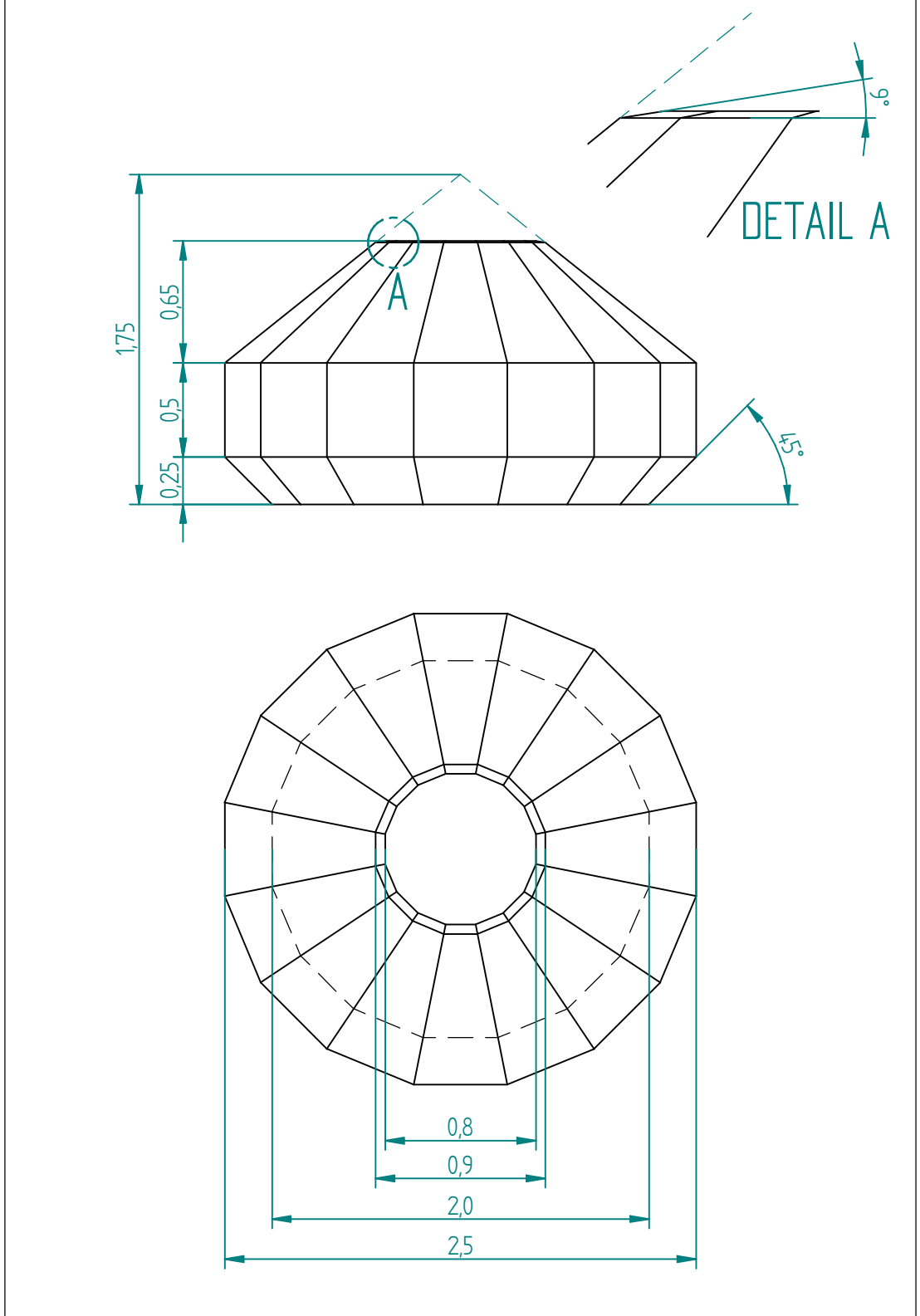

School of Engineering *The University of Edinburgh*		NAME	DATE	UNLESS OTHERWISE SPECIFIED DIMENSIONS ARE IN MILLIMETERS ANGLES ±0.1° LINEAR DISTANCES ±0.01 mm
	DRAWN	G. Giriat	09/10/11	
TITLE: Standard design diamond 800 µm culet	DWG NO SDD-800c	SCALE: 30:1	SIZE: A4	
	MATERIAL: Diamond			

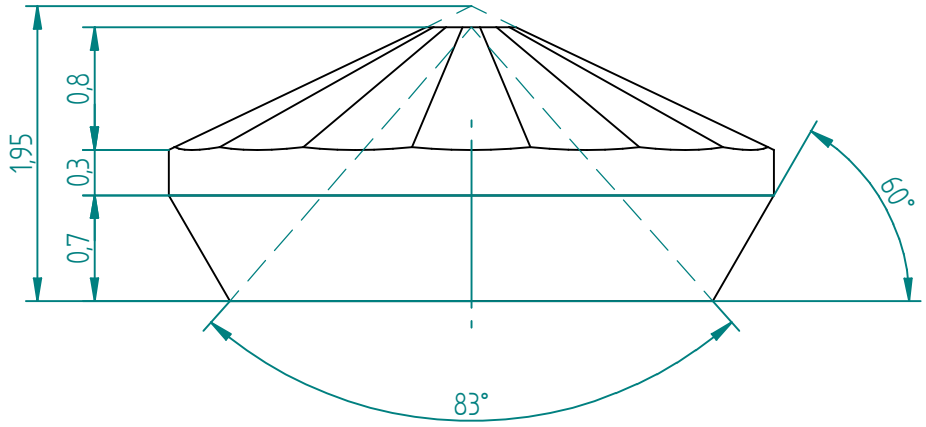

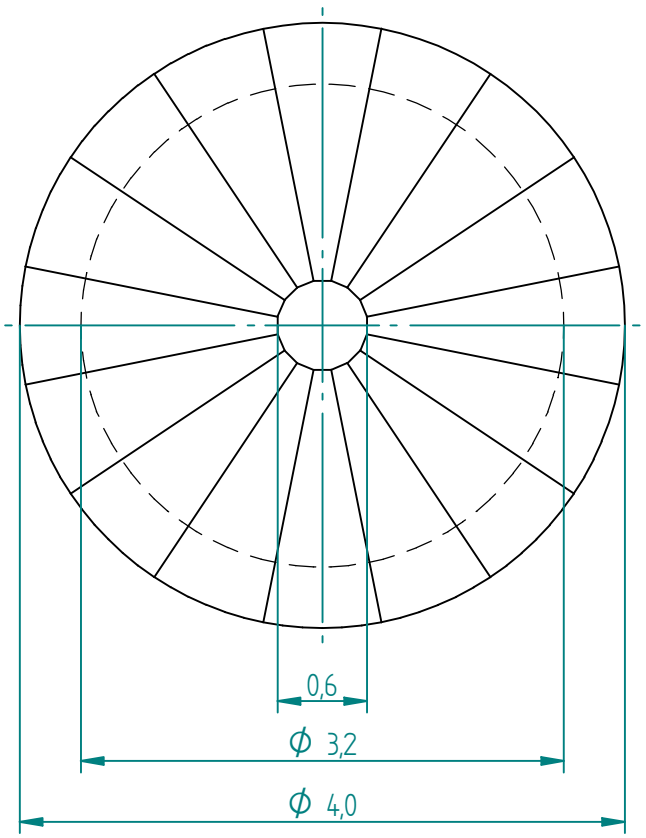

School of Engineering *The University of Edinburgh*		NAME	DATE
	DRAWN	G. Giriat	09/10/11
TITLE: Boehler—Almax design diamond 600 µm culet	DWG NO: BAD-600c	SCALE: 20:1	SIZE: A4
	MATERIAL: Diamond		

UNLESS OTHERWISE SPECIFIED
DIMENSIONS ARE IN MILLIMETERS
ANGLES ±0.1°
LINEAR DISTANCES ±0.01 mm

Appendix G
Publication

Publication arising from this thesis:

"Turnbuckle diamond anvil cell for high-pressure measurements in a superconducting quantum interference device magnetometer" G. Giriat, W. Wang, J. P. Attfield, A. D. Huxley and K. V. Kamenev, Review of scientific instruments, **81**, 073905, (2010).

"Turnbuckle piston-cylinder cell for magnetic susceptibility measurements at high-pressure" G. Giriat, A. F. Kusmartseva, A. Prescimone, E. K. Brechin, T. Mallah, J. P. Attfield and K. V. Kamenev, Review of scientific instruments, (submitted 2012).

"Miniature diamond anvil cell for low-temperature crystallography" G. Giriat, S. A. Moggach, C. Cameron, S. Parsons and K. V. Kamenev, Journal of Applied Crystallography, (submitted 2012).

Bibliography

[1] F. P. BUNDY, H. T. HALL, H. M. STRONG, and R. H. WENTORF, "Man-Made Diamonds," *Nature,* vol. 176, pp. 51-55, 1955.

[2] H. P. BOVENKERK, F. P. BUNDY, H. T. HALL, H. M. STRONG, and R. H. WENTORF, "Preparation of Diamond," *Nature,* vol. 184, pp. 1094-1098, 1959.

[3] M. I. Eremets, *High Pressure Experimental Methods*. Oxford: Oxford University Press, 1996.

[4] P. W. Bridgman, "Compressions and Polymorphic Transitions of Seventeen Elements to 100,000 kg/cm^2," *Physical Review,* vol. 60, p. 351, 1941.

[5] P. W. Bridgman, "The Resistance of 72 Elements, Alloys and Compounds to 100,000 Kg/cm²," *Proceedings of the American Academy of Arts and Sciences,* vol. 81, pp. 165-251 1952.

[6] C. E. Weir, E. R. Lippincott, A. Van Valkenburg, and E. N. Bunting, "Infrared Studies in the 1- to 15-Micron Region to 30,000 Atmospheres," *Journal of Research, National Bureau of Standards,* vol. 63A, pp. 55-62, 1959.

[7] J. C. Jamieson, A. W. Lawson, and N. D. Nachtrieb, "New Device for Obtaining X-Ray Diffraction Patterns from Substances Exposed to High Pressure," *Review of Scientific Instruments,* vol. 30, pp. 1016-1019, 1959.

[8] G. J. Piermarini, "Alvin Van Valkenburg and the diamond anvil cell," *High Pressure Research: An International Journal,* vol. 11, pp. 279-284, 1993.

[9] W. Bassett, "Diamond anvil cell, 50th birthday," *High Pressure Research,* vol. 29, pp. 163-186, 2009.

[10] S. Block and G. Piermarini, "The diamond cell stimulates high-pressure research.," *Physics Today,* vol. 29, p. 44, 1976.

[11] D. J. Dunstan and I. L. Spain, "The technology of diamond anvil high-pressure cells: I. Principles, design and construction," *Journal of Physics E: Scientific Instruments,* vol. 22, p. 913, 1989.

[12] I. L. Spain and D. J. Dunstan, "The technology of diamond anvil high-pressure cells: II. Operation and use," *Journal of Physics E: Scientific Instruments,* vol. 22, p. 923, 1989.

[13] A. Jayaraman, "Diamond anvil cell and high-pressure physical investigations," *Reviews of Modern Physics,* vol. 55, pp. 65-108, 1983.

[14] A. Jayaraman, "Ultrahigh pressures," *Review of Scientific Instruments,* vol. 57, pp. 1013-1031, 1986.

[15] G. Piermarini and S. Block, "The Diamond Anvil Pressure Cell," 1978.

[16] A. Katrusiak, "High-pressure crystallography," *Acta Crystallographica Section A,* vol. 64, pp. 135-148, 2008.

[17] I. R. Walker, "Considerations on the selection of alloys for use in pressure cells at low temperatures," *Cryogenics,* vol. 45, pp. 87-108, 2005.

[18] Y. Uwatoko, T. Fujiwara, M. Hedo, F. Tomioka, and I. Umehara, "The development of a high pressure micro-cell for magnetization and specific heat measurements: the effect of pressure on the magnetism in CeAg," *Journal of Physics: Condensed Matter,* vol. 17, pp. S1011-S1016, 2005.

[19] J. Sanchez-Benitez, S. Tancharakorn, M. K. Hutchinson, and K. V. Kamenev, "High-pressure cell for a SQUID magnetometer with a plug for in situ pressure measurements," *Journal of Physics: Conference Series,* vol. 121, p. 122001, 2008.

[20] M. Mito, "Magnetic Measurements on Molecule-Based Magnets under High Pressure," *Journal of the Physical Society of Japan,* vol. 76SA, p. 182, 2007.

[21] R. Nakai, F. Nakamura, and T. Suzuki, "Development of a Piston-Cylinder Pressure Cell using Nonmagnetic and High-Yield Strength Alloys for a SQUID Magnetometer," *Journal of the Physical Society of Japan,* vol. 76, pp. 219-220, 2007.

[22] S. Reich and T. Godin, "A miniature pressure cell for a SQUID magnetometer," *Measurement Science and Technology,* vol. 7, pp. 1079-1082, 1996.

[23] J. Kamarád, Z. Machátová, and Z. Arnold, "High pressure cells for magnetic measurements — Destruction and functional tests," *Review of Scientific Instruments,* vol. 75, pp. 5022-5025, 2004.

[24] K. V. Kamenev, S. Tancharakorn, N. Robertson, and a. Harrison, "Long symmetric high-pressure cell for magnetic measurements in superconducting quantum interference device magnetometer," *Review of Scientific Instruments,* vol. 77, p. 073905, 2006.

[25] K. Kamishima, M. Hagiwara, and H. Yoshida, "Investigation of a strong titanium alloy KS15-5-3 and the application to a high pressure apparatus for magnetization measurements," *Review of Scientific Instruments,* vol. 72, pp. 1472-1476, 2001.

[26] P. L. Alireza, S. Barakat, and A. M. Cumberlidge, "Developments on susceptibility and magnetization measurements under high hydrostatic pressure," *Journal of the Physical Society of Japan,* vol. 76, pp. 216-218, 2007.

[27] T. C. Kobayashi, H. Hidaka, H. Kotegawa, K. Fujiwara, and M. I. Eremets, "Nonmagnetic indenter-type high-pressure cell for magnetic measurements," *Review of Scientific Instruments,* vol. 78, p. 023909, 2007.

[28] M. Mito, M. Hitaka, T. Kawae, K. Takeda, T. Kitai, and N. Toyoshima, "Development of Miniature Diamond Anvil Cell for the Superconducting Quantum Interference Device Magnetometer," *Japanese Journal of Applied Physics,* vol. 40, p. 6641, 2001.

[29] M. Ohba, W. Kaneko, S. Kitagawa, T. Maeda, and M. Mito, "Pressure Response of Three-Dimensional Cyanide-Bridged Bimetallic Magnets," *Journal of the American Chemical Society,* vol. 130, pp. 4475-4484, 2008.

[30] C. Weir, S. Block, and Piermari.G, "SINGLE-CRYSTAL X-RAY DIFFRACTION AT HIGH PRESSURES," *Journal of Research of the National Bureau of Standards Section C-Engineering and Instrumentation,* vol. C 69, p. 275, 1965.

[31] G. J. Piermarini and C. E. Weir, "A Diamond Cell for X-Ray Diffraction Studies at High Pressures," *Journal of Research of the National Bureau of Standards Section a-Physics and Chemistry,* vol. 66, pp. 325-331, 1962.

[32] L. Merrill and W. A. Bassett, "Miniature diamond anvil pressure cell for single crystal x-ray diffraction studies," *Review of Scientific Instruments,* vol. 45, pp. 290-294, 1974.

[33] R. LeToullec, J. P. Pinceaux, and P. Loubeyre, "The membrane diamond anvil cell: A new device for generating continuous pressure and temperature variations," *High Pressure Research,* vol. 1, pp. 77-90, 1988.

[34] R. LeToullec, P. Loubeyre, J. P. Pinceaux, H. K. Mao, and J. Hu, "Single crystal X-ray diffraction with a synchrotron source in a mdac at low temperature," *High Pressure Research,* vol. 8, pp. 691-696, 1992.

[35] R. LeToullec, P. Loubeyre, J. P. Pinceaux, H. K. Mao, and J. Hu, "A system for doing low temperature-high pressure single crystal X-ray diffraction with a synchrotron source," *High Pressure Research,* vol. 6, pp. 379-388, 1992.

[36] R. Boehler and K. De Hantsetters, "New anvil designs in diamond-cells," *High Pressure Research,* vol. 24, pp. 391-396, 2004.

[37] S. A. Moggach, D. R. Allan, S. Parsons, and J. E. Warren, "Incorporation of a new design of backing seat and anvil in a Merrill-Bassett diamond anvil cell," *Journal of Applied Crystallography,* vol. 41, pp. 249-251, 2008.

[38] J. S. Smart, *Effective Field Theories of Magnetism*: Saunders, 1965.

[39] L. J. De Jongh and A. R. Miedema, "Experiments on simple magnetic model systems," *Advance in physics,* vol. 23, pp. 1-260, 1974.

[40] R. L. Carlin, *Magnetochemistry*: Springer-Verlag, 1986.

[41] D. Bloch, "The 10/3 law for the volume dependence of superexchange," *Journal of Physics and Chemistry of Solids,* vol. 27, pp. 881-885, 1966.

[42] D. Bloch, F. Chaisse, and R. Pauthenet, "Effects of Hydrostatic Pressure on the Magnetic Ordering Temperatures and the Magnetization of Some Ionic Compounds," *Journal of Applied Physics,* vol. 37, pp. 1401-1402, 1966.

[43] D. Bloch and C. Vettier, "Magnetic phase transitions and hydrostatic pressure or uniaxial stress experiments," *Journal of Magnetism and Magnetic Materials,* vol. 15–18, Part 2, pp. 589-592, 1980.

[44] D. Bloch, "Contribution a L'étude Des Propriétés Magnétiques Des Solides Sous Pression Hydrostatique," *Annales De Physique,* vol. 1, pp. 93-125, 1966.

[45] L. J. De Jongh and R. Block, "On the exchange interactions in some 3d-metal ionic compounds: I. The 180° superexchange in the 3d-metal fluorides XMF3 and X2MF4 (X=K, Rb, Tl; M=Mn, Co, Ni)," *Physica B+C,* vol. 79, pp. 568-593, 1975.

[46] R. Ritter, L. Jansen, and E. Lombardi, "Exchange-Perturbation Treatment of Magnetic Ordering in Nonconducting Solids," *Physical Review B,* vol. 8, pp. 2139-2154, 1973.

[47] S. T. Bramwell, "Temperature dependence of the isotropic exchange constant," *Journal of Physics: Condensed Matter,* vol. 2, p. 7527, 1990.

[48] M. Imada, A. Fujimori, and Y. Tokura, "Metal-insulator transitions," *Reviews of Modern Physics,* vol. 70, pp. 1039-1263, 1998.

[49] Y. Moritomo, H. Kuwahara, Y. Tomioka, and Y. Tokura, "Pressure effects on charge-ordering transitions in Perovskite manganites," *Physical Review B,* vol. 55, pp. 7549-7556, 1997.

[50] K. V. Kamenev, M. R. Lees, G. Balakrishnan, D. M. Paul, W. G. Marshall, V. G. Tissen, and M. V. Nefedova, "Pressure Tuning of Magnetic Interactions in Layered $(La_{0.6}Nd_{0.4})_{1.2}Sr_{1.8}Mn_2O_7$ Manganite," *Physical Review Letters,* vol. 84, pp. 2710-2713, 2000.

[51] D. A. Sokolov, K. V. Kamenev, and M. Ishizuka, "Pressure-induced magnetic long-range order in $Pr_{1.4}Sr_{1.6}Mn_2O_7$ layered manganite (antiferromagnetism in $Pr_{1.4}Sr_{1.6}Mn_2O_7$)," *HIGH PRESSURE RESEARCH,* vol. 23, pp. 191-194, 2003.

[52] M. C. Aronson, S.-W. Cheong, F. H. Garzon, J. D. Thompson, and Z. Fisk, "Pressure dependence of the superconducting and Néel temperatures in a $La_2CuO_{4+\delta}$ crystal," *Physical Review B,* vol. 39, pp. 11445-11448, 1989.

[53] V. Doroshev, V. Krivoruchko, M. Savosta, A. Shestakov, and T. Tarasenko, "Pressure effect on the Néel temperature in La_2CuO_4," *Journal of Magnetism and Magnetic Materials,* vol. 157–158, pp. 669-670, 1996.

[54] G. Gorodetsky, R. C. Leung, F. P. Missell, and C. W. Garland, "On the volume dependence of superexchange in K_2NiF_4," *Physics Letters A,* vol. 64, pp. 251-252, 1977.

[55] C. Vettier and W. B. Yelon, "Magnetic properties of $FeCl_2$ at high pressure," *Physical Review B,* vol. 11, pp. 4700-4710, 1975.

[56] A. Narath and J. E. Schirber, "Effect of Hydrostatic Pressure on the Metamagnetic Transitions in $FeCl_2 \cdot 2H_2O$, $CoCl_2 \cdot 2H_2O$, $FeCl_2$, and $FeBr_2$," *Journal of Applied Physics,* vol. 37, pp. 1124-1125, 1966.

[57] C. Vettier, H. L. Alberts, and D. Bloch, "Tricritical Lines in Metamagnets," *Physical Review Letters,* vol. 31, pp. 1414-1417, 1973.

[58] K. C. Johnson and A. J. Sievers, "Hydrostatic-Pressure Study of Antiferromagnetic Resonance in $FeCl_2$," *Physical Review B,* vol. 7, pp. 1081-1083, 1973.

[59] S. Klotz, M. Braden, and J. M. Besson, "Inelastic neutron scattering to very high pressures," *Hyperfine Interactions,* vol. 128, pp. 245-254, 2000.

[60] M. Pasternak and R. Taylor, "High-pressure Mössbauer spectroscopy, a unique tool for unraveling the nature of electron correlations in Mott insulators," *Hyperfine Interactions,* vol. 128, pp. 81-100, 2000.

[61] G. M. Kalvius, E. Schreier, M. Ekström, O. Hartmann, S. Henneberger, A. Kratzer, R. Wäppling, E. Martin, F. J. Burghart, R. Ballou, J. Deportes, and C. Niedermayer, "High pressure μSR studies: rare earths and related materials," *Hyperfine Interactions,* vol. 128, pp. 275-303, 2000.

[62] M. Ishizuka, M. Terai, S. Endo, M. Hidaka, I. Yamada, and O. Shimomura, "Pressure-induced magnetic phase transition in the two-dimensional Heisenberg ferromagnet K_2CuF_4," *Journal of Magnetism and Magnetic Materials,* vol. 177–181, pp. 725-726, 1998.

[63] M. Ishizuka, I. Yamada, K. Amaya, and S. Endo, "Change of Magnetism in the Two-Dimensional Heisenberg Ferromagnet K_2CuF_4 Observed at High Pressures," *Journal of the Physical Society of Japan,* vol. 65, pp. 1927-1929, 1996.

[64] H. Manaka, I. Yamada, T. Kitazawa, M. Kobayashi, M. Ishizuka, and S. Endo, "Observation of Pressure-Induced Structural Transition in K_2CuF_4 by Phonon-Raman Scattering Experiments: Change of the Orbital Ordering by Pressure," *Journal of the Physical Society of Japan,* vol. 66, pp. 2989-2992, 1997.

[65] H. Stout and L. H. Jensen, *X-ray Structure Determination: A practical guide, 2nd edition*. Oxford: OUP, 1985.

[66] P. Glusker and K. N. Trueblood, *Crystal Structure Analysis - A Primer*: Oxford University Press, 1985.

[67] P. Glusker, L. M., and M. Rossi, *Crystal Structure Analysis for Chemists and Biologists*. New York: VCH, 1994.

[68] M. J. TURNER, R. W. CLOUGH, H. C. MARTIN, and L. J. TOPP, "Stiffness and Deflection Analysis of Complex Structures," *Journal Of The Aeronautical Sciences,* vol. 23, p. 805, 1956.

[69] W. C. Moss, J. O. Hallquist, R. Reichlin, K. A. Goettel, and S. Martin, "Finite element analysis of the diamond anvil cell: Achieving 4.6 Mbar," *Applied Physics Letters,* vol. 48, pp. 1258-1260, 1986.

[70] W. C. Moss and K. A. Goettel, "Finite element design of diamond anvils," *Applied Physics Letters,* vol. 50, pp. 25-27, 1987.

[71] S. Merkel, R. J. Hemley, and H.-k. Mao, "Finite-element modeling of diamond deformation at multimegabar pressures," *Applied Physics Letters,* vol. 74, pp. 656-658, 1999.

[72] D. M. Adams, A. G. Christy, and A. J. Norman, "Optimization of diamond anvil cell performance by finite element analysis," *Measurement Science and Technology,* vol. 4, p. 422, 1993.

[73] G. Krauss, H. Reifler, and W. Steurer, "Conically shaped single-crystalline diamond backing plates for a diamond anvil cell.," *Review of Scientific Instruments,* vol. 76, p. 105106, 2005.

[74] T. Pippinger, R. Miletich, and M. Burchard, "Multipurpose high-pressure high-temperature diamond-anvil cell with a novel high-precision guiding system and a dual-mode pressurization device," *Review of Scientific Instruments,* vol. 82, p. 95108, 2011.

[75] *ANSYS, Inc.* Available: http://www.ansys.com/

[76] N. Tateiwa and Y. Haga, "Evaluations of pressure-transmitting media for cryogenic experiments with diamond anvil cell," *Review of Scientific Instruments,* vol. 80, p. 123901, 2009.

[77] N. Tateiwa and Y. Haga, "Appropriate pressure-transmitting media for cryogenic experiment in the diamond anvil cell up to 10 GPa," *Journal of Physics: Conference Series,* vol. 215, p. 012178, 2010.

[78] T. Kenichi, P. C. Sahu, K. Yoshiyasu, and T. Yasuo, "Versatile gas-loading system for diamond-anvil cells," *Review of Scientific Instruments,* vol. 72, pp. 3873-3876, 2001.

[79] A. Kurnosov, I. Kantor, T. Boffa-Ballaran, S. Lindhardt, L. Dubrovinsky, A. Kuznetsov, and B. H. Zehnder, "A novel gas-loading system for mechanically closing of various types of diamond anvil cells," *Review of Scientific Instruments,* vol. 79, pp. 45110-45115, 2008.

[80] K. Takemura, "Pressure scales and hydrostaticity," *High Pressure Research,* vol. 27, pp. 465-472, 2007.

[81] S. Klotz, J.-C. Chervin, P. Munsch, and G. Le Marchand, "Hydrostatic limits of 11 pressure transmitting media," *Journal of Physics D: Applied Physics,* vol. 42, p. 75413, 2009.

[82] K. Takemura, "Evaluation of the hydrostaticity of a helium-pressure medium with powder x-ray diffraction techniques," *Journal of Applied Physics,* vol. 89, p. 662, 2001.

[83] G. J. Piermarini, S. Block, and J. D. Barnett, "Hydrostatic limits in liquids and solids to 100 kbar," *Journal of Applied Physics,* vol. 44, pp. 5377-5382, 1973.

[84] T. Varga, A. P. Wilkinson, and R. J. Angel, "Fluorinert as a pressure-transmitting medium for high-pressure diffraction studies," *Review of Scientific Instruments,* vol. 74, pp. 4564-4566, 2003.

[85] V. A. Sidorov and R. A. Sadykov, "Hydrostatic limits of Fluorinert liquids used for neutron and transport studies at high pressure," *Journal of Physics: Condensed Matter,* vol. 17, p. S3005, 2005.

[86] *Developed by Prof. Keizo Murata and Idemitsu Kosan Co., Ltd.* Available: http://www.idemitsu.com/

[87] K. Yokogawa, K. Murata, H. Yoshino, and S. Aoyama, "Solidification of High-Pressure Medium Daphne 7373," *Japanese Journal of Applied Physics,* vol. 46, pp. 3636-3639, 2007.

[88] K. Murata, H. Yoshino, H. O. Yadav, Y. Honda, and N. Shirakawa, "Pt resistor thermometry and pressure calibration in a clamped pressure cell with the medium, Daphne 7373," *Review of Scientific Instruments,* vol. 68, pp. 2490-2493, 1997.

[89] K. Murata, K. Yokogawa, H. Yoshino, S. Klotz, P. Munsch, A. Irizawa, M. Nishiyama, K. Iizuka, T. Nanba, T. Okada, Y. Shiraga, and S. Aoyama, "Pressure transmitting medium Daphne 7474 solidifying at 3.7 GPa at room temperature," *Review of Scientific Instruments,* vol. 79, pp. 85101-85106, 2008.

[90] J. M. Besson and J. P. Pinceaux, "Melting of Helium at Room Temperature and High Pressure," *Science,* vol. 206, pp. 1073-1075, 1979.

[91] R. A. Forman, G. J. Piermarini, J. D. Barnett, and S. Block, "Pressure Measurement Made by the Utilization of Ruby Sharp-Line Luminescence," *Science,* vol. 176, pp. 284-285, 1972.

[92] J. D. Barnett, S. Block, and G. J. Piermarini, "An Optical Fluorescence System for Quantitative Pressure Measurement in the Diamond-Anvil Cell," *Review of Scientific Instruments,* vol. 44, pp. 1-9, 1973.

[93] G. J. Piermarini, S. Block, J. D. Barnett, and R. A. Forman, "Calibration of Pressure-Dependence of R1 Ruby Fluorescence Line to 195 Kbar," *Journal of Applied Physics,* vol. 46, pp. 2774-2780, 1975.

[94] H. K. Mao, J. Xu, and P. M. Bell, "Calibration of the Ruby Pressure Gauge to 800 kbar Under Quasi-Hydrostatic Conditions," *J. Geophys. Res.,* vol. 91, pp. 4673-4676, 1986.

[95] R. J. Hemley, C. S. Zha, A. P. Jephcoat, H. K. Mao, L. W. Finger, and D. E. Cox, "X-ray diffraction and equation of state of solid neon to 110 GPa," *Physical Review B,* vol. 39, pp. 11820-11827, 1989.

[96] K. Nakano, Y. Akahama, Y. Ohishi, and H. Kawamura, "Ruby Scale at Low Temperatures Calibrated by the NaCl Gauge : Wavelength Shift of Ruby R1 Fluorescence Line at High pressure and Low Temperature," *Japanese Journal of Applied Physics,* vol. 39, pp. 1249-1251, 2000.

[97] J. C. Chervin, B. Canny, and M. Mancinelli, "Ruby-spheres as pressure gauge for optically transparent high pressure cells," *High Pressure Research,* vol. 21, pp. 305-314, 2001.

[98] K. Syassen, "Ruby under pressure," *High Pressure Research,* vol. 28, pp. 75-126, 2008.

[99] A. Eiling and J. Schilling, "Pressure and temperature dependence of electrical resistivity of Pb and Sn from 1-300K and 0-10 GPa-use as continuous resistive pressure monitor accurate over wide temperature range; superconductivity under pressure in Pb, Sn and In," *Journal of Physics F: Metal Physics,* vol. 11, p. 623, 1981.

[100] B. Bireckoven and J. Wittig, "A diamond anvil cell for the investigation of superconductivity under pressures of up to 50 GPa: Pb as a low temperature manometer," *Journal of Physics E: Scientific Instruments,* vol. 21, p. 841, 1988.

[101] Y. Akahama and H. Kawamura, "Pressure calibration of diamond anvil Raman gauge to 410 GPa," *Journal of Physics: Conference Series,* vol. 215, p. 12195, 2010.

[102] D. J. Dunstan, "Theory of the gasket in diamond anvil high-pressure cells," *Review of Scientific Instruments,* vol. 60, pp. 3789-3795, 1989.

[103] V. I. Levitas, S. B. Polotnyak, and A. V. Idesman, "Large elastoplastic strains and the stressed state of a deformable gasket in high pressure equipment with diamond anvils," *Strength of Materials,* vol. 28, pp. 221-227, 1996.

[104] W. C. Moss and K. A. Goettel, "The stability of a sample in a diamond anvil cell," *Journal of Applied Physics,* vol. 61, pp. 4951-4954, 1987.

[105] M. Ishizuka, "Composite bimetallic gasket and compact mechanical anvil retainer for magnetic measurements in a diamond-anvil cell to 30 GPa," *Review of Scientific Instruments,* vol. 76, p. 123902, 2005.

[106] S. b. Merkel and T. Yagi, "X-ray transparent gasket for diamond anvil cell high pressure experiments," *Review of Scientific Instruments,* vol. 76, p. 046109, 2005.

[107] D. E. Graf, R. L. Stillwell, K. M. Purcell, and S. W. Tozer, "Nonmetallic gasket and miniature plastic turnbuckle diamond anvil cell for pulsed magnetic field studies at cryogenic temperatures," *High Pressure Research,* vol. 31, pp. 533-543, 2011.

[108] D. Solli and R. Jeanloz, "Nonmetallic gaskets for ultrahigh pressure diamond-cell experiments," *Review of Scientific Instruments,* vol. 72, p. 2110, 2001.

[109] M. I. Eremets, A. G. Gavriliuk, I. a. Trojan, D. a. Dzivenko, and R. Boehler, "Single-bonded cubic form of nitrogen.," *Nature materials,* vol. 3, pp. 558-63, 2004.

[110] G. Zou, Y. Ma, H.-k. Mao, R. J. Hemley, and S. A. Gramsch, "A diamond gasket for the laser-heated diamond anvil cell," *Review of Scientific Instruments,* vol. 72, p. 1298, 2001.

[111] D. Erskine, P. Y. Yu, and G. Martinez, "Technique for high-pressure electrical conductivity measurement in diamond anvil cells at cryogenic temperatures," *Review of Scientific Instruments,* vol. 58, p. 406, 1987.

[112] J. F. Lin, J. Shu, H. K. Mao, R. J. Hemley, and G. Shen, "Amorphous boron gasket in diamond anvil cell research," *Review of scientific instruments,* vol. 74, p. 4732, 2003.

[113] C. D. Martin, Y. Meng, V. Prakapenka, and J. B. Parise, "Gasketing optimized for large sample volume in the diamond anvil cell: first application to $MgGeO_3$ and implications for structural systematics of the perovskite to post-perovskite transition," *Journal of Applied Crystallography,* vol. 41, pp. 38-43, 2008.

[114] N. Funamori and T. Sato, "A cubic boron nitride gasket for diamond-anvil experiments," *Review of Scientific Instruments,* vol. 79, p. 053903, 2008.

[115] J.-M. Besson, *High-pressure techniques in chemistry and physics : a practical approach*. Oxford ;: Oxford University Press, 1997.

[116] K. R. Hirsch and W. B. Holzapfel, "Diamond anvil high-pressure cell for Raman spectroscopy," *Review of Scientific Instruments,* vol. 52, pp. 52-55, 1981.

[117] T. Yamanaka, T. Fukuda, T. Hattori, and H. Sumiya, "New diamond anvil cell for single-crystal analysis," *Review of Scientific Instruments,* vol. 72, pp. 1458-1462, 2001.

[118] R. Boehler, "New diamond cell for single-crystal x-ray diffraction," *Review of Scientific Instruments,* vol. 77, p. 115103, 2006.

[119] M. I. Eremets, "Megabar high-pressure cells for Raman measurements," *Journal of Raman Spectroscopy,* vol. 34, pp. 515-518, 2003.

[120] H. K. Mao and P. M. Bell, "Design of a diamond-windowed, high-pressure cell for hydrostatic pressures in the range 1 bar to 0.5 Mbar," *Carnegie Inst. Washington Yearb.,* vol. 74, pp. 402-405, 1975.

[121] H. K. Mao, R. J. Hemley, and A. L. Mao, "RECENT DESIGN OF ULTRAHIGH-PRESSURE DIAMOND CELL," in *HIGH-PRESSURE SCIENCE AND TECHNOLOGY - 1993, PTS 1 AND 2*, AMERICAN INSTITUTE OF PHYSICS 500 SUNNYSIDE BOULEVARD, WOODBURY, NY 11797-2999, 1994, pp. 1613-1616.

[122] R. L. Smith and Z. Fang, "Techniques, applications and future prospects of diamond anvil cells for studying supercritical water systems," *Journal of Supercritical Fluids,* vol. 47, pp. 431-446, 2009.

[123] R. M. Hazen and L. W. Finger, "High-temperature diamond-anvil pressure cell for single-crystal studies," *Review of Scientific Instruments,* vol. 52, pp. 75-79, 1981.

[124] D. R. Allan, R. Miletich, and R. J. Angel, "A diamond-anvil cell for single-crystal x-ray diffraction studies to pressures in excess of 10 GPa.," *Review of Scientific Instruments,* vol. 67, p. 840, 1996.

[125] G. Piermarini and S. Block, "Ultrahigh pressure diamond-anvil cell and several semiconductor phase transition pressures in relation to the fixed point pressure scale," *Review of Scientific Instruments,* vol. 46, p. 973, 1975.

[126] D. Braithwaite, G. Chouteau, and G. Martinez, "Inductive measurement of the critical temperature of high-T c superconductors in a diamond anvil cell," *Measurement Science and Technology,* vol. 1, p. 1347, 1990.

[127] S. Endo, J. Yamada, S. Imada, M. Ishizuka, K. Kindo, S. Miyamoto, and F. Ono, "Development of magnetization measurement under high pressure and pulsed high magnetic field," *Review of Scientific Instruments,* vol. 70, pp. 2445-2447, 1999.

[128] Y. A. Timofeev, V. V. Struzhkin, R. J. Hemley, H.-k. Mao, and E. A. Gregoryanz, "Improved techniques for measurement of superconductivity in diamond anvil cells by magnetic susceptibility," *Review of Scientific Instruments,* vol. 73, pp. 371-377, 2002.

[129] D. D. Jackson, C. Aracne-ruddle, V. Malba, S. T. Weir, S. A. Catledge, and Y. K. Vohra, "Magnetic susceptibility measurements at high pressure using designer diamond anvils," *Review of Scientific Instruments,* vol. 74, pp. 2467-2471, 2003.

[130] D. D. Jackson, V. Malba, S. T. Weir, P. A. Baker, and Y. K. Vohra, "High-pressure magnetic susceptibility experiments on the heavy lanthanides Gd, Tb, Dy, Ho, Er, and Tm," *Physical Review B,* vol. 71, p. 184416, 2005.

[131] D. D. Jackson, S. K. McCall, S. T. Weir, A. B. Karki, D. P. Young, W. Qiu, and Y. K. Vohra, "Cubic Laves ferromagnet $TbNi_2Mn$ investigated through ambient-pressure magnetization and specific heat and high pressure ac magnetic susceptibility," *Phys. Rev. B,* vol. 75, p. 224422, 2007.

[132] M. Ishizuka, K. Amaya, and S. Endo, "Precise magnetization measurements under high pressures in the diamond-anvil cell," *Review of scientific instruments,* vol. 66, pp. 3307-3310, 1995.

[133] M. Ishizuka and S. Endo, "Measurements of superconducting transitions at pressures up to 83 GPa," *Physica B: Condensed Matter,* vol. 265, pp. 254-257, 1999.

[134] M. Ishizuka, H. Manaka, and I. Yamada, "Magnetic behaviour of the two-dimensional Heisenberg ferromagnet Cs_2CuF_4 under high pressure: a sensitive magnetic measurement in a diamond-anvil cell to 26 GPa," *Journal of Physics: Condensed Matter,* vol. 18, pp. 2935-2941, 2006.

[135] S. T. Weir, J. Akella, C. Aracne-Ruddle, Y. K. Vohra, and S. A. Catledge, "Epitaxial diamond encapsulation of metal microprobes for high pressure experiments," *Applied Physics Letters,* vol. 77, pp. 3400-3402, 2000.

[136] O. P. Welzel and F. M. Grosche, "Patterned anvils for high pressure measurements at low temperature," *Review of Scientific Instruments,* vol. 82, p. 33901, 2011.

[137] S. Tominaga, Y. Komorida, M. Mito, H. Deguchi, S. Takagi, K. Koyama, and M. Hamada, "AC susceptibility measurements on ceramic YBa2Cu3O7. y superconductor in the GPa region," *Journal of Physics: Conference Series,* vol. 150, p. 052271, 2009.

[138] *easyLab Technologies Ltd*. Available: http://www.easylab.co.uk/

[139] P. L. Alireza and G. G. Lonzarich, "Miniature anvil cell for high-pressure measurements in a commercial superconducting quantum interference device magnetometer," *Review of Scientific Instruments,* vol. 80, p. 023906, 2009.

[140] T. Goto, Y. Shindo, H. Takahashi, and S. Ogawa, "Magnetic properties of the itinerant metamagnetic system $Co(S_{1-x}Se_x)_2$ under high magnetic fields and high pressure," *Physical Review B,* vol. 56, pp. 14019-14028, 1997.

[141] M. I. Eremets and Y. A. Timofeev, "Miniature diamond anvil cell: Incorporating alignment," *Review of Scientific Instruments,* vol. 63, pp. 3123-3126, 1992.
[142] N. Tateiwa, Y. Haga, Z. Fisk, and Y. Onuki, "Miniature ceramic-anvil high-pressure cell for magnetic measurements in a commercial superconducting quantum interference device magnetometer," *Review of Scientific Instruments,* vol. 82, p. 53906, 2011.
[143] H. Fujiwara, H. Kadomatsu, and K. Tohma, "Simple clamp pressure cell up to 30 kbar," *Review of Scientific Instruments,* vol. 51, pp. 1345-1348, 1980.
[144] C. Pfleiderer, "Miniature ac susceptometers for use inside clamp type pressure cells," *Review of Scientific Instruments,* vol. 68, pp. 1532-1535, 1997.
[145] N. Fujiwara, T. Matsumoto, K. Koyama-Nakazawa, A. Hisada, and Y. Uwatoko, "Fabrication and efficiency evaluation of a hybrid NiCrAl pressure cell up to 4 GPa," *Review of Scientific Instruments,* vol. 78, p. 073905, 2007.
[146] *DYNAMIC-CERAMIC LTD*. Available: http://www.dynacer.com/
[147] *Kennametal Inc.* Available: http://www.kennametal.com/
[148] W. Wang, D. A. Sokolov, A. D. Huxley, and K. V. Kamenev, "Large volume high-pressure cell for inelastic neutron scattering," *Review of Scientific Instruments,* vol. 82, p. 73903, 2011.
[149] T. E. Davidson and D. P. Kendall, "THE DESIGN OF PRESSURE VESSELS FOR VERY HIGH PRESSURE OPERATION," BENET R&E LABORATORIES, NEW YORK1969.
[150] C. Vettier, "Neutron scattering studies of rare earth compounds at high pressure," *Journal of the Less Common Metals,* vol. 149, pp. 13-23, 1989.
[151] J. Diederichs, A. K. Gangopadhyay, and J. S. Schilling, "Pressure dependence of the electronic density of states and T_c in superconducting Rb_3C_{60}," *Physical Review B,* vol. 54, pp. R9662-R9665, 1996.
[152] H. Fukuda, H. Fujii, H. Kamura, A. Uchida, M. Kosaka, and Y. Uwatoko, "Near the collapse of ferromagnetism in $CeFe_2$ under high pressures," *Journal of Magnetism and Magnetic Materials,* vol. 226, pp. 1200-1202, 2001.
[153] I. Umehara, F. Tomioka, A. Tsuboi, T. Ono, M. Hedo, and Y. Uwatoko, "Design of micro pressure cell for measurements of specific heat and magnetization," *Journal of Magnetism and Magnetic Materials,* vol. 272-276, pp. 2301-2302, 2004.
[154] A. T. Rowley and A. Myers, "A SQUID-based high pressure magnetic susceptometer," *Journal of Physics E: Scientific Instruments,* vol. 20, p. 146, 1987.
[155] *The Squid Handbook: Applications of Squids and Squid Systems, Volume II*. Weinheim, Germany: Wiley-VCH, 2006.
[156] M. McElfresh, "Fundamentals of Magnetism and Magnetic Measurements Featuring Quantum Design's Magnetic Property Measurement System," San Diego1994.
[157] *Bruker Corporation*. Available: http://www.bruker.com
[158] *Oxford Cryosystems*. Available: http://www.oxcryo.com/

[159] D. L. Decker, W. A. Bassett, L. Merrill, H. T. Hall, and J. D. Barnett, "High-Pressure Calibration A Critical Review," *J. Phys. Chem. Ref. Data,* vol. 1, pp. 1-79, 1972.
[160] W. A. Bassett and T. Takahash, "Silver Iodide Polymorphs," *American Mineralogist,* vol. 50, pp. 1576-1594, 1965.
[161] S. L. Wunder and P. E. Schoen, "Pressure Measurement at High-Temperatures in the Diamond Anvil Cell," *Journal of Applied Physics,* vol. 52, pp. 3772-3775, 1981.
[162] T. Yamanaka, T. Fukuda, T. Hattori, and H. Sumiya, "New diamond anvil cell for single-crystal analysis," *Rev. Sci. Instrum.,* vol. 72, pp. 1458-1462, 2001.
[163] D. J. Dunstan and W. Scherrer, "Miniature cryogenic diamond-anvil high-pressure cell," *Rev. Sci. Instrum.,* vol. 59, pp. 627-630, 1987.
[164] P. Goddard, S. Tozer, J. Singleton, A. Ardavan, A. Abate, and M. Kurmoo, "Superconductivity, incoherence and Anderson localization in the crystalline organic conductor (BEDT-TTF)$_3$Cl$_2$•2H$_2$O at high pressures," *Journal of Physics: Condensed Matter,* vol. 14, pp. 7345-7361, 2002.
[165] C. Martin, C. C. Agosta, S. W. Tozer, H. a. Radovan, T. Kinoshota, and M. Tokumoto, "Critical Field and Shubnikov-de Haas Oscillations of k-(BEDT-TTF)$_2$Cu(NCS)$_2$ under Pressure," *Journal of Low Temperature Physics,* vol. 138, pp. 1025-1037, 2005.
[166] M. Kano, H. Mori, Y. Uwatoko, and S. Tozer, "Anisotropy of the upper critical field in ultrahigh-pressure-induced superconductor (TMTTF)$_2$PF$_6$," *Physica B: Condensed Matter,* vol. 404, pp. 3246-3248, 2009.
[167] *NGK Berylco U.K. Ltd.* Available: http://www.ngkberylco.co.uk/
[168] *ALMAX INDUSTRIES*. Available: http://www.almax-industries.com/
[169] *AEP Transducers S.R.L.* Available: http://www.aep.it/
[170] *NOVA SWISS*. Available: http://www.novaswiss.ch/
[171] Q. Design, "Sample Mounting Considerations - MPMS Application Note 1014-201," ed, 2000.
[172] J. S. Miller, "Three-dimensional network-structured cyanide-based magnets," *MRS BULLETIN,* vol. 25, pp. 60-64, 2000.
[173] E. Ruiz, A. Rodríguez-Fortea, S. Alvarez, and M. Verdaguer, "Is It Possible To Get High T_C Magnets with Prussian Blue Analogues? A Theoretical Prospect," *Chemistry: A European Journal,* vol. 11, pp. 2135-44, 2005.
[174] M. Verdaguer, "Rational synthesis of molecular magnetic materials: a tribute to Olivier Kahn," *POLYHEDRON,* vol. 20, pp. 1115-1128, 2001.
[175] M. Verdaguer, A. Bleuzen, C. Train, R. Garde, F. F. d. Biani, and C. Desplanches, "Room-Temperature Molecule-Based Magnets," *Philosophical Transactions: Mathematical, Physical and Engineering Sciences,* vol. 357, pp. 2959-2976, 1999.
[176] H. U. Güdel, H. Stucki, and A. Ludi, "The Crystal Structure of Manganese(II) Hexacyanochromate(III), Mn$_3$[Cr(CN)$_6$]$_2$.xH$_2$O," *Inoganica Chimica Acta,* vol. 7, pp. 121-124, 1973.
[177] G. Giriat, "Study of magnetic interactions under pressure," MSc by research 2005.

[178] M. Zentková, Z. Arnold, J. Kamarád, V. Kavečanský, M. Lukáčová, S. Mat'aš, M. Mihalik, Z. Mitróová, and A. Zentko, "Effect of pressure on the magnetic properties of $TM_3[Cr(CN)_6]_2$•12H2O," *Journal of Physics: Condensed Matter,* vol. 19, p. 266217, 2007.

[179] G. Giriat, A. Harrison, D. R. Allan, K. V. Kamenev, and D. S. Middlemiss, "Tuning magnetic superexchange in a Prussian Blue Analogue with pressure," *Unpublished,* 2007.

[180] J. Catafesta, J. Haines, J. E. Zorzi, A. S. Pereira, and C. A. Perottoni, "Pressure-induced amorphization and decomposition of $Fe[Co(CN)_6]$," *Physical Review B,* vol. 77, p. 064104, 2008.

[181] D. Aoki, F. Hardy, A. Miyake, V. Taufour, T. D. Matsuda, and J. Flouquet, "Properties of ferromagnetic superconductors," *Comptes Rendus Physique,* vol. 12, pp. 573-583, 2011.

[182] D. Aoki, A. Huxley, E. Ressouche, D. Braithwaite, J. Flouquet, J.-P. Brison, E. Lhotel, and C. Paulsen, "Coexistence of superconductivity and ferromagnetism in URhGe," *Nature,* vol. 413, pp. 613-616, 2001.

[183] N. T. Huy, A. Gasparini, D. E. de Nijs, Y. Huang, J. C. P. Klaasse, T. Gortenmulder, A. de Visser, A. Hamann, T. Görlach, and H. v. Löhneysen, "Superconductivity on the Border of Weak Itinerant Ferromagnetism in UCoGe," *Physical Review Letters,* vol. 99, p. 67006, 2007.

[184] N. Tateiwa, T. C. Kobayashi, K. Hanazono, K. Amaya, Y. Haga, R. Settai, and Y. Onuki, "Pressure-induced superconductivity in a ferromagnet UGe_2," *Journal of Physics: Condensed Matter,* vol. 13, p. L17, 2001.

[185] D. Aoki, A. Huxley, E. Ressouche, I. Sheikin, J. Flouquet, J. P. Brison, and C. Paulsen, "Superconductivity in two itinerant uranium ferromagnets: UGe_2 and URhGe," *Journal of Physics and Chemistry of Solids,* vol. 63, pp. 1179-1182, 2002.

[186] A. P. Gonçalves, M. S. Henriques, J. C. Waerenborgh, L. C. J. Pereira, E. B. Lopes, M. Almeida, S. Mašková, L. Havela, A. Shick, Z. Arnold, D. Berthebaud, O. Tougait, and H. Noël, "Peculiarities of U-based Laves phases," *IOP Conference Series: Materials Science and Engineering,* vol. 9, p. 12090, 2010.

[187] S. Mat'as, M. Mihalik, A. A. Menovsky, Z. Arnold, and O. Mikulina, "Magnetic properties of UNi_2 single crystal," *ACTA PHYSICA SLOVACA,* vol. 48, pp. 811-814, 1998.

[188] V. Sechovsky, L. Havela, J. Hrebik, A. Zentko, P. Diko, and J. Sternberk, "The origin of magnetism in UNi_2," *Physica B+C,* vol. 130, pp. 243-244, 1985.

[189] S. Ishiwata, M. Azuma, M. Takano, E. Nishibori, M. Takata, M. Sakata, and K. Kato, "High pressure synthesis, crystal structure and physical properties of a new Ni(ii) perovskite $BiNiO_3$," *Journal of Materials Chemistry,* vol. 12, pp. 3733-3737, 2002.

[190] S. J. E. Carlsson, M. Azuma, Y. Shimakawa, M. Takano, A. Hewat, and J. P. Attfield, "Neutron powder diffraction study of the crystal and magnetic structures of $BiNiO_3$ at low temperature," *Journal of Solid State Chemistry,* vol. 181, pp. 611-615, 2008.

[191] S. Ishiwata, M. Azuma, and M. Takano, "Pressure-induced metal-insulator transition in $BiNiO_3$," *Solid State Ionics,* vol. 172, pp. 569-571, 2004.

[192] M. Azuma, S. Carlsson, J. Rodgers, M. G. Tucker, M. Tsujimoto, S. Ishiwata, S. Isoda, Y. Shimakawa, M. Takano, and J. P. Attfield, "Pressure-induced intermetallic valence transition in $BiNiO_3$," *Journal of the American Chemical Society,* vol. 129, pp. 14433-6, 2007.

[193] M. Mizumaki, N. Ishimatsu, N. Kawamura, M. Azuma, Y. Shimakawa, M. Takano, and T. Uozumi, "Direct observation of the pressure-induced charge redistribution in $BiNiO_3$ by x-ray absorption spectroscopy," *Physical Review B,* vol. 80, p. 233104, 2009.

[194] M. Azuma, W.-t. Chen, H. Seki, M. Czapski, S. Olga, K. Oka, M. Mizumaki, T. Watanuki, N. Ishimatsu, N. Kawamura, S. Ishiwata, M. G. Tucker, Y. Shimakawa, and J. P. Attfield, "Colossal negative thermal expansion in $BiNiO_3$ induced by intermetallic charge transfer," *Nat Commun,* vol. 2, p. 347, 2011.

[195] M. Q. Cai, G. W. Yang, X. Tan, Y. L. Cao, L. L. Wang, W. Y. Hu, and Y. G. Wang, "First-principles study of pressure-induced metal-insulator transition in $BiNiO_3$," *Applied Physics Letters,* vol. 91, p. 101901, 2007.

[196] S. Ishiwata, M. Azuma, M. Hanawa, Y. Moritomo, Y. Ohishi, K. Kato, M. Takata, E. Nishibori, M. Sakata, I. Terasaki, and M. Takano, "Pressure/temperature/substitution-induced melting of A-site charge disproportionation in $Bi_{1-x}La_xNiO_3$ ($0<x<0.5$)," *Physical Review B,* vol. 72, p. 45104, 2005.

[197] S. Vaucher, M. Li, and S. Mann, "Synthesis of Prussian Blue Nanoparticles and Nanocrystal Superlattices in Reverse Microemulsions," *Angewandte Chemie International Edition,* vol. 39, pp. 1793-1796, 2000.

[198] M. Yamada, M. Arai, M. Kurihara, M. Sakamoto, and M. Miyake, "Synthesis and Isolation of Cobalt Hexacyanoferrate/Chromate Metal Coordination Nanopolymers Stabilized by Alkylamino Ligand with Metal Elemental Control," *Journal of the American Chemical Society,* vol. 126, pp. 9482-9483, 2004.

[199] L. Catala, A. Gloter, O. Stephan, G. Rogez, and T. Mallah, "Superparamagnetic bimetallic cyanide-bridged coordination nanoparticles with $T_B = 9$ K," *Chemical Communications,* pp. 1018-1020, 2006.

[200] V. Blanco-Gutierrez, R. Saez-Puche, and M. J. Torralvo-Fernandez, "Superparamagnetism and interparticle interactions in $ZnFe_2O_4$ nanocrystals," *Journal of Materials Chemistry,* vol. 22, pp. 2992-3003, 2012.

[201] Y. Prado, L. Lisnard, D. Heurtaux, G. Rogez, A. Gloter, O. Stephan, N. Dia, E. Riviere, L. Catala, and T. Mallah, "Tailored coordination nanoparticles: assessing the magnetic single-domain critical size," *Chemical Communications,* vol. 47, pp. 1051-1053, 2011.

[202] D. Brinzei, L. Catala, N. Louvain, G. Rogez, O. Stéphan, A. Gloter, and T. Mallah, "Spontaneous stabilization and isolation of dispersible bimetallic coordination nanoparticles of $Cs_xNi[Cr(CN)_6]_y$," *Journal of Materials Chemistry,* vol. 16, pp. 2593-2599, 2006.

[203] V. Gadet, T. Mallah, I. Castro, M. Verdaguer, and P. Veillet, "High-T_C molecular-based magnets: a ferromagnetic bimetallic chromium(III)-nickel(II) cyanide with $T_C = 90$ K," *Journal of the American Chemical Society,* vol. 114, pp. 9213-9214, 1992.

[204] E. Coronado, M. C. Giménez-López, G. Levchenko, F. M. Romero, V. García-Baonza, A. Milner, and M. Paz-Pasternak, "Pressure-tuning of magnetism and linkage isomerism in iron(II) hexacyanochromate.," *Journal of the American Chemical Society,* vol. 127, pp. 4580-1, 2005.

[205] A. Zentko, M. Zentkova, V. Kavecansky, M. Mihalik, Z. Mitroova, Z. Arnold, J. Kamarad, M. Cieslar, and V. Zelenak, "Effect of pressure on magnetic properties of $TM_3[Cr(CN)_6]_2 \bullet nH_2O$ nanoparticles," *ACTA PHYSICA POLONICA A,* vol. 113, pp. 489-493, 2008.

[206] R. N. Muller, L. Vander Elst, and S. Laurent, "Spin Transition Molecular Materials: Intelligent Contrast Agents for Magnetic Resonance Imaging," *Journal of the American Chemical Society,* vol. 125, pp. 8405-8407, 2003.

[207] R. A. Sadykov, N. S. Bezaeva, A. I. Kharkovskiy, P. Rochette, J. Gattacceca, and V. I. Trukhin, "Nonmagnetic high pressure cell for magnetic remanence measurements up to 1.5 GPa in a superconducting quantum interference device magnetometer," *Review of Scientific Instruments,* vol. 79, p. 115102, 2008.

[208] S. Baragetti, A. Terranova, and M. Vimercati, "Friction behaviour evaluation in beryllium-copper threaded connections," *International Journal of Mechanical Sciences,* vol. 51, pp. 790-796, 2009.

[209] *Omega Engineering Limited*. Available: http://www.omega.co.uk/

[210] A. Dawson, D. R. Allan, S. Parsons, and M. Ruf, "Use of a CCD diffractometer in crystal structure determinations at high pressure," *Journal of applied crystallography,* vol. 37, pp. 410-416, 2004.

[211] G. Ventura and V. Martelli, "Low temperature thermal conductivity of PVC," in *Astroparticle, Particle, Space Physics, Radiation Interaction, Detectors and Medical Physics Applications*, Como, 2009, pp. 145-149.

[212] B. Sundqvist, "Thermal diffusivity and thermal conductivity of Chromel, Alumel, and Constantan in the range 100-450 K," *Journal of Applied Physics,* vol. 72, pp. 539-545, 1992.

[213] R. W. Powell, C.-Y. Ho, and P. E. Liley, "Thermal conductivity of selected materials.," *National Standard Reference Data Series (United States, National Bureau of Standards),* vol. No. 8, p. 165, 1966.

[214] R. J. DICKINSON, "THERMAL CONDUCTION ERRORS OF MANGANIN-CONSTANTAN THERMOCOUPLE ARRAYS," *PHYSICS IN MEDICINE AND BIOLOGY,* vol. 30, pp. 445-453, 1985.

[215] M. Tarnopolsky and I. Seginer, "Leaf temperature error from heat conduction along thermocouple wires," *Agricultural and Forest Meteorology,* vol. 93, pp. 185-194, 1999.

[216] M. H. Attia, A. Cameron, and L. Kops, "Distortion in Thermal Field Around Inserted Thermocouples in Experimental Interfacial Studies, Part 4: End Effect," *Journal of Manufacturing Science and Engineering,* vol. 124, pp. 135-145, 2002.

[217] J. W. Woolley, M. A. Bestor, M. L. Weaver, and K. A. Woodbury, "Obtaining the Sensed Temperatures From a Detailed Model of a Welded Thermocouple," in *ASME Conference Proceedings*, 2008, pp. 649-655.

[218] S. Gondipalli, S. Bhopte, B. Sammakia, and V. Calmidi, "NUMERICAL AND EXPERIMENTAL STUDY OF THE EFFECT OF THERMOCOUPLE WIRE ATTACHMENT ON THERMAL CHARACTERIZATION OF A HIGH PERFORMANCE FLIPCHIP PACKAGE," in *2010 12TH IEEE INTERSOCIETY CONFERENCE ON THERMAL AND THERMOMECHANICAL PHENOMENA IN ELECTRONIC SYSTEMS*, NEW YORK, 2010.

[219] *Neoptix*. Available: www.neoptix.com

[220] A. Kelly, "Composite materials after seventy years," *Journal of Materials Science,* vol. 41, pp. 905-912, 2006.

[221] Y. Huang, P. H. Frings, and E. Hennes, "Mechanical properties of Zylon/epoxy composite," *Composites Part B: Engineering,* vol. 33, pp. 109-115, 2002.

[222] G. C. Davies and D. M. Bruce, "A stress analysis model for composite coaxial cylinders," *Journal of Materials Science,* vol. 32, pp. 5425-5437, 1997.

[223] A. D. Hibbs, R. E. Sager, S. Kumar, J. E. McArthur, A. L. Singsaas, K. G. Jensen, M. A. Steindorf, T. A. Aukerman, and H. M. Schneider, "A SQUID-based ac susceptometer," *Review of Scientific Instruments,* vol. 65, pp. 2644-2652, 1994.

[224] *Toyobo Co.,Ltd.* . Available: http://www.toyobo-global.com

[225] K. Rosseel, F. Herlach, W. Boon, and Y. Bruynseraede, "Zylon-reinforced high magnetic field coils for the K.U. Leuven pulsed field laboratory," *Physica B: Condensed Matter,* vol. 294-295, pp. 657-660, 2001.

[226] *Ensinger, Inc.* Available: http://www.ensinger-online.com

[227] *Quantum Design, Inc.* Available: http://www.qdusa.com

[228] D. B. McWhan, D. Bloch, and G. Parisot, "Apparatus for neutron diffraction at high pressure," *Review of Scientific Instruments,* vol. 45, pp. 643-646, 1974.

[229] *XYZ*. Available: http://www.xyzmachinetools.com/

[230] *WhizCut*. Available: http://www.whizcut.com/